UNIVERSITÄT DUISBURG ESSEN

Open-Minded

Novel micro- and nano-patterned water desalination membranes

Dissertation

zur Erlangung des akademischen Grades eines Doktors der Naturwissenschaften

- Dr. rer. nat.-

vorgelegt von

Ibrahim Mohamed Ahmed ElSherbiny

geboren in Giza, *Ägypten*

Fakultät für Chemie

der

Universität Duisburg-Essen

Essen 2017

To all who believes in me and

supports me .... Thank you!

Approved by the examining committee on March, 19th 2018:

Chair: **Prof. Dr. Eckart Hasselbrink**

Advisor: **Prof. Dr. Mathias Ulbricht**

Reviewer: **Prof. Dr.-Ing Stefan Panglisch**

Declaration:

The work presented here was carried out in the period from May 2013 till June 2017 at the Department of Technical Chemistry II – Faculty of Chemistry – University of Duisburg-Essen, and partially in labs of Center for Environmental and Smart Technology – Fayoum University – Egypt, under supervision of Prof. Dr. Mathias Ulbricht.

Hereby, I declare that this dissertation represents my own work, except where due acknowledgement is made.

Signature: Ibrahim ElSherbiny

- Ibrahim ElSherbiny -

Abstract

Nowadays, water desalination using reverse osmosis membranes has been recognized as one of versatile steady technologies that can potentially fulfill the global growing needs for drinking water. Polyamide thin-film composite (PA TFC) membranes are currently the most abundantly used membrane materials for most of the desalination plants. They have been remarkably developed over the last decades toward efficient separation agents exhibiting improved performance and extended operating time. Among several suggested strategies, the introduction of the "super-switching" concept is considered as a new interesting trend for sustainable water desalination technology. The "super-switching" properties can be specifically adapted to water desalination membranes via consolidating two different phenomena; "surface micro-patterning" and "double stimuli-responsivity".

Here, a novel surface micro-patterning approach is presented as a promising platform toward PA TFC membranes of superior performance. Micro-patterned PA TFC membranes were successfully fabricated using two microfabrication methods, combined processes of vapor- and liquid non-solvent induced phase separation micro-molding, as well as micro-imprinting lithography, followed by systematic refinement of the interfacial polymerization conditions on the patterned membrane supports. The micro-patterned PA TFC membranes were observed to exhibit superior water permeability, ~ 2 – 2.4 times compared to flat PA TFC membranes, without sacrificing the membrane selectivity. A detailed concentration polarization analysis employing different membrane orientations, with patterned grooves "parallel" and "perpendicular" to the direction of feed cross-flow, was also carried out. The results emphasized the merits of implementing the micro-patterned TFC membranes in promoting the separation performance, especially at high feed concentrations. "Parallel" orientation was always favorable because of remarkable reduction of concentration polarization as a result of enhanced surface mixing.

Afterward, a convenient surface modification method was investigated and adapted in order to prepare "super-switching" desalination membranes via grafting of a double stimuli-responsive layer, made from poly(*N*-isopropylacrylamide) homopolymer and its copolymers with poly(acrylic acid), atop the micro-patterned PA TFC membranes. The results revealed the ability of the surface-modified micro-patterned PA TFC membranes to switch between very high hydrophilicity and high hydrophobicity upon changing of pH, temperature, or

combinations thereof. Additionally, the grafted layer was observed to enhance the membrane performance through a possible “repairing mechanism” for the selective PA layer.

Furthermore, the antifouling propensity of the newly developed PA TFC membranes toward colloidal silica fouling was studied employing dead-end filtration mode at no stirring conditions. The membrane surface topography and roughness were emphasized to be the most influential parameters, while the chemical surface modification had a secondary impact.

Overall, the detailed development steps of different membrane layers in order to prepare surface-modified micro-patterned PA TFC membranes are systematically introduced in this work and reinforced by the relevant characterization and testing experiments.

Acknowledgment

I would like to express my great appreciation to **Prof. Dr. Mathias Ulbricht** for offering me this great opportunity to pursuing my Ph.D. study in his working group. I am very grateful for his guidance, fruitful discussions and valuable comments. His willingness to give his time so generously and endless support to me are always highly appreciated.

I would like also to express my deep gratitude to **Dr. Ahmed S. G. Khalil**, Director of Center for Environmental and Smart Technology – Fayoum University – Egypt, for his sincere advice, constructive critiques, supporting and motivating me. I owe him a big part of my success.

The current work is a part of "SURSYS" project (grant # 57072353) funded by German Academic Exchange Service (DAAD) and financed by the Federal Foreign Office of Germany.

I would like to offer my special thanks to **Prof. Dr.-Ing Stefan Panglisch** for his acceptance to be a reviewer for my dissertation project. I highly appreciate his precious comments and recommendations. My deep thanks are also extended to **Prof. Dr. Eckart Hasselbrink** for kindly being the chair of the examination committee.

Moreover, I wish to acknowledge the great support and precious efforts provided by the team at the Center for Water and Environmental Research (ZWU) at University of Duisburg-Essen, in particular, **Simon Kresmann** and **Dr. Michael Eisinger**.

I would like also to highly appreciate the sincere assistance and logistic support provided by Dipl.-Ing. **Inge Danielzik**, Dipl.-Ing. **Tobias Kallweit**, **Claudia Schenk** and Mrs. **Roswitha Nordmann**.

Furthermore, I am very thankful to all the current and former friends, and colleagues at the department of Technical Chemistry II for the friendly and motivating working environment. In particular, I would like to thank **Ahmed Abdel Samad**, **Xi Lin** and **Alexander Dundua** for the fruitful discussions and suggestions during the work progression. Special thanks are devoted to **Inga Stratmann** and **Qirong Ke** for their sincere support and great help. My grateful thanks are also extended to **Marta Bojarska**, **Martyna Gajda**, **Marc Thomas**, **Jens Meyer**, **Thorsten van den Berg**, **Dominic Büning**, **Miao Li**, and **Franka Ennen** for their useful advice and help. I would like also to thank **Philipp Jahn** for working together during his master training and offering me figure 3.1. Additionally, I would like to acknowledge the support provided by my colleagues at the Center for Environmental and Smart Technology –

Fayoum University – Egypt, besides my colleagues at Faculty of Science – Ain Shams University – Egypt, in particular, **Mohamed Gad**.

In parallel, I would like to express my great appreciation to my best friend **Ahmed Ghanem** for his endless support, sincere help and encouraging me. I wish him a good luck for his doctoral study.

At last, I owe the deepest gratitude to my parents and brothers for their love, ultimate support and motivating me during the most stressful times.

Thank you very much for you all and I wish you the best of luck!

Ibrahim ElShubiny

Two scientific papers have been published out of this work:

1. Ibrahim M.A. ElSherbiny, Ahmed S.G. Khalil, Mathias Ulbricht, Surface micro-patterning as a promising platform towards novel polyamide thin-film composite membranes of superior performance, *Journal of Membrane Science* 529 (**2017**) 11-22
2. Ibrahim M.A. ElSherbiny, Rami Ghannam, Ahmed S.G. Khalil, Mathias Ulbricht, Isotropic macroporous polyethersulfone membranes as competitive supports for High performance polyamide desalination membranes, *Journal of Membrane Science* 493 (**2015**) 782-793.

List of contents

1 Introduction

A key statement we all often read, "*water is at the core of sustainable development*", in World Water Development Report 2015 by UNESCO's World Water Assessment Program [1], has become recently most obvious. Human health, food and energy security, urbanization and industrial growth, besides climate change are critical issues where policies and decisions are strongly influenced by the fresh water situation. Briefly, the global water demand is determined by population growth, food and energy security policies, macro-economic processes, e.g., trade globalization, as well as changing consumption patterns. Unsustainable development plans, governance failures, and water overuse have generated immense pressures on water resources. Additionally, the competition for water increases the risk of conflicts and inequitable access to water supply and sanitation leading to detrimental impacts on human health and world economies. It is found that only diarrheal diseases, caused mainly by unsafe drinking water and improper sanitation, result in 1.8 million deaths each year [2]. The overall annual economic loss in Africa due to a lack of clean water and basic sanitation is estimated at $28 billion [3].

Freshwater is found to constitute 2.5 % of Earth's water, < 1 % of which is accessible and currently used; however, ~ 97 % of Earth's water exits in oceans and seas as saltwater, and ~ 0.5% as brackish water in surface estuaries and salty underground aquifers [3, 4]. According to UNESCO reports, only 10 % of the freshwater is employed for domestic use that is absolutely not enough since 1.2 billion people worldwide have no safe drinking water and 2.6 billion lack the adequate sanitation [5]. Groundwater supplies are diminishing, about 20 % of the world's aquifers has already been over-exploited [1]. It is expected that the global water demand will increase by 55 % in 2050, basically because of industrial growth, thermal electricity generation and domestic use [6]. Subsequently, the potential of current fresh water

capacity to fulfill the growing demands is being challenged and no sustainable development unless the balance between demand and supply is restored.

Alternatively, the world's oceans and seas could satisfy the growing water needs employing the appropriate purification techniques [7]. Water desalination using reverse osmosis (RO) technology is currently the leading purification method and it is experiencing substantial growth [8, 9]. Numerous seawater desalination plants have been built in water-stressed regions, and they are expected to increase in the near future. In 2016, the global water production using RO desalination exceeded 38 billion m^3 per year that is nearly twice the water production using RO desalination in 2008 [10]. Nevertheless, RO technology is still more energy-intensive, in comparison with conventional freshwater treatments [9, 11]. In addition, there are growing concerns regarding the potential environmental impacts of seawater desalination plants [9]. Therefore, notwithstanding the potency of RO technology as promising straightforward alternative to tackle the increasing global water needs, an amelioration of all process components is still required to make RO technology more energy-efficient and accessible for more water-stressed countries.

1.1 Problem definition

Water desalination is a technology that converts saline water into a clean water. Today, RO is the leading desalination technology. In RO, a semi-permeable membrane is used to separate pure water from seawater under operating pressure higher than upstream osmotic pressure [9, 12]. Therefore, water desalination using RO technology is an energy-intensive process [7]. Nevertheless, the amount of power required to operate RO plants has declined dramatically over the past 40 years [13, 14], as a result of continual improvement in RO technology and module designs, development of efficient membranes, in addition to installation of energy recovery devices. This led to a substantial decrease in the energy consumption from about 12 kWh/m^3 in the 1970s to 2.5 – 3.5 kWh/m^3 nowadays [9, 11, 15].

Since 1980s, robust polyamide (PA) thin-film composite (TFC) membranes were developed as efficient RO membrane materials that exhibit high intrinsic water permeability as a result of ultrathin PA barrier layer (~100 nm), and stable performance over a wide pH range [16]. The transport mechanism across such membranes is governed by a solution-diffusion mechanism [17]. Nowadays, PA TFC membranes exhibit water permeability of ~ 3.5 x 10^{-12} m^3/m^2.s.Pa and are able to reject about 99.6 to 99.8 % of all dissolved salts [14]. The theoretical minimum energy required to separate pure water from seawater is estimated by assuming that the

separation occurs as a reversible thermodynamic process [18], and equals in magnitude but opposite in sign to the free energy of mixing [19]. For example, the theoretical minimum energy of desalination for seawater at 35,000 ppm salinity and at 50 % recovery is 1.06 kWh/m^3 [9]. Nevertheless, the actual energy consumption is essentially higher. Fritzmann et al. revealed that the additional energy can be more than 1 kWh/m^3 due to the pretreatment and post-treatment steps, besides brine discharge stages [13].

In response to that, membrane scientists have proposed different refinement routes to improve the energy efficiency of the water desalination RO technology. However, the development of the membrane materials and module design have attracted more attention rather than the desalination process itself, because it is already operated close to the thermodynamic limit [9]. Ultrahigh-permeability membranes have recently been suggested as possible alternatives to the current PA TFC membranes [9, 11, 20]. It was argued that improving the membrane permeability would reduce the required operating pressure and; consequently, diminish the energy consumption. Generally, ultrahigh-permeability membranes were attempted to be fabricated by incorporating either aligned carbon nanotubes [21, 22] or aquaporins [23] into (PA) barrier layer. Modified membranes by carbon nanotubes showed more potential for flux enhancement; however, more efforts are still necessitated to produce membranes exhibiting selectivity comparable to PA TFC membranes [9, 11, 20]. These membranes, however, are expected to be very expensive. Moreover, to date, there is no experimental evidence that such membranes can exhibit selectivity suitable for desalination [20].

The insignificance of ultrahigh-permeability membranes on the process efficiency is also predicted for PA TFC membranes. Empirical investigations emphasized that it is difficult to improve furtherly the water permeability of PA TFC membranes without sacrificing the membrane selectivity [24]. However, simulation studies has shown that improving the water permeability of RO seawater desalination membranes from 2 L/h.m^2.bar to 10 L/h.m^2.bar will reduce the energy consumption by 3.7 % only [25]. Furthermore, the concentration polarization and fouling rate are also expected to be induced by high water fluxes, indeed, that will impair the water transport and the permeate salinity at advanced working times [26].

Therefore, more reliable and efficient amelioration strategies are suggested. The minimum energy for desalination can be substantially diminished by eliminating the pretreatment steps or reducing the pretreatment demands; however, this can be achieved only via development of new fouling-resistant PA TFC membranes with tailored surface characteristics, accompanied

by effective managing of the hydrodynamics near the feed side of the membrane surface [9, 20]. Accomplishing this target is a daunting mission since any improvement to membrane surface characteristics or the membrane modules should not have detrimental influence on the membrane selectivity, i.e., the quality of the desalted water.

1.2 Aim of the work

The concept of "super-switching" membrane surfaces is suggested as a new interesting approach to improve the separation performance and antifouling propensity of PA TFC membranes and consequently, reduce the minimum energy for desalination. The "super-switching" properties can be specifically adapted to water desalination membranes via consolidating two different phenomena; "surface micro-patterning" and "double stimuli-responsivity". An illustration for the suggested membrane model is presented in **Figure 1.1**. Each phenomenon has been individually investigated in literature for diverse applications; nevertheless, to the best of our knowledge, it is the first time to combine these two approaches for water desalination PA TFC membranes.

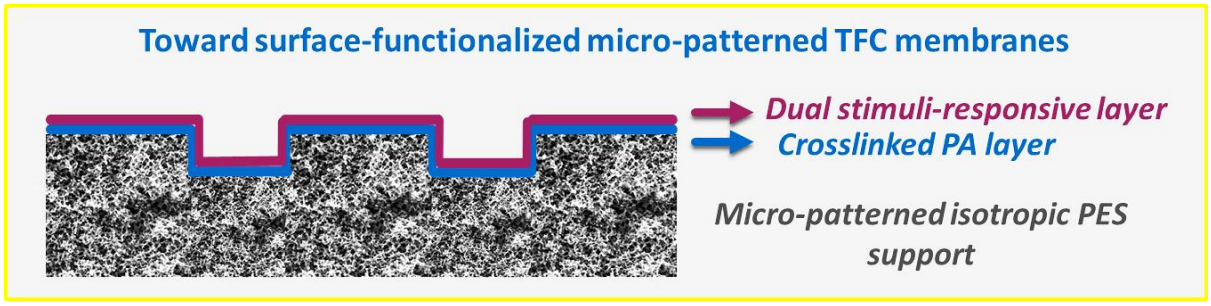

Figure 1.1: Illustration for the suggested PA TFC membrane model

The potential of the suggested membrane system to promote the membrane performance toward sustainable membrane-based water desalination process can be interpreted by deep looking to the expected merits of each approach. Altering the membrane surface topography via introducing of specific surface micro-patterns is believed to increase the active membrane surface area, promote surface roughness, improve the hydrodynamics, i.e., mixing and shear stress, near the membrane surface and influence the particle deposition behavior [27, 28]. In parallel, the controlling of surface wetting properties by grafting of a thin layer of double stimuli-responsive atop micro-patterned PA TFC membranes is expected to offer PA TFC membranes the capability of switching between super-hydrophilicity and super-hydrophobicity states [29], for the first time, which may be beneficial to enhance the antifouling propensity as well as the membrane cleaning process.

1.3 Scope of the work

In the way to achieve the research objectives, numerous topics concerning development of different membrane layers are addressed. The research can be classified into four main work packages, namely;

(i) Development of robust isotropic PES base membranes and their feasibility as supports for PA TFC membranes

(ii) Development of surface micro-patterned PA TFC membranes

(iii) Surface modification of micro-patterned PA TFC membranes toward membranes of super-switching wettability

(iv) Evaluation of antifouling propensity using colloidal silica fouling experiments

The tasks and the outputs for each work package can be briefly described in the following:

Work package (i) Development of robust isotropic PES base membranes and their feasibility as supports for PA TFC membranes:

1. Optimization of PES/PVP/NMP/TEG casting solution and adaptation of casting conditions, e.g., exposure time to humid air, based on research findings by Susanto et al. [30].
2. Refinement of experimental conditions of typical interfacial polymerization reaction [31], and investigation of the influence of support's characteristics on the performance and surface properties of PA barrier layer.

- *Characterization of base membrane*:
  Investigation of pore and transport characteristics, besides membrane porosity, surface chemistry, hydrophilicity and morphology.
- *Characterization of flat PA TFC membranes*:
  Measurement of separation performance (dead-end filtration of NaCl solution) and pure water permeability. Additionally, investigation of membrane surface chemistry, charge, hydrophilicity, morphology and roughness.

Work package (ii) Development of surface micro-patterned PA TFC membranes:

1. Development of micro-patterned PES support using optimized casting solution in work package (i). Two surface micro-patterning techniques are exploited, phase separation micro-molding (PSμM), as well as micro-imprinting lithography (MIL). The difference in the surface micro-patterning fidelity and mechanism is explored.

2. Adaptation of PA layer formation atop micro-patterned PES supports.
3. Investigation of the influence of surface micro-structures on both separation performance and concentration polarization parameters.

- *Characterization of micro-patterned supports*:
  Investigation of the change in the pore and transport characteristics, in addition to membrane surface chemistry, hydrophilicity, morphology and surface roughness.
- *Characterization of micro-patterned PA TFC membranes*:
  Measurement of perm-selective properties employing dead-end and cross-flow filtration experiments of NaCl solutions of different feed concentrations. In parallel, investigation of membrane surface chemistry, charge, hydrophilicity, morphology and roughness.

Work package (iii) Surface modification of micro-patterned PA TFC membranes toward membranes of super-switching wettability:

1. Surface modification of micro-patterned PA TFC membranes by acylamide-based polymer coating materials. In situ surface coating method using carbodiimide coupling was employed as an example for "*grafting to*" approach, while surface-initiated atom transfer radical polymerization was exploited as an example for "*grafting from*" approach.
2. Synthesis and characterization of acrylamide-based polymer coating materials by free-radical polymerization.

- *Characterization of surface-modified micro-patterned PA TFC membranes*:
  Evaluation of super-switching properties by measurement of static water contact angle at different temperature and pH values by means of captive bubble method. Assessment of perm-selective properties after the surface modification process employing dead-end filtration experiments of various feed solutions, NaCl, $CaCl_2$ and Na_2SO_4, in addition to dead-end filtration of buffer solutions at pH 3 and pH 7. In parallel, investigation of membrane surface chemistry, charge, morphology and roughness.

Work package (iv) Evaluation of antifouling propensity using colloidal silica fouling experiments:

1. Study the colloidal silica fouling of the surface-modified and pristine flat and micro-patterned PA TFC membranes using two silica model particles, nano-particles (50 nm) and micro-particles (500 nm).

2. Investigation of the applicability of cake filtration model.
3. Analysis of the silica cake layer by means of scanning electron microscope.
4. Investigation of the influence of external stimuli on the colloidal fouling behavior for selected membranes. The investigated stimuli include, effect of temperature, effect of stirring, and combined effect of temperature and stirring.
5. Suggestion of a mechanism describing the deposition of silica micro-particles on the micro-patterned membrane surfaces.

This page is intended to be empty

2 Theory and literature review

2.1 Water desalination technology

Desalination is a general physical term describing the process of removing salt from seawater to produce fresh water [8]. Fresh water is defined to comprise less than 1000 mg/L of salts, expressed by total dissolved solids or TDS [32]. If TDS increases to be more than 1000 mg/L, most of the water's physical properties, e.g., taste, color, hardness, corrosivity, are changed. The WHO recommends a TDS standard level for drinking water to be below 1000 mg/L [13]. Nevertheless, most of the current desalination facilities are designed to realize a TDS level of ≤ 500 mg/L [8, 33].

In parallel, the salinity of the feed water can differ according to the source. Typically, the feed for the water desalination plants is one of two types, seawater (TDS range 30,000 – 45,000 mg/L), and brackish water (TDS range 1000 – 10,000 mg/L). However, seawater RO membranes in the markets are designed to reject salts up to 60,000 mg/L [8].

In principle, water desalination processes fall into two different categories namely, thermal desalination processes, or distillation, and membrane-based desalination processes, mainly RO technology. Thermal desalination has been known for hundreds of years as a simple physical process to produce fresh water, but the first drinking water distillation plant was opened in the 1950s [34]. Because of the lack of fresh water resources, the Middle East countries have pioneered the technology of seawater distillation, first using multi-effect distillation process (MED), afterward more advanced process called multi-stage flash (MSF) distillation [35]. In parallel, membrane-based desalination processes have been rapidly developed since 1960s [36]. Nowadays, RO technology dominates the water desalination processes by 80 % share in the total number of installed desalination plants worldwide [8].

The largest seawater desalination plant using RO technology has opened in Sorek, Israel in 2013. It produces about 624,000 m^3/day [37]. However, the highest fresh water production worldwide, ~ 728,000 m^3/day, has been achieved by Ras Al Khair desalination plant that was opened in 2014 in Saudi Arabia by combining RO and MSF technologies [38].

2.2 Development of RO membrane materials

The first RO membrane was made of a hand-cast symmetric cellulose acetate membrane by Reid and Breton in late 1950s [39]. This membrane exhibited 98 % salt rejection, but the permeability was very low. Later, Loeb and Sourirajan developed asymmetric cellulose acetate membrane comprising dense layer ~ 200 nm over a thick macroporous support [36]. This membrane was of a great importance since it could bring the RO technology to large-scale production. Then, cellulose triacetate RO membrane was developed because of its higher thermal and pH stability than cellulose diacetate membrane; however, its susceptibility to compaction was a major downside [40]. Cellulose acetate membranes remained the best RO membrane until 1969.

Afterward, the first non-cellulosic RO membrane was introduced by Richter and Hoehn [41]. It consisted of aromatic PA hollow fiber membrane and it was employed for brackish water desalination. Nevertheless, this membrane suffered from low resistance towards disinfectants; subsequently, more chlorine-resistant asymmetric RO membranes based on polypiperazine-amides were developed [42]. On the other hand, these membranes weren't commercialized because of their relatively low salt rejection [43].

Polysulfone membrane materials was introduced as potential supports of good resistance to compaction, reasonable flux, in addition to good chemical stability [72]. Additionally, they underpinned the implementation of interfacial polymerization to fabricate composite RO membranes such that Cadotte developed NS-100 RO membrane by interfacial polymerization between polyethylenimine and toluene di-isocyanate [44]. NS-100 was the first successful non-cellulosic membrane exhibiting comparable flux, high monovalent salt rejection as well as higher thermal and chemical stability [45]. Nevertheless, it endured no resistance to chlorine.

Thereafter, Cadotte found that high selective and water permeable RO membranes can be produced using interfacial polymerization reaction between aromatic amines and aromatic acyl halides, containing at least three carbonyl halide groups [46]. The best example was FT-30 RO membrane that was prepared by interfacial polymerization reaction between 1,3-benzenediamine (m-phenylene diamine, MPD) with 1,3,5-benzenetricarbonyl trichloride (tri-

mesoyl chloride, TMC) [16] (**Figure 2.1**). FT-30 membranes exhibited a distinguishable surface morphology, "ridge and valley", which was found to increase the effective surface area for water permeation. Pilot studies emphasized that FT-30 can reject salts by 99.2 % and produce pure water flux of 1 m^3/m^2.day at operating pressure of 55 bar. Also, they showed high mechanical, chemical and thermal resistance, along with an acceptable degree of tolerance to chlorine [47].

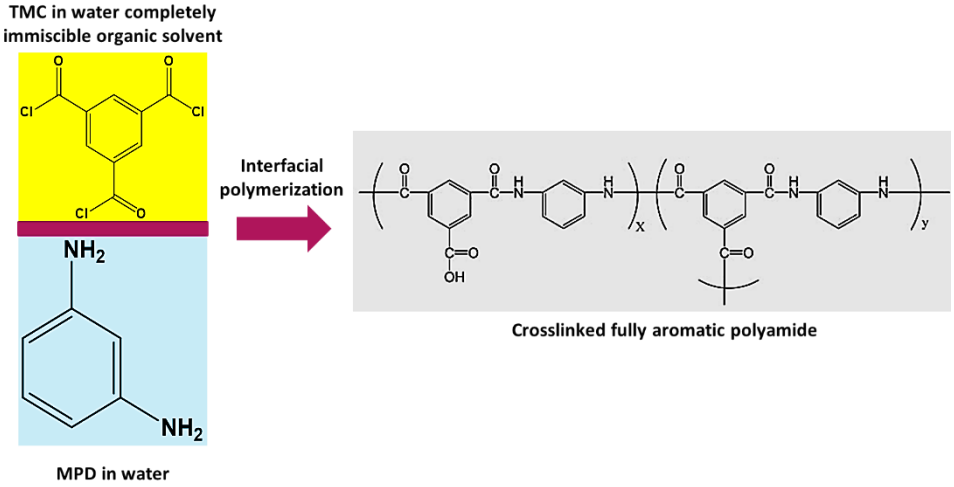

Figure 2.1: Synthesis of crosslinked fully aromatic polyamide via interfacial polymerization as introduced by Cadotte

2.3 Polyamide thin film composite membranes

Nowadays, RO membrane market is dominated by PA TFC membranes, which are typically consisting of three layers (**Figure 2.2 (a)**), (i) a polyester non-woven fabric as mechanical support, usually 120 – 150 µm thickness. (ii) macroporous interlayer made of asymmetric micro- / ultra-filtration polysulfone of about 40 – 50 µm thickness, (iii) ultrathin polyamide barrier layer of 100 – 200 nm thickness [7, 11, 46]. One of the major advantages of such TFC structure is the ease of achieving optimal separation performance by tailoring each layer individually.

As seen from the structure, the polyester fabric cannot be used as a direct support for the PA barrier layer due to its highly irregular porous structure, hence macroporous interlayer of good mechanical and chemical stability was employed. The barrier PA layer is typically very thin to obtain high water permeability; however, the pore structure is symmetric and the pore size has to be lower than 0.6 nm to achieve salt rejection ≥ 99 % [9, 11, 48]. The current membrane structure is very close to FT-30 membrane that was developed by Cadotte and dominated the RO membrane market for a long time. FT-30 membranes exhibited some advantages over the traditional cellulose acetate asymmetric membranes, higher water flux and membrane

selectivity, enhanced thermal resistance, wide operational pH range, improved structural robustness, and better resistance to hydrolysis and biological attack; however, they are susceptible to oxidative degradation [7, 11, 12].

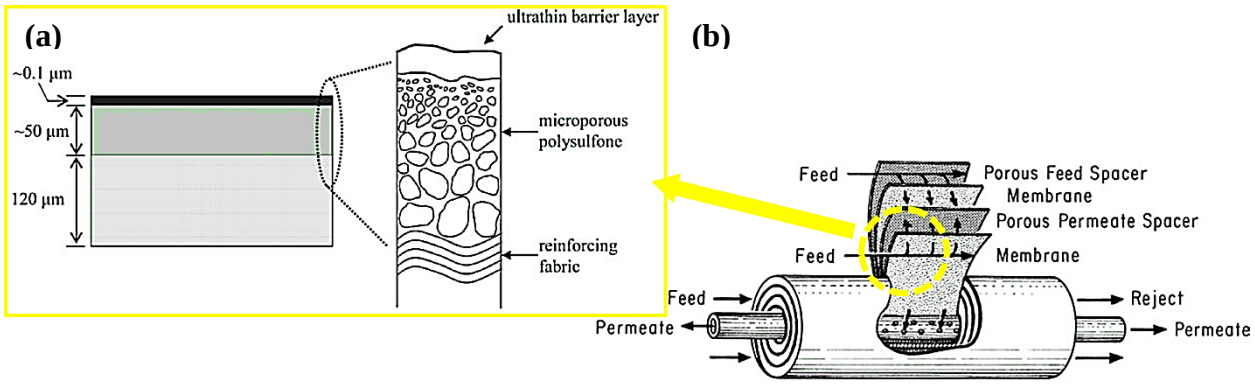

Figure 2.2: (a) Schematic diagram of PA TFC membrane, (b) Illustration for spiral wound module, adapted from [7]

PA spiral wound membrane modules are the most abundantly employed membrane design in RO desalination plants (**Figure 2.2 (b)**). This configuration offers high effective membrane area available for water transport, simple scaling up operation, low replacement costs, besides it is the least expensive and viable module configuration made of flat sheet TFC membranes [49]. Since it was developed decades ago, its basic components, spacers, feed channels and vessels, have been substantially improved to achieve enhanced hydrodynamic characteristics to minimize the fouling, scaling and possible pressure drops [7, 11]. In comparison with cellulose acetate hollow fibers, PA spiral wound membranes exhibit higher salt rejection and net driving force [11]. Nevertheless, there is still a need to develop an adequate scaling up technology to manufacture the hollow fiber configuration from the PA flat sheets, which is expected to lead to a revolution in RO desalination technology because of its higher packing density that will have a major influence on the energy demands [9].

The chemistry and perm-selectivity of PA TFC membranes have been extensively studied. In the following subsections more insights into different preparation methods, influence of fabrication conditions and support's characteristics on PA properties and selectivity, in addition to the possible transport mechanisms through PA barrier film will be briefly introduced.

2.3.1 Common fabrication approaches

Since the mid of 1970s till today, the interfacial polymerization method is the most efficient procedure to synthesis PA TFC membranes on a wide range of supports with different thicknesses using or without additives [50, 51]. Nevertheless, several alternative synthesis

routes have been proposed to enhance the fabrication efficiency, obtain more controlled synthesis procedure, and promote the scaling up process. For example, Hu and Mi developed a layer-by-layer deposition method to prepare graphene oxide-modified PA membranes [52]. Also, Chen et al. introduced an automated spin-coater assisted layer-by-layer assembly to fabricate crosslinked fully aromatic PA films [53].

2.3.1.1 Synthesis of PA TFC membranes via interfacial polymerization

Interfacial polymerization (IP) method, firstly introduced by Wittbecker and Morgan in 1959 [54], is a procedure employed for rapid synthesis of high molecular weight PA polymer thin films at room temperature [48]. Generally, the preparation of PA barrier layer on macroporous support starts with the imbibition of the support in an aqueous solution of diamine monomer, usually MPD, thereafter the support is immersed in a water immiscible organic solution of tri-functional acid chloride, TMC in n-hexane (**Figure 2.1**). Because of the difference in the chemical potentials of the two immiscible solutions, the monomers diffuse toward the interface to initiate the chemical reaction [55]. More specifically, MPD was emphasized to diffuse into the organic layer, due to its partial miscibility in n-hexane, and reacts with TMC; consequently, the reaction is known to be diffusion-controlled in the organic phase [48].

The kinetics of the PA film formation via IP has been comprehensively studied in practice as well as using advanced simulation models. The main findings of these studies can be briefly presented in the following points:

- IP method is an irreversible reaction of two highly reactive intermediates at the interface [56]. Also, the PA film is grown in the organic phase [57]. Recent modeling has found that PA films are formed through growth and aggregation of oligomer clusters [58].
- IP is a self-limiting reaction, i.e., it produces a dense PA film that hinders further diffusion of diamine monomers across the film; consequently, the total layer thickness of the PA films are typically ultrathin (100 – 200 nm) [59].
- Recently, it has been simulated and observed that IP produces “crumpled” PA film, whose individual thickness is in range of 5 – 10 nm, and the crumpling results in rough PA films [58, 60].
- The produced PA films are typically inhomogeneous, exhibiting different gradients of trapped unreacted groups, besides local density variations [58].
- The organic side of the PA film has been observed to exhibit a nonporous structure, whereas the aqueous side has looser and more porous structure [59].

Moreover, the presence of unreacted functional groups, i.e., acyl and amino groups, has emphasized to influence the surface charge of the produced PA films, which in turn, affects the separation performance and antifouling propensity [48, 51]. The surface charge can be manipulated by changing the environmental pH that induces protonation and deprotonation of the surface functional groups, resulting in charged PA TFC membranes.

Furthermore, the PA film formation is accompanied by liberating hydrochloric acid as a byproduct, which was reported to locally impact the diamine monomer reactivity, and hence it can affect the PA film porosity [48, 51].

2.3.2 Different parameters influencing PA TFC membranes

The surface characteristics, separation performance and stability of PA TFC membranes prepared by IP method have been emphasized to be dependent on a wide range of parameters. Those are IP reaction parameters, e.g., monomers' concentration, reactant diffusion coefficients, reaction time, type of solvent, curing time and temperature, polymer molecular weight, degree of crosslinking, in addition to the characteristics of the macroporous support [11, 50, 61].

2.3.2.1 Influence of reaction / preparation parameters

2.3.2.1.1 Influence of monomers chemistry and concentration

The characteristics of the PA TFC membranes have been found to change dramatically according to the employed monomers. In general, numerous aliphatic and aromatic monomers were investigated for the preparation of PA TFC membranes. Commonly, aromatic polyamides are often more favored due to their higher degree of chain rigidity, leading to better performance, in addition to their stability over a wide pH range [51]. In literature, PA TFC membranes have been frequently prepared using two alternative diamine monomers, MPD or piperazine (PIP), and TMC. The produced MPD- and PIP-based TFC membranes were found to exhibit completely different surface characteristics and separation performance due to the difference in the reactivity between the two monomers [11, 50, 51]. Moreover, other monomers have been also investigated in order to improve the chemical stability, performance and antifouling propensity [50, 62].

In parallel, the monomer concentration has been also affirmed to play a significant role in determining the performance and characteristics of the final TFC membranes. Generally speaking, high initial monomer concentrations were observed to result in formation of a thin dense PA film with relatively low porosity, whereas low initial concentrations yields a looser

thick PA film [48]. Furthermore, Xu et al. have recently introduced a detailed study concerning the impact of varying [MPD:TMC] concentration ratio on PA layer morphology as well as the separation performance [63]. They found that the rate of PA formation is affirmed to be mainly influenced by the proportion of diffused MPD. Also, at a fixed [MPD:TMC] ratio, at [20:1], increasing initial monomers' concentrations results in PA barrier layers of substantial different morphologies and layer thickness; however, the PA TFC membranes prepared using MPD of 2 wt.% and TMC of 0.1 wt.% exhibited the best separation performance.

2.3.2.1.2 Influence of organic solvent properties and curing temperature

The characteristics and the separation performance of PA TFC membranes showed also a strong dependence on the organic solvent properties and the curing temperature [31, 64]. The organic solvent was emphasized to affect the MPD diffusivity and solubility in the organic phase; consequently, it affects the IP kinetics as well as surface and perm-selective properties of the produced PA membranes. Ghosh et al. concluded that high performance RO membranes are obtained by employing organic solvents of high surface tension and low viscosity [31].

Increasing the curing temperature was also found to increase the water permeability and the surface roughness, while it decreases the salt permeability and the membrane hydrophilicity [31, 64]. This was interpreted by vaporizing the residual solvent and promoting the crosslinking inside the PA film when the membrane is thermally cured at a temperature close to the boiling point of the organic solvent. Accordingly, the optimal curing temperature and curing time was affirmed to be strongly related to the type of organic solvent.

2.3.2.1.3 Influence of additives

In addition to the influence of IP reaction conditions, the inclusion of additives into the monomer solutions have widely been employed as a potential route to achieve competent separation performance. The mechanism of action by the additives has been reported to include controlling the monomers' solubility, diffusivity, protonation, or hydrolysis; besides they can also accelerate the rate of IP reaction via scavenging the harmful byproducts [11, 31, 51, 62, 65]. Many examples of these additive materials have been reported. Triethylamine (TEA) and 10-camphorsulfonic acid (CSA) are among the most frequently employed additives to amine monomer solution during the IP reaction of MPD and TMC. They were found to inhibit amine monomer protonation and acid chloride hydrolysis; in addition, they were assumed to protect the macroporous support during the curing of the membrane at relatively high temperatures [11, 31, 65]. Alike the use of TEA, sodium hydroxide was also reported to consume the

liberated hydrochloric acid and improve the amine reactivity [11]. Also, the incorporation of mono- and polyhydric additives into the amine monomer solution has been recently investigated [66].

Another group of additives, e.g., dimethyl sulfoxide, acetone, isopropanol, was also mentioned to improve the mutual miscibility of water and n-hexane resulting in enhanced MPD diffusivity and improved water permeability [11, 62]. Furthermore, some additives were also reported to be used for the organic layer. For example, Mickols patented the incorporation of a complexing agent, e.g., triphenyl phosphate, into the organic solution, which was found to inhibit the concurrent hydrolysis of the liberated hydrogen halides; consequently, its enhances the IP reaction and improves the water permeability [67].

2.3.2.2 Impact of support's characteristics

Several studies have shown that optimization of the support structures has a great potential in tailoring the characteristics and the performance of PA TFC membranes [51, 61, 68, 69]. The porous sublayer is exploited not only as a mechanical support, but it has been found to influence the surface and perm-selective properties of the PA TFC membranes. This is because it acts as a platform for the IP reaction, so it plays a significant role during the IP kinetics. Generally, membrane supports of average barrier pore size in range of 1 – 100 nm were revealed to offer stable interface for IP reaction [51]. Sublayers of lower pore sizes are difficult to pre-wet, and others of pore sizes in µm range are suffering from liquid evaporation. The support hydrophilicity was also found to improve the wetting by the aqueous monomer solution prior to the interfacial polarization reaction. Therefore, the location of the interface where IP reaction occurs is distinct for hydrophobic and hydrophilic sublayers [51].

Indeed, Ghosh and Hoek observed a direct influence of the support surface hydrophilicity and porosity on the thickness, morphology and permeability of the PA layer [68]. They concluded that hydrophobic porous supports produced rough and more permeable PA layers because less PA was formed within the pores, whereas hydrophilic less porous supports yielded less rough and thinner PA films of lower permeability.

Recently, Zhang et al. have emphasized that supports with high surface porosity often produce thicker and adherent PA layers exhibiting high crosslinking degree, protruding crumpled surface morphology as well as low swelling affinity in water, while the opposite characteristics were found upon employing sublayers made from the same polymeric material but with low surface porosity [69].

2.3.3 Basis of transport mechanism in PA TFC RO membranes

Because of the high potency of the RO water desalination technology, the mechanism of water and solute transport through RO membranes have been experimentally and computationally studied in detail. Subsequently, nowadays, the transport in RO membrane materials can be understood in two scales, nanoscale, i.e., understanding the transport mechanism inside the selective PA film and the influence of surface morphology (**sections 2.3.3.1**, **2.3.3.2**, **2.3.3.3**), and macroscale, e.g., concentration polarization phenomenon (**section 2.3.3.4**).

2.3.3.1 Solution-diffusion model

Transport through PA TFC membranes is mainly governed by solution-diffusion model since the suggested interstitial void size within the PA barrier layer is lower than 6 A° [9, 20, 70]. In principle, the solution-diffusion model is based on the diffusion phenomena, a process by which a matter is transported from one part to another inside the system by a concentration gradient, i.e., from the high concentration to the low concentration. Diffusion is described by Fick's law:

$$J_i = -D_i \frac{dC_i}{dx_i}$$

Equation 1: Fick's law of diffusion

Where, J_i is the flux of component i, D_i is the diffusion coefficient, $\frac{dC_i}{dx_i}$ describes the concentration gradient, and the negative sign indicates that the diffusion is always down the chemical potential gradient, i.e., concentration gradient.

Briefly, the water transport across an PA barrier layer occurs in three separate steps (**Figure 2.3 (a)**), (a) absorption of water molecules into the membrane surface layer, (b) diffusion through the barrier layer, (c) desorption of water molecules from the permeate side [8]. The diffusion of water molecules through the PA barrier layer is derived by the water concentration gradient. It was found that the rates of absorption and desorption at the both membrane interfaces are always much higher than the diffusion rate within the PA barrier layer.

The mathematical description of the solution-diffusion model is based on two main assumptions, pressure within the membrane is uniform; and the chemical potential gradient is represented as a concentration gradient. By means of prolonged mathematical derivations [12,

17], the water flux, J_v, is found to be correlated to the applied hydrostatic pressure and concentration gradient across the membrane by the following equation:

$$J_v = A'(\Delta P - \Delta\pi)$$

Equation 2: Water flux in RO membrane according to solution-diffusion model

Here, A' is water permeability, ΔP is the transmembrane pressure, and $\Delta\pi$ is the osmotic pressure difference across the membrane. According to this equation, to accomplish water desalination using semipermeable membrane, the applied trans-membrane pressure must be higher than the osmotic pressure difference between the feed and permeate solutions (**Figure 2.3 (b)**). This phenomenon is called "reverse osmosis" [7, 12]. The osmotic pressure of diluted salt concentrations can be estimated by means of van't Hoff equation:

$$\pi \cong MRT$$

Equation 3: Van't Hoff equation

Here, M is molar solute concentration in feed solution, R is universal gas constant, and T is absolute temperature.

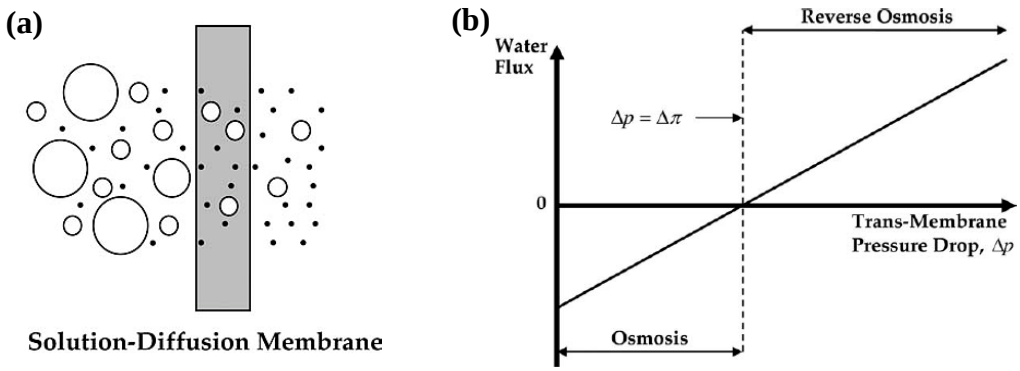

Figure 2.3: (a) Schematic illustration for solution-diffusion model, (b) Membrane flux vs. trans-membrane pressure according to solution-diffusion model [7]

Moreover, the salt flux, J_{salt}, across RO membrane can be described using the following equation:

$$J_{salt} = B\left(C_{feed} - C_{permeate}\right)$$

Equation 4: Salt flux in RO membrane according to solution-diffusion model

Here B is salt permeability. Accordingly, the salt flux is concluded to be apparently independent on the trans-membrane pressure, which implies that the membrane can become more selective when the applied hydrostatic pressure increases [12]. In other words, solution-diffusion model assumed the salt transport and water transport through RO membrane to be completely independent. Later, this has been found to be inaccurate. A potential coupling

effect, mainly due to convection, has been emphasized to exist between solvent and solute transports through dense membranes [17]. Maxwell–Stefan equations for multicomponent diffusion in gases were successfully extended to explain the multicomponent diffusion in dense polymer films, and suggesting a theoretical model that can fit with the experimental results [71]. Generally, experiments found that water flux and salt flux are coupled. When water flux increases through dense membranes, salt concentration in the feed side will also increase and the osmotic pressure difference across the membrane will change; consequently, the salt transport will increase. Indeed, this advanced understanding to the transport phenomenon through the dense PA films induced substantial changes to the mathematical equations; however, the classical solution-diffusion model is still employed due to the fact that the consequences of the coupling effects on membrane selectivity in the current desalination membrane systems are judged to be insignificant [17].

The membrane selectivity can be measured using many methods; however, the membrane salt rejection is frequently employed as a universal qualifying method. Moreover, the influence of various operational parameters on the perm-selective properties of the RO membranes have been extensively investigated [7, 8, 12]. Generally, the separation performance of RO membranes is affected by parameters including applied operating pressure, feed concentration, as well as operating temperature. At the beginning of RO process, the water flux increases as the applied pressure is increased, whereas, the salt rejection is found to increase rapidly till it reaches a maximum value, afterward it becomes nearly constant. On the other hand, increasing the feed concentration, at a constant operating pressure, has an injurious impact. As the feed concentration increases, the osmotic pressure increases; consequently, the trans-membrane pressure difference across the membrane decreases hence the water flux decreases. Also, increasing the upstream concentration will increase the solute, salt, transport through the membrane.

Furthermore, increasing the operating temperature is observed to increase both the water and salt transport across the RO membrane due to increasing in diffusion [12]. Nevertheless, in real RO desalination plants, the water desalination is always performed at constant pressure or at constant water flux; accordingly, increasing the operating temperature is found to increase the permeate salinity [8].

2.3.3.2 Donnan membrane exclusion

Most of PA TFC membranes are found to exhibit negative surface charge as a result of the dissociation of ionizable surface unreacted groups, commonly carboxylic groups, at the operating pH [11, 72]. These negative surface charges are found to reject negatively charged ions or molecules resulting in partial accumulation of positively charged ions near the membrane surface, in a phenomenon called "Donnan membrane exclusion" [7, 72]. In many studies, Donnan effect has been emphasized to underpin the rejection of charged solute species, in particular, for charged NF membranes. The rejection of monovalent salts by negatively charged membranes is observed to be influenced by the feed salinity such that it has been found to decrease as the feed salinity, or concentration of divalent salts, increases [8]. This may be explained by a possible shielding of the membrane fixed surface charges. Moreover, changing the operating pH can also impact the rejection of charged solute species [72]. The majority of PA RO membranes have their isoelectric point (IEP) at low pH, mostly 3 – 4, so that they exhibit negative surface charge at normal operating pH, 6 – 7 [8, 73]. Increasing the operating pH is found to promote the membrane negative surface charges; consequently, enhancing the rejection of charged species.

2.3.3.3 Modern understanding of transport mechanism in crumpled PA films

Nowadays, advanced imaging tools along with smart modeling software are successfully exploited to find out more insights into the real reasons of the high permeability of dense PA film, as well as the merits or shortcomings of their unique surface morphology. For many years, the surface morphology of PA TFC membranes is always referred to be one of two, 'ridge-and-valley" or "nodular morphology". The type of the morphology was emphasized to be dependent on the monomer types and the porosity of the employed support [61, 68, 69, 74]. Nevertheless, the recent published work has shown that the surface morphology of fully aromatic PA film is slightly different and it contains more fine nanostructures. In general, the "ridge-and valley" morphology is observed to comprise ridges, protuberances, besides flat area (**Figure 2.4**). Each protuberance is a hollow water-filled void covered with sub-10 nm thin dense PA layer with ridges curl-like leaves on the top, besides it may stick with other unites, so that they may be visualized from the top as bigger ridges [58, 63, 75]. In addition, the dense layer of the flat regions is connected with the thinner dense layer atop the protuberances and ridges to form a complete distinct barrier layer. The protuberances and ridges have irregular interconnecting cavities and tunnels linked to the pores on the back side, or permeate side, of the PA film. These

impregnated voids, tunnels and cavities are supposed to account for the high water permeability of PA TFC membranes rather than the enhancement in membrane surface area [58, 75, 76].

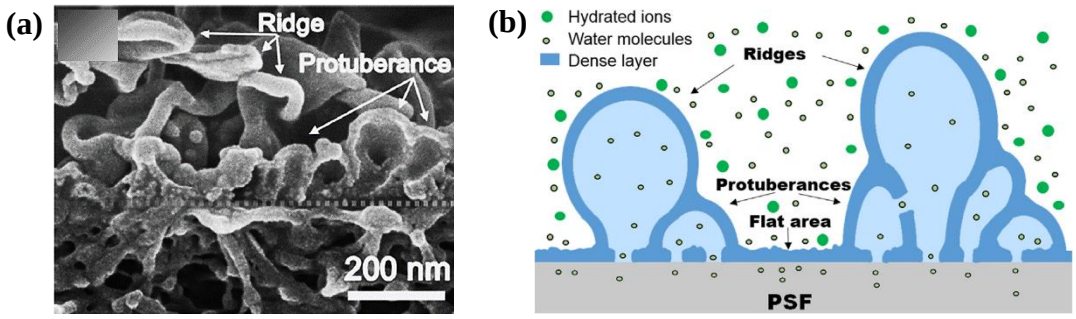

Figure 2.4: (a) SEM micrograph for dense PA layer, (b) Schematic illustration for cross-sectional morphology of PA film [75]

Moreover, the optimal positioning of these voids within the PA films is computationally studied. It is found that high water permeability is achieved when the voids formed closer to the bottom of the barrier layer; however, the presence of voids near the PA surface has bad impact on the membrane permeability [77]. Furthermore, a strong correlation between the porosity of the back side of the barrier layer and the void structure in the PA film as well as the membrane separation performance has recently been revealed [63].

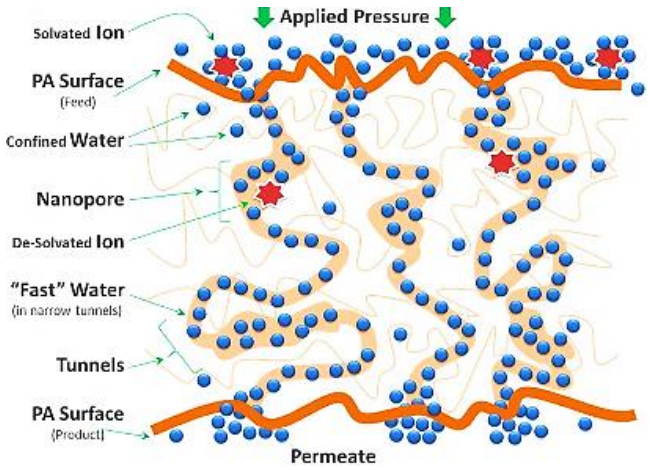

Figure 2.5: Schematic illustration summarizing recent features of PA membranes emerged from molecular modeling studies [58]

In parallel, a sophisticated simulated model has recently been introduced [58] (**Figure 2.5**). The fully crosslinked PA layer is envisioned as vibrant dynamic polymer network composed of tangled chains containing tortuous water-filled channels that can undergo localized dimensional changes, e.g., swelling, twisting, shrinkage, upon applying a differential pressure. Although, the formed tunnels and nano-pores are quasi-stable depending on the local solvation

and the type of solute, they are assumed to interpret the preferential solute rejection and enhanced water transport through fully crosslinked PA dense thin films.

2.3.3.4 Concentration polarization phenomenon

During the water desalination using RO technology, the water and the dissolved salts permeate at substantially different rates, such that the water transport is dominating but the salts are almost rejected. Accordingly, concentration gradients form in the upstream and downstream solutions. This phenomenon is known as "concentration polarization" [7, 8, 12]. When RO membrane module is operated at high recovery rate, the retained salts in the upstream solution accumulate at the membrane surface forming a thin stagnant layer, called "boundary layer", causing an increase in the local osmotic pressure. Consequently, a pressure drop occurs resulting in a reduction in water permeability accompanied by an increase in the salt transport through the membrane [8].

2.3.3.4.1 Mathematical description of concentration polarization in RO systems using boundary layer film model

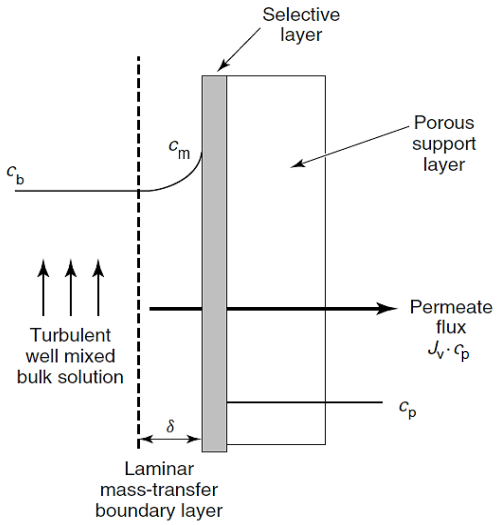

Figure 2.6: Salt concentration gradients adjacent to RO desalination membrane [12]

In RO water desalination process, water and salt are brought toward the membrane surface via the flow of solution through the membrane, J_v. Nevertheless, RO membrane permeate preferentially water and reject salt; consequently, salt accumulates at the membrane surface until a sufficient gradient has formed, i.e., the salt concentration near the membrane surface, C_m, is higher than the salt concentration at the bulk, C_b (**Figure 2.6**). This mass imbalance in the boundary layer allows the retained salt to diffuse back to the bulk solution. Thereafter, a steady state is reached when the convective flow towards the membrane and back diffusive

transport in the boundary layer equilibrate the permeate salt flux. The transport of salt at any point within the boundary layer can be simply described by the mass balance equation:

$$J_v C_b - D\frac{dC}{dx} = J_v C_p$$

Equation 5: Mass balance equation for salt transport across the boundary layer

Here, $[J_v C_b]$ is convective flux towards the membrane, $[D\frac{dC}{dx}]$ represents the back diffusive flux and $[J_v C_p]$ is the permeate salt flux. Later, Brian integrated the mass balance equation over the thickness of the boundary layer, and introduced the concentration polarization equation [78]:

$$\frac{C_m - C_p}{C_b - C_p} = e^{\frac{J_v \delta}{D}}$$

Equation 6: Concentration polarization based on boundary layer film model

Where, δ is the boundary layer thickness. In addition, the ratio of salt concentration near the membrane surface, C_m, to the salt concentration in the bulk, C_b, can determine the extent of concentration polarization, known as "concentration polarization modulus":

$$C.P.M. = \frac{C_m}{C_b}$$

Equation 7: Concentration polarization modulus

When $C.P.M.$ is close to unity, this means that there is no concentration polarization, whereas as the modulus deviates farther from unity, the influence of concentration polarization on membrane perm-selective properties becomes more important. For RO process, $C.P.M.$ has values between 1.1 and 1.5. The concentration polarization can be minimized by prohibiting the formation of boundary layer via improving the turbulent mixing at the membrane surface. Many techniques have been suggested to promote the hydrodynamic effects, e.g., operating at high cross-flow velocity, pulsing the feed, or using membrane spacers [12].

2.3.4 Membrane fouling

It has long been recognized that membrane fouling, energy consumption, and operation costs are among the main limitations to the optimal performance of pressure-driven membrane separation processes. Fouling is a phenomenon of accumulation or deposition of retained solutes on the membrane surface, and it deteriorates the membrane performance either temporarily or permanently [79]. Therefore, the lifespan of RO membranes is emphasized to be mainly correlated to the quality of the feed water, as well as the operation conditions [80].

Generally, two main fouling phenomena are observed for the membrane materials; surface fouling, “external fouling”, and fouling in membrane pores, “internal fouling” [8]. However, RO, and tight NF, membranes are fundamentally fouled via surface fouling [81]. Membrane fouling can occur from a variety of contaminants, called "foulants", existing in the feed solution. Depending on the foulant’s nature, four main fouling types are defined [82, 83]. *Colloidal fouling* refers to the deposition of retained colloidal and particulate matter; *Organic fouling* refers to the deposition or adsorption of dissolved or colloidal organic materials; *Biofouling* refers to an adhesion and the subsequent accumulation of microorganisms and development of biofilm on the membrane surface; *Inorganic fouling* refers to precipitation of sparingly soluble inorganic compounds at concentrations higher than their solubility products.

In parallel, foulant-foulant and foulant-membrane interactions are well-known to control the foulant's' accumulation in most of the membrane-based separation processes. In general, the tendency of membrane to be fouled is determined by a series of physical and chemical parameters, the operating conditions, e.g., hydrodynamic conditions (e.g., flux and cross-flow velocity, recovery rate), pressure, temperature, the feed water characteristics (e.g., pH, solute concentration, ionic strength), as well as the nature of foulant and its physicochemical properties (i.e., shape, size, surface charge), in addition to the membrane’s surface properties (i.e., surface roughness, surface wettability, charge density) [82-84]. Overall, fouling in seawater RO plants are primarily caused by particulate matter, organic compounds, and biological growth on membrane surface and spacers, besides it can occur in several layers [85]. The precipitation is found to be not likely to occur in seawater RO plants because they are usually operated at low recovery rates [86, 87]. On the other hand, the fouling in brackish water RO systems is conversely higher due to the salt precipitation and membrane scaling as a result of the higher recoveries possible for brackish water [8]. Nevertheless, RO plants can experience generally all series of contaminants because the nature of foulants is site-specific and strongly related to pretreatment procedures.

2.3.4.1 Particle fouling mechanisms

Suspended and colloidal particles are known to foul a membrane by coagulating, accumulating on the surface or within the pores, and adversely affect both the quantity (permeate flux) and quality (solute concentration) of the product water [85, 88]. There are four main mechanistic models that are generally used to describe membrane fouling (**Figure 2.7**) [89, 90]:

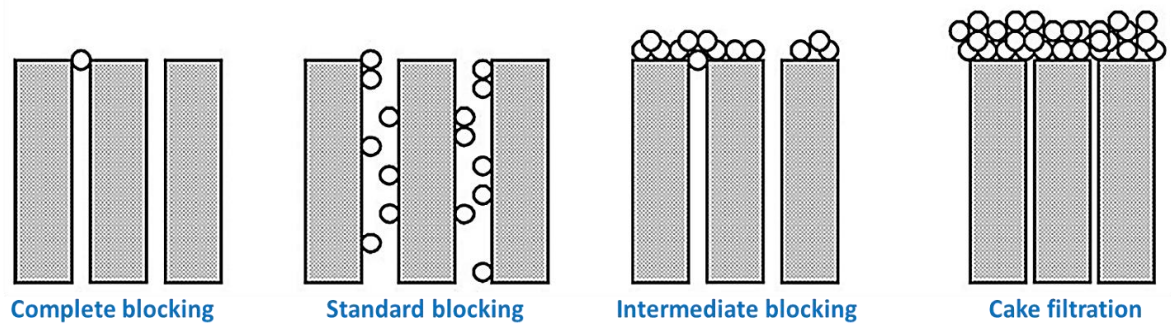

Figure 2.7: Schematic illustration of the main particle fouling mechanisms [89]

- *Complete blocking* assumes that each particle reaching the membrane surface blocks a pore, prevents any flow through it, leading to a seal of pore entrances. No superimposing of the particles is predicted.
- *Standard blocking* proposes deposition of the particles within the membrane pores and the membrane pore volume decreases proportionally to the number of deposited particles. As the pores are constricted, the membrane permeability is diminished.
- *Cake filtration* is a mechanism that interprets the particles accumulation or deposition on the membrane top surface, which causes an additional hydraulic resistance to filtration.
- *Intermediate blocking* suggests a combined mechanism, in which, a fraction of the particles blocks the pore entrances, as in complete blocking model, and the rest deposits on the membrane surface forming a cake layer.

For particle filtration experiments carried out in a constant transmembrane pressure mode with feed flow normal to the membrane surface using spherical particles that are completely retained, there are four mathematical equations addressing the relationship between the total permeate volume (V) and filtration time (t) for each mechanistic model (**Table 2.1**) [91]. Afterward, Hermia demonstrated that a common characteristic equation accounting for the different fouling models can be derived by differentiating fouling equations [92]:

$$\frac{d^2t}{dV^2} = K\left(\frac{dt}{dV}\right)^n$$

Equation 8: Hermia general characteristic equation

Table 2.1: Mathematical expressions for main particle fouling mechanisms*

Fouling mechanism	Mathematical expression	Value of blocking index (n)
Complete blocking	$K_bV = Q_0(1 - e^{-K_bt})$	2
Standard blocking	$\frac{K_st}{2} = \frac{t}{V} - \frac{1}{Q_0}$	1.5
Intermediate blocking	$K_iV = \ln(1 + K_iQ_0t)$	1
Cake filtration	$K_cV = \frac{2t}{V} - \frac{2}{Q_0}$	0

*: where Q_0 is the initial flow rate and K is a constant with a subscript indicating the blocking mechanism.

The unifying equation, by Hermia, is found to be applicable to dead end filtrations and the initial time periods of cross-flow filtrations. However, this common equation does not take into account the fact that all fouling mechanisms could occur simultaneously and interactively [93]. At advanced stages of fouling, the flux decline is found to be affected by multiple mechanisms; i.e., pore blockage, adsorption, cake formation, and cake consolidation [93]. Some of the fouling mechanisms exhibit a kind of significant and permanent effects since foulant particles become lodged either within or on the membrane; i.e., compression of cake, permanent blockage within the membrane, while other mechanisms result in a temporary flux loss; i.e., temporary pore blockages.

2.3.4.2 Applicability of cake filtration mechanism to RO and NF membranes

A number of researchers reported on the low validity of the blocking laws to the unstirred dead-end filtrations because the theory of blocking laws assumes no back-transport of the retained colloids from the vicinity of the membrane surface to the bulk of the feed suspension [92, 94]. However, for the cake filtration, the depositing particles are not assumed to block the membrane pores, either because the membrane is already dense and no pores exist to get blocked, or because the pores are already covered by other particles and therefore they are not available [89]. RO and tight NF membranes don't exhibit distinguishable pores and are considered to be essentially non-porous [88]. When analyzing colloidal fouling of these membranes, it was revealed that colloidal fouling is mainly caused by the accumulation of

foulant particles on the membrane surface forming a “permeable” cake of increasing thickness, which adds a hydraulic resistance to filtration and deteriorates the membrane's functions [88, 89].

Wang and Tarabara studied for the first time the colloidal fouling of salt-rejecting membranes BW30-65 and NF90 employing dead-end filtration mode at unstirred conditions using colloidal silica particles (~ 55 nm) [89]. According to the results, cake filtration was clearly identified as the dominant fouling mechanism responsible for the flux decline during later filtration stages. Nevertheless, 18 % and 53 % of RO and NF flux data; respectively, could fit with the intermediate blocking mechanism during the initial filtration stages. The authors assumed two possible interpretations for this irregular behavior. The first was based on the existence of some surface defects, or more permeable regions, that would function as “pores” during initial filtration stages [95]. Once these permeable regions are covered completely by the silica particles, cake filtration mechanism would occur afterward [96]. Whereas, the second was based on the transient behavior expected for the cake porosity during the initial stages of the cake growth. However, the latter reason is limited to the physicochemical nature of the foulant particles and the surface characteristics of the membrane.

2.3.4.3 Contribution of cake layer formation to concentration polarization phenomenon

The operating results from well-controlled RO and NF plants demonstrated that the deposited cake layer, because of colloidal fouling, may exacerbate the concentration polarization and cause far more flux decline [96, 97]. This phenomenon is called “cake-enhanced concentration polarization” (CECP) **(Figure 2.8)**. The CECP was found to arise from the hindered back diffusion of retained solutes from the fouled-membrane surface to the bulk solution by the deposited cake layer [96, 98], in which the solutes have to diffuse through tortuous paths. Additionally, the solutes captured in this stagnant cake layer are not exposed to the shear flow induced by hydrodynamic conditions as much as those in a free flow channel. These two combined effects increase remarkably the concentration and the osmotic pressure of solutes at the membrane surface [96-98].

Lee et al. investigated the impact of colloidal silica fouling (300 nm) and feed water recovery on the separation performance of TFC RO and NF membranes [99]. They observed that the permeate flux declined linearly and NaCl rejection remained nearly constant when the feed water recovery was increased and the feed solution contained salt only. Inversely, substantial decline for both permeate flux and NaCl rejection was found when the feed water recovery was

increased in presence of colloidal fouling. The authors attributed that to "cake-enhanced osmotic pressure".

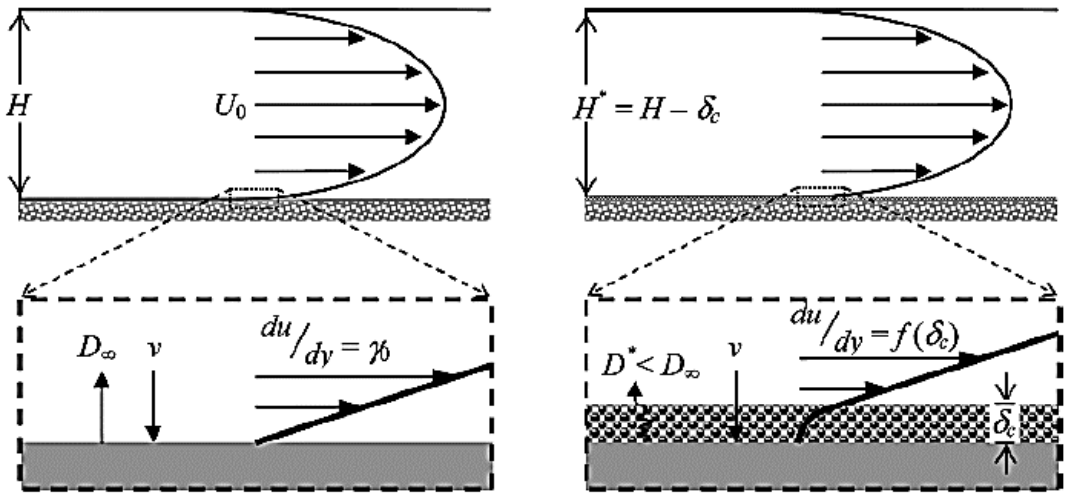

Figure 2.8: Conceptual illustration of cake-enhanced concentration polarization in cross-flow membrane filtration [96]

Description: The bulk cross-flow velocity, U_0, determines the wall shear rate, γ_0. Tangential flow and salt ion back-diffusion, D, are hindered within the deposit cake layer causing cake-enhanced membrane surface salt concentration and the resulting CEOP. In this diagram, the subscript ∞ and superscript $*$ of D indicating the bulk and hindered diffusion coefficients, respectively. The local permeate is labeled by v, while the cross-flow filter channel height is H, the cake thickness is δ_c, and the effective fouled channel height is H^*.

2.3.4.3.1 Cake-enhanced osmotic pressure

Flux decline associated with filtration of colloids-containing salt solution may be described by [96]:

$$J = \frac{\Delta P - \Delta \pi_m^*}{\mu(R_m + R_c)}$$

Equation 9: Flux at cake-enhanced concentration polarization

Here, R_c is the transient hydraulic resistance imparted by the deposited colloidal cake layer, and $\Delta \pi_m^*$ is the cake-enhanced osmotic pressure drop. Cake layer hydraulic resistance is described via Carmen-Kozeny equation as a function of the mass of deposited cake layer per unite membrane surface area, M_d [96]:

$$R_c = \left[\frac{180(1-\epsilon)}{\rho_p d_p^2 \varepsilon^3}\right] M_d$$

Equation 10: Carmen-Kozeny equation

Where ϵ is the cake layer porosity, d_p is the particle size, ρ_p is the particle density. Accordingly, cake layer hydraulic resistance increases with reduced colloid particle size and reduced cake layer porosity. The colloid cake layer thickness was found to be related to the cake layer mass by $\delta_c = M_d/\rho_p$ (1- ϵ) [100]. Consequently, the cake-enhanced osmotic pressure drop (CEOP) is calculated as follows [96]:

$$\Delta\pi_m^* = \Delta P - J\mu R_m - J\mu \left[\frac{180(1-\epsilon)}{\rho_p d_p^2 \varepsilon^3}\right] M_d$$

Equation 11: Cake-enhanced osmotic pressure drop

Hence, the CEOP depends on the characteristics of the deposited cake layer, e.g., porosity and thickness, as well as the colloid particle size.

Moreover, an interesting observation was reported by Kim et al. [101], who studied the salt rejection behavior coupled with membrane fouling in seawater RO lab-scale systems using model foulants, humic acid, sodium alginate, and silica nanoparticles (120 nm). They found that salt mass transfer inside the fouling layer structure was differently altered depending on the foulants' type. Organic foulants, i.e., humic acid and sodium alginate, formed a denser fouling layer than silica nanoparticles. So, silica fouling layer creates "cake enhanced" concentration polarization that accelerates the salt rejection decreasing rate, whereas the organic fouling layer hindered the convection of the salt towards the membrane surface causing a "cake reduced" concentration polarization that deaccelerates the salt rejection decreasing rate.

2.3.4.3.2 Influence of hydrodynamic conditions

General speaking, the colloidal fouling was found to be more severe at high permeate flux values and/or lower cross-flow velocity [73, 88, 102, 103]. High permeate flux results in high solute mass transfer, and increases hydrodynamic drag towards membrane surface. Moreover, Cohen and Probstein studied the influence of Reynold numbers on the rate of growth of the colloidal foulant layer at different flow regimes [104]. They emphasized that the rate of fouling is weakly correlated to Reynolds numbers in the laminar flow regime, while turbulent flow experiments showed substantial dependence on Reynolds numbers. This was interpreted by the interplay between convection and back-diffusion. In laminar flow, the convection of submicron colloid particles dominates the back-diffusion, Brownian diffusion, whereas the turbulent flow

was found to enhance the rate of back diffusion, shear-induced diffusivity, in relation to convection.

Furthermore, the shear rate over a membrane surface is affirmed to play a significant role in membrane fouling by determining the solutes mass transfer and, subsequently, influencing the concentration polarization [73, 96-98]. Hoek et al. introduced a detailed study on the impacts of shear rate and cross-flow membrane filter geometry on the colloidal fouling of RO and NF membranes by silica nanoparticles (100 nm) under laminar flow conditions [97]. Overall, they found that increasing shear rate, at fixed channel height, decreased the initial osmotic pressure drop, colloid deposition and resultant flux decline, while salt rejection was enhanced. In addition, at constant feed flow rate, high shear in a filter with a reduced channel height is found to diminish the initial osmotic pressure drop, colloid deposition and flux decline dramatically. In parallel, at a fixed shear rate, changing the channel height didn't affect the initial salt rejection and osmotic pressure drops; however, the flux decline and CEOP increased substantially in the filter with a greater channel height.

2.3.4.4 Colloidal silica fouling

Colloidal particles are existing in natural water, and their sizes are ranging from few nanometers to few micrometers. Colloidal fouling of RO membranes was not recognized as a serious problem to the early RO membranes since most of these systems were operating on well waters. The excellent filtering action of most aquifers would often eliminate/adsorb any colloidal matter before it could interrupt the RO system [105]. Nowadays, the implementation of RO technology is extended to purify various sources of water, e.g., brackish water, seawater. As a result, the presence of high levels of silica along with sparingly soluble salts may pose substantial problems.

2.3.4.4.1 Chemistry of Silica

Silica is the most abundant material available on the earth crust, accounting for about 75 wt.% [106, 107]. It has many crystalline and amorphous forms. Crystalline silica usually shapes like quartz and it has low solubility in water (< 6 ppm) [108]. Amorphous silica is the most common form and it has a much higher solubility in water (100 – 140 ppm) [109]. Silica in natural water exists in soluble, colloidal and suspended (particulate) forms, all are of concern for RO system operators. The silica content of natural water is proposed to be in a range of 1 – 30 ppm, and in a range of 20 – 100 ppm for well water, whereas its concentration can exceed

1000 ppm in brackish water [110]. The dissolution of silica in water can be represented by the following reaction [111]:

$$\mathbf{SiO_2 + 2H_2O \rightarrow Si(OH)_4}$$

So the soluble form of silica is initially monomeric, which is often called mono-silicic acid. The silicic acid monomer is weak tetravalent acid, with pK_a values of 9.7, 11.8 and 12, and consequently, it is almost un-dissociated in natural water till pH 8 [111, 112]. Silica remains in its monomeric state in water at 25 °C for long periods, as long as the concentration remains less than about 2 x 10^{-3} M (~ 120 ppm) [110]. At higher concentrations, mono-silicic acid polymerizes rapidly to form, initially, polysilicic acids of low molecular weight and thereafter larger polymeric species which are in colloidal forms [111]. The polymerization reaction occurs via dehydration mechanism to form Si-O-Si anhydride bonds as follows [112]:

$$\mathbf{nSi(OH)_4 \rightarrow (OH)_3Si - O - Si(OH)_3}$$

$$\mathbf{dimer \rightarrow oligomers \rightarrow colloidal\ inorganic\ polymers \rightarrow (SiO_2)_n}$$

Hence, silicon dioxide (SiO_2, silica) is the net stable product at normal conditions. This condensation reaction is strongly pH- and concentration-dependent, as well as it is found to be catalyzed by the presence of salts, e.g., $CaCl_2$ and $MgCl_2$ [111]. Colloidal silica has a very low surface charge at low pH values and a negative charge at neutral pH or higher [111, 113].

2.3.4.4.2 Deposition mechanism of silica from water and fouling of RO membranes

Depending on the physical form of the silica in water, whether dissolved or colloidal/suspended, two main mechanisms were proposed [110, 111, 114].

- Dissolved silica precipitates from supersaturated solution in one of three ways:
  1. It can precipitate as an impervious glass-like film on membrane surface that has –OH groups.
  2. It can precipitate as colloidal particles remaining in suspension. This occurs in a case of the insufficient area of solid surface for precipitation and silica concentration > 200 ppm, at respective pH. $Si(OH)_4$ polymerizes to dimers, and these further condense to form small 3-dimensional polymers (colloidal particles).
  3. It can precipitate as biogenic amorphous silica by living organisms. This usually occurs in natural waters.
- The colloidal silica particles can deposit on the membrane surface, at conditions close to those causing coagulation or precipitation, and form a more porous film that is often white

and opaque when dried. However, the colloidal silica concentration should be sufficiently low because a concentrated sol would be rapidly gelled and no deposition occurred.

Based on the aforementioned deposition mechanisms, Sheikholeslami and Tan [111] commented that silica fouling occurs generally in RO plants in case that the concentration of dissolved silica exceeds its solubility limit. The polymerized silica may react with the retained salts at suitable pH forming metal silicates. Afterward, the silicate gets more viscous as it precipitates on the membrane surface, and when it dehydrates it becomes hard like cement. This undesired deposition of silica in RO plants causes a limited recovery and increases the operating costs.

Subsequently, they defined two relevant categories of fouling, "precipitation" fouling and "particulate" fouling. The first occurs when monomeric silica get polymerized at the membrane surface; also called "scaling". In contrast, "particulate" fouling refers to the accumulation of silica colloids, which are already formed in the bulk, at the membrane surface. Therefore, the main distinction between the two fouling mechanisms is whether the polymerization occurs at/near the membrane surface resulting in a molecular deposition, or it occurs in the bulk causing a colloidal silica deposition.

2.3.4.5 Studies on colloidal fouling of PA TFC membranes

In addition to the aforementioned study by Wang and Tarabara [89], colloidal silica fouling of various commercial PA TFC RO and NF membranes was also extensively studied using cross-flow filtration mode at different flow regimes (Reynolds number) to investigate the influence of PA characteristics morphology and surface properties, as well as the characteristics of colloidal silica particles on the fouling rate, and, consequently, build up the relevant fouling mechanism(s).

A number of theoretical and experimental studies indicated that the rate of colloidal silica deposition onto RO and NF membranes is controlled by an interplay between double layer repulsion, due to surface chemistry, and the opponent hydrodynamic force resulting from the convective flow toward the membrane, because of high silica concentration in the bulk, which is called "permeation drag" [73, 88, 104, 115]. The effectiveness of each phenomenon is found to be strongly dependent on the membrane type and the physical properties of the foulant. Zhu and Elimelech [88] emphasized that the fouling rate of PA TFC membrane is dominated by permeation drag due to high permeate fluxes, and double layer repulsion hasn't a significant role, whereas the permeation rate through cellulose acetate membranes was lower;

consequently, double layer repulsion effect hinders the deposition of silica colloids causing lower fouling rates. PA TFC membranes are affirmed to exhibit higher colloidal fouling rates than cellulose acetate membranes even at identical initial permeation rates that lead to comparable transverse membrane hydrodynamics, i.e., ruling out permeation drag effect [88, 115]. The same fouling behavior was also reported when the colloidal silica fouling experiments were carried out in presence of an anionic surfactant, which was used to mask variations in chemical and electro-kinetic surface characteristics of both membranes [116]. Accordingly, the discrepancy in membranes' surface morphology, which essentially leads to different surface roughness, is concluded to be the most influential parameter that determines the fouling propensity [88, 115, 117]. The higher fouling propensity of PA TFC membranes was mainly attributed to protruding surface roughness resulting from characteristic "ridge-and-valley" surface morphology.

A mechanism was suggested to describe the deposition of colloidal silica particles on PA TFC membranes, especially at initial stages of fouling [73, 88]. The water convection and particle transport are assumed to be derived more toward the bottom of the "valleys" where "path-of-least resistance" is located. So, silica particles accumulate firstly in the "valleys" regions of PA structure. If the deposited particle is of respective size, it becomes wedged by the valley constrictions and restricts the permeate flow. Subsequently, the valley becomes rapidly clogged leading to more severe flux decline than in smooth membranes. Later, this mechanism was supported by an interesting experiment based on atomic force microscopy (AFM) [118]. AFM in conjunction with the silica probe technique were employed to quantify the variations in electrical double-layer interactions and adhesion of silica micro-sphere (~ 4 µm) at different points on PA TFC membrane in NaCl solutions. The adhesion of the colloid probe was found to be lower at the peaks of the PA morphology than in the valleys with a certain difference, increasing with decreasing the salt concentration. These observations and suggested mechanisms were furtherly supported by estimating Derjaguin–Landau–Verwey–Overbeek (DLVO) interaction energy for a sphere silica particle (radius = 50 nm and colloid surface potential = - 25 mV) deposited on a reconstructed membrane surface analogous to NF70 membrane [119, 120]. The local interaction energy patterns revealed that when a silica particle approaches a rough PA surface its lateral movement becomes restricted by the presence of domains of repulsive interaction (peaks), and eventually, it gets trapped in low-energy pockets (valleys), so-called "Funneling effect".

Moreover, Zhu and Elimelech explored also the impact of other operational parameters, feed colloid concentration and ionic strength [88]. They concluded that as silica particle concentration increases, the convective flow toward the membrane surface increases and, hence, the overall rate of colloid deposition onto the membrane increases. In parallel, high fouling rates were measured at high ionic strength. This was explained by a significant reduction in double layer repulsion effect; consequently, the fouling rate was controlled by permeation drag. Nevertheless, Vrijenhoek et al. investigated the influence of other membrane surface properties on initial colloidal fouling rate for some commercial PA TFC membranes. They implied that neither zeta potential nor contact angle values are correlated to the fouling behavior. Furthermore, Boussu et al. studied the colloidal silica fouling for some commercial NF membranes under turbulent conditions (Re = 30,000) [84]. Contrary to what was settled before [73, 88, 115, 119], the membrane hydrophobicity was observed to be the most effective parameter, and the surface roughness was revealed to have a minor influence and only during filtration of small colloid particles. In parallel, they suggested that feed of large colloid particles with a negative surface charge is the most beneficial for an NF process at neutral pH.

2.3.4.6 Strategies for mitigating the colloidal fouling

Taking into account the detrimental impacts of colloidal fouling, accompanied by the enduring concentration polarization phenomena, a considerable work has been reported on mitigating the colloidal fouling and promoting the membranes' antifouling propensity in RO plants. These studies are basically comprising pretreatment of the feed solution, surface modification of the membrane, enhancing hydrodynamic conditions, and remediation of the fouled membrane [121, 122]. Nevertheless, the most frequently used approaches nowadays in real RO plants are the effective feed solution treatment, employing feed spacers, and the cleaning of the fouled membrane elements. Maeda [123] reported that clear reduction in silica (down to 0.1 ppb) and other solutes can be attained via initial filtration of the feed through RO membrane, followed by multiple treatments with ion-exchange beds along with a second filtration through RO membrane. In parallel, enhancing the hydrodynamic conditions indicates modifying the feed flow path near the membrane surface to induce feed mixing and promote back diffusion. This is commonly achieved in RO plants via using "feed spacers". More about the chaotic mixing at laminar flow conditions is introduced in **section 2.4.2.1**.

The frequency of the chemical cleaning process could range from a daily routine to a long term annual processes. In general, the chemical cleaning agents fall commonly into six categories: alkalis, acids, metal chelating agents, surfactants, oxidation agents and enzymes [8,

121]. These cleaning agents can fully restore the flux even though they can also impair the membrane's selectivity. The cleaning action is interpreted by a possible alteration in morphology or surface chemistry of the foulants upon reaction with cleaning agents [124]. However, Kosutic and Kunst [125] found that there might be also an irreversible change in the structure of NF membranes upon chemical cleaning. In addition, cleaning agents may also be adsorbed on the membrane surface and make it more hydrophilic [126]. Other researchers investigated some combined physicochemical cleaning processes, in which some physical cleaning methods, e.g., hydrodynamic forward or reverse flushing, permeate back pressure, automatic sponge ball cleaning, are coupled with the addition of chemical agents to enhance the cleaning efficiency [127].

The membrane fouling has been commonly emphasized to be substantially influenced by the membrane surface characteristics. Therefore, surface modification has been considered as a potential route to promote the membranes' antifouling propensity via manipulating the membrane surface hydrophilicity, charge or roughness [79, 128]. Modifying the membrane surface charge and hydrophilicity is revealed to control the membrane-foulant interactions [84, 98, 121], whereas altering the membrane surface roughness, and recently topography, is affirmed to influence the hydrodynamics near the membrane surface and the membrane-foulant interactions [27, 119, 120, 129]. Alternatively, Yang et al. and Himstedt et al. have recently suggested magnetic field responsive surface mixing as a new combined approach to enhance the hydrodynamic conditions and promote the antifouling properties of NF membranes [137, 139]. The basis, common methods, simulated influences and reported experiments for surface patterning and surface modification are discussed in detail in **sections 2.4** and **2.5**, respectively.

2.4 Surface micro-patterning of polymeric membranes

2.4.1 How to prepare surface micro-patterned membrane?

Several micro-fabrication approaches have been introduced to prepare patterned sheets and hollow fiber membranes; however, in this work, attention is mainly devoted to lithographic methods reported to produce surface patterned membrane sheets. The first trial toward micro-fabricating of polymeric membranes was introduced by Ehrfeld et al. in 1988 [130]. The process was developed at the Karlsruhe Nuclear Research Center, and comprised three steps, namely X-ray lithography, galvano-forming, and vacuum reaction injection molding, referred as "LIGA" process. In details, X-ray lithography was used to produce primary polymer template (mold), then a metal negative replica of this mold was obtained using

electrodeposition. Finally, the metal negative replica was used for methacrylate-based casting resins to produce a copy that is identical to the primary structure. This process was reported to produce micro-structured membranes with high aspect ratio, high porosity and uniform pore size distribution. Nevertheless, it had some drawbacks, complexity, costly process and limited to MF membranes exhibiting minimum pore size of ~ 500 nm.

In parallel, uncommon surface micro-patterning approach was discussed by Okada and Matsuura [131]. They considered the cellulose membranes with surface wrinkles, which are often formed during the phase inversion process under certain circumstances and regarded as undesirable. Consequently, the surface patterns were irregular waves that existed only on the membrane side facing the gelation media, whereas the other side was almost smooth. The formation of this pattern was controlled via addition of sodium chloride to the coagulation bath, water. Sodium chloride was found to influence the rate of water intrusion into the cast film; consequently, altering the film swelling and creating surface wrinkles patterns.

Later, more straightforward microfabrication technique, called "Phase Separation Micro-Molding", PSμM, was introduced for the first time in 2003 [132]. It was based on the polymer phase separation mechanism, so PSμM offered the possibility of employing a wide range of polymeric materials to prepare patterned membranes of various geometry, aspect ratio and porosity. The mechanism and the common reported methods to treat its major downsides are discussed in detail in **section 2.4.1.2**.

Another feasible and straightforward surface micro-patterning method was developed by Y. Ding's group. [133]. The new developed method combined two mechanistic techniques of "Nanoimprinting Lithography", NIL, which was firstly introduced by Chou et al.; NIL via "*direct thermal embossing*" [134] and NIL via "*compression molding*" [135]. Compression molding was known as a low-cost high-throughput micro-fabricating technology, and combining it with direct thermal embossing offered a possibility to imprint polymeric membranes at temperatures lower than their glass transition temperatures, T_g. More about the method developed by Y. Ding's group, NIL, is presented in **section 2.4.1.3**.

Furthermore, Gohari et al. have suggested an alternative method to produce nano-sized line pattern on the surface of mixed matrix membranes via incorporating inorganic hydrophilic nanoparticles into the PES/PVP casting solutions as fillers [136]. Fe–Mn binary oxide particles, 20 – 30 nm in diameter, was used as fillers and to enhance the surface hydrophilicity of the membranes.

2.4.1.1 Controlling of polymer phase separation to obtain well-defined porous membranes

Most of the polymeric membrane formation methods are considered as phase separation processes, in which an initially homogenous polymer solution is transformed into a two phase system, i.e., a solid, polymer-rich phase that forms the matrix of the membrane and a liquid, polymer-poor phase that leads to the membrane pores [137]. This process can be brought about via alteration of the thermodynamic state of the cast film. There are two main alternatives that are frequently used, imbibition of the non-solvent liquid from a coagulation bath as in the Loeb-Sourirajan process, LIPS [36], or the membranes can be alternatively formed by absorption of water vapor from a humid atmosphere into the proto-membrane film, VIPS. VIPS was firstly introduced by Zsigmondy and Bachmann [138] and later refined by Goetz [139].

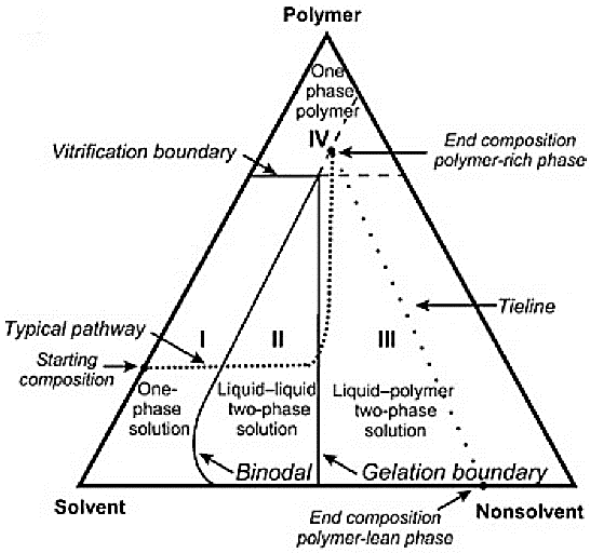

Figure 2.9: Typical pathway of a cast film made of an amorphous polymer on ternary phase diagram during phase separation process [147]

The typical pathway of a cast polymer film on ternary phase diagram during a phase separation process is presented in **Figure 2.9** [140, 141]. Briefly, the three axes represent the concentrations of polymer, solvent, and non-solvent in the system. Region I represents homogenous (one phase) solution, where the casting process starts. After crossing the binodal boundary, in region II, two liquid phases coexist in the same solution; one being rich in polymer and the other containing merely solvent and non-solvent. As soon as the composition has passed the gelation boundary to region III, the polymer density throughout the cast film starts to fluctuate; consequently, the film becomes unstable and separates into a liquid polymer-lean phase and a glassy polymer-rich phase, known as “gelation”. In the vitrification area, also known as “glass transition” [142], region IV, the polymer precipitates. At the endpoint, on the binodal boundary, the film reaches its final configuration, a liquid polymer-lean phase and a

glassy solid polymer-rich phase, membrane, represented by the end points of the tieline [140, 141].

To understand how the polymer phase separation mechanism influences the final membrane structure, Reuvers et al. developed a mechanistic model [143]. It demonstrated two types of

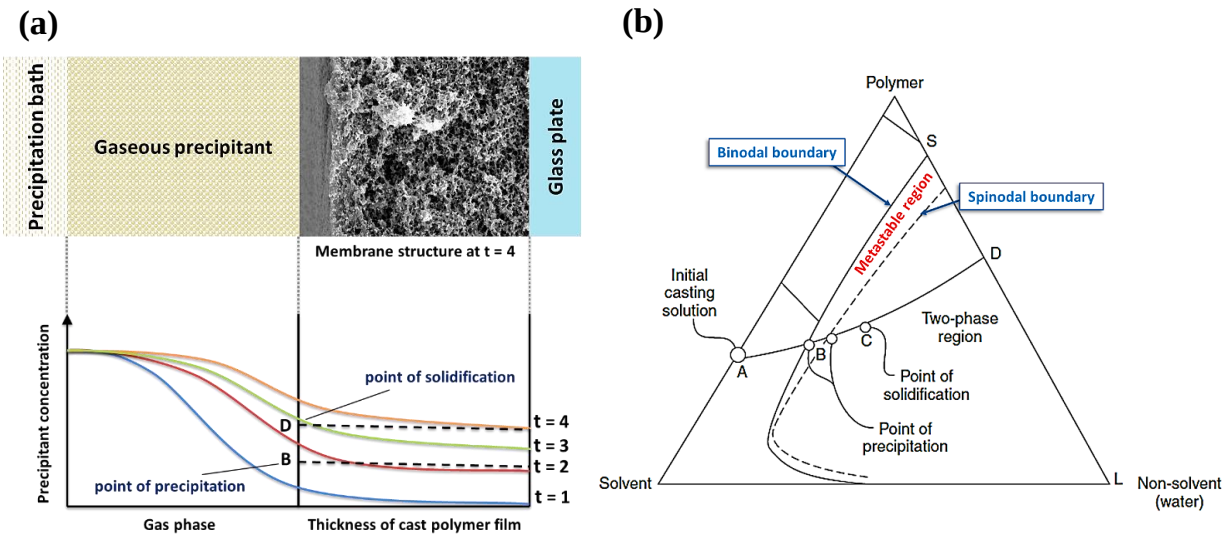

Figure 2.10: (a) Concentration profile of the precipitant in the casting solution during the formation of symmetric-structured membranes, adapted from [144], (b) typical ternary phase diagram showing the thermodynamic metastable region, adapted from [144]

demixing that can take place during the phase separation process; "instantaneous" and "delayed" demixing. Membranes formed by delayed demixing mechanism (typical for VIPS) are found to exhibit a homogenous and macrovoid-free porous structure without formation of a dense layer, neither on the top nor the bottom side of the membrane. Strathmann and Kock interpreted this symmetric structure by considering the concentration profile of the coagulating agent during the phase separation process (**Figure 2.10 (a)**) [144]. It was emphasized that the rate limiting step for the transport of non-solvent into the cast polymer film, precipitation, is the slow mass transfer on vapor phase side, which results in uniform concentration profiles in the film causing the polymer solution precipitates at virtually the same time over the entire film cross section. On a microscopic scale; however, there are still some regions of higher and lower polymer concentrations, which act as nucleation centers for polymer precipitation. These microscopic regions are randomly distributed throughout the cast polymer film leading to a randomly distributed polymer structure that would induce the sponge porous structure, typical pore morphology for isotropic membranes prepared using VIPS [144].

2.4.1.1.1 Designing of the casting polymer solution to obtain isoporous PES membranes

Many thermodynamic aspects, e.g., phase diagrams, polymer-solvent interactions, solvent-non-solvent interactions and interfacial stability, as well as the kinetics of phase separation mechanism, i.e., exchange rate between solvent and non-solvent, and rate of polymer solidification, were found to determine the final membrane structure [145].

For example, the type of precipitant and the solvent was emphasized to determine, to far extent, both the activity coefficient of the polymer in the solvent-precipitant mixture, and the concentration of the polymer at the point of precipitation / solidification [144]. Nevertheless, as a principle, a low polymer concentration tends to precipitate as a membrane of finger-like structure, whereas high polymer concentration tends to form a membrane with a sponge pore morphology [146]. The sponge-structured membranes are more favorable because of their propensity to exhibit isotropic pore size distribution throughout the entire membrane thickness. However, the polymer concentration, especially in case of high molecular weight polymers, shouldn't exceed certain limit to avoid the formation of a dense skin layer, which is occurred by gelation or vitrification mechanism depending on the viscosity of the polymer solution [141].

General speaking, to obtain skinless isotropic membranes, a slower, or delayed, demixing mechanism is recommended, such that the membranes should be precipitated from thermodynamic metastable polymer systems (**Figure 2.10 (b)**) [137, 140, 144]. The delayed demixing mechanism can be realized by following up one or more of these practical approaches, choosing a non-solvent of low miscibility with the solvent, adding of specific additives to the casting solution or the coagulation bath, or decreasing the exchange of solvent and precipitant by either adding a small amount of a non-solvent to the casting solution or by adding a certain amount of the solvent to the coagulation bath [144, 147].

Greenwood et al. introduced a reproducible procedure to prepare skinless isotropic macroporous PES membranes using a specific polymer casting solution, composed of PES, NMP as a solvent and low molecular weight aliphatic glycol, e.g., di- or triethylene glycol (TEG), as a hygroscopic non-solvent [148]. They also pinpointed the limits for the composition of essential dope constituents in order to achieve symmetric pore size distribution; these membranes exhibited hydrophobic surfaces. Later, Susanto et al. presented an analogous method to fabricate isotropic PES MF membranes of stable hydrophilic character from a casting solution consisting of PES, NMP, TEG, besides a triblock copolymer containing

hydrophilic polyethylene glycol and hydrophobic polypropylene glycol segments, known as Pluronic [30].

2.4.1.1.2 Macromolecular additives – Influence of polyvinylpyrrolidone

The introduction of specific additives to either the casting solution or the coagulation bath in order to control the membrane characteristics has been known as a viable and effective approach. Several researchers have studied the role of additives in modifying the phase separation mechanism and offered many possible explanations [144, 147, 149]. Strathmann and Kock explained the effect of additives in terms of alteration of the activity coefficient of the polymer, the solvent or the coagulating agent that affects strongly the precipitation rate [144]. For example, certain additives to the precipitation bath, e.g., salts, sugars, glycerin, are capable of reducing the rate of precipitation and promoting the formation of denser sponge structure [150]. Whereas the same additives in the casting solution may increase the rate of precipitation; consequently, a finger structure is obtained [144].

In parallel, there are three common macromolecular additives to the PES casting solutions that are frequently used, namely, polyvinylpyrrolidone (PVP), polyethylene glycol and Pluronic [151]. PVP is one of the most versatile polymeric additives due to its very good miscibility with many polymeric materials, in addition it is well soluble in water as well as other solvents. As a result, it can influence the solution viscosity and control the intrinsic porosity of the membranes, consequently, it has been known as a "porogen".

For example, Lafreniere et al. found that the interaction between PES and PVP is strongest when the PVP/PES weight ratio close to unity, which increased the bubble point diameter and enhance the permeation rate [152]. Whereas, PVP was observed to act differently at PES/PVP weight ratio < 0.5, i.e., higher proportion of PES was used [153]. Miyano et al. explained that by the reduction in hydrodynamic size of PES molecules due to high total polymer concentration that led to a decrease in pore size of the resultant membrane. In parallel, Ochoa et al. revealed that the addition of small quantities of PVP with different molecular weights increased the permeability of PES membranes without adversely affecting their selectivity [154]. The same influence at low PVP proportions was also reported by Ismail and Hassan [155].

Moreover, PVP was also found to promote the hydrophilic character of PES membranes [156]. Furthermore, the impact of PVP addition on the mechanical properties of the PES membranes was also investigated [157]. Amirilargani et al. observed that the addition of 1 wt.%

of PVP K-15 to PES casting solution yielded membranes exhibiting good mechanical properties, while further PVP addition had a counteractive influence.

2.4.1.2 Phase separation micro-molding (PSµM)

PSµM is a versatile replication technique based on phase separation mechanism [7] (cf. **section 2.4.1.1**), in which, a thin film of a polymer solution is cast on a mold with a desired micro-meter sized relief structure, usually made of silicon (**Figure 2.11**). Thereafter, the change in thermodynamic state disturbs the equilibrium of the polymer film causing a phase separation process into two phases; polymer-rich phase and polymer-lean phase. This change can be realized via immersion in a non-solvent liquid, consequently it is generally known as "liquid-induced PSµM", LIPSµM [147]. Afterward, the polymer-rich phase solidifies forming the membrane matrix and, indeed, it assimilates the profile of the mold.

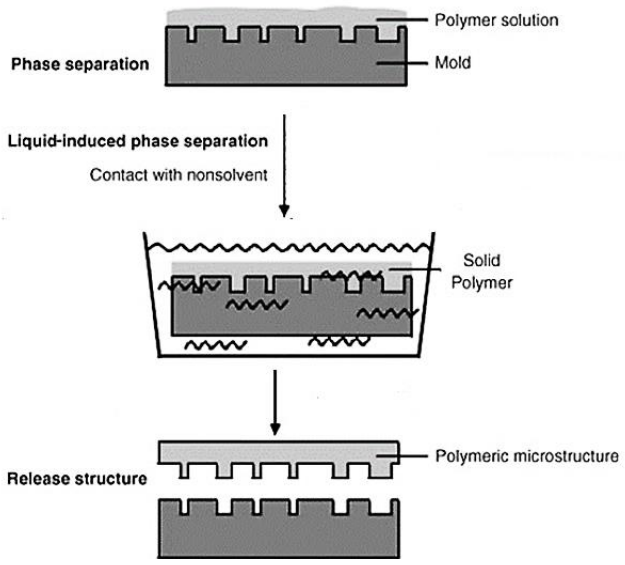

Figure 2.11: Schematic illustration of liquid-induced phase separation micro-molding, LIPSµM, adapted from [132]

The pore morphology of the produced membranes can vary widely e.g., a very open, sponge-like configuration, a few isolated pores surrounded by polymer, or completely dense configuration. As described before, the intrinsic porosity and the pore morphology are strongly dependent on the kinetics of demixing during the phase separation process that was emphasized to be influenced by several thermodynamic parameters (cf. **section 2.4.1.1)**.

2.4.1.2.1 Shrinkage phenomena – Advantage of easy membrane detachment

During the transformation of the cast polymer film into the (proto)membrane by means of liquid-phase separation, the dimensions of the cast film change substantially causing shrinkage

(syneresis) [142]. As a result, in LIPSµM, the shrunken film leaves small gaps between the mold cavities and the replica, upon precipitation, which guarantee the easy release of the membrane from the mold. In principle, the shrinkage was found to occur in two directions, parallel or perpendicular, with the mold and the film. Vogelaar et al. ascribed the easy release advantage in LIPSµM to the inherent shrinkage in parallel orientation with the mold and the film [147]. In addition, they found that the easy release advantage is essentially independent of the surface composition of the mold, and the perpendicular shrinkage depends strongly on the process parameters, e.g., the composition of the polymer solution. Nevertheless, excess shrinkage was found to cause deformations to some complicated replicas, and hinder the replication of relatively "shallow" molds; consequently, molds of high aspect ratio is favorably replicated by this method. Generally, in comparison with other lithographic methods, the easy release advantage of LIPSµM results in a very low defect rate and preserving the replicated microstructures over extended areas [132, 147].

2.4.1.2.2 Main downsides: pore size gradient and skin layer formation

Aside the potential of LIPSµM as a versatile microfabrication method, some obstacles were found during the application. One major downside is that the polymer phase separation is always induced from the non-structured side, i.e., the side that is in direct contact with the precipitation medium. Therefore, the coagulating agent, non-solvent, diffuses into the polymer film from the flat side creating a variation in its local concentrations throughout the film thickness, leading to non-uniform precipitation rate that results in a hierarchal pore size gradient across the micro-structured membrane (**Figure 2.12 (a)**). The pore size was found to decrease toward the non-structured side. Often, a dense skin is formed on this interface, subsequently, the selective layer is located on the non-structured side. In response to that, the

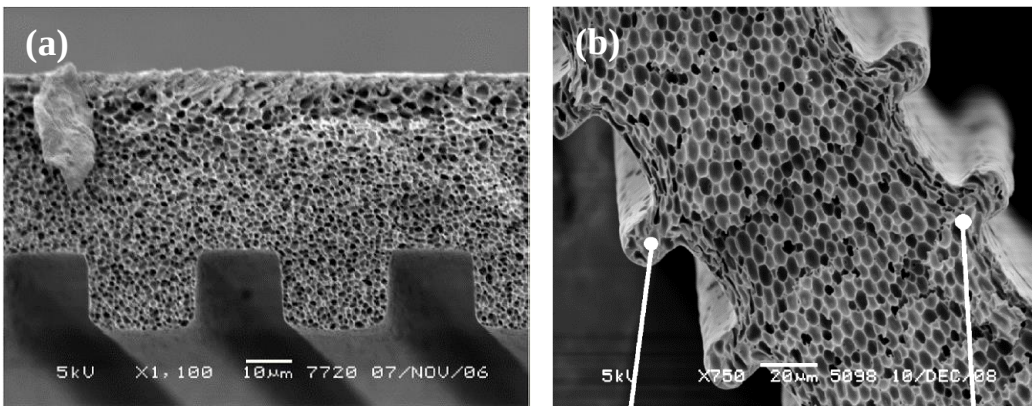

Figure 2.12: SEM micrographs for bi-structured PES membranes obtained using two different modes of PSµM: (a) LIPSµM, (b) VIPSµM [158]

founders of PSµM have developed the counterpart method to produce micro-structured membranes exhibiting homogenous pore size distribution, namely vapor-induced phase separation micro-molding, VIPSµM [158].

As described before, the addition of a non-solvent component to a polymer solution modifies its thermodynamic state, such that when a certain composition of the non-solvent is attained, the polymer phase separation proceeds. In VIPS, the non-solvent is introduced in its vapor state, via exposing the cast polymer film to a flow of the non-solvent vapors that will be absorbed [137, 140]. The mechanism of VIPS process has already been discussed in **section 2.4.1.1.1**. Therefore, in VIPSµM, water vapor permeable molds made of polydimethylsiloxane, PDMS, on nonwoven supports are employed to realize a sustained and respective non-solvent flow that is required to induce the polymer phase separation. PDMS is indeed known of its high permeability to water vapor [158, 159], besides its mechanical and chemical stability; it showed a good stability toward NMP, frequently used solvent for common polymeric materials [158]. The main steps in VIPSµM method developed by Bikel et al. are presented in **Figure 2.13**. Also, a SEM micrograph for a bi-structured PES membrane obtained by VIPSµM is shown in **Figure 2.12 (b)**.

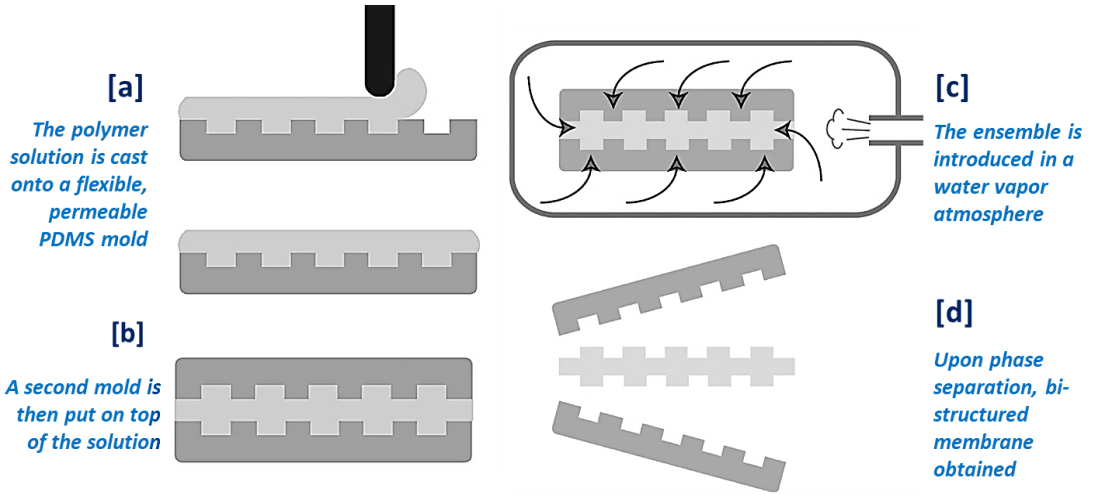

Figure 2.13: Schematic illustration for vapor-induced phase separation micro-molding, VIPSµM [158]

Additionally, Bikel et al. have investigated the controlling of PDMS molds to the water vapor transport during VIPSµM via changing the mold's thickness. They found that increasing the thickness of the PDMS mold up to 300 µm causes a noticeable growth of the pores and achieves more symmetric pore size distribution. Also, PDMS showed good contribution toward the shrinkage and shortening of coagulation times, in case of bi-structuring mode [158].

Furthermore, Won et al. have developed a modified soft-lithographic method to treat the main limitations of the soft molding method, PSμM; (i) incapability of replication of multidirectional patterns; (ii) formation of dense layer on the non-structured side [158, 160]. The motivation of this method was to shift the interface where the polymer phase separation is initiated because the position of this interface defines the location of the undesired dense layer [161]. Therefore, they suggested a modified immersion-precipitation method, a non-woven fabric is placed on the top of the cast polymer film prior to immersion in coagulation bath. This modified immersion-precipitation method was found to shift the interface between the polymer film and the non-solvent from the bottom side to the top of the polymer film, structured side.

2.4.1.2.3 Parameters influencing the fidelity of the soft-lithographic methods

As discussed before in details, many lithographic methods can be employed to obtain surface patterned membranes; however, the choice of the relevant method along with the adaptation of the related experimental parameters are considered as the main barrier toward defining a sustainable and efficient surface micro-patterning technique. The main experimental parameters are found to include pattern characteristics, e.g., geometry, aspect ratio, the material of the employed mold and whether a pretreatment is required or not, composition of the polymer casting solution, casting conditions, e.g., humidity, gap thickness, casting / loading speed, in addition to precipitation conditions, e.g., composition of coagulation medium, precipitation time and temperature.

In reaction to that, Won et al. have investigated the most influential parameters to prepare prism-patterned PVDF UF membranes of high fidelity [162]. The molecular weight of the PVDF and its weight percentage composition in the casting solution have emphasized to affect strongly the pattern fidelity and the pore structure. They concluded that the lower the molecular weight of base polymer, the faster the polymer phase separation rate; consequently, higher pattern fidelity is achieved. In addition, they have investigated the impact of the mold material because it would affect the spreading of the PVDF casting solution on the mold. It is agreed that the polymeric solution should wet and spread out uniformly on the mold to replicate efficiently the desired pattern. Accordingly, they compared the work of adhesion of PVDF casting solution on four different molds, PDMS, poly(urethaneacrylate) (PUA), polystyrene (PS), and PDMS mold with hydrophilized surface. It was found that PUA mold exhibited the highest work of adhesion, while PDMS mold showed the lowest work of adhesion. Furthermore, the SEM micrographs of the produced prism-patterned membranes employing the four molds are presented in **Figure 2.14**. The PVDF patterned membrane fabricated using

PDMS mold showed the highest pattern fidelity. Therefore, it was concluded that the pattern fidelity is promoted, if the work of adhesion between the polymer solution and the mold is minimized.

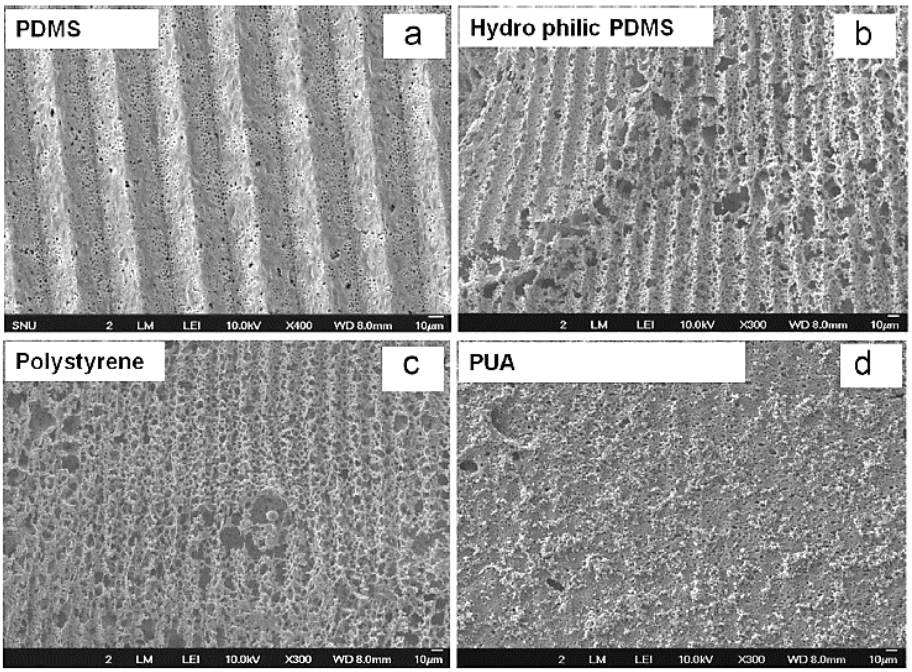

Figure 2.14: SEM micrographs of prism-patterned PVDF membranes prepared using four different molds [162]

In parallel, Gençal et al. have recently investigated the influence of exposure time to humid air, relative humidity of 75 %, on the pattern fidelity of micro-patterned PES MF membranes obtained using VIPSμM [163]. They found that the micro-patterned membranes required longer exposure times than the flat membranes in order to realize symmetric porous structure; however, the pattern fidelity was found to decrease with increasing the exposure time to humid air. Therefore, the preparation conditions of VIPSμM should be specifically refined for each surface micro-patterning system.

2.4.1.3 Nanoimprinting lithography (NIL)

NIL is a feasible and robust technique capable of fabricating high patterning resolution, sub-10 nm features, at relatively low cost and high throughput [135, 164]. The molds employed in NIL should normally be made of mechanically stable materials. In addition, the materials, to be imprinted, have to be able to easily deform to fill the molds' cavities, and quickly solidify prior to mold separation [165]. Therefore, they are usually made of polymers [164, 165]. As aforementioned, NIL can be realized by several mechanistic techniques; however, in this work, attention is only devoted to thermal embossing and compression molding techniques.

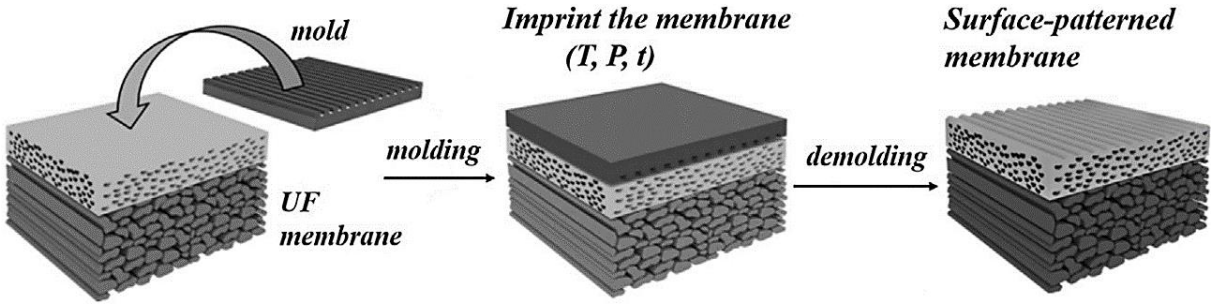

Figure 2.15: Schematic illustration of surface patterning using NIL process [165]

Concerning the thermal embossing technique of NIL, the pattern replication mechanism was found to be based on pressure-induced viscoelastic deformation of a polymer material, namely "squeeze flow" of viscous polymer that is supported on a rigid substrate, into the cavities of a rigid mold under controlled thermal mechanical environment [166-168]. For instance, these viscoelastic deformations were reported to be occurred at a temperature above T_g, or melting temperature (T_m) of the polymer under a few MPa, afterward the temperature is reduced below T_g, or T_m, before the release of pressure. Therefore, high surface patterning resolution can be obtained by controlling the main NIL processing parameters, temperature, pressure and imprinting time [166, 168] (**Figure 2.15**). Notwithstanding, the adaptation of NIL processing parameters was found to be restricted to the pattern design and the molecular weight of the polymer material [169], Wang and Ding found that the pressure-induced viscoelastic mechanism is independent on the aspect ratio of the pattern cavities and the thickness of the polymeric membrane material [166].

Nevertheless, employing the conventional NIL process, imprinting at a temperature > T_g (or T_m), to the polymeric materials was found to cause detrimental pore sealing / collapsing due to the viscous flow of the polymer that resulted in impermeable membranes at normal operating pressures [165, 170, 171]. Inversely, Ding's working groups emphasized that a successful

surface patterning without significant pore collapsing effect could be realized at temperatures < T_g of the polymer [133, 165, 170] (**Figure 2.16**). However, the mechanical deformation mechanism(s) that may account for the surface-patterning process at such low imprinting temperatures remain unclear.

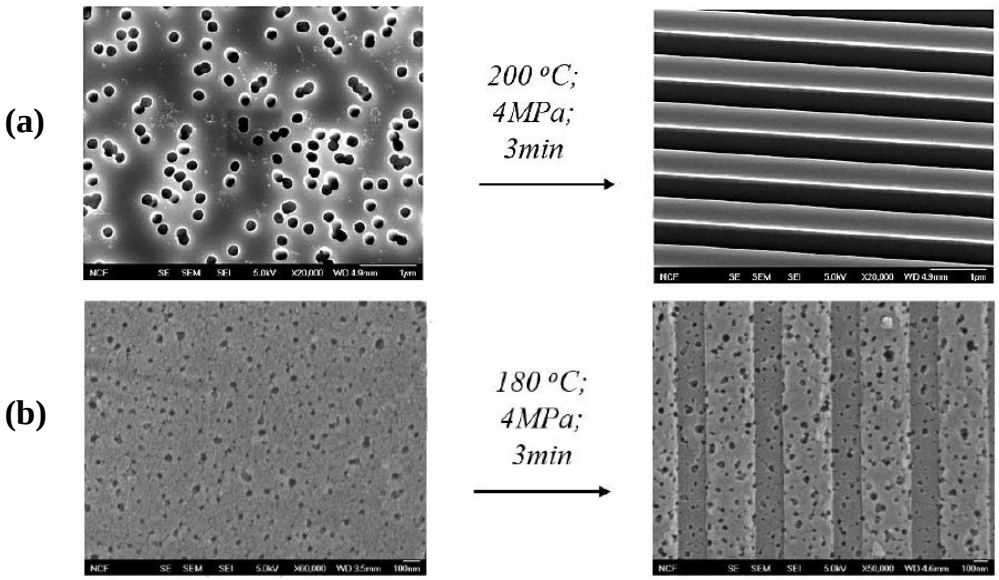

Figure 2.16: SEM micrographs for pristine and surface patterned membranes imprinted using NIL: (a) at T > T_m, (b) at T < T_g [165]

Description: (a) surface patterning of nitrocellulose MF membrane using NIL at 200 °C (above T_m; 160 - 170 °C), (b) surface patterning of PES UF membrane using NIL at 180 °C (below T_g; 215 °C).

Ding's group has tried to explain the mechanism underlying the surface pattering process using the developed low-temperature-NIL method and propose answers to all related inquiries [165, 170]. They assumed that the successful surface patterning of commercial PES membranes reflects their capability of undergoing substantial plastic deformation, at least on the surface, as a result of their high inherent porosity (70 – 80 %), which makes their plastic deformation possible under relatively low pressures, irrespective of the membrane chemistry.

Additionally, the mechanical investigation of the influence of the applied loadings on the porous polymeric membranes emphasized that surface patterning mechanism of PES membranes most probably follows the compressive deformation behavior of open-cell cellular foams [165, 172]. Unlike the viscous flow of polymers at T > T_g, the plasticity in PES membranes originated from certain rotation/twist/bending mechanism of cell/pore walls upon applying pressure at specific temperature (< T_g). Also, cell/pore walls inside PES membrane matrix are assumed to experience the influence of stress-concentrations, and, under much higher effective loading, the plastic deformation becomes non-recoverable; consequently, the

membrane pore structure is permanently altered. Generally, the overall membrane porosity and the molecular weight cut off (MWCO) are reduced after the NIL process.

Moreover, the pattern formation process was modelled using finite element analysis [165, 170]. The simulation showed that the pressure dependence of the pattern height was nonlinear at pressure < yield strength of PES membrane, but it became linear at loadings > yield strength of PES membrane; however further increase in pressure caused a smaller increase in pattern height because of membrane densification. Furthermore, the deformation during the NIL process was found to be non-uniform at the membrane surface due to non-equal contact between the mold and the membrane, such that the contact regions exhibited a normal stress that is higher than the applied load, whereas the areas within the cavities showed much lower stress.

2.4.2 Surface micro-patterning as a promising platform to enhance separation performance and promote antifouling propensity

Manipulating the membrane surface topography has been widely modeled and experimentally investigated as an effective strategy to upgrade the membrane-based water treatment processes. This modern concept was motivated by several studies, which showed clearly to what extent the hydrodynamic conditions and the foulants' deposition behavior can be influenced by both the membrane surface roughness and the geometry/topography of the employed membranes [97, 119, 120].

2.4.2.1 Chaotic flow / mixing at laminar flow conditions

In most of membrane-based water purification processes, the flow is laminar, i.e., low Reynolds numbers, and there are no fluctuations of velocity that tend to homogenize the fluids as in turbulent flow at high Re, consequently, the molecular diffusion is slow. In such operating conditions, the mixing is poor, and the membrane osmotic pressure drop is occurred after short operating time. In order to enhance the mixing effects at laminar flow conditions, Stroock et al. suggested a method based on bas-relief of specific surface patterns at the bottom of micro-channels [173]. They found that patterned surface topography inside fluid paths can generate chaotic flows in contexts other than pressure-driven flows. Afterward, they broadened this concept to generate chaotic electroosmotic flows, in presence of a steady electric field, via pattering the charge density on the inner surface of a channel [174].

These studies have recently motivated the membrane companies to introduce the "feed spacers", mostly plastic net placed on the membrane surface, which were designed to create

flow instabilities, chaotic mixing, to enhance mass transfer and reduce concentration polarization [175]. However, aside from their benefits, feed spacers have been found to increase pressure drop along the flow channel and induce accumulation of foulants particles on the membrane and spacer surfaces that requires further investigation and improvements [176-178].

2.4.2.2 Particle deposition on topographically heterogeneous surfaces

AFM force-distance curves, firstly developed by Ducker et al. [179] by combining AFM and colloid-probe technique, showed that the potential energy barrier for a deposition of silica micro-sphere particle on a rough membrane surface was lower in comparison with smoother corresponding surface [119, 180]. Also, the magnitude of the electrical double-layer repulsion on a rough membrane was reduced on the protruding asperities, peaks [118]. However, the adhesion of the colloid probe was lower at the peaks than in the valleys (cf. **section 2.3.4.5**). Consequently, the deviation in the interaction energy between the foulant particles and the membrane surface was concluded to be strongly correlated to the size of the surface-features rather than to their periodicity [119, 120, 180].

The interaction energy of colloidal sphere rigid particles on topographically heterogeneous, patterned, surfaces was extensively simulated using mathematical models that were mostly based on DLVO theory [181]. Briefly, DLVO theory describes the total interaction energy between two surfaces as the sum of the electrostatic double-layer and van der Waals interactions. Martines et al. [182] have modeled the DLVO interaction between a microsphere and regular nano-patterned surface of various shapes and dimensions. The simulation predicts that the nano-protrusions, nano-pillars, would enhance the adhesion of particles on a surface, especially at reduced pillars' dimension. Moreover, the changes induced by hollow roughness, nano-pits, were less significant; however, nano-pits were predicted to increase the energy barrier at lower particle concentrations, thus hampering particle deposition. These hypotheses have also been upheld through the simulations done by Bendersky and Davis [183], which found that nano-topography, in form of an array of cylindrical nano-pillars, would decrease the potential energy barrier for unfavorable surfaces.

2.4.2.3 Surface micro-patterned membranes: Simulation of hydrodynamic conditions and particle deposition behavior

In response to the outcomes of the aforementioned investigations, several recent theoretical studies and experimental trials have suggested surface patterned membranes as innovative

competent solution for sustainable and efficient membrane-based water purification processes. Nevertheless, the designing of the relevant geometry and dimension of the membrane surface patterns along with optimization the adequate operating conditions are still considered as big challenges towards the broad application of these new members.

A number of theoretical and computational studies, supported by some preliminary experiments, have been reported on the hydrodynamics and particle deposition behavior on patterned membranes with various topographical surface micro- and nano-structures. Ngene et al., as one of the first groups, have studied the deposition of polystyrene micro-particles and biofilm formation on micro-patterned membranes of different geometries under laminar flow conditions [184]. They observed the deposition of polystyrene particles and biofilm growth upstream of the surface structures regardless of their orientation relative to the feed flow. Also, the flow profile simulations showed recirculation zones behind star- and circular-shaped geometries. Moreover, there is a threshold portion of particles that can be deposited on the surface microstructures, afterward, there is an equilibrium-like state between the deposition and the detachment of the particles.

In parallel, the flow characteristics and deposition behavior of three model foulants, activated sludge, PMMA particles (1.3 µm) and latex particles (2 µm), on prism-patterned PVDF membranes of different pattern's dimensions have been consecutively simulated and investigated experimentally, at different cross-flow velocities within the laminar flow condition [27, 129, 185]. In these numerical and practical studies, the feed flow direction was perpendicular to the alignment of surface patterns.

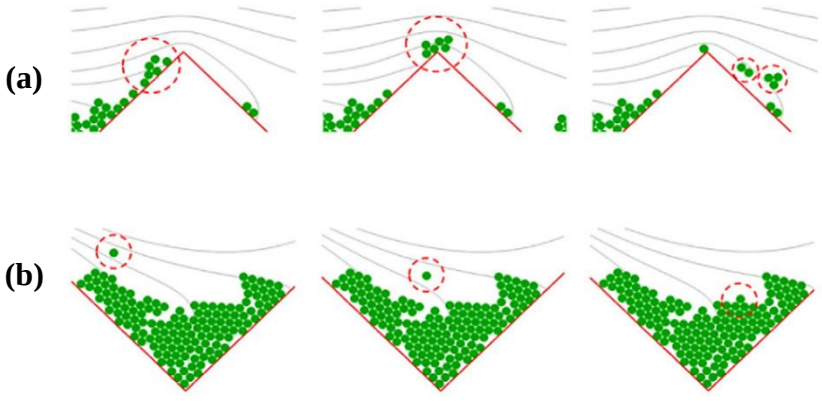

Figure 2.17: Deposition of PMMA particles at Re = 50 (a) on apex regions and (b) in valley regions [129]

Generally, prism surface-patterns that were introduced to the membrane surface were found to reduce outstandingly the foulant deposition. However, the local distribution of the foulant's

particles on the membrane surface was observed to vary remarkably such that the foulants' particles tend to accumulate mainly in the lower regions of the surface pattern, valleys, where vortexes were formed. Inversely, the local wall shear stress was higher in the upper regions, apex, resulting in prohibiting the attachment of the foulant's particles. The merits of these prism surface patterns on mitigating the deposition of PMMA particles even under very low Reynolds number (Re = 50) were affirmed [129]. Stagnant flow zones and, consequently, very low shear stress along with particles accumulation were found in the valley regions, whereas higher shear stress near the apex regions facilitated the detachment of PMMA particles (see **Figure 2.17**).

Furthermore, the influence of the size of the surface patterns on deposition of latex particles under two different Re values within the laminar flow conditions was investigated, and the fouling mechanisms were modeled [185]. A larger pattern was found to be less effective than a smaller pattern under low Re, whereas it was very successful in hampering particle fouling under high Re (see **Figure 2.18**). Under high Re, vortex was formed in the valley regions, proposing that particles entering the valley regions had a chance to return to the bulk cross-flow stream because the distance between the vortex and the bulk stream was shorter. Additionally, modified surface patterns were developed by introducing intervals to prism patterns, which resulted in enhancing the vortex and reducing the portion of permeation stream in the valley regions.

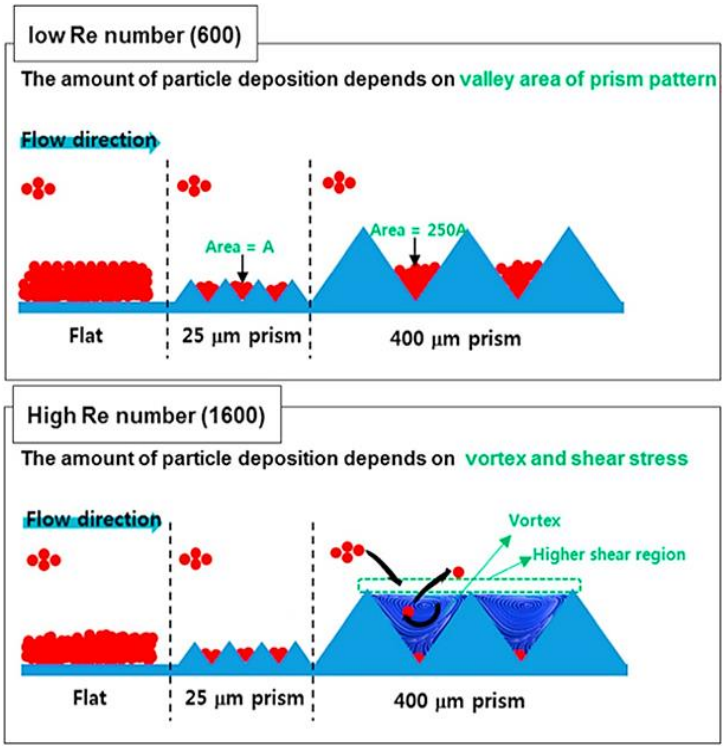

Figure 2.18: Influence of the size of the surface patterns on deposition of latex (2 μm) particles under different Reynolds numbers [185]

2.4.2.4 Surface micro-patterned membranes: Experimental investigation of antifouling propensity of patterned UF membranes

Culfaz et al. were among the first to prepare micro-structured hollow fiber PES membranes, employing modified dry-wet phase inversion method [160], and explore practically their propensity for colloidal silica fouling, in both dead-end and cross-flow filtration modes, as well [28, 186]. In dead-end constant flux filtrations, the fouling resistance increases faster upon using structured fibers than with round fibers [28]. In addition, the smaller silica particles, 20 nm, were found to deposit more within the grooves of the structured fibers, whereas the alkali-stabilized bigger silica particles, 60 nm, showed a homogenous deposition across the surface of the structured fiber, and the thickness of the deposit was similar to that on the round fiber. The observed difference in the deposition behaviors was explained in terms of discrepancy in the back diffusion that results in a thick polarization layer with very low resistance in case of smaller particles, but bigger particles formed a thinner polarization layer of much higher resistance [28]. Nevertheless, the cross-flow filtration experiments showed that both the micro-structured and the round fibers exhibited similar fouling behavior; increasing Re values increased the critical fluxes significantly [186].

Thereafter, Won et al. examined the water flux and the fouling behavior of various patterned PVDF UF membranes, prepared by a modified immersion precipitation method, in a membrane bioreactor for wastewater treatment [161]. The surface patterns were found to improve the water flux in proportion to the roughness factor of the patterned membrane. Also, the deposition of microbial cells on the patterned membranes was significantly impaired due to the local flow turbulences induced by the apex of the surface structures. Additionally, they investigated the influence of surface patterns' height on the adhesion of microbial cells on prism-patterned PVDF UF membranes, using a cross-flow filtration system, in which the flow direction is perpendicular to the alignment of the surface structures [162]. Prism-patterned membranes with greatest pattern's height (18 – 20 µm) exhibited the lowest microbial adhesion that was interpreted by increasing local wall shear stress at the apex regions, as discussed earlier in their computational studies [27].

In parallel, Gohari et al. studied the fouling of nano-patterned UF membranes by cross-flow filtrations of bovine serum albumin at different membrane alignment to the feed flow direction, under turbulent flow conditions, feed flow rate = 200 L/h and Re > 2800, [136]. They found that the protein fouling could be mitigated when the feed solution is perpendicular to the

patterned lines, whereas the fouled membrane surfaces were effectively washed when the flow was parallel to the surface patterned lines.

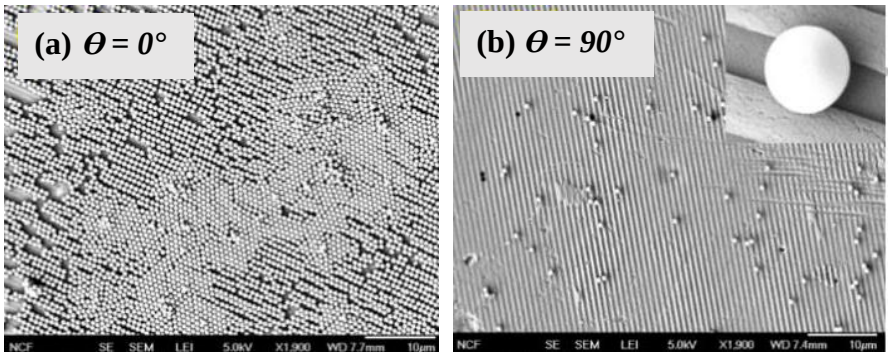

Figure 2.19: Anisotropic deposition of silica colloidal particles on the surface nano-patterned PES membrane [165]

Furthermore, Maruf et al. have extensively investigated the critical flux and the colloidal silica fouling of surface nano-imprinted PES UF membranes under laminar flow condition [133, 165, 187]. The imprinted surface patterns were found to prohibit remarkably the fouling by colloidal silica particles, as evidenced by a 19 – 45 % increase in the apparent critical flux [133]. Also, the magnitude of critical flux increased by increasing of particle size and cross-flow velocity; consequently, the back diffusion of silica particles was understood to be governed by shear-induced diffusivity mechanism. Additionally, the critical flux was also affirmed to be increased with increasing the surface patterns' height, which was explained by improving the back diffusion mechanism as a result of enhancing the effective shear rate at the membrane surface [129, 187]. Nevertheless, the SEM micrographs for the fouled membranes showed an anisotropic deposition of the silica particles on the patterned PES membranes, such that the surface coverage decreased with an increase in the orientation angle between the surface patterns and the feed flow direction, θ, (**Figure 2.19**). In addition, an alignment of the silica particles along the surface grooves was noticed, suggesting that the presence of the surface patterns may influence the packing, or entropy, of the silica particles, an effect known as "graphoepitaxy" [188].

2.4.3 Surface patterned PA TFC membranes and their performance

Many technical issues are observed to accompany the exploitation of the feed spacers (cf. **section 2.4.2.1**). As a result, the application of the surface micro-patterning approach to membranes for water desalination technology has been recently suggested as a promising trend toward suitable solutions for colloidal / particle fouling in RO plants. Nevertheless, it is technically challenging to find out the adequate method to achieve that.

PA TFC membranes are the most abundantly used water desalination membranes. As mentioned before, they are mostly composed of ultrathin cross-linked PA barrier (< 200 nm) atop a porous UF / MF support made of PS or PES (cf. **section 2.3**). Subsequently, only two alternative routes can be followed up to obtain surface micro-patterned TFC membranes. First is to figure out the suitable lithographic technique for direct application on PA TFC membranes, whereas second is to fabricate a micro-patterned support, thereafter the PA layer can be prepared by conventional IP method.

Short time ago, it was prevalently believed that it is extremely difficult to plastically deform PA TFC membrane by employing high temperature and pressure, as in NIL (cf. **section 2.4.1.3**), without causing fracture in the cross-linked PA barrier layer that would result in membrane failure [165, 189, 190]. However, Weinman and Husson have recently suggested that regular nano-patterns can be directly imprinted to the surface of PA TFC membranes employing silicon stamp and using thermal embossing technique [191]. The silicon stamps comprised of a 606 nm period between peaks, a 190 nm groove depth, and a 303 nm line width. In this work, they patterned commercial NF membranes, consisting of semi-aromatic PA layer based on PS and supported by polyester fabric, at 45 °C under certain applied force. The fracture in the barrier layer was investigated by measuring water permeability and rejection of magnesium sulfate salt. According to the result, the separation performance wasn't observed to be adversely affected by the surface patterning process and no fracture in the PA layer was noticed. They defended that by calculating the local strain in PA layer under the patterning conditions to be 10.6 ± 5.6 %, while Chung et al. quantified the strain at the onset of cracking, ε*, for nanoscale cross-linked PA thin films to be 14.0 ± 4.1 % [192].

Nevertheless, one can conclude that the direct imprinting of NF membranes seems to be feasible to some extent, depending on the employed technique and the patterning conditions, since their standard operation doesn't require superior selective properties analogous to RO membranes whose interstitial void size within the selective PA layer shouldn't exceed 0.6 nm.

Instead, more viable surface patterning approach, based on the second alternative route, has been already presented by Maruf et al. [189]. Commercial PES UF membranes were firstly imprinted using NIL process, at previously adapted conditions [133], afterward, the patterned membranes were used as supports for PA preparation by conventional IP method. The employed silicon mold exhibited parallel line-and-space gratings (a periodicity of 834 nm, groove depth of 200 nm, and a line-to-space ratio of 1:1). The consistency of the PA growth on the patterned UF membranes was observed to be influenced by the amine concentration

rather than IP reaction time [190]. Increasing the amine monomer concentration increased the degree of non-conformal growth, regardless the type of the monomer system, which was attributed to the thickening action by the high IP progression at increased amine monomer concentration. It was meant by non-conformal growth that PA layer within the pattern valleys is thicker than that atop the pattern ridges. Furthermore, the influence of modifying the surface topography on the antifouling propensity of surface-patterned TFC membranes was also investigated [189, 193]. The patterned TFC membranes exhibited relatively higher water flux in comparison with non-patterned counterparts; consequently, the onset of scaling on patterned TFC membranes was somewhat faster. However, the patterned membranes were statistically emphasized to exhibit substantial higher flux during the final hour of filtration, besides the SEM analysis for the fouled membranes showed a sparser distribution of gypsum crystals on the patterned surface, which was interpreted by the enhanced hydrodynamic effects due to using patterned TFC membranes [189]. Moreover, the patterned TFC membranes were observed to exhibit lower flux decline and a higher tendency for pure water flux recovery after long-term fouling permeation experiments using NaCl-glycerol-BSA mixture as a feed solution [193].

Nevertheless, the developed nano-patterned TFC membranes showed modest NaCl rejection behavior, < 90 %, so they were classified as tight NF or loose RO membranes [189]. Subsequently, further refinement for the patterning methodology, designing the respective surface pattern, and adaptation of the preparation conditions, in addition to investigation of the relevant testing protocol are still required. These reported trials toward fabrication of high performance surface patterned TFC membranes implies the potency of the surface patterning approach to develop new generation of PA TFC membranes. Micro-imprinting lithography (MIL) could potentially be an alternative to holding the superior intrinsic properties of the barrier PA layer along with promoting the conformity of the surface microstructures

2.5 Surface modification of PA TFC membranes

PA TFC membranes are revealed to exhibit free carboxylic acid groups, resulting from eventual hydrolysis of unreacted acyl groups besides chain ends, in addition to free unreacted amino-groups on chain ends [194, 195]. These groups can be exploited as potential reactive sites for binding of certain coatings that, generally, tend to improve membrane surface charge and hydrophilicity as well as reduce surface nano-roughness; consequently, this promotes antifouling propensity and enhance the cleaning efficiency [79, 196]. Numerous surface modification techniques have been employed to treat the surface of PA TFC RO and NF

membranes, ranging from direct chemical treatment, also known as "hydrophilization treatments", to surface coating, in addition to surface grafting, mostly by chemical bonding via one of two major mechanisms "*grafting to*" or "*grafting from*" [196-198].

Nevertheless, most of the surface modification approaches are still suffering from some downsides [196, 199]. For instance, the immobilized coatings could add additional resistance to the permeation flux, accordingly developing hydrophilic coating materials, e.g., hydrogels, is revealed to be more convenient. Additionally, the employed surface modification method may impair the membrane selectivity because the coating layer may mask the PA surface charges that are essential to reject the salts. Subsequently, hydrophilic coating materials that comprise carboxylic and/or amine groups, e.g., acrylamide-based homo- and copolymers, polydopamine, zwitterionic materials … etc., could potentially be more favorable to improve the membranes' fouling resistance without detrimental impact on the perm-selective properties [196, 198].

2.5.1 Stimuli-responsive materials

Synthetic polymeric materials able to sense and respond to external or internal stimuli, known as "stimuli-responsive materials", are considered one of the emerging areas of scientific interest that have been already used in several applications [200]. In particular, the exploitation of stimuli-responsive materials in improving the membranes' separation performance and fouling resistance have recently attracted attention as an effective approach [201]. These materials exhibit abrupt transition in their physical or chemical properties, e.g., swelling behavior, hydrophobicity / hydrophilicity, permeability, surface active or selective properties, sorption capacity besides optical properties [202], upon application of a small change in environmental condition, "stimulus", e.g., temperature [203], pH [204], ionic strength [205], electric field [200], magnetic field [206], light [207]. Some polymeric materials can respond to a combination of two or more stimuli. However, the change in temperature and pH are the most commonly used stimuli [202, 208]. Afterward, the materials return to its initial state when the trigger used is removed. The stimuli-responsive materials can be used in the form of hydrogel [202], micelles [209], particles [210], and membranes [198].

The stimuli-responsive hydrogels have been abundantly used to improve the fouling resistance of RO membranes, as an application of stimuli-responsive swelling/deswelling behavior [208, 211]. In brief, the swelling/deswelling behavior of hydrogels fall into two cases, continuous or discontinuous transitions [212]. The discontinues, also known as "critical",

transition is the major phenomena in stimuli-responsive hydrogels. It is a spontaneous phenomenon caused by at least one of four fundamental molecular interactions, van der Waals, hydrophobic, hydrogen bond or ionic interactions. Accordingly, an infinitesimal change of the thermodynamic balance between these interactions can lead to a conversion of the hydrogel among two distinct phases. The dominating attractive or repulsive forces, respectively, cause absorption or expulsion of the solvent molecules from the polymer network, resulting in two thermodynamic phases, swollen or collapsed state [212].

2.5.1.1 Thermo-responsive polymers

Thermo-responsive polymers are the most classical stimuli-responsive materials, and one of the most commonly used coatings to modify RO membranes. They exhibit coil-to-globule phase transition, an abrupt change of solubility in water-based solutions, at lower critical solution temperature (LCST) [200]. When the environmental temperature is below the LCST, the polymer chains are completely soluble, "coil" state, as a result of extensive intermolecular hydrogen bonds between polymer chains and the water molecules besides the restricted intramolecular hydrogen bonds among polymer chains. But when the temperature is raised higher the LCST, collapsing of the polymer chains, "globular" state, is occurred due to disruption of the intermolecular hydrogen bonds and dominating of intramolecular hydrogen bonds [200, 201]. Poly(*N*-isopropylacrylamide), PNIPAAm, is the most common example for thermo-responsive polymers. Another examples are poly(*N*-vinylcaprolactone), poly(*N,N'*-diethylacrylamide), poly(vinyl methyl ether), poly(ethylene glycol) [201].

Thermo-responsive polymers with low LCST have been already exploited for cleaning the fouled membranes [213, 214]. In brief, the thermo-responsive polymer is dissolved in the cleaning solution; consequently, it diffuses into the deposited foulant layer on the membrane surface at temperature below LCST. Thereafter, the temperature is raised to be above LCST, so the thermo-responsive polymer becomes insoluble, forming "globular" structure. As a result, the foulant layer is broken up or becomes loose, and it can be easily washed out. Subsequently, it can be concluded that the surface modification of RO membranes using thermo-responsive polymers will enhance the fouling resistance by promoting the surface hydrophilicity, as well as improving the membrane cleaning efficiency as a result of coil-globule phase transition [214].

2.5.1.1.1 PNIPAAm homo-polymers

Poly(*N*-isopropylacrylamide) (PNIPAAm) has received a unique attention as the most abundantly used thermo-responsive material because of its highly reversible responses to thermal stimulus [200, 203]. PNIPAAm is a water soluble polymer exhibiting LCST of about 32 °C in aqueous solutions, firstly observed by Heskins and Guillet [215]. Below the LCST, the polymer chains are hydrophilic, swollen and exhibiting chain-extended conformations, as a result of the intermolecular hydrogen bonding with the water molecules. Above LCST, the hydrogel shrinks, dehydrates, transforms into collapsed globular form because the intramolecular hydrogen bonding between the CO and NH groups dominate over the intermolecular hydrogen bonding (**Figure 2.20**) [216]. The coil-to-globule phase transition of PNIPAAm was clearly seen using AFM [217].

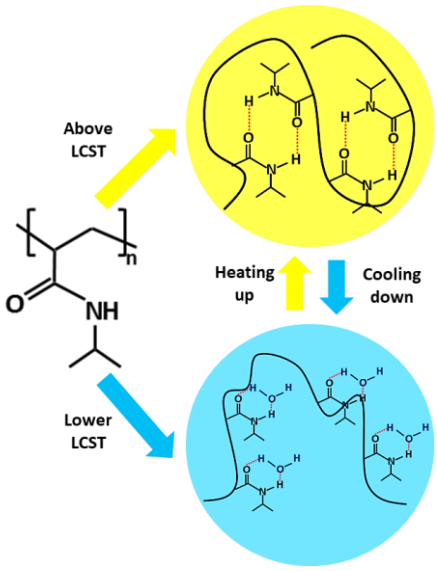

Figure 2.20: Reversible swelling/deswelling behavior of PNIPAAm hydrogel below and above the LCST

2.5.1.2 pH-responsive polymers

pH-responsive polymers are materials containing an ionizable functional groups, commonly carboxyl and pyridine groups, capable of accepting or donating protons upon changing of the environmental pH [201, 204]. They are generally classified as polyacids and polybases. Polyacids are one group of pH-responsive polymers that contain, so called “alkali swellable”, carboxyl groups, e.g., poly(acrylic acid) (PAAc), and poly(methacrylic acid). They have pK_a values in range of 4.7 – 5 [218]. At low pH, carboxyl groups are protonated and the hydrophobic interactions dominate, leading to repelling of the water molecules and a volume shrinkage, collapsing, of the polymer. At basic pH, carboxyl groups are deprotonated resulting in high negative charge density in the polymer, causing a swelling and extended structure.

Inversely, pH-responsive polybases contain, "acid swellable", pyridine groups, e.g., poly(*N,N'*-dimethyl aminoethyl methacrylate) and PVP. They are able to accept protons at acidic pH conditions giving rise to internal charge repulsions between neighboring protonated pyridine groups, leading to an extended structure [219].

2.5.1.3 Double stimuli-responsive materials

In parallel, there is a growing trend to design multiple-stimuli-responsive polymeric materials containing covalently or physically bonded segments responsive to different stimuli [200, 201, 220]. There are many examples for multi-responsive polymeric materials that have been already investigated in literature. For example, a multi-responsive material consisting of a temperature responsive segment, NIPAAm, besides pH- and photo-double responsive segments, spirobenzopyran, exhibits temperature, pH, and photo-responsiveness in aqueous solutions [221]. Another interesting example, Szczubialka et al. have reported on synthesis of a quadruple-responsive terpolymer comprising AAc segment, pH-responsive, and NIPAAm segment, temperature-responsive, in addition to cinnamoyloxyethyl acrylate segments, temperature- and UV-responsive [222]. Therefore, there are many opportunities for designing multiple-responsive polymeric materials that could be beneficial as coatings for RO membranes to enhance antifouling propensity and cleaning efficiency.

2.5.1.3.1 Random copolymers based on NIPAAm: P(NIPAAm-co-AAc)

It was emphasized that the coil-to-globule phase transition of stimuli-responsive polymers can be thermodynamically and kinetically controlled by adjusting the polymer chemical composition [200]. The LCST of PNIPAAm can be manipulated by copolymerization with other monomers [215, 220]. Generally, copolymerization with hydrophilic moieties, e.g., acrylamide (AAm), acrylic acid (AAc), would shift coil-to globule phase transition to higher temperatures, i.e., LCST increases, while incorporation of hydrophobic moieties, e.g., butyl methacrylate, was found to decrease LCST. Random copolymerization of NIPAAm and hydrophilic co-monomers containing ionizable groups would yield double-stimuli responsive polymer.

Poly(*N*-isopropylacrylamide-co-acrylic acid), P(NIPAAm-co-AAc) random copolymers were found to be temperature- and pH-responsive materials. They were found to exhibit temperature-sensitive swelling-deswelling changes depending on the AAc mol.% and the environmental pH range [220] (**Figure 2.21**). It was revealed that, at AAc composition < 10 mol.%, phase transition point increase with increasing of AAc mol.%, while P(NIPAAm-co-

AAc) random copolymers can lose their temperature responsivity, LCST disappears, if the AAc mol.% is higher than 10%. This was attributed to the high AAc content that causes sufficient solubility to offset the aggregation of the thermo-responsive segments, NIPAAm. Furthermore, the influence of the environmental pH on phase transition of P(NIPAAm-co-AAc) random copolymers was investigated. At pH ~ 4 (below pK_a of AAc), LCST increases gradually with increasing AAc content, and considerable proportions of AAc up to ~ 40 wt.% can be used. On the other hand, at pH 7.4 (above pK_a of AAc), LCST increases rapidly with increasing AAc content, and conveys upper limit at AAc content < 10 wt.%.

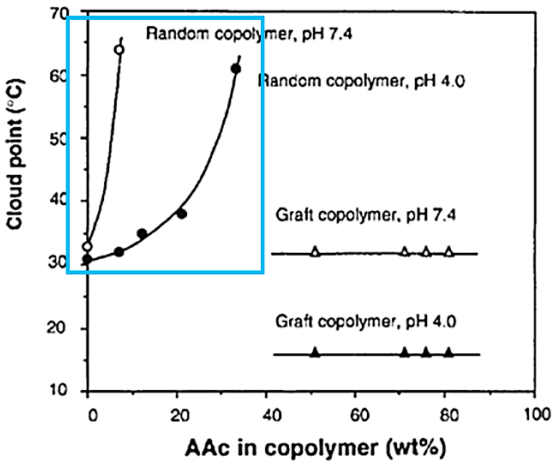

Figure 2.21: Influence of AAc content on phase transition of P(NIPAAm-co-AAc) random copolymer at different environmental pH values [220]

2.5.2 Surface modification of TFC membranes using stimuli-responsive functional polymers

The surface modification of TFC RO and NF membranes using stimuli-responsive functional materials have received widespread attention as an effective pre- and post-treatment approaches to promote the membranes' fouling resistance and cleaning efficiency [196, 197, 211, 223]. Yu and coworkers modified commercial TFC membranes employing coatings, made from P(NIPAAm) homo-polymer and its copolymer with P(AAc) by free radical polymerization, using in-situ surface coating method [208, 211]. Also, Belfer working group introduced a method based on redox-initiated radical grafting of hydrophilic acrylic polymers onto PA NF membranes [224]. In addition, Tomer et al. employed surface-initiated atom transfer radical polymerization to modify NF 270 membranes by grafting of acrylamide-based block copolymer brushes from PNIPAAm-modified TFC membranes [223]. In parallel, Mondal and Wickramasinghe used photo-induced graft polymerization to graft PNIPAAm coatings from benzophenone-functionalized surface of NF 270 membrane [225].

Indeed, it was emphasized that a successful membrane modification method should satisfy two conditions: (a) it is important to hold on the useful properties of the pristine membrane; (b) efficient introduction of functional moieties to the membranes [198].

Tethering or immobilization of polymer coatings onto a membrane surface could be realized reversibly or irreversibly [226]. Irreversible grafting is essentially accomplished by chemical bonding via one of two distinct surface-selective approaches, "*grafting to*" and "*grafting from*". In brief, the "*grafting to*" mechanism immobilize pre- synthesized and end-functionalized stimuli-responsive polymers onto the membrane surface, whereas the "*grafting from*" technique is a heterogeneous, surface-initiated polymerization process whereby polymer chains grow from the immobilized initiator sites on the membrane surface [198, 226]. Physisorption, a reversible process achieved by self-assembly of end-functionalized polymers on a membrane surface under certain conditions, can also be considered as another form of "grafting to" mechanism [197].

In parallel, the polymer chain grafting density is a critical parameter to be considered during designing of the adequate surface modification procedures since it influences to far extent the final performance of the membrane [198]. For instance, high grafting density may be required to isolate the underlying membrane form the strong fouling medium; however, this was observed to impair the stimuli-responsiveness because the polymer chains are trapped / packed in an extended configuration. In "*grafting to*" approach, the grafting density was found to be mainly influenced by the polymer molecular weight, while in case of "*grafting from*" technique, the grafting density and the polymer molecular weight were claimed to be independent parameters.

2.5.2.1 Surface modification via "grafting from" technique

In principle, the surface modification using "grafting from" approach, also known as "surface-initiated polymerization", is carried out in two main steps, (a) chemical immobilization of the initiator on to the membrane surface; (b) initiation of polymer chain growth by dispersing the monomers into the reaction mixture where the membrane is immersed [198, 216]. The surface modification of TFC membranes using this approach have been extensively reported [122, 196, 223]. This is because the capability of the technique to yield covalently bonded polymer chains of various grafting degrees and layer thicknesses. The control on the grafting density can mostly be achieved via tuning the initial density of immobilized initiator [216]. Additionally, high grafting density and thicker grafting layers of

about 100 nm can be realized since the monomers can easily penetrate through the grafted segments [201]. Numerous methods can be employed to modify TFC membranes by "*grafting from*" mechanism, e.g., photo-initiated grafting (UV and non-UV), plasma-initiated grafting, thermal grafting, and redox-initiated grafting, besides controlled radical grafting methods, e.g., atom transfer radical polymerization (ATRP) and reversible addition-fragmentation chain transfer (RAFT) polymerization [198].

2.5.2.1.1 Surface-initiated ATRP

Surface-initiated ATRP, SI-ATRP, has successfully been used to graft a wide range of acrylamide-based stimuli responsive materials from the surface of TFC membranes [122, 223, 227]. ATRP is considered as one of the most convenient "*grafting from*" methods because of the controlled polymer chain growth and grafting density, besides the availability of various monomers [228, 229]. Additionally, it offers a good control over the polymer molecular weight and attains low poly dispersity [216, 228]. Typically, the initiator in ATRP reaction is an alkyl halide, and the catalyst is a complexed copper(I)/copper(II) system [228]. Subsequently, most of ATRP reactions can be performed under relatively mild conditions using wide range of solvents [230]. Aqueous-based bulk-ATRP reactions have also been widely used; however, aqueous-based SI-ATRP was reported to be less efficient and relatively less controlled [216, 231]. Tomer et al. were modified NF 270 membranes by grafting acrylamide-based copolymer using SI-ATRP [223]. They observed that the membrane surface roughness increased unexpectedly after the modification, in addition to non-linear chain growth accompanied by rapid increase in the layer thickness at early polymerization times. They attributed these observations to the "characteristic" lack of control during water-accelerated ATRP reaction. Several acrylamides have been reported to be prepared with better control upon using different solvent mixtures [232, 233]; however, theses solvent systems are less tolerant to PA TFC membranes [223].

2.5.2.2 Surface modification via "grafting to" technique

Membrane surface functionalization using stimuli-responsive materials via "*grafting to*" approach has often been carried out either by physisorption or chemical grafting of pre-synthesized polymer chains into the surface of PA TFC membranes. Both techniques exploit the free carboxylic- and amino-groups existing on the PA barrier layer. Many examples for surface modification of TFC membranes are presented in section **2.5.3**.

Surface coating techniques, by physisorption or chemical coupling, are considered as the most convenient and straightforward procedures to treat RO and NF membranes [196]. Simply, surface coating comprises two steps, (a) immersion of the activated TFC membrane in a coating solution; (b) evaporation of residual solvent at moderate temperature to form the coating layer. The pretreatment of the membranes, coating conditions, and post-treatment procedures were revealed to influence the membrane characteristics, e.g., surface hydrophilicity and surface roughness, in addition to the membrane performance [196, 208, 211].

2.5.2.2.1 Carbodiimide coupling chemistry

The grafting of functional polymers containing carboxylic-groups to amine reactive surfaces, PA layer, via carbodiimide coupling chemistry can potentially be used as a viable surface modification method [197]. Kang et al. have introduced a surface modification method of PA TFC membranes based on carbodiimide coupling [234]. They grafted poly(ethylene glycol) derivatives to free carboxylic-groups at TFC membrane surface to produce a modified TFC membrane exhibiting improved resistance against organic fouling. In addition, carbodiimide activated amide formation was also used by Yang et al. to immobilize carboxylated magnetic nano-particles to amine-modified NF 270 membrane to prepare magnetic-field responsive NF membranes [122]. Furthermore, Xu et al. improved the anti-biofouling and chlorine-resistant properties of a commercial aromatic PA RO membrane by means of carbodiimide-induced grafting of imidazolidinyl urea [235].

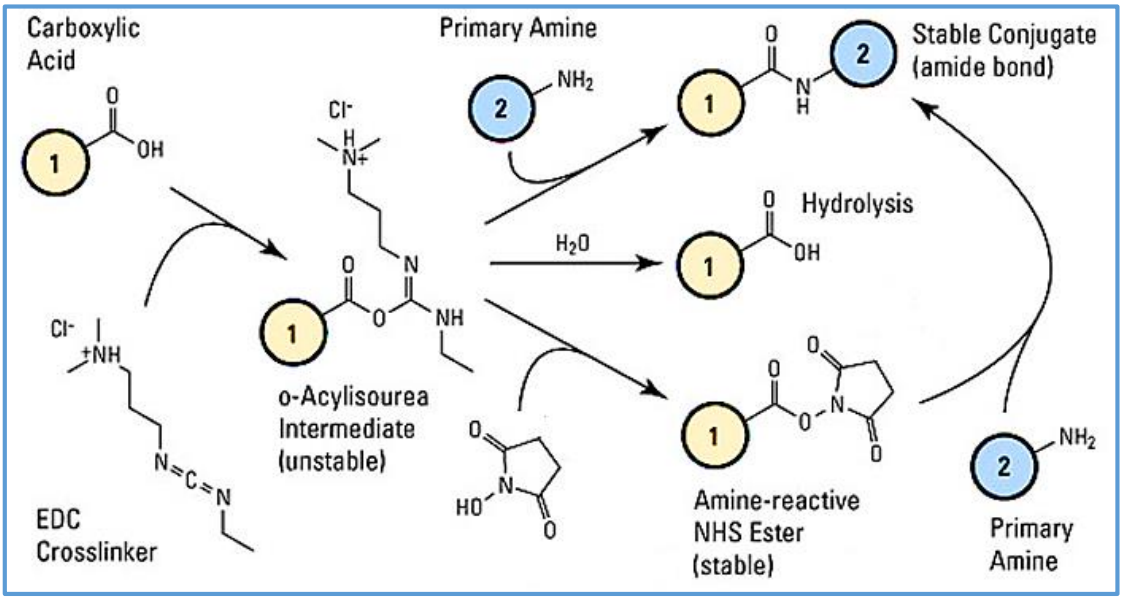

Figure 2.22: Scheme for carbodiimide coupling chemistry [236]

The carbodiimide, 1-ethyl-3-(3-dimethylaminopropyl) carbodiimide "EDC", is a coupling reagent that is used for the activation of carboxylic acid groups in aqueous solutions, afterward the activated ester is reacted with primary amines via amide bond formation [236]. The scheme for carbodiimide coupling chemistry is introduced in **Figure 2.22**. Detailed mechanism can be found elsewhere [236].

2.5.3 Other reported examples for surface modification of PA TFC membranes

Based on the surface chemistry of PA TFC membranes, numerous surface modification approaches comprising of hydrophilization treatment and/or surface coating, or surface grafting were employed. Kulkarni et al. suggested a hydrophilization protocol of commercial PA TFC membranes based on selective dissolution at solvable sites along the PA chain to eliminate defects in the barrier layer using a mixture of protic acids, e.g., hydrofluoric, hydrochloric, sulfuric, nitric acid, and mild alcohols, e.g., ethanol, isopropanol [237]. The hydrophilizing mixture was observed to increase the surface hydrophilicity and decrease the surface roughness; however, the fouling resistance of the treated RO membranes was not evaluated. Later, it was emphasized that this kind of treatment should be carefully used since it may cause a detrimental breakdown of the PA structure [197]. In the same context, Kuehne et al. found that washing and treatment of freshly prepared PA TFC membrane using glycerol and then drying at the oven could enhance greatly the flux by 70 % [238]. They revealed that glycerol is only a passive substance that works as preserving agent to keep the porosity of the membrane during the oven drying process.

Surface coating of TFC membranes via physical adsorption was also reported. For example, Wilbert et al. coated commercial PA RO membranes using polyethylene-oxide surfactants [239]. The surface roughness of PA membranes was observed to be reduced after the modification, and improved antifouling properties were reported. Polyelectrolytes were also used for surface modification of RO membranes. Zhou et al. introduced a simple method based on electrostatic self-assembly of polyethyleneimine on commercial TFC membrane [240]. Additionally, PVA polymers were employed as hydrophilic coatings to PA RO membranes that were able to improve the fouling resistance [241].

Moreover, poly(ethylene glycol) was introduced as a good candidate for the antifouling coatings because of the flexibility of its long chains that can disrupt the foulants deposition. For example, Rana et al. developed an antifouling coating layer of hydrophilic polyurethane end-capped with polyethylene glycol [242]. Also, Wang et al. introduced an interesting surface

coating approach combining layer-by-layer technique and click chemistry to assembly low-fouling polyethylene glycol acrylate multilayer on commercial RO membranes [243]. Layer-by-layer technique was reported to be a facile technique to prepare antifouling polyelectrolyte coatings with controlled layer thickness [196]. In addition, McCloskey et al. found that polydopamine coatings can improve the organic fouling resistance of TFC membranes [244]. Also, zwitterionic-based materials, e.g., poly carboxybetaine, showed a great potential as antifouling coatings for RO membranes [245]. Recently, Nikolaeva et al. have introduced an antifouling coating made from hydrophilic hyperbranched poly(amido amine) [246].

2.6 Toward designing of super-wetting/anti-wetting surfaces

Interestingly, many studies on the characteristics of biological surfaces emphasizes that a macroscopically smooth surface can exhibit commonly a microscopic roughness on different length scale [247-250]. A unique typical example is the water droplets rolling off on lotus leaves, known as "lotus effect" firstly introduced by Barthlott and Neinhuis [248]. The super-hydrophobicity of lotus leaves was investigated and the surface was scanned using SEM (**Figure 2.23 (a)**). The lotus leaf was observed to contain micro- and nano-hierarchical structures (~ 120 nm) on top of micro-papillae (5 – 9 µm) [249]. The combination of these micro- and nano-surface roughness along with the hydrophobic epicuticular wax crystalloids layer are believed to interpret the super-hydrophobicity phenomenon. Another interesting example for the super-hydrophobic biological surfaces is the water strider insect, "*Gerris remiges*" [250]. Water striders are found to exhibit non-wetting legs that enable them to stand on water surfaces (**Figure 2.23 (b)**). The SEM analysis showed that these non-wetting legs composed of numerous oriented needle-shaped setae with diameters, ranging from 3 µm down to several hundred nanometers and each micro-seta exhibits nano-grooves forming a super-hydrophobic hierarchical structure (**Figure 2.23 (c)**).

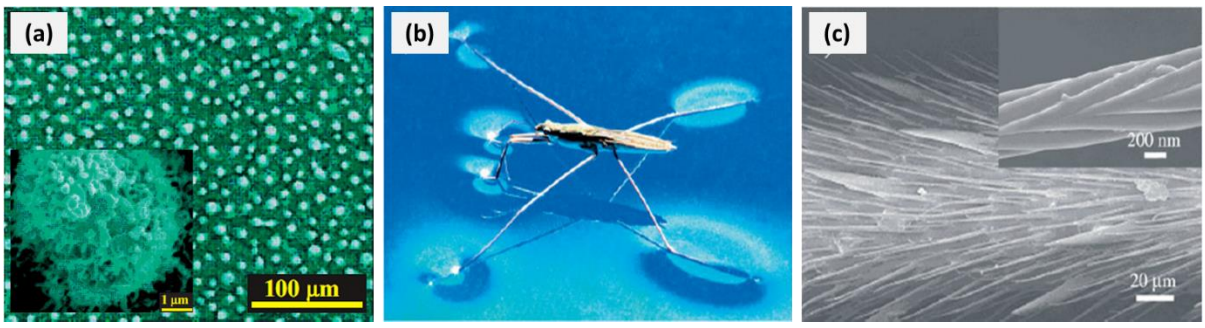

Figure 2.23: (a) SEM micrograph for a super-hydrophobic lotus leaf [249], (b) photograph of super-hydrophobic legs of *Gerris remiges* [250], (c) SEM micrograph for insect's non-wetting leg showing oriented needle-shaped setae with nano-grooves [250]

Wetting is found to play a key role in determining the morphology and stability of a liquid on a given surface since it controls the dynamics of liquid spreading [251]. Some applications require fast and homogeneous wetting, while others favor anti-wetting or self-cleaning. The controlling of solid surfaces' wettability is a premier aspect of surface chemistry that have substantial influence on many liquid-based applications, e.g., membranes.

2.6.1 Theories describing the wetting behavior of rough solid surfaces

In principle, the wetting properties of any solid surface depend on the surface free energy, which is defined as "the work required to increase the size of the surface of a phase", energy per unit area, so it has a universal unit mN/m. Generally, the term surface free energy is used for solid surfaces; however, when a liquid phase is concerned surface tension, γ, is often used instead.

2.6.1.1 Young's model

Consider a liquid droplet on a flat surface (**Figure 2.24 (a)**), the wettability is determined by the surface free energy of the substrate, which is commonly calculated using the well-known Young's equation [252]:

$$\gamma_{SV} = (\gamma_{SL} + \gamma_{LV}) \cos \theta_Y$$

Equation 12: Young's equation

Here, θ_Y is called Young's contact angle, and γ_{SV}, γ_{SL}, besides γ_{LV} are the different interfacial tensions, solid/vapor, solid/liquid, and liquid/vapor, respectively. Young's equation assumes that the solid surface is chemically homogenous and topographically smooth [251]. Nevertheless, the real surfaces are chemically heterogeneous and rough; consequently, the surface roughness have to be considered during the estimation of the solid surfaces' wettability [247, 251]. Therefore, two main theories, Wenzel and Cassie equations, are always employed to correlate the surface roughness parameter with the "apparent", or measured, contact angle of a liquid droplet on a solid surface.

2.6.1.2 Wenzel model

Wenzel recognized the distinction between the total or "actual surface" of a solid substrate and what was termed as its superficial or "geometric surface", the surface as measured in the plane of the interface. Accordingly, in case of perfect smoothness, actual surface and geometric surface should be identical, while, at the surface of any real solid, the actual surface will be

greater than the geometric surface due to the surface roughness. Wenzel termed this surface ratio as "roughness factor", r [253]:

$$\mathrm{r} = \frac{\text{actual surface}}{\text{geometric surface}}$$

Equation 13: Roughness factor by Wenzel

According to Wenzel model, when a liquid droplet is dispensed on a rough surface the liquid fills the grooves of the rough surface completely (**Figure 2.24 (b)**), and Wenzel apparent contact angle is estimated [253]:

$$\gamma_{LV} \cos\theta_W = \mathrm{r}\,(\gamma_{SV} - \gamma_{SL})$$

Equation 14: Wenzel equation

Where, θ_W is Wenzel apparent contact angle. By combining Wenzel equation and Young's equation (**Equation 12**), the following relation is found:

$$\cos\theta_W = \mathrm{r}\cos\theta_Y$$

Equation 15: Relation between Wenzel eq. and Young's eq.

Based on **Equation 15**, clear relations can be concluded. If the θ_Y of a liquid on a smooth surface is less than 90°, the θ_W on a rough surface will be smaller, $\theta_W < \theta_Y$. On the other hand, when the θ_Y of a liquid on a smooth surface is more than 90°, the θ_W on a rough surface will be higher, $\theta_W > \theta_Y$. These relations can be described in one statement as "surface roughness promotes the wettability caused by the surface chemistry".

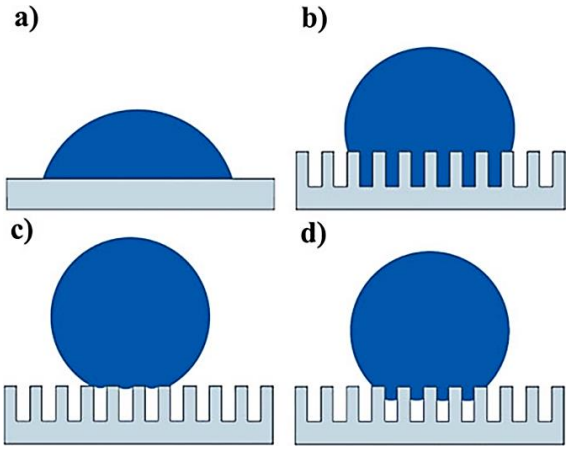

Figure 2.24: Influence of surface structure / roughness on the wetting behavior of the solid surfaces, (a) Young's model, (b) Wenzel model, (c) Cassie model, (d) Transition from Cassie model to Wenzel model [247]

2.6.1.3 Cassie theory – Wettability of Porous surfaces

Cassie and Baxter investigated the wettability behavior of rough porous solid surfaces [254]. They assumed a formation of vapor pockets that are trapped underneath the liquid droplet leading to a case of composite surface (**Figure 2.24 (c)**). Subsequently, Cassie apparent contact angle, θ_C, is expressed by the following model:

$$\cos\theta_C = f_{SL}\cos\theta_{SL} + f_{LV}\cos\theta_{LV}$$

Equation 16: Cassie equation

Where, f_{SL} is the area fraction of the solid-liquid interface, f_{LV} is the area fraction of the liquid-vapor interface, θ_{SL} is close to Young's contact angle, and θ_{LV} is equal to 180° [247, 254]. Knowing that f_{SL} + f_{LV} = 1, therefore, Cassie model can be correlated to Young's equation [247]:

$$\cos\theta_C = f_{SL}(\cos\theta_Y + 1) - 1$$

Equation 17: Correlating Cassie model to Young's equation

According to **Equation 17**, it is revealed that for a hydrophobic flat surface exhibiting Young's contact angle that is more than 90°, the surface roughness will increase the apparent contact angle, Cassie contact angle. However, unlike Wenzel equation, in case of a smoother and less hydrophobic surface with Young's contact angle that is lower than 90°, the surface roughness may still lead to an increase in the apparent contact angle, according to Cassie theory, due to the trapped hydrophobic vapor pockets underneath the liquid droplet [247, 254].

Briefly, it was observed that the solid-liquid interface for rough porous surfaces may exhibit a transition from Cassie model to Wenzel case if the liquid droplet is pressed physically. In addition, for some real rough surfaces, the solid-liquid interface may show two distinct apparent contact angles, θ_C and θ_W. When a liquid droplet is dispensed, afterward, the liquid droplet will fill the grooves of the rough surface and a change from Cassie model to Wenzel model occurs leading to a decrease in the apparent contact angle (**Figure 2.24 (d)**) [247].

2.6.2 Artificial surfaces with super-hydrophobicity and super-hydrophilicity

Inspired by super-hydrophobic biological surfaces in nature, e.g., lotus leaves and water strider legs, artificial super-hydrophobic surfaces can be generally fabricated via two alternative approaches, (a) introducing surface micro-/nano-structures on chemically hydrophobic substrates; (b) chemical modification of micro-/nano-structured surfaces using materials of low surface free energy [249].

Super-hydrophilic surfaces can also be prepared by means of increasing the surface roughness and enhancing the surface free energy [247]. Bico et al. revealed that if a droplet of a wetting liquid is dispensed on a rough surface, the roughness may be spontaneously invaded, i.e., absorbed completely into the surface grooves and the top surface becomes dry, "3D capillary effect", depending on the surface pattern and the wetting properties of the liquid [255]. As a result, the liquid–solid interface for a hydrophilic surface is often governed by Wenzel mode. Feng and Jiang simulated this wicking phenomenon using the following equation [247]:

$$\cos\theta_T > (1 - f_{SL})/(\mathrm{r} - f_{SL})$$

Equation 18: Condition for super-hydrophilic surface

Accordingly, if Young's contact angle of a corresponding hydrophilic flat surface is lower than a threshold value, θ_T, the liquid droplet will be absorbed into the surface grooves, and super-hydrophilic surface can be obtained [247].

2.6.3 Surfaces with reversible super-hydrophobicity and super-hydrophilicity

Interestingly, under certain circumstances, some solid surfaces can exhibit any two of these static wetting behaviors, super-hydrophobicity, super-hydrophilicity, super-oleophobicity, and super-oleophilicity (**Figure 2.25**). For a micro-/nano-patterned solid surface along with very high surface free energy, super-hydrophilicity and super-oleophilicity can coexist; consequently the substrate will show super-amphiphilicity [256]. For a micro-/nano-patterned solid surface accompanied by very low surface energy, super-hydrophobicity and super-oleophobicity can coexist and super-amphiphobicity is attained [257].

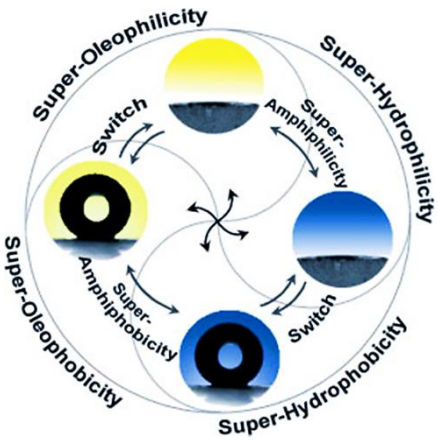

Figure 2.25: Illustration of possible relationships between the four fundamental super-wetting/anti-wetting properties [247]

In parallel, the surface chemistry or geometrical structure of a rough solid surfaces can be tuned dynamically resulting in so-called "smart" surface, which is able to switch reversibly between super-hydrophilicity and super-hydrophobicity, or between super-oleophobicity and super-oleophilicity [247].

Many exemplary surfaces with reversible wettability have been prepared using light irradiation, electric-field, or thermal treatments; however, the range of the wettability transition

is found to be limited [29, 247] As a result, Feng and Jiang have suggested a new approach, based on Wenzel and Cassie models, stating that if the wettability of a flat surface can be tuned between hydrophilicity and hydrophobicity, its tunable wettability can be further amplified by introducing micro-/nano-surface structures.

Hence, for stimuli-responsive surfaces, the responsive wettability can be amplified by manipulating the surface texture in order to produce smart surfaces. A powerful example has been introduced by Xia et al. [29]. In which, they fabricated a smart silicon substrate that is able to switch reversibly between super-hydrophilicity and super-hydrophobicity upon varying both the temperature within a narrow range of about 10 °C, and the environmental pH from pH 2 to pH 11 (**Figure 2.26 (a)**). The smart silicon substrate was fabricated by grafting of a thin double stimuli-responsive layer (~ 17 – 21 nm), made from P(NIPAAm-co-AAc), from the surface of a micro-structured silicon (**Figure 2.26 (b)**) using SI-ATRP.

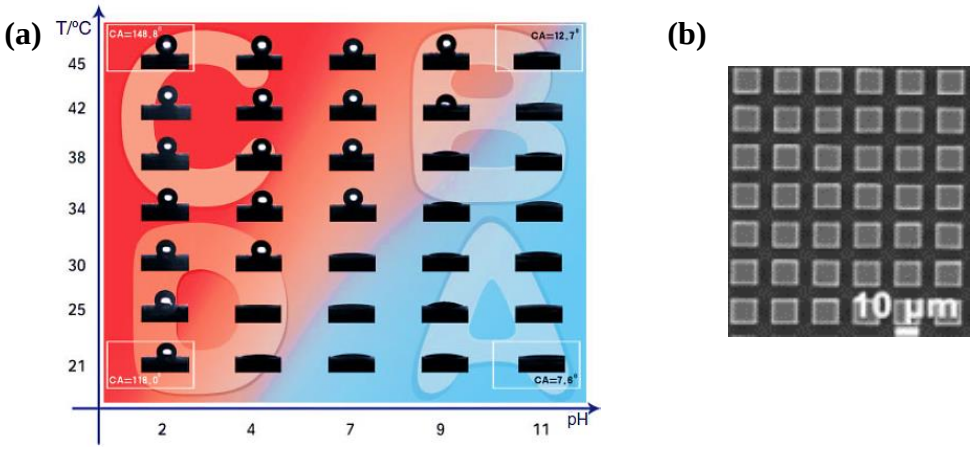

Figure 2.26: (a) Reversible switching between super-hydrophilicity and super-hydrophobicity upon changing of temperature / pH, (b) SEM micrograph of a surface micro-structured silicon substrate [29]

3 Materials and methods

3.1 Materials

All the materials and chemicals that were used in the current work are listed in the following table.

Table 3.1: Materials and chemicals used in this work

Material / Chemical	CAS #	Company
1,3,5-Benzenetricarboxylic acid chloride (Trimesoyl chloride; TMC; 98 %)	4422-95-1	Acros
1,3-Benzenediamine (*m*-Phenylenediamine; MPD; ≥ 99 %)	108-45-2	Acros
Acetonitrile (HPLC; 99.9 %)	75-05-8	Fisher Chemical
Acrylic acid anhydrous (AAc; contains 200 ppm MEHQ as inhibitor; 99 %)	79-10-7	Sigma-Aldrich
Argon (ALPHAGAZ 1 Ar; 99.999 %)	-	Air Liquide
Boron oxide (B_2O_3; -40 mesh; 98 %)	1303-86-2	Acros
Calcium chloride dihydrate ($CaCl_2.2H_2O$; ≥ 99 %)	10035-04-8	Fluka
Citrate acid anhydrous powdered, pure Ph. Eur., USP, BP, E 330 (99.5 - 100.5 %)	77-92-9	AppliChem GmbH
Copper(I) bromide (CuBr; 99.999 %)	7787-70-4	Sigma-Aldrich
Copper(II) bromide ($CuBr_2$; 99 %)	7789-45-9	Sigma-Aldrich
D(+)-10-Camphorsulfonic acid (CSA; 99 %)	3144-16-9	Acros

Diethyl ether	60-29-7	Fisher chemicals
Dimethyl sulfoxide-d_6 (DMSO-d_6, 99.9 %)	2206-27-1	Deutero GmbH
Ethanol absolute	64-17-5	Fisher chemicals
Hydrochloric acid (HCl, 1M)	--	Bernd Kraft
Inhibitor removers (replacement packing for removing hydroquinone and monomethyl ether hydroquinone)	--	Sigma-Aldrich
LUDOX® TM-50 colloidal silica (50 wt.% suspension in H_2O)	7631-86-9	Sigma-Aldrich
Methanol (HPLC; 99.9 %)	67-56-1	Fisher Chemical
Micro-particles based on silicon dioxide (SiO_2; 0.5 µm)	--	Sigma-Aldrich
Molecular sieve 4 Å (0,4 nm; type 514; pearls)	1318-02-1	Carl ROTH GmbH + Co. KG
N-(3-Dimethylaminopropyl)-*N′*-ethylcarbodiimide hydrochloride (EDC; Premium)	25952-53-8	Sigma-Aldrich
N,N,N′,N″,N″-Pentamethyldiethylenetriamine (PMDETA; 99%)	3030-47-5	Sigma-Aldrich
N,N'-Azobisisobutyronitrile (AIBN, 98 %)	78-67-1	Sigma-Aldrich
n-Hexane (for analysis; 95 %)	110-54-3	Acros
N-Hydroxysuccinimide (NHS; 98 %)	6066-82-6	Sigma-Aldrich
N-isopropylacrylamide (NIPAAm; stabilized; 99 %)	2210-25-5	Acros
Nitrogen (ALPHAGAZ 1 N_2; 99.999 %)	--	Air Liquide
N-methyl-2-pyrrolidone (NMP; EMPLURA®; 99 %)	872-50-4	Merck
Phosphate buffer solution (pH 7)	--	Bernd Kraft
Polyethersulfone (PES; Ultrason E6020P)	25608-63-3	BASF
Polysulfone (PSF; 26 kDa)	25135-51-7	Sigma-Aldrich
Polyvinylpyrrolidone (PVP; K 30)	--	Serva Feinbiochemica GmbH & Co.
Polyvinylpyrrolidone (PVP; K 30; average M_w 40 kDa)	9003-39-8	Sigma-Aldrich
Potassium chloride (KCl, 1M)	--	Bernd Kraft

Potassium dihydrogen phosphate (KH_2PO_4; pure Ph. Eur. NF; 98 – 100.5 %)	7778-77-0	AppliChem GmbH
Potassium hydroxide (KOH, 1M)	--	Bernd Kraft
Silicone elastomer (Sylgard® 184)	--	Dow Corning
Sodium chloride (NaCl; AnalaR NORMAPUR; 99.9%)	7647-14-5	VWR
Sodium dodecyl sulfate (SDS; ≥ 99 %)	151-21-3	Sigma-Aldrich
Sodium hydroxide (NaOH, 1M)	--	Bernd Kraft
Sodium phosphate dibasic (Na_2HPO_4; ACS reagent; ≥ 99 %)	7558-79-4	Acros
Sodium sulfate anhydrous powdered (Na_2SO_4; ≥ 99 %)	7757-82-6	AppliChem GmbH
Tetraethylenepentamine (TEPA; 98 %)	112-57-2	Acros
Triethylamine (TEA; ≥ 99 %)	121-44-8	Sigma-Aldrich
Triethylamine (TEA; for synthesis; ≥ 99 %)	121-44-8	Merck
Triethylene glycol (TEG; 99 %)	112-27-6	Acros
Water (Milli-Q; ultrapure; 18.1 MΩ cm^{-1})	-	Millipore
2-Bromoisobutyryl bromide (BMPB; 98 %)	20769-85-1	Sigma-Aldrich

3.2 Preparation of isotropic PES membranes

First, solvent NMP and non-solvent TEG were mixed in predefined ratios. Then, PVP (7 - 12 wt.%) was dissolved in NMP-TEG mixture. Thereafter, PES (10 - 15 wt.%) was added. The polymer mixture was kept under stirring (60 rpm) at ambient temperature for ca. 5 days till clear homogenous viscous solution was obtained. PES polymer solution without PVP was also prepared for sake of comparison. The clear polymer solutions were then cast by means of a computer-controlled casting machine (**Figure 3.1**) on a clean glass plate using a stainless-steel casting knife with a gap thickness of 200 µm at a fixed casting speed of 5 mm/s, equivalent to shear rate of 25 s^{-1}. Once it was cast, the polymer film was immediately exposed to humid air (relative humidity, RH: 80 % at 22 – 23 °C) for a specific exposure time (from ~ 5 s to 3 min). Afterward, the typically turbid polymer film was totally immersed in a coagulation bath containing deionized water for 2 h at room temperature. The membranes were then immersed in an excess of deionized water overnight for complete precipitation. Drying was done by sequential immersing in water/ethanol (1:1) and ethanol, each for 2 h, followed by ultimate

solvent removal at ambient conditions. No thermal post drying process was employed to keep the obtained membrane pore structure.

Figure 3.1: Image for computer-controlled casting machine

3.3 Preparation of flat aromatic PA TFC membranes

Flat aromatic PA TFC membranes were prepared via in situ IP reaction of MPD and TMC employing an unstirred non-dispersion method [31, 68]. The IP procedures were consecutively refined over many stages for different purposes. First, the essential IP conditions, i.e., monomers concentrations, reaction time and curing temperature were initially investigated. PA TFC membranes of high salt rejection was emphasized to be obtained from [MPD:TMC] based monomer systems of ratio [20:1] along with employing curing temperature > 70 °C, which is in consistent with the literature [31, 48, 64]. Thereafter, the impact of introducing some additives to the aqueous diamine monomer solution, and the influences of the flat base membranes' characteristics on the separation performance of the composite membrane were comprehensively studied. Furthermore, the IP procedures were additionally adapted for the micro-patterned base membranes (section **3.4.4**).

Here, the description of the experiments concerning the investigation of the impact of using additives to MPD monomer system, and employing different supports on the characteristics and separation performance of PA TFC membranes is introduced. Three base membranes were investigated as supports for flat aromatic PA TFC membranes, one isotropic PES membrane prototype that exhibited the best pore and transport characteristics (obtained from section **3.2**), and two other membranes for comparison. Their specifications are as follows:

a. A commercial PES (CEPS) microfiltration membrane (nominal pore size of 0.1 µm) obtained from Sartorius-Stedim GmbH, Göttingen, Germany,

b. Polysulfone (PSF) membrane was prepared by NIPS process [68] as follows: 18 wt.% PSF was added to 78 wt.% NMP and agitated for several hours till complete dissolution. Then, the polymer solution was cast on a clean glass plate at casting speed of 5 mm/s using a stainless-steel knife with a gap thickness of 200 µm, followed by instantaneous immersion into a coagulation bath containing de-ionized water at ambient temperature for 30 min, finally washed thoroughly with de-ionized water and stored.

In addition, three monomer mixtures were investigated:
[2 wt.% MPD + 0.1 wt.% TMC],
[2 wt.% MPD + 2 wt.% TEA + 0.1 wt.% TMC], and
[2 wt.% MPD + 2 wt.% TEA + 4 wt.% CSA + 0.1 wt.% TMC]

IP procedures: The support membrane was firstly placed on a glass plate and fixed with another one with 43 mm circular hole (**Figure 3.2 (a)**). Then, the hole was filled with aqueous MPD solution, with or without additives, for 2 min. Excess reagent was drained off the support surface for 5 min (lag time). Thereafter, the membrane was contacted with a n-hexane solution containing TMC for 15 s. The resulting composite was heat-cured at 75 °C, for 10 min. Afterward, the membrane was finally stored in lab refrigerator at 5 °C.

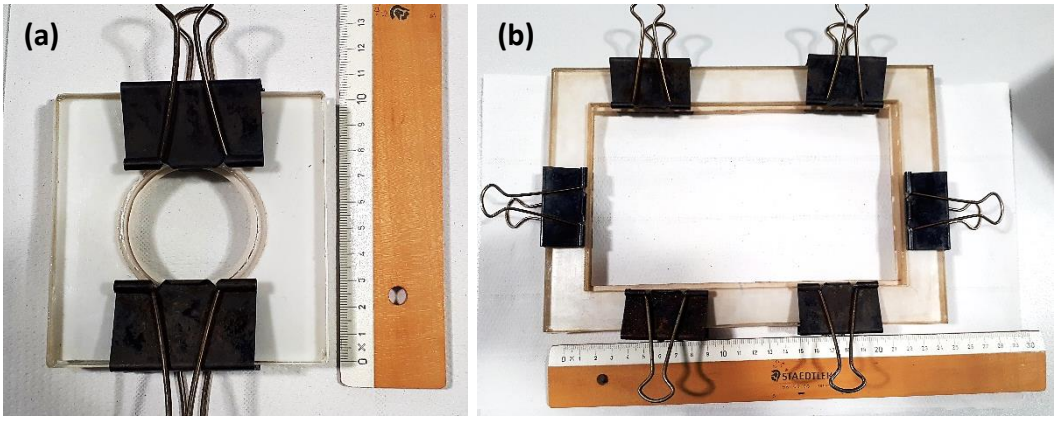

Figure 3.2: Illustration of the glass modules used in PA preparation

3.4 Surface micro-patterned PA TFC membranes

3.4.1 Preparation and pretreatment of PDMS molds

A 4-in. silicon wafer with parallel lines pattern (i.e., an array of straight grooves with regular branches) fabricated by photolithography at IBM Research, Zurich, Switzerland, was used as a master to prepare PDMS molds. Silicon elastomer and curing agent were weighed by the ratio of (10:1 w/w). Then, the mixture was vigorously whisked to ensure uniform distribution of the curing agent, and the mixture was degassed for almost 2 h. Thereafter, the bubble free PDMS

solution was poured in a petri-dish containing the master and cured overnight at 65 °C. Only one pattern of fixed features and dimensions was utilized in this work. An optical microscope (OLYMPUS, CX40RF200) image of the employed PDMS mold accompanied by dimensions of the surface micro-structures are presented in **Figure 3.3**.

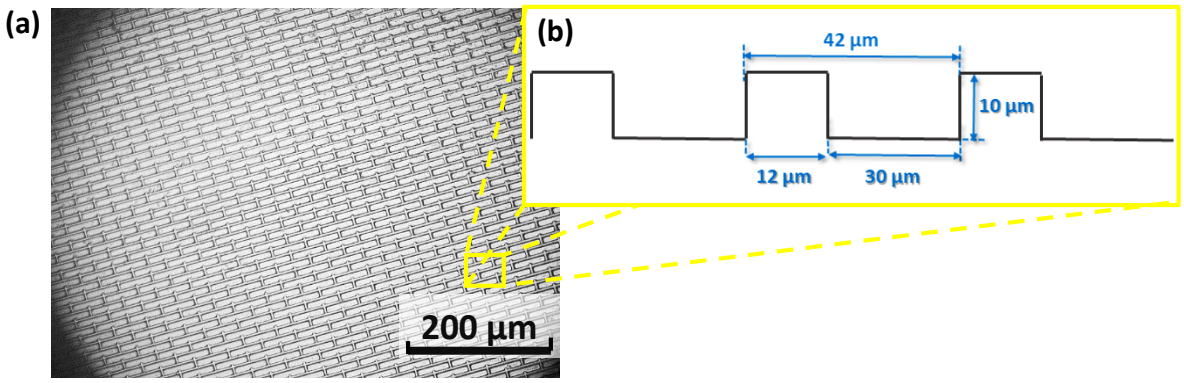

Figure 3.3: (a) An optical microscope image for the prepared PDMS mold, (b) Dimensions of surface features of the prepared PDMS mold

Prior to using, PDMS mold was hydrophilized via either oxygen plasma treatment at 0.75 mbar and 100 W for 45 min using plasma cleaner (Femto-QLS, Diener Electronic GmbH), or it was immersed in SDS solution (1 g/L) under intensive stirring for at least 30 min.

3.4.2 Preparation of micro-patterned PES supports using PSµM

Micro-patterned PES membranes were prepared using a PES casting solution that was pre-optimized in **section 3.2**. Briefly, NMP (32 wt.%) and TEG (43.5 wt.%) were mixed, then PVP (12 wt.%) was dissolved. Thereafter, PES (12.5 wt.%) was added to the solution. The solution was kept under stirring at ambient temperature till clear viscous solution was obtained. Afterward, this solution was cast on the pretreated PDMS molds at a casting speed of 5 mm/s using a casting knife with a gap thickness of 200 µm (**Figure 3.4**). The cast polymer film was

Figure 3.4: Illustration for the micro-patterning setup using PSµM

then exposed to humid air (RH: 80 %) at 22 – 23 °C for 30 min. Thereafter, the turbid patterned polymer film was completely precipitated in de-ionized water, and the same washing and drying protocol was followed (cf. **section 3.2**).

3.4.3 Preparation of micro-patterned PES supports using MIL

The predefined PES casting solution (cf. **section 3.4.2**) was prepared. Then, it was cast on a plain glass plate at casting speed of 5 mm/s using a stainless-steel knife of a gap thickness of 250 µm. Thereafter, the polymer film was immediately exposed to humid air (RH: 80 %) at 22 – 23 °C for 3 min. Afterward, the turbid polymer film was immersed in a coagulation bath containing de-ionized water. The flat membranes were immersed overnight in an excess of deionized water for complete precipitation, washed and then dried (cf. **section 3.2**).

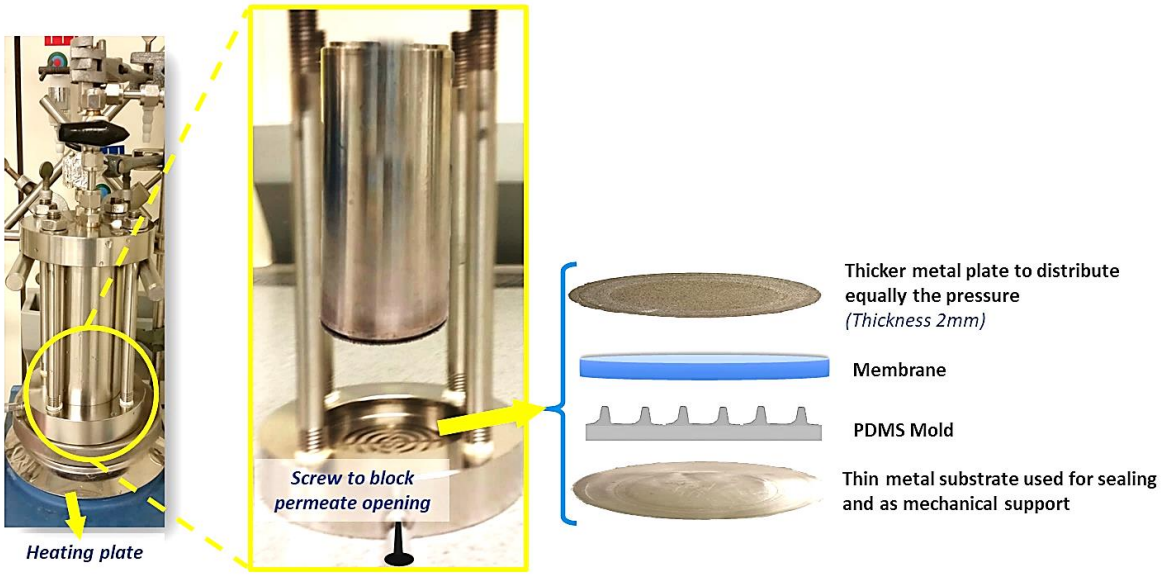

Figure 3.5: Illustration for the well-suited MIL setup

The desired pattern was then imprinted on the prepared flat PES membranes using stainless-steel nano-filtration cell and PDMS mold as a simplified low-cost method. The custom setup was assembled as shown in (**Figure 3.5**). The flat PES membrane was placed on the PDMS mold that was supported by a plain metal plate. Another thicker metal plate was introduced atop to equilibrate the applied loading. The normal permeate opening of the filtration cell was closed and the system was preheated for 40 min. Then a pressure of 10 bar was applied using inert gas and the setup was held over for 35 min. It is worthy to mention that the imprinting process was performed at 60 °C in case that a non-porous metal plate was used atop the membrane, whereas the temperature was raised to 110 °C if the non-porous plate was replaced by a porous one. Finally, the samples were checked using the optical microscope.

3.4.4 Synthesis of adherent PA layer on micro-patterned PES supports via adapted IP method

Adaptation of the PA synthesis on the patterned PES supports was carried out. The PA layer was firstly prepared via typical IP reaction of MPD and TMC using unstirred non-dispersion method. A detailed description was presented before (cf. **section 3.3**). Briefly, the PES support was immersed in an aqueous monomer solution [2 wt.% MPD + 2 wt.% TEA + 4 wt.% CSA] for 2 min. Then, the excess reagent was drained off. Afterward, the membrane was immersed in a n-hexane solution containing 0.1 wt.% TMC for 15 s (reaction time), followed by heat curing.

In addition to this "typical method", two other modified methods, (A) and (B), employing the same monomer solutions' compositions were also investigated. Modified method (A) comprises immersion in aqueous solution for 5 min, lag time of 2 min, and reaction time of 30 s. Modified method (B) is based on performing the typical method, then storing at 5 °C for two days, and then repeating the typical method. All the prepared composite membranes were cured at 80 °C for 12 min, and finally stored in lab refrigerator at 5 °C for two days before testing or further modification.

Later, during the work progression, the rubber roll has replaced the "lag time" in the PA synthesis in order to achieve efficient and high throughput preparation procedure. Using the rubber roll along with bigger glass modules (rectangular shape, 20 cm x 12 cm) (cf. **Figure 3.2 (b)**) offered the possibility to prepare high performance PA samples with larger surface area.

3.5 Surface modification of flat and micro-patterned PA TFC membranes

3.5.1 Purification of chemicals

The NIPAAm monomer was purified from inhibitor and any other packaging/stabilizing agents via recrystallization from n-hexane. Briefly, predefined amount of NIPAAm monomer was added to n-hexane, by ratio of 1 g of NIPAAm per 10 ml of n-hexane. The solution was then warmed up at 42 °C till complete dissolution of NIPAAm, and cooked afterward for 30 min. Thereafter, the flask was placed in an ice bath and the pure NIPAAm monomer was recrystallized for 1 h. The NIPAAm monomer was filtered and dried under vacuum for 3 h.

The AAc monomer was purified from methylated hydroquinone inhibitor via addition of considerable amount of inhibitor removal beads, then it was stored overnight away from the light in lab refrigerator before using.

N,N'-Azobisisobutyronitrile (AIBN) was also recrystallized. About 8 – 10 g of AIBN was added to 200 ml of pure methanol and kept under stirring for 2 h at ambient temperature, thereafter, the flask was placed in lab refrigerator at 5 °C for 24 h. Afterward, the recrystallized AIBN was filtered, dried under vacuum, and then stored in a dark bottle in lab refrigerator.

Furthermore, acetonitrile was dried prior to using. 1 liter of acetonitrile was mixed with 50 g of boron oxide, and cooked for 2 h under flow of inert gas. Then, it was refluxed, and the pure acetonitrile condensate was collected and stored in a clean and dry glass bottle containing activated molecular sieve beads.

3.5.2 Grafting of P(NIPAAm-co-AAc) copolymers from micro-patterned PA TFC membranes via SI-ATRP

3.5.2.1 Initiator immobilization

The immobilization of the initiator (2-bromoisobutyryl bromide, BMPB) onto PA TFC membranes was firstly adapted. The feasibility of four different initiator immobilization procedures was investigated using Flat PA TFC membranes, afterward, the well-suited conditions were applied to the micro-patterned counterparts. The stability and the selectivity of the PA layer after the initiator immobilization was of major concern. Subsequently, the separation performance of the initiator-functionalized PA TFC membranes was evaluated using dead-end RO filtrations of three salts, NaCl, Na_2SO_4 and $CaCl_2$ as described later in **section 3.7.2.1.1**. The detailed description of the adaptation experiments is presented in **Table 3.2**. Prior to initiator immobilization reaction, the PA TFC membranes were dried overnight under vacuum at 40 °C; no further pretreatment was performed.

Table 3.2: Adaptation of initiator immobilization step

Experiment code	Description
Experiment: I.I.1 (Himstedt et al. [227])	Immersion in (80 mM BMPB + 100 mM TEA in anhydrous acetonitrile) for 2 h at 26 °C
Experiment: I.I.2 (Yang et. al. [122])	Immersion in (80 mM BMPB + 10 mM TEA in anhydrous acetonitrile) for 2 h at 26 °C
Experiment: I.I.3 (Tomer et al. [223])	Immersion in (2 mM BMPB + 2 mM TEA in anhydrous acetonitrile) for 2 h at 26 °C

Experiment: I.I.4	**a.** Membrane + EDC (2 mg/ml) + NHS (3 mg/ml) in phosphate buffer (PB) at pH 4.4 and 26 °C for 1 h → (***NHS-activated membrane***) **b.** Immersion of (***NHS-activated membrane***) in TEPA [150 mg/50 ml of PB at pH 7] at 26 °C for 2 h → (***TEPA-modified membrane***) **c.** Immersion of (***TEPA-modified membrane***) in (80 mM BMPB + 100 mM TEA in anhydrous acetonitrile) for 2 h at 26 °C

In all experiments, the membranes were fixed by using special glass modules (cf. **Figure 3.2 (a)**), and 15 ml of the initiator solution was added to each sample. Then, they were kept for under stirring at 250 rpm and at 26 °C (Heidolph Titramax 1000, equipped with Heidolph Inkubator 1000). Afterward, the initiator-functionalized membranes were rinsed one time with acetonitrile, then two times with water/methanol mixture (1:1, v/v), each for 1 min, and they were finally dried overnight under vacuum at 40 °C.

3.5.2.2 Grafting of P(NIPAAm-co-AAc) from initiator-functionalized PA TFC membrane

Initiator-functionalized membranes were placed in Schlenk flasks, one membrane per flask, then the flasks were sealed. The flasks were then degassed and backfilled with argon gas five times, ~ 2 min each. In parallel, a reaction solution (without catalyst) was freshly prepared in a separate flask. It was also degassed and purged with argon gas five times. The reaction solution comprised of [1.02 g of recrystallized NIPAAm + 0.02 ml of purified AAc (equivalent to 3 mol.% AAc) + 0.14 ml of PMDETA] per 5 mL of 1:1 (v/v) water/methanol solvent mixture [29]. Thereafter, the flasks were placed in a water bath and preheated up to 60 °C. Then, 0.032 g of CuBr (0.23 mmol.) was added to the reaction solution at vigorous stirring under continuous flow of argon gas. Afterward, the reaction solution was transferred into the degassed Schlenk flasks (25 mL per flask) and the reaction mixture was occurred at 60 °C for 2 h.

After ATRP reaction, a quenching solution [250 mg of $CuBr_2$ and 625 µL of PMDETA dissolved in 50 ml of 1:1(v/v) methanol/water solution] was quickly added, and then the membranes were removed and cleaned using 1:1 (v/v) water/ethanol mixture. The cleaned surface modified-membranes were finally dried overnight in a vacuum oven at 40 °C. Subsequently, the degree of grafting (DG) in $\mu g/cm^2$ was calculated according to **Equation 19**:

$$DG = \frac{W_m - W_{um}}{A_M}$$

Equation 19: Degree of grafting

Where, W_{um} is weight of unmodified membrane, i.e., initiator-immobilized membrane, W_m is weight of modified membrane after ATRP reaction and drying, and A_M is membrane surface area.

3.5.3 Surface modification of PA TFC membranes via in situ surface coating method

3.5.3.1 Synthesis of P(NIPAAm) homo-polymer via FRP

P(NIPAAm) was synthesized by free radical polymerization (FRP) of NIPAAm monomer in 1,4-dioxane (75.0 wt.%) as a solvent using AIBN as an initiator (0.3 mol.% of monomer). In details, 9.00 x 10^{-2} mol. of recrystallized NIPAAm was firstly dissolved in 25 ml of 1,4-dioxane. Then, the reaction solution was degassed and purged with argon gas three times, ~ 2 min for each. Thereafter, the reaction flask was placed in oil bath and preheated up to 60 °C. Then, the initiator solution [2.71 x 10^{-4} mol. of recrystallized AIBN in 4.8 ml of 1,4-dioxane] was quickly added to the reaction solution, and the polymerization reaction was started. The reaction was performed at 60 °C under flow of argon gas for 5 h.

Afterward, the solvent was evaporated by means of rotary evaporator (LABOROTA 4001, Heidolph) under 105 mbar at 40 °C for almost 2 h. The polymer was purified by dissolving in the lowest amount of 3:2 (v/v) acetone/methanol solvent mixture overnight, and then it was recrystallized using diethyl ether as a precipitant by ratio of (1:20) in ice bath. Thereafter, the polymer was dried in a vacuum oven at 40 °C for 3 days and finally stored in lab refrigerator.

3.5.3.2 Synthesis of P(NIPAAm-co-AAc) random copolymers via FRP

Two linear random P(NIPAAm-co-AAc) copolymers, comprising 3.5 and 7.0 mol.% of AAc, were synthesized via FRP by copolymerization of NIPAAm and AAc monomers in 1,4-dioxane (75.0 wt.%) as a solvent using AIBN as an initiator (0.3 mol.%) [208]. The composition of the employed reaction solutions is introduced in **Table 3.3**. The monomers were firstly dissolved in 1,4-dioxane. Then, the reaction solution was degassed and purged with argon gas three times, ~ 2 min for each. The reaction flask was placed in oil bath and preheated up to 70 °C. Thereafter, the initiator solution was quickly added, and the copolymerization reaction was started. The copolymerization reaction was carried out at 70 °C under flow of argon gas for 5 h.

Table 3.3: Composition of reaction solutions used for preparation of P(NIPAAm-co-AAc) by FRP

Copolymer	NIPAAm (mol.)	AAc (mol.)	AIBN (mol.)	1,4-Dioxane (ml)
P(NIPAAm-co-3.5mol%AAc)	9.00×10^{-2}	3.26×10^{-3}	2.81×10^{-4}	30.482
P(NIPAAm-co-7mol%AAc)	9.00×10^{-2}	6.77×10^{-3}	2.91×10^{-4}	31.224

Afterward, the solvent was evaporated, and the copolymers were purified and dried as described before (**section 3.5.3.1**).

3.5.3.3 Routine characterization of P(NIPAAm) and P(NIPAAm-co-AAc)

3.5.3.3.1 Quantitative determination of actual AAc content

The actual mol.% of AAc in the prepared copolymers was firstly analyzed using attenuated total reflection (ATR) Fourier transform infrared (FTIR) spectroscopy (Varian Scimitar 1000 FT-IR, Varian Inc.). A total of 32 scans were performed at ambient conditions.

A precise estimation of the actual content of AAc was carried out using NMR spectroscopy (DRX 500, Bruker). The ^{1}H-NMR spectrum of predefined amount of dried copolymer dissolved in deuterated dimethyl sulfoxide (d_6-DMSO) was recorded at 500 MHz. The actual mol.% of AAc was calculated by integrating the area under the peak assigned to –OH group (1 proton) in AAc unit at ~ 12 ppm to those attributed to terminal methyl groups (6 protons) in NIPAAm unit at 1.10 ppm.

The actual mole fraction of AAc in the prepared copolymers was additionally quantified using "Back-titration" method [258]. In details, a certain amount of dried copolymer (50 – 60 mg) was dissolved in 20 ml of Mili-Q water. Thereafter, 10 ml of 0.1 N NaOH was added to the copolymer solution, followed by vigorous shaking for 30 min at ambient temperature. Back-titration was then performed using 0.1 N HCl as a titrant and phenolphthalein as an indicator. The reported results were the average of data obtained from three samples of the same copolymer.

3.5.3.3.2 Gel permeation chromatography

The molecular weight and polydispersity of the prepared P(NIPAAm) homo-polymer and P(NIPAAm-co-AAc) copolymers were analyzed by gel permeation chromatography (GPC) using a GRAM column coupled with a differential viscometer and refractometer (ETA-2020) at 60 °C. The eluent was dimethylacetamide (DMAc) containing 0.01M LiBr. The eluent was

pumped by (PU-2080 Plus, Jasco) at a flow rate of 1 ml/min. Universal calibration method was used to calculate the number average molecular weight, $\overline{M_n}$, and the polydispersity index, PDI.

3.5.3.3.3 Determination of cloud point

The cloud point (CP), or LCST, of the prepared P(NIPAAm) and P(NIPAAm-co-AAc) was measured by determination of the phase transition of the polymer solution (0.2 wt.% polymer in citrate-phosphate buffer) upon increasing of the temperature (20 – 50 ºC) at two different pH values 3 and 7. The phase transition was determined by measuring both the optical absorbance and transmittance at wavelength of 500 nm using double beam UV-Visible spectrophotometer (Evolution 201 UV-Vis, Thermo Fischer Scientific). The cuvette chamber is connected to oil thermostat (Huber Unistat Tango, Germany). A special heating up program was installed to the thermostat, in which the temperature was adjusted to 20 ºC, and it was held over for 12 min. Then, it was heated up by 5 degrees for 2 min till the temperature became 25 ºC, thereafter, it was held over again for 12 min … etc. These steps were repeated till the temperature of the solution became 50 ºC. The absorbance/transmittance was measured each 4 min and the CP was determined using two alternative estimations, CP is the temperature at 10 % absorbance [220], or CP is the temperature at 50 % transmittance [211].

3.5.3.4 Grafting of P(NIPAAm) and P(NIPAAm-co-AAc) to PA TFC membranes

3.5.3.4.1 Qualitative determination of dominant membrane surface charge of PA TFC membranes

Prior to the refinement of the surface coating procedures, the dominant membrane surface charge of the prepared flat and micro-patterned PA TFC membranes was qualitatively determined by means of salt rejection experiments using three salts, NaCl, Na_2SO_4 and $CaCl_2$. The experimental procedures and the calculations were fully described in **section 3.7.2.1.1**.

3.5.3.4.2 Refinement experiments of surface coating method

The surface coating process of PA TFC membranes by P(NIPAAm) and P(NIPAAm-co-AAc) using carbodiimide coupling chemistry was adapted. A series of different surface coating procedures were suggested (**Table 3.4**). All the adaptation experiments were carried out using flat PA TFC membranes, afterward, the well-suited conditions were used to modify the micro-patterned PA TFC membranes. During the adaptation experiments, major attention was devoted to investigating the influence of different surface coating conditions on the stability and the selectivity of PA layer, by measuring the separation performance of surface modified

membranes using three salts, NaCl, Na_2SO_4 and $CaCl_2$. The experiments and the calculations were fully described in **section 3.7.2.1.1**. In parallel, the efficiency of coating procedures was also assessed via determination of the degree of grafting (**Equation 19**).

Before the coating experiments, PA TFC membranes were dried overnight under vacuum at 40 °C, without any pretreatment. During the coating experiments, the membranes were fixed by means of glass modules (cf. **Figure 3.2 (a)**). Afterward, the surface modified membranes were washed with Milli-Q water, and then dried overnight under vacuum at 40 °C.

Table 3.4: Description of the experiments employed for the adaptation of surface coating process

Experiment code	Description
Experiment: S.C.1	Immersion of membrane in 15 ml of homo-/co-polymer in **Milli-Q water** (1 mg/ml) at 26 ˚C for 4 h
Experiment: S.C.2	Immersion of membrane in 15 ml of homo-/co-polymer in **PB** (1 mg/ml) at **pH 7** and 26 ˚C for 4 h
Experiment: S.C.3	Immersion of membrane in 15 ml of homo-/co-polymer in **PB** (1 mg/ml) at **pH 3** and 26 ˚C for 4 h
Experiment: S.C.4	Immersion of membrane in 15 ml of [copolymer (1 mg/ml) + **EDC*** in **PB** at **pH 4.4**] at 26 ˚C for 4 h
Experiment: S.C.5	**a.** Preparation of ***NHS-activated copolymer***: mixing of copolymer (1 mg./ml) + **EDC*** + **NHS**** in **PB** at **pH 4.4** for **1 h** at 26 ˚C **b.** Raising pH of solution to **pH 7** using KOH **c.** Immersion of membrane in 15 ml of ***NHS-activated copolymer*** solution at pH 7 at 26 ˚C for 4 h
Experiment: S.C.6	Immersion of membrane in 15 ml of [copolymer (1 mg/mL) + **EDC*** + **NHS**** in **PB** at **pH 7**] at 26 ˚C for 4 h
Experiment: S.C.7	**a.** Immersion of membrane in 15 ml of [EDC (2 mg/ml) + NHS (3 mg/ml) in PB at pH 4.4] at 26 °C for 1 h → ***NHS-activated membrane*** **b.** Immersion of ***NHS-activated membrane*** in 15 ml of TEPA solution [150 mg of TEPA in 50 mL of PB at pH 7] at 26 °C for 2 h → ***TEPA-modified membrane*** **c.** Preparation of ***NHS-activated copolymer***: mixing of copolymer (1 mg./ml) + **EDC*** + **NHS**** in **PB** at **pH 4.4** for **1 h** at 26˚C.

	d. Raising pH of solution to **pH 7** using KOH. **e.** Immersion of ***TEPA-modified membrane*** in 15 ml of ***NHS-activated copolymer*** solution at 26 ˚C for 4 h.

*: EDC was used in 10-fold molar excess to carboxylate groups. Actual mol.% of AAc (cf. **section 3.5.3.3.1**)was considered in the calculations.

**: NHS was used in 1.5 molar times EDC. As an example, the portions of EDC and NHS added to 40 ml of PB were as follows:
- P(NIPAAm-co-3.5mol%AAc): 40 ml (40 mg copolymer + 16.12 mg EDC + 24 mg NHS)
- P(NIPAAm-co-7mol%AAc): 40 ml (40 mg copolymer + 27.6 mg EDC + 41.4 mg NHS)

3.6 General description for the characterization scheme exploited during different membrane's preparation steps

3.6.1 Characterization of pore structure of membrane support

The pore size distribution, bubble point (largest) pore diameter, as well as mean flow pore diameter (average barrier pore diameter) for the base membranes were measured by means of gas flow/liquid displacement method using Capillary Flow Porometer, CFP-34RTG8A-X-6-L4, (PMI Inc., Ithaca, NY, USA). The "wet-up/dry-up" measurement mode was used. Membranes sample were cut to a diameter of 25 mm, then immersed in the wetting liquid ("Galwick", 1,1,2,3,3,3-hexafluoropropene, γ = 16 dyne/cm) to fill completely the pores in the sample. Afterward, a nitrogen gas was used to displace the liquid from the pores and the pressure required to empty/open the most constricted pore is measured. The pore structure characteristics were estimated using PMI software based on Young-Laplace equation:

$$p = \frac{4\gamma \cos\theta}{D}$$

Equation 20: Young-Laplace equation

Here, p is differential gas pressure required to displace liquid from sample's pores, γ is surface tension of wetting liquid, θ is contact angle, and D is pore diameter.

3.6.2 Estimation of intrinsic porosity of membrane support

The intrinsic porosity is a measure of a free volume, "space", inside the membrane matrix. The intrinsic porosity of the base membranes was estimated via two alternative methods; "*density method*" and "*swelling method*".

- Density Method: The membrane dimensions, i.e., thickness and radius, were measured, then the bulk volume was calculated. Thereafter, the membrane bulk density was

calculated by dividing the membrane's weight by its bulk volume. The intrinsic porosity was finally calculated using **Equation 21**:

$$Porosity\ (\%) = (1 - \frac{\rho_{bulk}}{\rho_{particle}}) \times 100$$

Equation 21: Estimation of intrinsic porosity using density method

- Swelling method: A membrane sample of known weight and bulk volume was soaked in water/ethanol solution (1:1) for 2 h followed by immersion in Milli-Q water for ~ 24 h. The intrinsic porosity was then estimated via employing **Equation 22** and **Equation 23**:

$$Pore\ volume = \frac{weight\ after\ swelling - weight\ before\ swelling}{density\ of\ water}$$

Equation 22: Calculation of membrane pore volume

$$Porosity\ (\%) = \frac{pore\ volume}{bulk\ volume} \times 100$$

Equation 23: Estimation of intrinsic porosity using swelling method

3.6.3 Membrane surface and cross section morphology

The membranes' top surface and cross section morphologies were scanned using a Quanta 400 FEG environmental scanning electron microscope (ESEM; FEI) at standard high vacuum conditions. A K-550 sputter coater (Emitech, U.K.) was used to coat the membranes' outer surface and cross section with silver. For cross section analysis, the membranes were broken in liquid nitrogen and sputtered for 1.5 min, whereas for analysis of outer membrane surface, the samples were sputtered for 0.5 min.

3.6.4 Analysis of membrane topography and estimation of surface roughness

3.6.4.1 Characterization of flat PA TFC membranes

Surface imaging analysis was performed for the flat PA TFC membranes, investigated in **section 3.3**, using an atomic force microscope (AFM; Nanosurf Flex AFM, Switzerland), equipped with scan head (Nanosurf C300 Controller), and rotated monolithic aluminum coated silicon probe (Tap190Al-G, 48 N/m, 190 KHz, BudgetSensors). The estimated tip radius is < 10 nm, tip height is 17 µm, and cantilever length is 225 µm. Air-dried membrane samples were fixed on a specimen holder, thereafter 5 µm x 5 µm sample areas were scanned utilizing tapping mode. The membranes' surface roughness was fully analyzed via estimation of root mean square roughness, S_q, (**Equation 24**), in addition to other surface roughness parameters, i.e.,

valley depth, S_V, (lowest recorded topographic value). and peak height, S_P, (highest recorded topographic value).

$$S_q = \sqrt{\frac{1}{MN}\sum_{k=0}^{M-1}\sum_{k=0}^{N-1}\left(z(x_k, y_l)\right)^2}$$

Equation 24: Root mean square roughness estimated by Nanosurf®

3.6.4.2 Quantitative surface topography and roughness analysis for micro-patterned membranes

The fidelity of replication by the investigated surface micro-patterning methods and the influence on the membranes' surface roughness were quantitatively analyzed using AFM. The AFM measurements were conducted using a Dimension ICON (Fa. Bruker) operated in a tapping mode under ambient conditions employing silicon probes (OTESPA, 42 N/m, 300 kHz). The scan size was 90 μm × 22.5 μm (2048 samples/line, 512 lines). The main surface roughness parameters [259], defined in **Table 3.5**, and the membrane active surface area were estimated with aid of NanoScope Analysis 1.5 software. Moreover, an estimated representation for the membranes' cross-sectional profile was also plotted.

Table 3.5: Definition of the measured surface roughness parameters [259]

Parameter	Definition / Equation
S_a	It is 3D roughness parameter. It refers to "**average roughness**" evaluated over the complete 3D surface: $S_a = \iint_a \lvert Z(x,y)\rvert (dx)dy$
S_q	It is 3D roughness parameter. It refers to "**root mean square roughness**" evaluated over the complete 3D surface: $S_q = \iint_a \left(Z(x,y)\right)^2 (dx)dy$
S_P	It is 3D roughness parameter. It refers to "**maximum peak height**", which is the height of the highest point.
S_V	It is 3D roughness parameter. It refers to "**maximum valley depth**", which is the depth of the lowest point.
S_Z	It is 3D roughness parameter. It refers to "**maximum height of the surface**": $S_Z = S_P - S_V$
$S_{kewness}$	It is 2D roughness parameter. It measures the "**symmetry of surface data**" about a mean data profile, expressed as:

$$S_{kewness} = \frac{1}{R_q^3}\frac{1}{N}\sum_{j=1}^{N} Z_j^3$$

Here, R_q is 2D root mean square roughness. Skewness is a non-dimensional quantity, which is typically evaluated in terms of positive or negative. A value of zero means an even distribution of data around the mean data plane; otherwise, an asymmetric distribution is suggested, e.g., a flat plane having a small sharp spike (> 0), or a small deep pit (< 0).

3.6.5 Characterization of membrane chemistry

3.6.5.1 Analysis of membrane surface chemistry using ATR-FTIR

The surface chemistry of PES base membranes and flat PA TFC membranes, investigated and developed in **sections 3.2** and **3.3**, respectively, was analyzed using ATR-FTIR (Jasco ATR-FTIR 430). In addition, the surface chemistry of micro-patterned membranes, investigated and developed in **sections 3.4** and **3.5**. was also analyzed by ATR-FTIR spectroscopy using Varian Scimitar 1000 FT-IR, Varian Inc. Prior to measurement, the samples were dried overnight in a vacuum oven at 40 °C. A total of 32 scans was performed at a resolution of 1.0 cm^{-1} and at ambient temperature.

3.6.5.2 Investigation of chemical composition using ^{1}H-NMR

The content of macromolecular additive (PVP) incorporated in PES membrane matrix, studied in **section 3.2**, was quantitatively estimated using NMR spectroscopy (DRX 500, Bruker). The ^{1}H-NMR spectrum of a piece of dried membrane dissolved in d_6-DMSO was recorded at 500 MHz. The actual wt.% of PVP was estimated by integrating the area under the peaks that are proportional to the number of protons in the repeating units (8H for PES and 6H for PVP).

3.6.5.3 Analysis of surface chemistry of flat surface-modified PA TFC membranes using XPS

The flat surface-modified PA TFC membrane were analyzed using X-ray photoelectron spectroscopy (VersaProbe II, Ulvac-PHI) to investigate the change in the composition of nitrogen and oxygen elements at the membrane surface before and after the surface modification using PNIPAAm and P(NIPAAm-co-AAc) polymers.

3.6.6 Analysis of membrane surface charge

The surface charge of the flat and micro-patterned PA TFC membranes, before and after the surface modification, was measured using SurPASS electro-kinetic analyzer (Anton-Paar GmbH, Austria). An adjustable gap cell with spacer, set at 100 µm, was used, and the measurements were always conducted in a 1 mM KCl solution in Milli-Q water. 0.1 M HCl and 0.1 M KOH solutions were used to adjust solution pH, and for potentiometric titrations, as well. Prior to measurement, the membrane sample was rinsed twice with Milli-Q water for 480 s at pressure of 400 mbar, followed by rinsing in 1 mM KCl. The streaming current was measured, afterward, it was exploited to estimate the zeta potential using the Helmholtz-Smoluchowski equation (**Equation 25**) [260]. All zeta potential data presented are the average of four measurements at the same pH value for each membrane sample.

$$\zeta = \frac{dl}{dp} \times \frac{\eta}{\varepsilon_0 \times \varepsilon} \times \frac{L}{A}$$

Equation 25: Helmholtz-Smoluchowski equation

Where, ζ is zeta potential, $\frac{dl}{dp}$ is slope of streaming current vs. differential pressure, η is the electrolyte viscosity, ε_0 is vacuum permittivity, ε is dielectric coefficient, also known as "relative permittivity", L is length of the streaming channel, and A is the cross section of the streaming channel.

3.6.7 Evaluation of membrane surface hydrophilicity

3.6.7.1 Measurement of static water contact angle at ambient conditions

Static water contact angles were measured for flat PES supports and PA TFC membranes, investigated in **sections 3.2** and **3.3**, respectively, employing "*sessile drop*" *method* using an optical contact angle goniometer (OCA 15 Plus; Dataphysics GmbH, Filderstadt, Germany). For each measuring point, 5 µL of Milli-Q water were dispensed by a micro-syringe on the membrane surface at ambient temperature 22 ± 1 ºC. A mathematical fitting method based on Young-Laplace model was utilized to calculate the water contact angle. At least five measurement points at different locations on the membrane surface were averaged to obtain static water contact angle for each membrane sample.

In parallel, the surface hydrophilicity of micro-patterned supports and PA TFC membranes, developed in **section 3.4**, was evaluated using "*captive bubble*" contact angle measurement mode. Here, the membrane sample was fixed on a holder and placed in water bath upside down

so that the active/top surface is faced the water. Air bubble of ca. 7 µL was dispensed on the membrane surface. A mathematical fitting method based on Ellipse model was exploited to calculate the water contact angle; by subtracting the measured angle from 180º. At least five measurements were performed for each sample, and the average value was presented.

3.6.7.2 Measurement of static water contact angle at different temperature and pH values

The switching behavior of flat and micro-patterned surface modified PA TFC membranes, developed in **section 3.5.3**, was evaluated by measuring the change in static water contact angle at different temperature and pH values using captive bubble measurement mode. The same measurement platform, described in **section 3.6.7.1**, was employed. In addition, the water bath was heated up and cooled down gradually, and the actual bath temperature was measured using a thermocouple (Pt100-1) connected to a data logger (ALEMO 2590, Ahlborn). At each temperature, the membrane sample was equilibrated for almost 10 min, thereafter an air bubble of ca. 7 µL was dispensed on the membrane surface and the contact angle was measured. The switching behavior, expressed by the change in static water contact angle, was investigated within a temperature range of 55 - 25 ºC in citrate-phosphate buffer at pH 3 and pH 7. The results are the average of at least two measurements for two different membrane samples

3.7 Evaluation of membrane performance

3.7.1 Measurement of pure water permeability

3.7.1.1 Measurement of pure water permeability for isotropic macroporous PES supports using microfiltration system

The pure water permeability experiments for the prepared PES supports were performed using a dead-end stirred cell (Amicon cell model 8050, Millipore Corp.) connected to 2,5 L feed tank and pressurized using nitrogen gas. First, initial water permeability was measured at transmembrane pressure of 0.5 bar for 3 min (2 times), then the membranes were compacted by filtrating of Milli-Q water at 1.5 bar for 40 min. Afterward, the pressure was reduced to 0.5 bar and the pure water permeability was measured again for 3 times. Subsequently, the pure water permeability was calculated using **Equation 26**:

$$Pure\ water\ permeability = \frac{m}{\rho\ t\ A\ \Delta P}$$

Equation 26: Pure water permeability

Where m is the mass of a permeate of density ρ collected for time t through a membrane sample of surface area A at transmembrane pressure ΔP.

3.7.1.2 Measurement of pure water permeability for flat and micro-patterned PA TFC membranes and surface-modified membranes using dead-end filtration mode

The pure water permeability for flat and micro-patterned PA TFC membranes and surface-modified membranes was determined using a 100-mL dead-end nano-filtration cell made of stainless steel. Milli-Q water was charged to the feed side and the permeate was collected at operating pressure of ~14 bar and ambient temperature. The pure water permeability was measured at steady state conditions and calculated using **Equation 26**. The presented data are the average of three measurements of three different samples for the same membrane type.

3.7.1.3 Measurement of pure water flux for micro-patterned PA TFC membranes at different pressure values using cross-flow filtration mode

The pure water flux for the micro-patterned PA TFC membranes was additionally measured at different operating pressures using a cross-flow lab-scale membrane testing unit (P-28; FOLEX AG, Seewen, Switzerland). The pure water flux was measured at two different membrane orientations; i.e., the membrane surface patterns are “parallel” or “perpendicular” to the direction of feed cross-flow. For each membrane sample, the pure water flux was measured over a range of applied pressure values, 4, 8, 12, 16, and 20 bar. The membranes were compacted for 1 h at each pressure value and then the permeate was collected. The averaged results of, at least, two measurements of three different samples for the same membrane type are presented.

3.7.2 Evaluation of separation performance

3.7.2.1 Salt rejection experiments using dead-end filtration mode

3.7.2.1.1 Salt rejection experiments at normal pH conditions

The separation performance, i.e., capability to separate dissolved salts from water, for flat and micro-patterned PA TFC membranes and surface-modified membranes was evaluated using a stainless steel nano-filtration cell at operating pressure of 14 – 16 bar using feed solution of 2,000 ppm salt in Milli-Q water, at ambient temperature and stirring rate of 700 rpm. The rejection propensity of three salts were tested, NaCl, Na_2SO_4 and $CaCl_2$. The salt rejection was determined by measuring the conductivity of feed and permeate samples using conductometer (856 Conductivity Module, Metrohm AG), then substituting in **Equation 27**:

$$Salt\ rejection\ (\%) = \left(1 - \frac{permeate\ conductance}{feed\ conductance}\right) \times 100$$

Equation 27: Calculation of salt rejection

Additionally, the permeability was calculated using **Equation 28**:

$$Solution\ permeability\ = \frac{m}{\rho\ t\ A\ (\Delta P - \Delta\pi)}$$

Equation 28: Calculation of solution permeability under RO conditions

Where, ΔP is the transmembrane pressure, and $\Delta\pi$ is the osmotic pressure difference across the membrane, which is calculated using **Equation 3**. All tests were performed at least 2 times for 3 different batches of the same membrane type, and the average values and standard deviations are presented.

3.7.2.1.2 Salt rejection experiments at different pH conditions

The influence of membrane surface charge on the separation performance of flat and micro-patterned surface-modified membranes was investigated at two pH values. Subsequently, two feed solutions were employed, citrate-phosphate buffer solution (0.1M) at pH 3 and phosphate buffer solution (0.1 M) at pH 7. The experiments were conducted using a dead-end nano-filtration cell at operating pressure of ~ 16 bar at ambient temperature and stirring rate of 700 rpm. The salt rejection and the solution permeability were determined using **Equation 27** and **Equation 28**, respectively.

3.7.2.2 "Directional" cross-flow filtration tests for micro-patterned PA TFC membranes and assessment of concentration polarization parameters

The influence of membrane orientation, i.e., alignment of membrane surface structures to feed-flow direction, on membrane's separation performance and main concentration polarization parameters was investigated using a cross-flow lab-scale testing unit (**section 3.7.1.3**). The cell chamber has a meander-shaped feed channel (4.1 mm wide and 2.8 mm high), and the active membrane area is 28 cm^2. All experiments were performed at fixed feed volume flow of 1.8 L/min that corresponds to a linear velocity of 2.6 m/s, resulting in Re = 7300 and indicating turbulent conditions for the feed/retentate cross-flow.

The micro-patterned PA TFC membranes were installed at two orientations, "parallel" and "perpendicular" to the feed-flow direction, and the performance was compared with that of the flat membranes. Freshly prepared micro-patterned membranes were used for each membrane orientation.

In order to study the concentration polarization phenomena, the following procedures were followed. NaCl solution (2,000 ppm, and afterward 10,000 ppm) was charged into the feed compartment. The membranes were compacted for 1 h at 8 bar prior to the measurement. The values of solution flux J_v, feed concentration C_b, and permeate concentration C_p were recorded at four applied pressure values (8, 12, 16, 20 bar). Permeate was collected for 1 h at each pressure value after equilibrium for 30 min. This protocol was employed for each membrane sample at each membrane orientation. Subsequently, the linear form of concentration polarization equation by Brian (**Equation 6**) [78] was exploited to estimate the main concentration polarization parameters:

$$ln(C_b - C_p) = -\frac{J_v \delta}{D} + ln(C_m - C_p)$$

Equation 29: Linear form of concentration polarization equation by Brian

Accordingly, a straight-line relationship was plotted between $ln(C_b - C_p)$ on (Y-axis) and J_v on (X- axis). The boundary layer thickness δ was estimated from the slope $\left[-\frac{\delta}{D}\right]$, by substituting NaCl diffusion coefficient D by 5.8×10^{-6} m^2/h [261]. Additionally, the membrane surface salt concentration C_m was calculated from the intercept [$ln(C_m - C_p)$]. Finally, the concentration polarization modulus $C.P.M.$ was estimated using **Equation 7** (cf. **section 2.3.3.4.1**).

All the experiments were carried out using at least 2 – 3 samples from three different batches for the same membrane type, and the average values and standard deviations are reported.

3.8 Colloidal fouling experiments

Prior to fouling experiments, the membranes were compacted by filtrating almost 1 liter of Milli-Q water through each membrane sample, of active membrane area ~ 11.34 cm^2, using cross-flow filtration system at 20 bar. Then, the compacted membrane samples were stored wet (under Milli-Q water) at lab refrigerator.

Before starting the particle fouling experiment, dead-end nano-filtration cell was filled with Milli-Q water, and the permeate, i.e., pure water, was collected for 30 min for each sample. Subsequently, the initial water flux was calculated. In parallel, the colloidal silica dispersion was prepared as follows; specific volume of concentrated silica dispersion is added to 100 ml of Milli-Q water in order to prepare 200 mg/L. Then, the solution is stirred vigorously for 15 min followed by sonication for another 15 min. Two types of concentrated silica dispersions

were employed, LUDOX® (50 nm) and micro silica particles (500 nm). Afterward, two groups of experiments were performed.

3.8.1 Colloidal fouling experiments without stirring

The colloidal fouling propensity of surface-modified flat and micro-patterned membranes was firstly evaluated at no stirring condition and compared with that of the pristine membranes. In addition, the applicability of the cake filtration mechanism was investigated, and the fitting range was determined.

Experimentally, Milli-Q water, used to measure initial water flux, was replaced with freshly-prepared 100 ml of colloidal silica suspension and the fouling experiment was performed at constant operating pressure of 16.5 – 17 bar, ambient temperature (23 – 25 °C), and static conditions, i.e., no stirring. The time was counted from the first permeate drop and the cumulative permeate weight was collected by means of a digital balance connected to the PC to record online the data. The particle fouling experiment was conducted till 96 – 98 ml of the silica solution is filtered, in case of dry cake-layer experiments, or till 85 – 90 ml of the solution is filtered; in case of wet cake-layer experiments. According to the next step, the fouled membrane was finally stored.

Subsequently, many performance relationships were plotted, solvent flux decline vs. permeate volume, relative flux decline (**Equation 30**) vs. permeate volume, and reverse cumulative flux vs. permeate volume. The latter relationship should yield a straight line if the silica fouling mechanism is governed by cake filtration mechanism [89].

$$relative\ flux = \frac{flux\ at\ any\ time\ during\ the\ fouling\ test}{initial\ water\ flux}$$

Equation 30: Relative flux

3.8.2 Influence of external stimuli on silica deposition behavior

This group of experiments was designed to investigate the influence of external stimulus, temperature, mixing, or both, on colloidal silica fouling of selected membranes. According to static fouling experiments, only colloidal silica particles of 50 nm was used as model foulant. The stimulus was preferentially switched on when 40 ml of the silica dispersion is filtered through the membrane, i.e., when the colloidal silica fouling is dominantly controlled by cake filtration mechanism.

Experimentally, as described before in **section 3.8.1**, the initial water permeability was firstly measured for the compacted membranes, thereafter, Milli-Q water was replaced by freshly

prepared 100 ml of silica dispersion (50 nm, 200 mg/L). The experiment was performed using dead-end nano-filtration cell at which a thermometer (Pt-100, TESTO 720) is fixed as illustrated in **Figure 3.6**. In parallel, the pure water permeability was also measured for the selected membranes at different temperatures as a *control experiment*. The heater was switched on at 40 °C when 35 ml of water is filtrated, afterward, the heater was switched off when 80 ml of water is filterated.

Figure 3.6: Illustration for adapted dead-end nano-filtration system used for particle fouling experiments

This page is intended to be empty

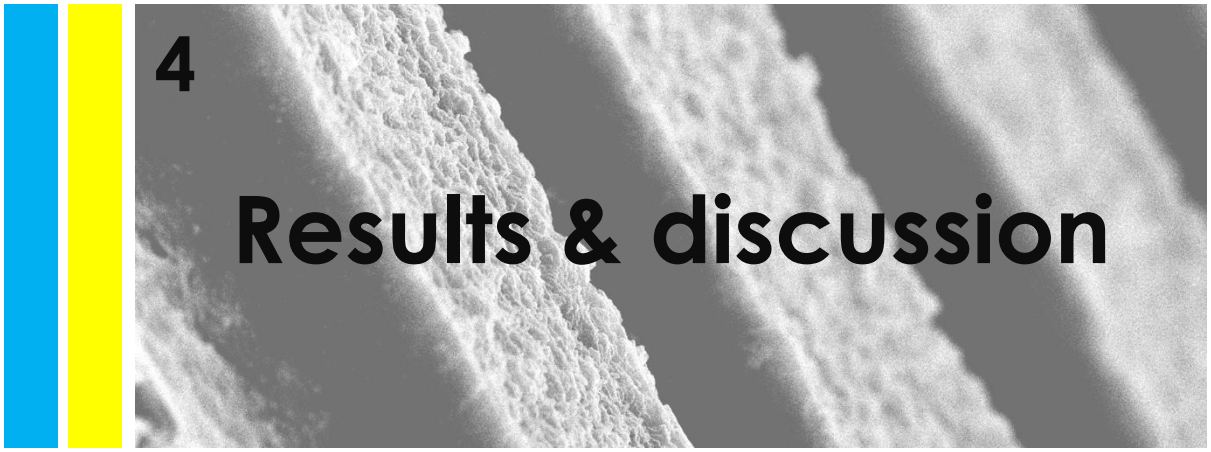

4 Results and discussion

4.1 Development of robust isotropic PES base membranes and their feasibility as supports for PA TFC membranes

One of the big challenges during the implementation of soft-lithographic techniques in order to prepare surface micro-patterned membranes is that the pattern is always transferred to the bottom side of the membrane [158]. In addition, other downsides are often observed, e.g. hierarchal pore size distribution, and skin layer formation (cf. **section 2.4.1.2.2**). Therefore, a formation of isotropic membrane structures via combined process of VIPS and LIPS is suggested. However, application of such symmetric membranes as supports for PA TFC membranes haven't been investigated yet. In this section, the preparation of flat PA TFC membranes based on isotropic PES supports is introduced.

4.1.1 Development of hydrophilic, highly water permeable and robust isotropic macroporous PES base membranes

4.1.1.1 Influence of polymer content at fixed exposure time to humid air

The impact of polymer content (PES and PVP) on the characteristics of PES membranes was studied. The proportions of PES were altered in range of (10 – 15 wt.%) and the fraction of PVP was varied from (7 - 12 wt.%) for each PES weight composition, whereas the fractions of NMP and TEG were kept at ratios of 27 and > 45 wt.%, respectively (see **Table 4.1**). The casting solution compositions were designed to be in a metastable state since it is commonly known that skinless isotropic membranes exhibiting high hydraulic permeability should be precipitated from thermodynamically metastable casting solutions [12, 30, 144]. TEG as a hygroscopic non-solvent additive was used to control the stability of the casting solution. The U.S. patent by Greenwood et al. [148] was employed as a guide for suited non-solvent fractions.

The pore characteristics for PES membranes prepared from different casting solutions at fixed exposure time to humid air, 3 min, are presented in **Figure 4.1**.

Generally, for membranes IB1 to IB9, it is obvious that the mean flow pore diameter decreased with increasing PVP fraction, for each PES weight percentage. Besides, the effect of changing solid polymer content on bubble point pore diameter is pronounced. Higher PES content along with considerable PVP fraction was found to promote the formation of smaller pores and to suppress macrovoid formation [153]. This can be interpreted in terms of the interaction between the two polymers, PES and PVP. The ratio of the number of functional groups in PVP to that in PES, calculated from the PVP/PES weight ratios, was in range of (0.47 - 0.96). Lafreniere et al. observed that the interaction between PVP and PES is the strongest when one to two amide groups in PVP interact with each sulfone group in PES [152]. This may also account for the unexpected high value for bubble point pore diameter of IB3 membrane, where PVP/PES ratio was 1.2 that may have promoted non-solvent diffusion into PES cast film and accelerated precipitation causing a formation of larger pore dimension.

Table 4.1: Composition of the casting solutions used for preparation of PES base membranes and values for the membranes' porosities

Membrane	Casting solution composition				Porosity (%)	
	PES	PVP	NMP	TEG	Density Method	Swelling Method
IB	10	-	40	50	77.5	77.3
IB1	10	7	27	56	84.8	85.0
IB2	10	9	27	54	71.7	69.8
IB3	10	12	27	51	83.5	84.0
IB4	12.5	7	27	53.5	80.0	82.1
IB5	12.5	9	27	51.5	81.1	82.8
IB6	12.5	12	27	48.5	79.3	81.5
IB7	15	7	27	51	77.2	72.6
IB8	15	9	27	49	78.2	80.7
IB9	15	12	27	46	68.7	72.4
IB10	15	12	43	30	67.0	64.7
IB11	17.5	12	40.5	30	70.7	73.6

On the other hand, although the PVP/PES weight ratio for IB9 membrane was also within the range (0.47 - 0.96), the high casting solution viscosity could be considered as a possible explanation for high bubble point pore diameter value. Increasing the casting solution viscosity, because of high polymer content, may have caused a trapping of considerable NMP portions in the precipitated film, leading to higher bubble point pore diameter. Accordingly, it may be

concluded that irrespective the PES/additive ratios, optimization of the fractions of base polymer and additive is inevitable. Investigation of PES contents > 15 wt.% was not applicable because of the quite high casting solution viscosity as well as the long time required for obtaining homogenous solution before casting, especially at high TEG contents.

Moreover, it is believed that the difference between mean flow and bubble point pore diameters should be as small as possible to assure a homogenous barrier structure. Subsequently, PES membranes prepared from casting solutions IB6 and IB8 seem to be closer to the desired isotropic structure than other membranes.

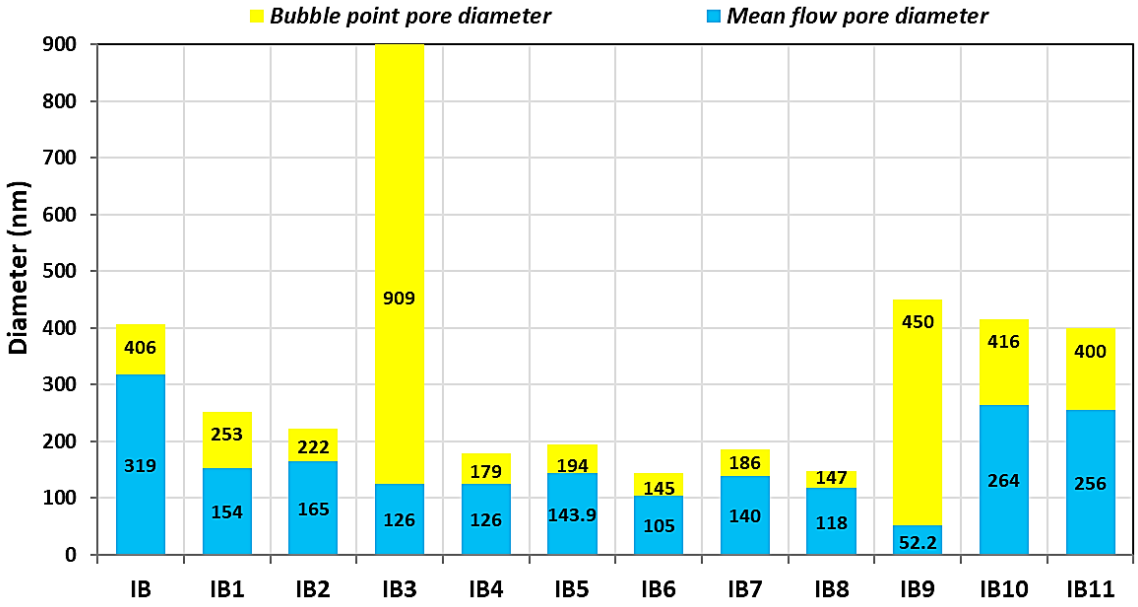

Figure 4.1: Pore characteristics from gas flow/pore dewetting permporometry for PES membranes prepared using casting solutions containing (PES:PVP:NMP:TEG) at different compositions at fixed exposure time (3 min)

PVP has been emphasized to act as a surfactant during the phase separation process that increases the interfacial area, i.e., mixing, between polymer-rich and water-rich phases [153]. Accordingly, either the voids agglomerates arising between numerous polymeric spheres, or the polymeric spheres agglomerates themselves were dispersed into smaller sizes, both resulting in membrane structures exhibiting lower pore size and higher porosity values. Porosity results are presented in **Table 4.1**. All the membranes exhibited high porosity values; however, no distinguished trend accounting for the relation between PVP content and porosity was observed.

The transport characteristics for PES membranes prepared from different casting solutions at fixed exposure time to humid air, 3 min, are introduced in **Figure 4.2**. The results of pure water

permeability measurements were emphasized to be in congruence with the pore size data. The addition of PVP was observed to cause a slight decrease in hydraulic permeability. This can be explained by the increase of casting solution viscosity due to high solid polymer content, which slows down the diffusional exchange of solvent and non-solvent during phase separation process, i.e., delayed demixing [262]. As a result, it restrains the evolution of mean flow pore diameter as well as it promotes the formation of isotropic pore structures. The lowest hydraulic permeability in case of IB9 membrane could be linked to the highest casting solution viscosity. Irrespective of the large bubble point pore diameter value, permeability was emphasized to be dominated by much smaller mean pore diameter.

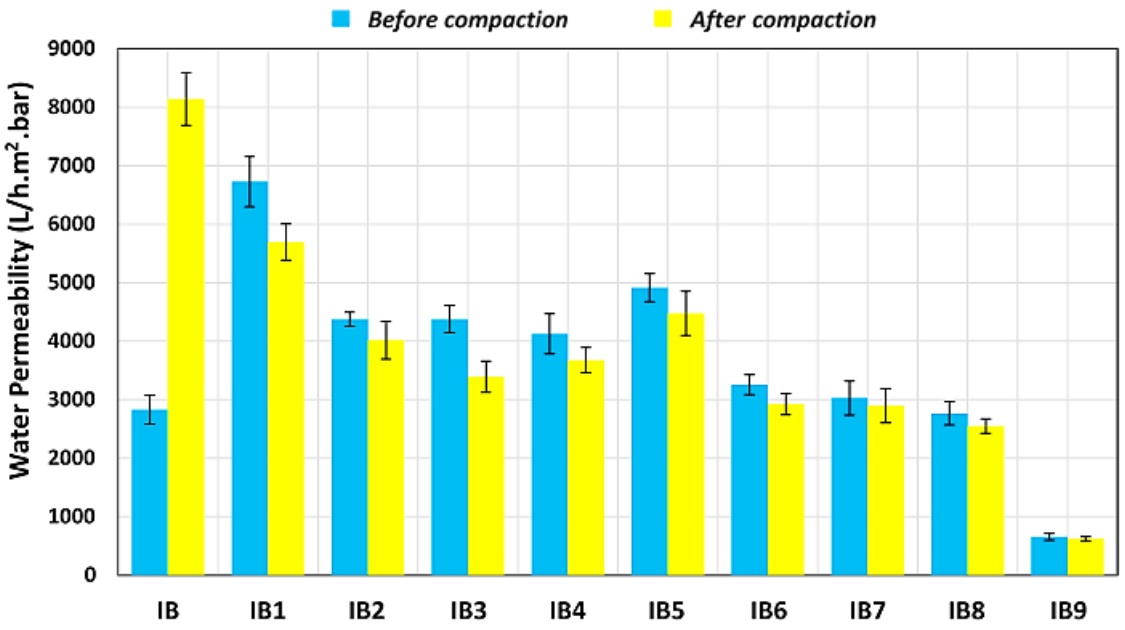

Figure 4.2: Transport characteristics for PES membranes prepared using casting solutions containing (PES:PVP:NMP:TEG) at different compositions at fixed exposure time (3 min)

Additionally, the change in hydraulic permeability values before and after compaction is implied to reflect the nature and stability of membrane's pore structure. Skinless, isotropic and robust membrane structure is essentially defined by a small change in hydraulic permeabilities before and after compaction. According to the results, IB6 and IB8 were chosen as the most suited casting solution compositions that should yield skinless isotropic PES membranes, despite of their relatively lower pure water permeability, 3260 and 2760 L/h.m^2.bar, respectively. In case of IB, the fortuitous high water permeability, measured after compaction, is strongly related to its lower water wettability (cf. **section 4.1.1.5**), apparently the membrane pores had not yet been fully wetted when recording the initial water fluxes.

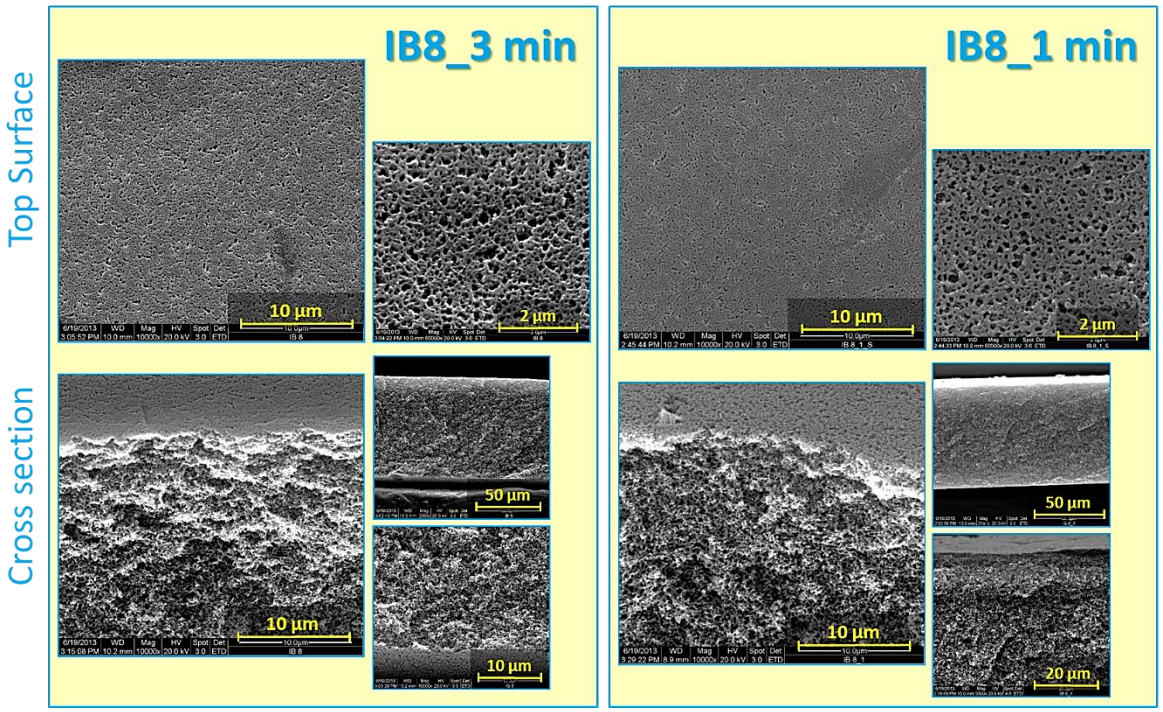

Figure 4.3: SEM micrographs for top surface and cross section morphologies at different magnifications for IB8 base membranes prepared at two different exposure times, 1 and 3 min

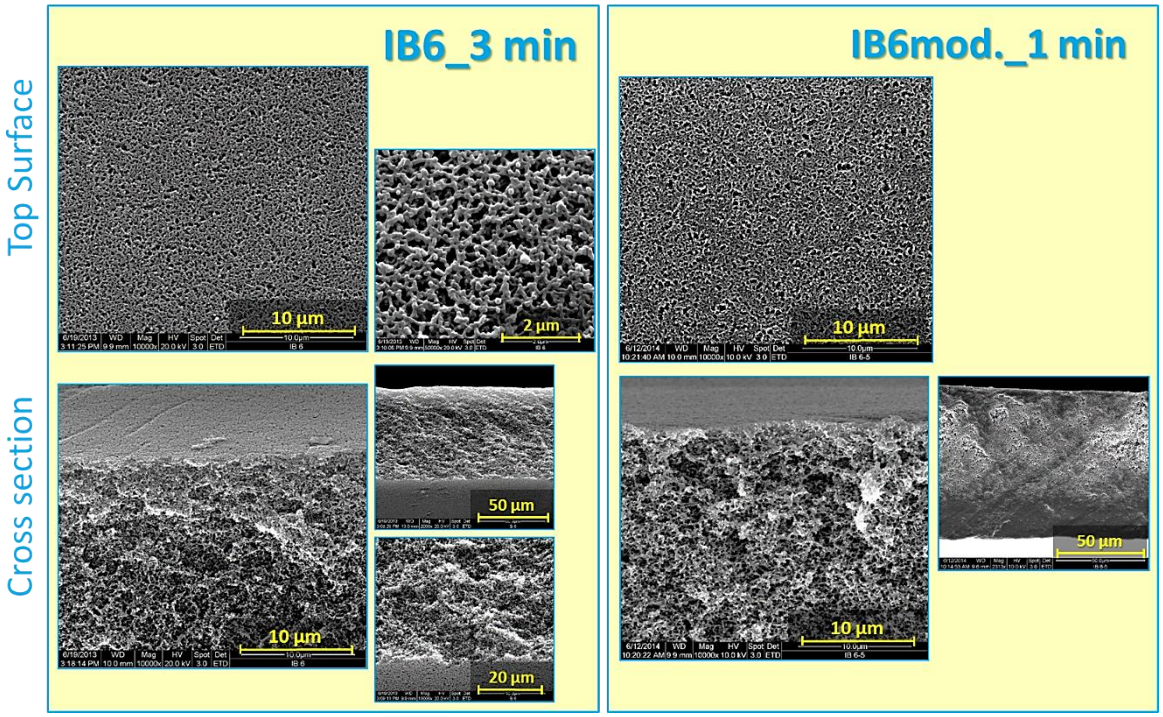

Figure 4.4: SEM micrographs of top surface and cross section morphologies at different magnifications for IB6 base membranes before and after adaptation of exposure time to humid air and [solvent:non-solvent] weight ratio

Furthermore, scanning electron micrographs for top surface and cross section morphologies for both membranes, IB8 and IB6, prepared at fixed exposure time, 3 min, (IB8_3 min and IB6_3 min) are shown in **Figure 4.3** and **Figure 4.4**, respectively. In top surface images, increasing PES fraction from 12.5 wt.% in IB6 to 15 wt.% in IB8 yielded a denser membrane surface. Nevertheless, the skinless isotropic sponge pore structure of IB6 and IB8 is confirmed by the cross section morphology. Moreover, the influence of PVP addition is eminent in terms of prohibiting macrovoids formation that is crucial to attain high mechanical stability and steady performance during high pressure operations [263].

4.1.1.2 Influence of non-solvent additive content at fixed exposure time to humid air

Two casting solutions containing lower TEG fractions, 30 wt.%, (IB10 and IB11) were also investigated. From **Figure 4.1**, the reduction in TEG content was found to have an undesirable impact on mean flow pore diameter such that IB10 and IB11 exhibited much higher mean flow pore diameter than the other membranes in that series. This was attributed to the fact that TEG is emphasized to increase the ability for water vapor absorption during VIPS process. So, it is usually used to realize uniform concentration profiles causing the cast film to precipitate at virtually the same time over the entire cross section. This was also reinforced by using NMP as a solvent, which requires long evaporation time. Hence, it is concluded that although reduction in TEG fraction offered a possibility to increase PES content, i.e., IB11, it was confirmed that TEG content should not be less than 40 wt.% to assure formation of isotropic membrane structures [30, 148].

4.1.1.3 Adaptation of exposure time to humid air

The exposure time to humid air (RH: 80 %) during the VIPS process was varied and the influence on the characteristics of PES membranes prepared using IB8 casting solution was investigated. The pore and transport characteristics for the resulting membranes were presented in **Figure 4.5**. IB8 casting solution was exploited in the adaptation experiments due to its higher polymer content than IB6; consequently, more explicit impacts on the membrane characteristics was expected. In principle, the precipitation behavior of polymer–solvent solutions is affirmed to be complicated by slow kinetics aroused from their high viscosity as well as existence in metastable state [264]. Therefore, the adaptation of exposure time to humid air is of high significance.

According to the results, the variation of the exposure time in range of (5 s – 3 min) had no major impact on the transport and pore characteristics. Nevertheless, exposure time of 1 min

was observed to produce PES membranes of mean flow pore diameter ~ 120 nm and relatively high water permeability (4120 L/h.m^2.bar). Top surface and cross section morphologies for IB8 membranes prepared at exposure times of 1 min and 3 min, IB8_1 min and IB8_3 min, were analyzed by means of SEM (**Figure 4.3**). IB8_1 min membrane was found to holdover the isotropic pore structure, whereas top surface micrographs showed that they exhibited relatively less porous outer membrane surface, in comparison with IB8_3 min membranes. Subsequently, exposure time of 1 min to humid air (RH: 80 %) was concluded to be the best suited interval in order to obtain highly permeable isotropic membrane structure.

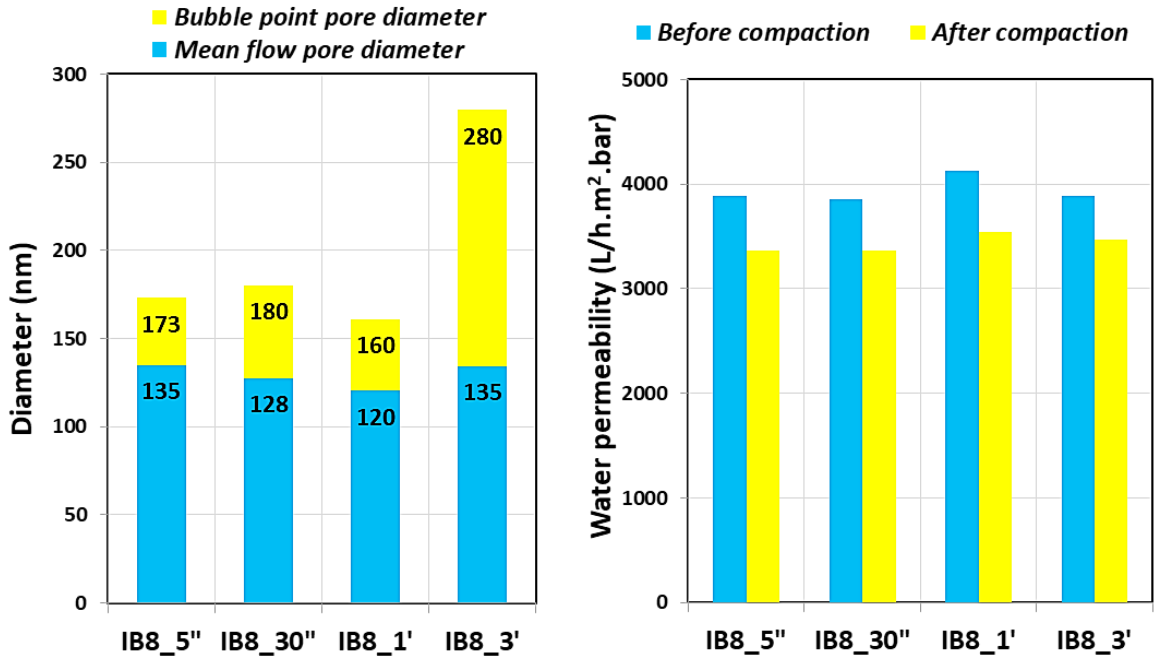

Figure 4.5: Pore and transport characteristics for PES membranes prepared using IB8 casting solution at different exposure times (5 s – 3 min) to humid air

4.1.1.4 Influence of [solvent:non-solvent] weight ratio

Based on the pore size and permeability results (cf. **section 4.1.1.1**), IB6 casting solution was preferentially selected to investigate how the preparation procedures of isotropic PES membranes with mean flow pore diameter of ~ 100 nm and high hydraulic permeability could be refined and made more robust. A slight increase in the [solvent:non-solvent] weight ratio was desired in order to improve the handling and the casting process by making the casting solution less instable. Accordingly, a series of six casting solutions containing the same solid polymer content but with varied [NMP:TEG] ratios, was suggested (see **Table 4.2**). Pore and transport characteristics for the obtained membranes are shown in **Figure 4.6**.

Table 4.2: Composition of the IB6-based casting solutions employed for the adaptation experiments of [solvent:non-solvent] weight ratio

Membrane	IB6 casting solution composition			
	PES	PVP	NMP	TEG
IB6_0	12.5	12	27	48.5
IB6_1	12.5	12	28	47.5
IB6_2	12.5	12	29	46.5
IB6_3	12.5	12	30	45.5
IB6_4	12.5	12	31	44.5
IB6_5	12.5	12	32	43.5

No detrimental impact on both the pore size and hydraulic permeability was found upon slight decreasing of TEG fraction; consequently, it was emphasized that it is possible to reduce TEG fraction by 5 wt.% without undesired consequences. This slight change in TEG fraction was found to improve clearly the efficiency of the preparation process, and the reproducibility of IB6 membranes, as well. Top surface and cross section SEM images for PES membranes prepared from IB6 casting solution before and after adaptation of the exposure time to humid air and the [solvent:non-solvent] weight ratio are presented in **Figure 4.4**. The isotropic cross section structure in both cases is explicit with no eminent alteration in top surface morphology. In conclusion, IB6 casting solution with [PES:PVP:NMP:TEG] proportions of [12.5:12:32:43.5] in combination with exposure time of 1 min to humid air (RH: 80 %) was emphasized to be the most suited preparation conditions to obtain robust isotropic PES

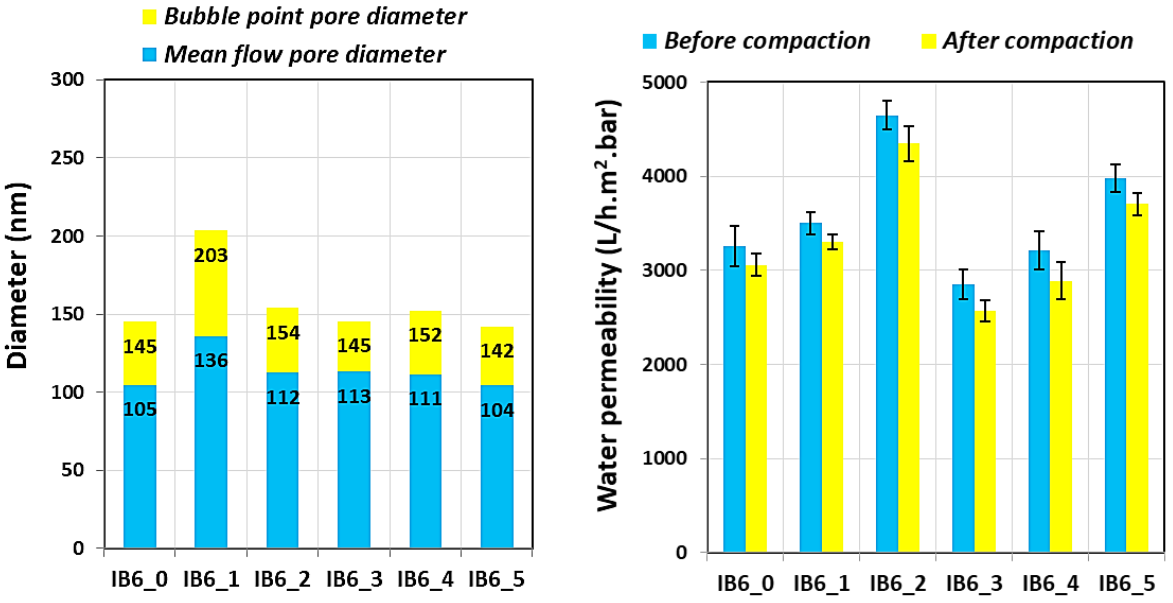

Figure 4.6: Pore and transport characteristics for PES membranes prepared using IB6 casting solutions of different [NMP:TEG] weight ratios at fixed exposure time, 1 min

membranes with average barrier pore diameter of ~ 100 nm and hydraulic permeability of about 4000 L/h.m^2.bar, with high reproducibility.

4.1.1.5 Chemical analysis and surface wettability of PES base membranes

Qualitative characterization of surface chemistry for three representative PES membranes, IB, IB6 and IB8 was performed using ATR-FTIR spectroscopy and IR charts are introduced in **Figure 4.7**. All membranes showed typical IR peaks of PES, i.e., stretching in benzene ring at ~ 1578 cm^{-1}, C=C stretching at ~ 1485cm^{-1}, besides aromatic ether stretching band at ~ 1241 cm^{-1}. Additionally, a significant peak was observed at 1668 cm^{-1} for only IB6 and IB8 membranes that is assigned to C=O stretching in tertiary amides as a result of PVP incorporation [265].

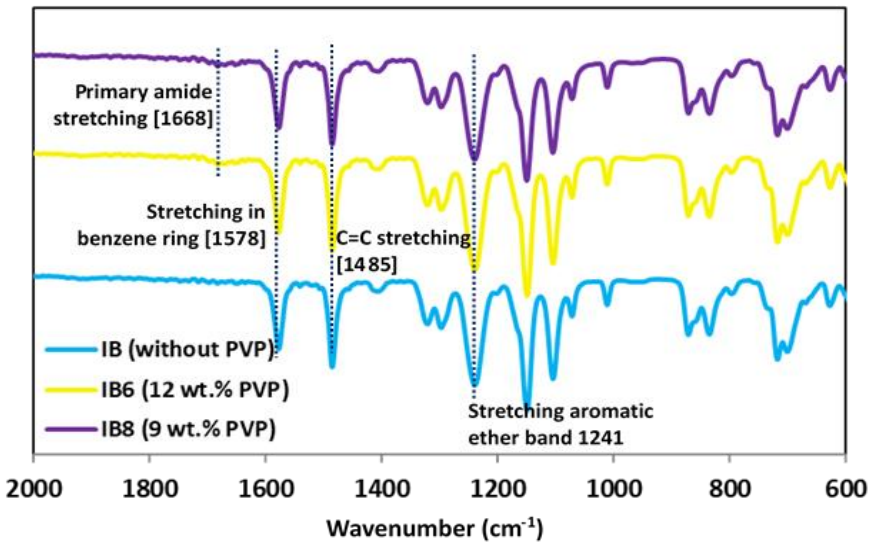

Figure 4.7:ATR-FTIR spectra for selected PES base membranes, IB, IB6 and IB8

Moreover, a precise estimation of the actual percentage of PVP, which is retained in the membrane matrix after preparation process, was carried out using ^{1}H-NMR analysis of the re-dissolved membranes. Taking in consideration that; peaks appearing at 8 – 7 ppm were attributed to the resonance of the aromatic protons in PES backbone; while peaks appearing in ranges of 3.25 – 2.95 and 2.3 – 1.8 ppm were assigned to the resonance of the protons present in the heterocyclic side group of PVP. Subsequently, the actual weight percentage of PVP in PES membranes was calculated by means of integration of the areas under the aforementioned peaks. IB6 and IB8 membranes were found to contain 10.2 and 8.9 wt.%, respectively. Such high additive fractions are explained by entrapment of PVP inside the forming membrane matrix during the phase separation process because of the high casting solution viscosity.

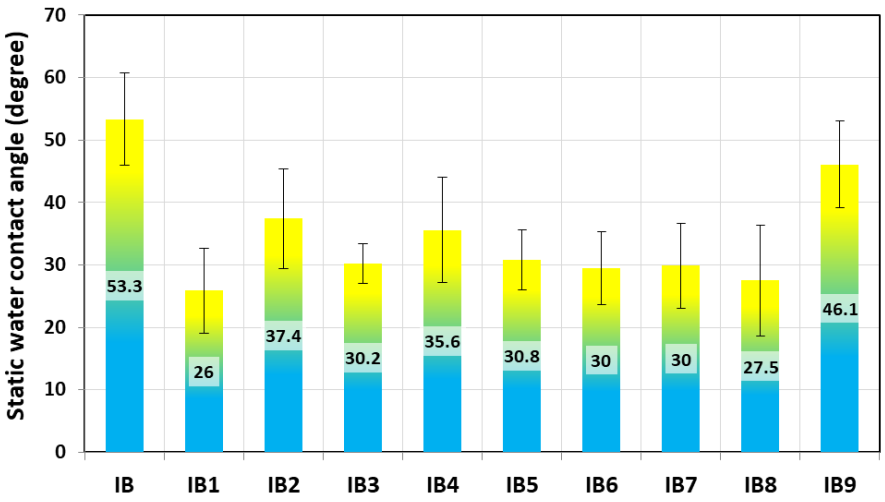

Figure 4.8: Water contact angles for PES base membranes prepared using casting solutions containing (PES:PVP:NMP:TEG) at different compositions

In parallel, the surface wettability of PES membranes was investigated by measuring the static water contact angle using sessile drop method. Generally, except for IB9, PVP addition was revealed to decrease the water contact angles for all membranes (**Figure 4.8**). Similar observation was reported by Li et al. [266]. PES membranes prepared from IB6 and IB8 casting solutions was observed to exhibit the lowest contact angle values; ~ 30° and ~ 27.5°, respectively. This could be interpreted by the modified surface characteristics as a result of the optimization of membrane pore structure. Furthermore, PES membrane prepared without PVP, IB, was found to have a contact angle of ~ 53° that is lower than reported contact angles (~ 76°), typically measured for non-porous PES film [267], which implies that the surface wettability is influenced not only by membrane chemistry but also by surface porosity and membrane morphology. Accordingly, the high water contact angle measured for IB9 membrane can be correlated to its irregular/heterogeneous pore structure that have been concluded from permporometry results (cf. **section 4.1.1.1**).

4.1.2 The feasibility of exploiting isotropic PES membranes as supports for PA TFC membranes

4.1.2.1 Influence of different monomer systems on characteristics and separation performance of PA TFC membranes

Preparation of PA TFC membranes using IP method was investigated employing three different base membranes, i.e., isotropic PES membrane developed in this work (IB6; cf. **section 4.1.1**), a commercial PES MF membrane (CPES), in addition to an anisotropic

polysulfone membrane (PSF) analogous to conventional supports that are currently employed for commercial PA TFC membranes [68].

Table 4.3: Compositions and abbreviations of the MPD-based monomer systems used for preparation of PA TFC membranes on different supports

Base membrane	MPD-based monomer systems		
	[2 wt.% MPD + 0.1 wt.% TMC]	[2 wt.% MPD + 2 wt.% TEA + 0.1 wt.% TMC]	[2 wt.% MPD + 2 wt.% TEA + 4 wt.% CSA + 0.1 wt.% TMC]
IB6	MT/IB6	MTT/IB6	MTCT/IB6
Commercial PES membrane	MT/CPES	MTT/CPES	MTCT/CPES
Polysulfone	MT/PSF	MTT/PSF	MTCT/PSF

A full description for MPD-based monomer systems under investigation along with the abbreviations standing for the produced membranes are listed in **Table 4.3**. Two additives were employed, CSA and TEA. The role of additives in promoting IP reaction has been discussed before (cf. **section 2.3.2.1.3**). In brief, CSA and TEA were reported to improve the imbibition of MPD into the support matrix by formation of a liquid layer on the membrane's surface, in addition to the catalyzing role of TEA that was found to equilibrate HCl, which is liberated from IP reaction and may affect PA film porosity [31, 268].

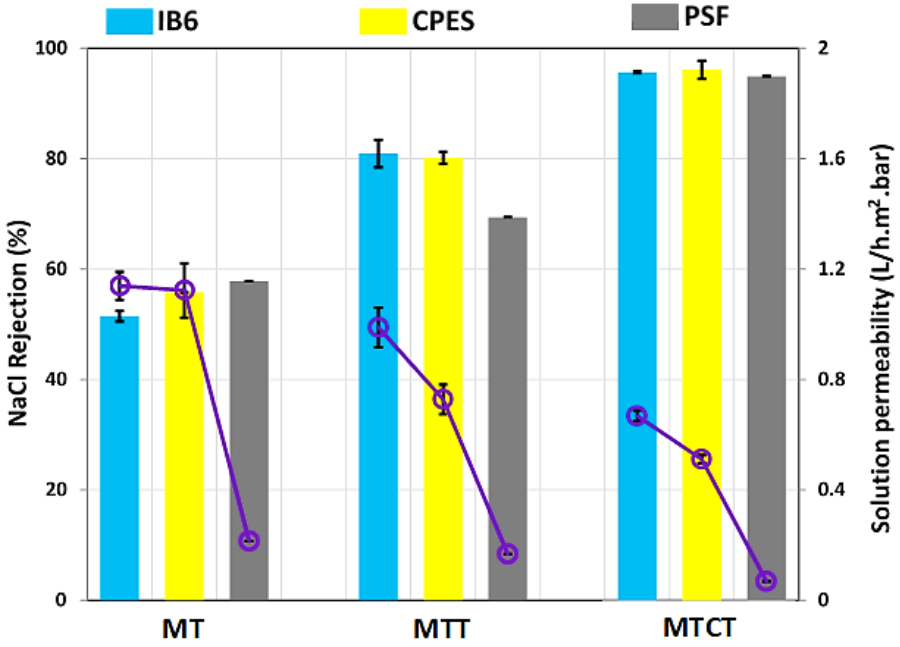

Figure 4.9: Separation performance for PA TFC membranes prepared using different MPD-based monomer systems on different supports

Separation performance for PA TFC membranes prepared on the three base membranes is shown in **Figure 4.9**. The rejection experiments were performed using 2,000 ppm NaCl as a feed solution at 16 bar and ambient temperature under vigorous stirring, 700 rpm; to minimize the concentration polarization. An explicit enhancement in membranes' selectivity was observed upon using TEA and CSA. The improvement in NaCl rejection was accompanied by a decrease in solution permeability as a result of forming an adherent, denser and less permeable PA barrier layer. PA TFC membranes prepared using MTCT monomer system were emphasized to exhibit the highest NaCl rejection (≥ 95 %). In parallel, PA TFC membranes based on IB6 supports were always observed to have higher permeability than the other investigated supports, CPES and PSF, which could be linked to the high porous well-defined isotropic structure of IB6. MTCT/IB6 membrane showed the best separation performance among the tested membranes, initial permeability of 0.7 L/h.m^2.bar accompanied by NaCl rejection of 96 %.

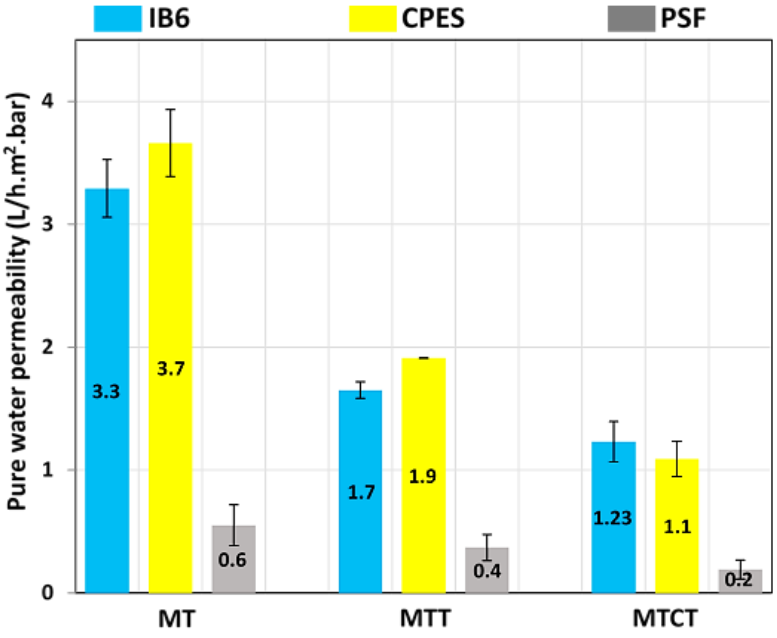

Figure 4.10: Pure water permeability for PA TFC membranes prepared using different MPD-based monomer systems on different supports

The pure water permeability data for the prepared PA TFC membranes were revealed to reinforce the aforementioned separation performance behavior. MTCT/IB6 showed high pure water permeability of 1.2 L/h.m^2.bar, whereas MTCT/CPES and MTCT/PSF had water permeabilities of 1.1 and 0.2 L/h.m^2.bar, respectively (see **Figure 4.10**). Subsequently, in contrast to the results reported by Ghosh and Hoek [68], PA TFC membranes based on hydrophilic porous supports exhibited much higher water permeability than those prepared on

hydrophobic ones. Therefore, the supports' characteristics were confirmed to have a key role in determining the final performance of PA TFC membranes as will be discussed later (cf. **section 4.1.2.2**).

Furthermore, the influence of aqueous monomer additives on the PA layer morphology was investigated for PA TFC membranes prepared on IB6 supports using SEM, and the top surface and cross section morphologies are presented in **Figure 4.11**. As seen in top surface images, all PA TFC membranes exhibited "ridge-and-valley" morphology to various extents such that the surface of MTCT/IB6 showed the densest morphology, full of protrusions. This can be attributed to the high porous well-defined structure of IB6 support along with incorporation of CSA and TEA. This is in congruence with a recent study by Zhang et al. [69]. They have emphasized that supports of high surface porosity produce adherent PA layers exhibiting high crosslinking degree and protruding crumpled surface morphology. In addition, MT/IB6 membrane was observed to suffer from unstable PA layer, which in turn could be responsible for its relatively poor selectivity.

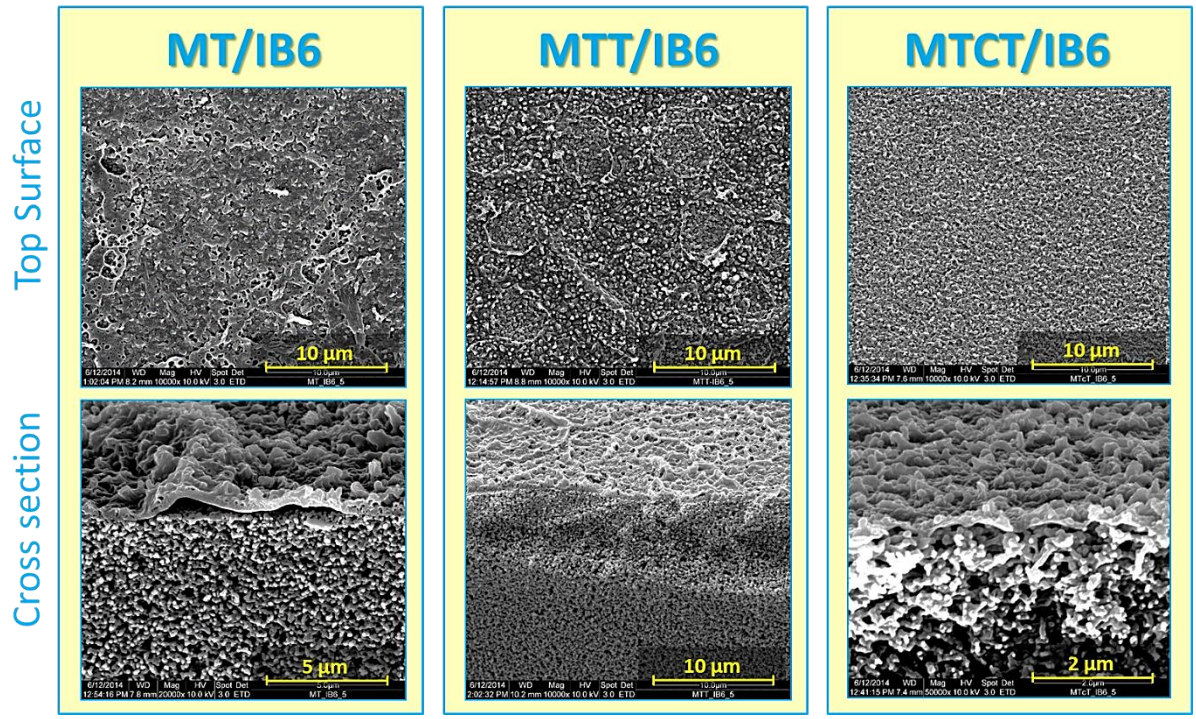

Figure 4.11: SEM micrographs for top surface and cross section morphologies of PA TFC membranes prepared using MPD-based monomer systems on IB6 base membrane

Quantitative surface roughness analysis for selected PA TFC membranes was carried out using AFM and the main roughness parameters are introduced in **Table 4.4**. MTCT/IB6 was observed to have the lowest root mean square roughness, S_q, of 53 nm among PA TFC membranes based on IB6. This could be related to the denser PA morphology that was seen in

SEM images. The surface roughness data for PA TFC membranes prepared on other supports will be discussed later (cf. **section 4.1.2.2**).

Table 4.4: Quantitative surface roughness analysis for PA TFC membranes prepared from MPD-based monomer systems on different supports

PA TFC membrane	Root mean square roughness, S_q (nm)	Roughness parameters (nm)		
		Peak height, S_P	Valley depth, S_V	Peak-valley height, S_Y
MT/IB6	93	383	-296	679
MTT/IB6	130	421	-340	761
MTCT/IB6	53	94	-56	150
MTCT/CPES	74	261	-244	505
MTCT/PSF	125	439	-345	784

The influence of additives on the surface chemistry of PA TFC membranes was investigated using ATR-FTIR spectroscopy. ATR-FTIR spectra for PA TFC membranes prepared using different MPD-based monomer systems on three base membranes, IB6, CPES and PSF are shown in **Figure 4.12**. It was reported that polymerization reaction of MPD and TMC can mostly result in two types of PA structures simultaneously [24, 269]; a cross-linked structure, and another linear structure with pendent carboxylic acid groups as a result of hydrolysis of unreacted terminal acyl chloride [270]. The cross-linked PA structure was affirmed in most of PA TFC membranes by IR bands at [~ 1630 cm^{-1}] that are attributed to C=O stretching amide (II) [265], whereas the linear PA fraction was assured by IR peaks at [~ 1740 cm^{-1}] that are assigned to C=O stretching in a pendant carboxylic acid groups [271]. These characteristic PA peaks were recorded for PA TFC membranes prepared using MTCT monomer systems atop the three base membranes besides some membranes prepared using other monomer systems; however, most of these peaks were invisible for the rest membrane samples. This could be justified by peaks' interference or their weak intensity. Moreover, PA TFC membranes prepared using MTCT monomer system exhibited additional peak at [1042 – 1036 cm^{-1}] that is assigned to S=O stretching in sulfonic groups [265], which in turn highlights the influence of CSA on altering the surface chemistry of PA TFC membranes. These sulfonic groups were revealed to promote clearly the NaCl rejection behavior of respective PA TFC membranes to high values (up to 95 – 97 %; cf. **Figure 4.9**) by Donnan membrane exclusion [72] (cf. **section 2.3.3.2**).

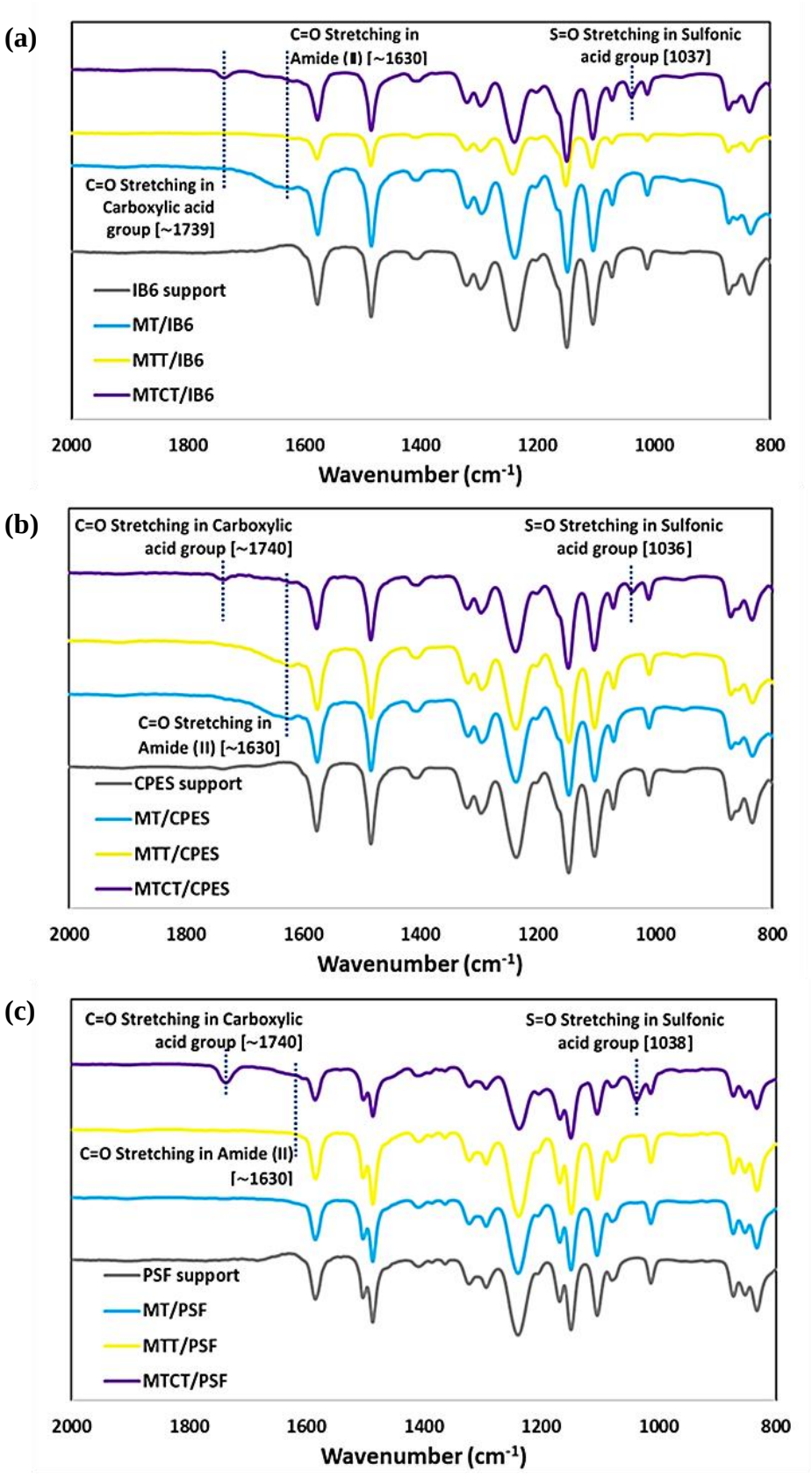

Figure 4.12: ATR-FTIR spectra for PA TFC membranes prepared using different MPD-based monomer systems on three base membranes: (a) IB6, (b) CPES, (c) PSF

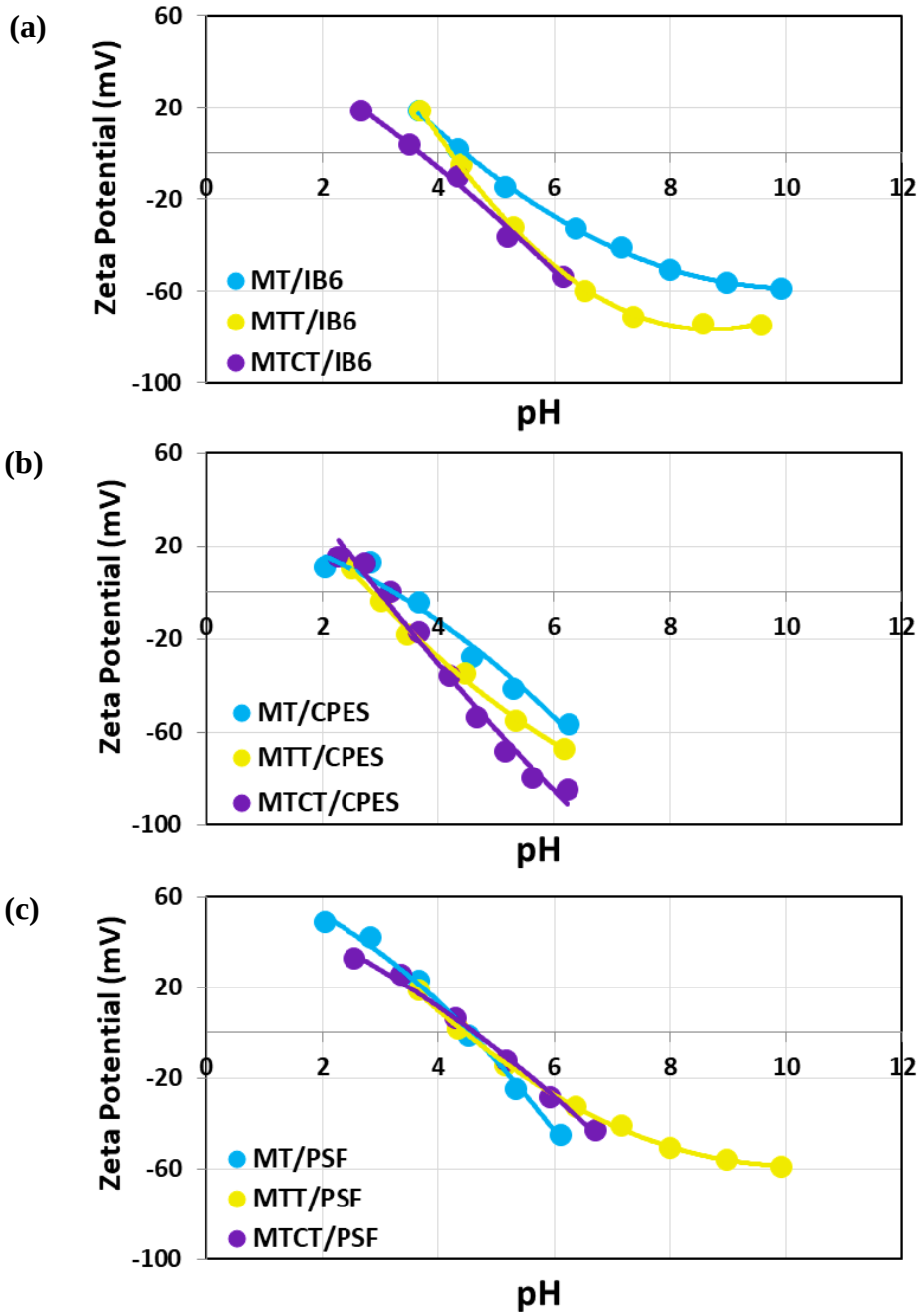

Figure 4.13: Zeta potential as function of pH for PA TFC membranes prepared using different MPD-based monomer systems on three base membranes: (a) IB6, (b) CPES, (c) PSF

In parallel, the membrane surface charge for PA TFC membranes prepared from different MPD-monomer systems atop the three supports was characterized by means of zeta potential measurements, and the charts are introduced in **Figure 4.13**. All PA TFC membranes exhibited negative surface charge at normal pH ranges. Additionally, the isoelectric point (IEP) of PA TFC membranes prepared from MTCT monomer system was observed to be more shifted toward lower pH ranges because of surface sulfonic groups because of incorporation of CSA. Nevertheless, the shift of IEP toward lower pH ranges was clearer for membranes based on IB6

and CPES rather than for those based on PSF. As argued later, the explicit hydrophobicity of PSF supports was believed to prohibit the diffusion of salt monomer solution inside the support matrix causing less incorporation of PA structures and resulting in relatively lower surface charge.

Furthermore, static water contact angle was also measured for PA TFC membranes using sessile drop method (cf. **Figure 4.14**). In line with ATR-FTIR and zeta potential measurement, PA TFC membranes prepared using MTCT monomer system were observed to exhibit the highest surface wettability by virtue of surface sulfonic and carboxylic groups. Nevertheless, PA TFC membranes based on PSF supports were emphasized to usually demonstrate the lowest surface hydrophilicity what could be strongly linked to the very hydrophobic nature of this base membrane (cf. **section 4.1.2.2**). Moreover, this observation could basically account for the lower pure water permeability measured for PSF-based PA TFC membranes (cf. **Figure 4.10**).

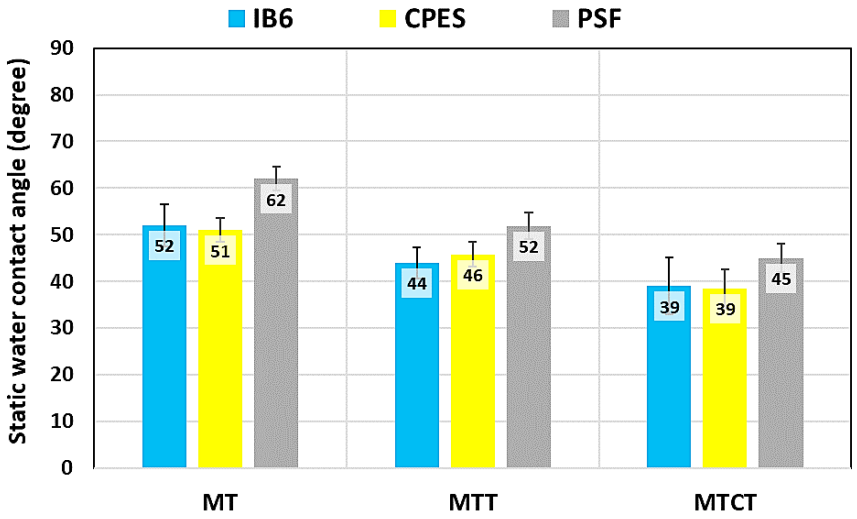

Figure 4.14: Water contact angles for PA TFC membranes prepared using different MPD-based monomer systems on different supports

Overall, the joint influences of different monomer systems on the characteristics and separation performance of PA TFC membranes prepared on the three base membranes had been elucidated. Accordingly, MTCT monomer system was affirmed to produce high performance water desalination membranes.

4.1.2.2 Influence of support's pore structure and surface properties on the characteristics of MTCT-based PA TFC membranes

Detailed physical and chemical characterizations were performed for the three base membranes, and the main results are shown in **Table 4.5**. As discussed before, IB6 membrane

exhibited optimized average barrier pore diameter of ~ 100 nm, whereas, CPES membrane was found to have an average barrier pore diameter of ~ 190 nm (instead of 100 nm); in contrast to the manufacturer's data sheet. PSF membrane had an average barrier pore diameter of 65 nm that is in accordance with results reported in [68] and indicates that the preparation conditions had been well transferred from that study to the current work.

Table 4.5: Physical and chemical characteristics for the three base membranes under investigation as supports for fabrication of PA TFC membranes

		IB6	CPES	PSF
Average barrier pore diameter (measured by PMI)		104 nm	187 nm	64 nm
Porosity	Density Method	74 %	71 %	33 %
	Swelling Method	79 %	75 %	14 %
PVP content		10.2 wt.%	7.1 wt.%	---
Water contact Angle		32.5 ± 5.6°	48.0 ± 2.9°	94.0 ± 6.5°

In addition, supports' surface chemistry was investigated using ATR-FTIR spectroscopy (see **Figure 4.15**). Characteristic IR peaks of polyethersulfone were affirmed for both IB6 and CPES membranes, and typical peaks for polysulfone were also found for PSF supports. Moreover, residuals of PVP were confirmed to be comprised in IB6 and CPES membranes by recording weak bands at ~ 1670 cm^{-1} that are assigned to C=O stretching in amide (III). Subsequently, the percentage of PVP in IB6 and CPES supports was quantified by means of ^{1}H-NMR spectroscopy to be 10.2 and 7.1 wt.%, respectively (cf. **section 4.1.1.5**). Static water contact angles were also measured for the three base membranes using sessile drop method.

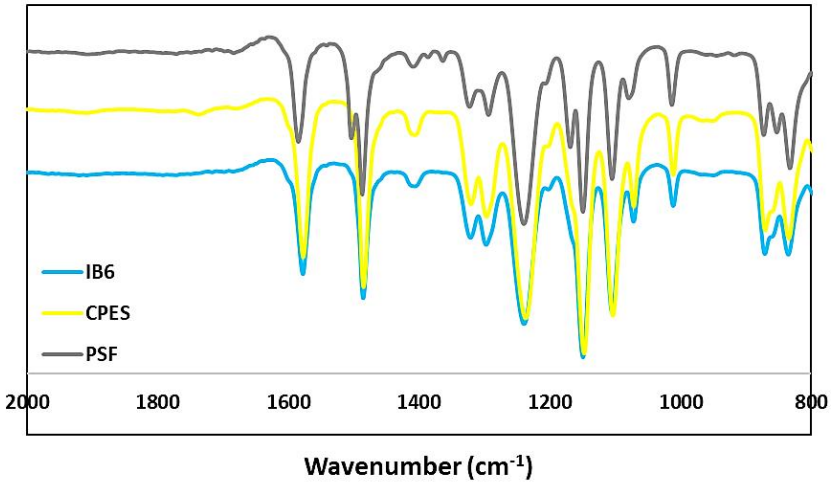

Figure 4.15: ATR-FTIR spectra for three base membranes under investigation as supports for PA TFC membranes

IB6 and CPES base membranes were emphasized to be hydrophilic by virtue of incorporation of PVP, while PSF support was revealed to exhibit explicit hydrophobic character.

Furthermore, the top surface and cross section morphologies for the three base membranes were characterized using SEM and the micrographs are presented in **Figure 4.16**. IB6 and CPES membranes were observed to exhibit well-defined isotropic pore structure over the entire cross-section despite of the difference in mean flow pore diameter. On the other hand, PSF was shown to have a typical anisotropic structure, with pronounced finger pore and macrovoid morphology in the support layer. Additionally, the top surface micrographs demonstrated the major discrepancy in surface porosity and pore dimensions among IB6 and CPES on one hand, and PSF with a much finer and less porous morphology on the other hand. Volume porosity was also estimated; IB6 and CPES were found to exhibit high values (> 70 %), whereas porosity of PSF was much lower (the value of only ~ 14 % was most probably affected by the poor wetting of PSF membrane by polar solvents).

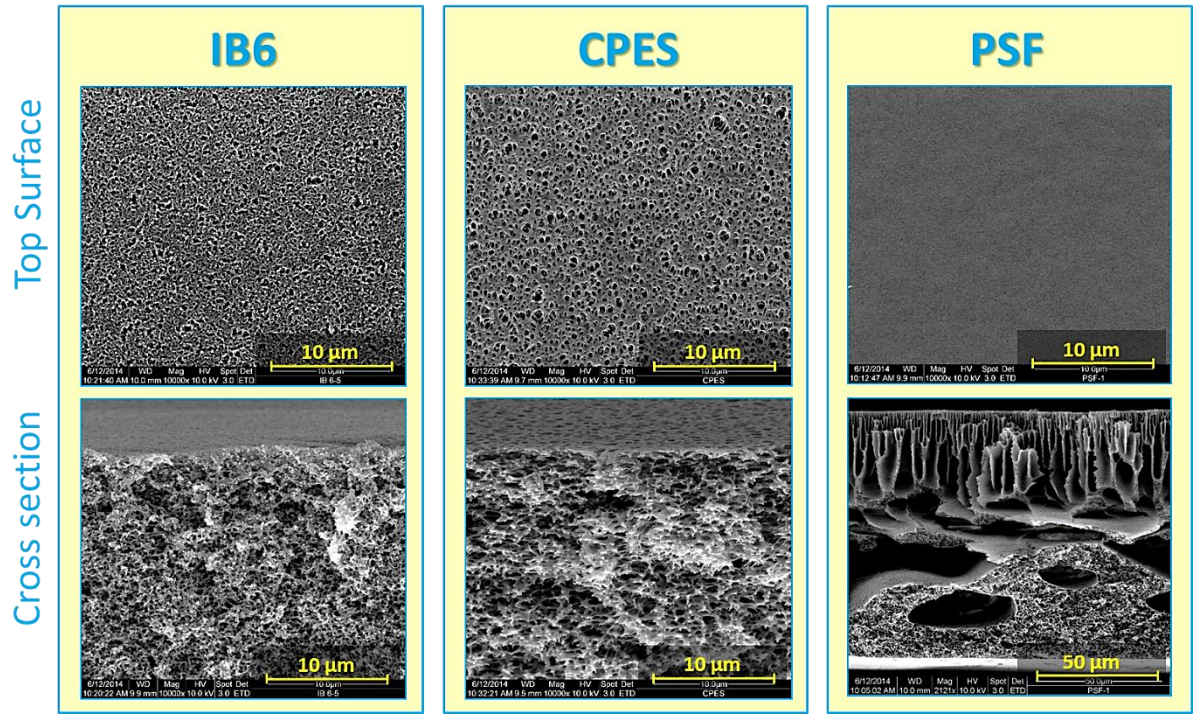

Figure 4.16: SEM micrographs of top surface and cross section morphologies for the three base membranes under investigation as supports for PA TFC membranes

With focus on the best performing MTCT-based monomer system, the influence of different support's pore structures on the morphology of PA layer was studied by means of SEM and AFM. The top surface and cross section morphologies are displayed in **Figure 4.17**, while AFM surface roughness data are introduced in **Table 4.4**. It was revealed that MTCT/IB6 exhibited typical "ridge-and-valley" morphology with dense protruding crumpled topography

(S_q of 53 nm), whereas MTCT/PSF had less dense and much rougher surface (S_q of 125 nm). Surface of MTCT/CPES was observed to be an intermediate between the two membranes with S_q of 74 nm. Furthermore, the apparent PA layer thickness was estimated using SEM to be ~ 70 nm, ~ 90 nm and ~ 200 nm in case of MTCT/IB6, MTCT/CPES, and MTCT/PSF, respectively. This large difference in the estimated thickness values was supported by "peak-valley height", S_Y, values determined by AFM (see **Table 4.4**). This value refers to the distance between the highest topographic line on the apex of PA layer and the lowest one (on a flat part of membrane surface or inside a bigger pore); consequently, it could also be employed to estimate the real thickness of PA layer. It was observed that MTCT/IB6 has the lowest S_Y value of ~ 150 nm, whereas S_Y was ~ 500 and ~ 780 nm in case of MTCT/CPES and MTCT/PSF, respectively. Accordingly, this may contribute to the high measured pure water permeability and solution permeability for MTCT/IB6 compared to MTCT/CPES and MTCT/PSF membranes.

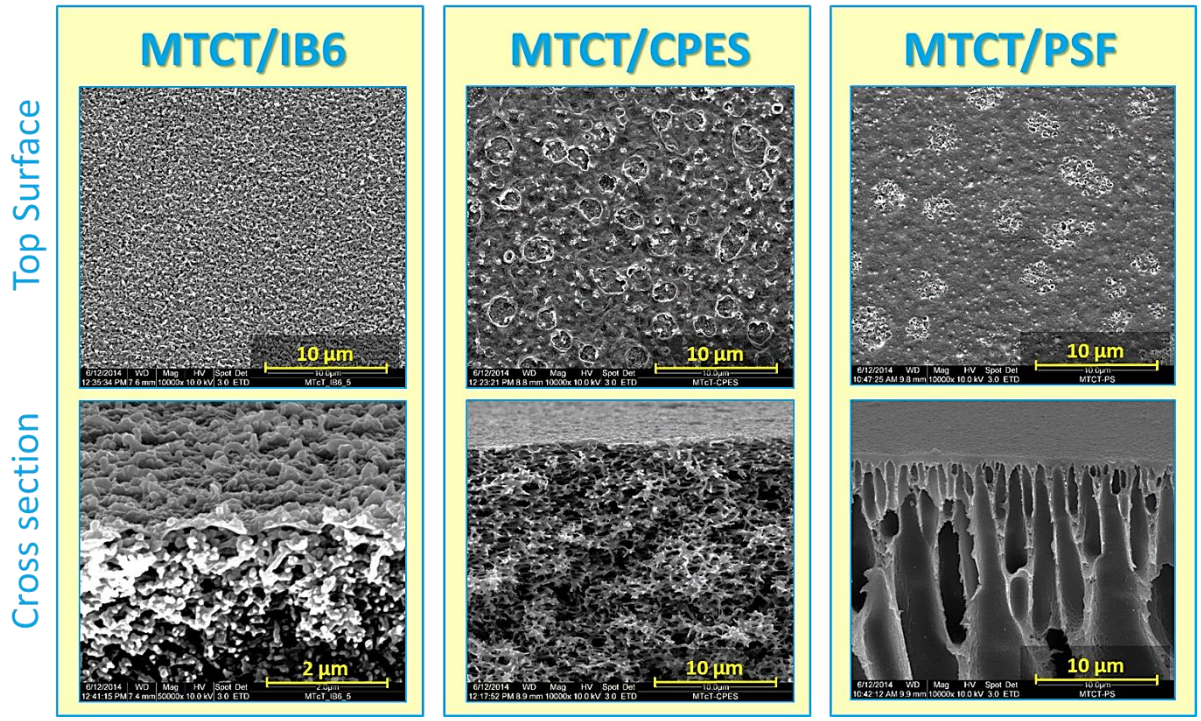

Figure 4.17: SEM micrographs of top surface and cross section morphologies for PA TFC membranes prepared using MTCT monomer system on the three supports

Overall, the hydrophilicity of IB6 and CPES base membranes was confirmed to influence the surface characteristics of the formed PA layer, and hence, its separation performance. It was reported that during IP reaction, MPD diffuses more slowly out of hydrophilic membrane pores [68]. Therefore, the support hydrophilicity could limit the initial violent MPD interaction with TMC and lead to better control of the PA film structure and surface roughness. Subsequently,

it is concluded that thinner, smoother, denser and less salt permeable PA layers were formed on hydrophilic isotropic supports (IB6 and CPES) because most of PA formed inside the pores. Nevertheless, MTCT/IB6 showed higher pure water and solution permeabilities because of the optimized lower mean flow pore diameter (~ 100 nm) of IB6 support, which is implied to realize the minimum amount of PA formed inside the pores that is essential to achieve high selectivity without sacrificing the permeability. This assumption is supported by the lower S_Y value of MTCT/IB6; compared to MTCT/CPES of higher mean flow pore diameter (~ 190 nm). On the other hand, a thicker, rougher, less dense, and hence, more salt permeable PA layer is formed on hydrophobic anisotropic membranes (PSF) due to the fact that most of PA was formed above the support's surface.

4.1.2.3 Impact of the developed isotropic structures on the stability of the performance of MTCT-based PA TFC membranes

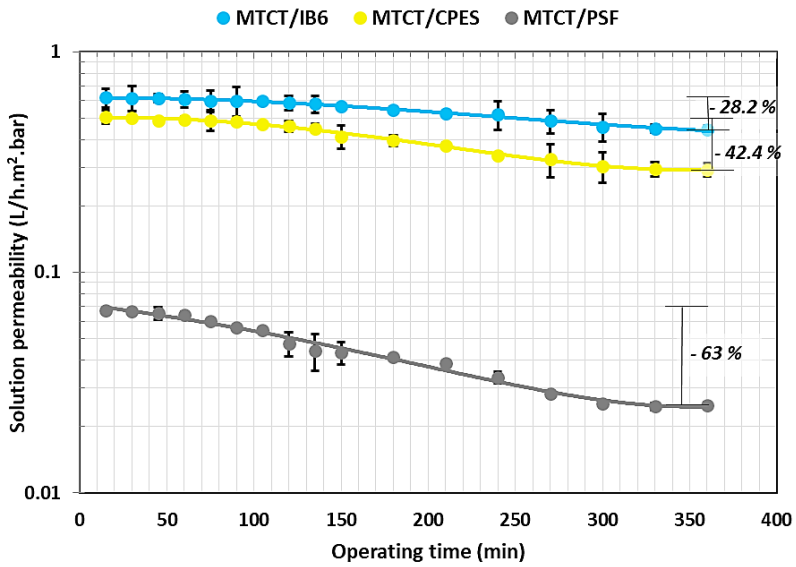

Figure 4.18: Permeability for PA TFC membranes prepared using MTCT monomer system on three different substrates during 6 hours under RO conditions

Toward more understanding of the merits of application of such new isotropic optimized structures as supports for PA desalination membranes, the solution permeability for MTCT/IB6 membrane versus MTCT/CPES and MTCT/PSF membranes was measured for 6 hours under RO conditions, i.e., at operating pressure of ~ 16 bar using 2,000 ppm NaCl feed solution under vigorous stirring at 25 °C (**Figure 4.18**). MTCT/IB6 was observed to exhibit the smallest permeability decline of 28 %. However, MTCT/CPES showed a permeability decline of 42 % despite the isotropic structure of CPES. This could apparently be due to the much larger mean flow pore diameter, ~ 190 nm. MTCT/PSF had adversely a permeability decline of 63 % that

indicates clearly the instability against compaction upon employing anisotropic structures as supports for water desalination membranes. These results emphasize the relative mechanical stability and high workability afforded by the newly developed hydrophilic IB6 supports exhibiting isotropic pore structure of an optimized barrier pore diameter of ~ 100 nm.

4.2 Development of surface micro-patterned PA TFC membranes

In this section, the development of novel and efficient surface micro-patterned PA TFC membranes is introduced. PES supports were micro-patterned using two microfabrication methods, combined processes of vapor- and liquid non-solvent induced phase separation micro-molding (VIPSµM and LIPSµM, respectively), as well as micro-imprinting lithography (MIL). The optimized [PES:PVP:NMP:TEG] casting solution and robust isotropic PES base membranes that were developed in **section 4.1.1** were exploited here in order obtain micro-patterned isotropic PES supports. Additionally, the fidelity of the surface micro-patterning techniques was comprehensively studied and different mechanisms are proposed.

Afterward, employing the experience gained in **section 4.1.2**, the preparation of thin PA film atop the developed micro-patterned PES supports was adapted. The separation performance was investigated for both dead-end and cross-flow configurations. Moreover, a concentration polarization analysis using different membrane orientations, i.e., with patterned grooves "parallel" and "perpendicular" to the direction of feed cross-flow, and at various feed concentrations was conducted. The influence of surface structures on the membrane performance was explored with a focus on the difference in the micro-patterning resolution.

Accordingly, the work in this section is presented in the following sequence; i) development of micro-patterned PES supports using both PSµM and MIL, ii) adaptation of PA synthesis, iii) assessment of separation performance and estimation of the concentration polarization parameters.

4.2.1 Development of micro-patterned PES supports using PSµM

Micro-patterned PES supports were prepared using a combined process of VIPSµM and LIPSµM. An illustration for the micro-patterning setup using PSµM has already been shown in **Figure 3.4**. Briefly, a polymer film was cast on a glass plate containing some openings, 50 mm each, where PDMS molds were placed. As demonstrated in the theory part (cf. **section 2.4.1.2**), many parameters were found to influence the demixing kinetics, and consequently, the membrane's final topography and porous structure. Anisotropic pore size distribution, as well as skin formation, should be avoided to produce symmetric patterned supports with high flux. Accordingly, the same dope composition that was optimized in **section 4.1.1** was used here; however, the casting conditions had to be adapted to achieve maximum conformity and hold the replicated features over the entire membrane surface. In the current work, two major parameters were refined, exposure time to humid air prior to precipitation, i.e., VIPSµM, and

the work of adhesion between the casting solution and PDMS mold. **Figure 4.19** presents SEM micrographs for top surface morphology of micro-patterned PES membranes prepared using "untreated", i.e., hydrophobic, PDMS at 1 min exposure time to humid air (RH: 80 %; same condition as flat membranes). An explicit deformation in the replicated pattern was observed. This was interpreted by trapping of air bubbles during the casting process because of the hydrophobicity of the "untreated" PDMS molds, and consequently, the poor wetting by the casting solution.

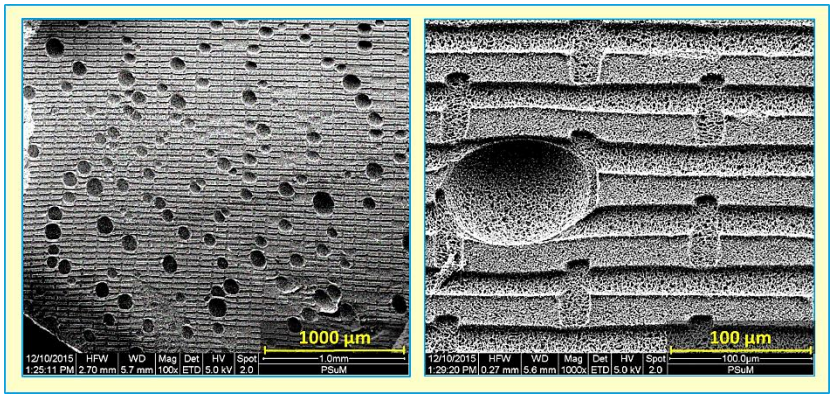

Figure 4.19: SEM micrographs for micro-patterned PES prepared using "untreated" PDMS at 1 min exposure time to humid air

Therefore, the mold material and the work of adhesion between the mold and the casting solution were affirmed to influence the fidelity of the replicated patterns [162]. PDMS molds were treated, hydrophilized, prior to use by means of plasma cleaner and/or treatment in SDS solution (1 g/L). Concerning pretreatment via plasma cleaner, various conditions were investigated; however, only two conditions, treatment at 0.7 mbar for 30 min, and treatment at 0.85 mbar for 45 min, were promising (see **Figure 4.20 (a - d)**).

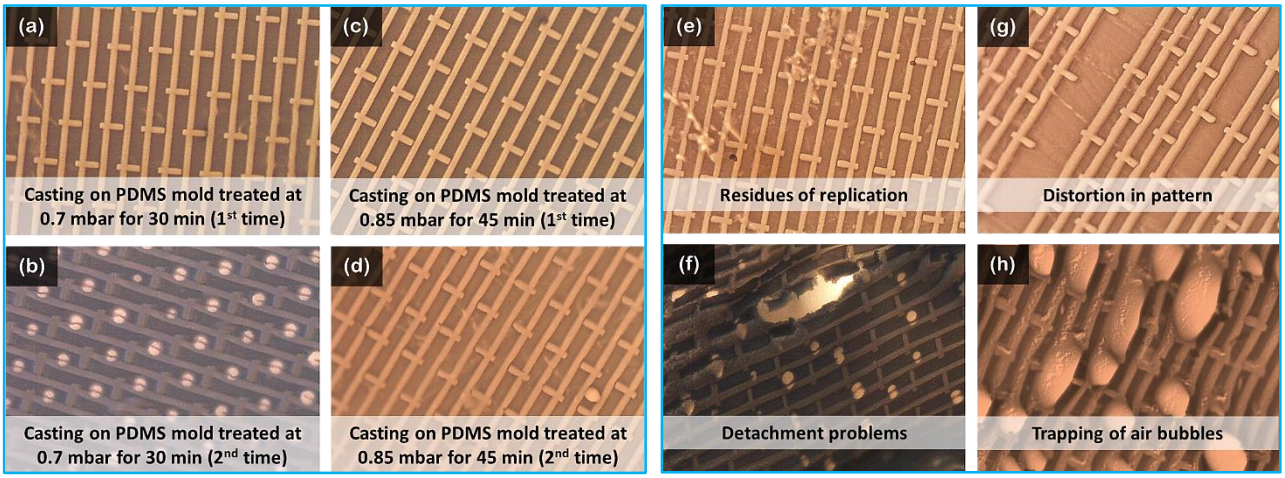

Figure 4.20: Optical microscope images for micro-patterned PES prepared using PSµM, (a) –(d): multiple casting on treated PDMS molds using plasma cleaner at two conditions, (e) – (h): other micro-patterned PES membranes suffering from different problems

Nevertheless, the treated PDMS molds were observed to lose the temporary hydrophilic character upon using. Therefore, the durability of the pretreatment process was confirmed to be a crucial parameter. A number of optical microscope images for patterned PES membranes suffering from distortion in replication, detachment problems, and trapping of air bubbles due to multiple use are shown in **Figure 4.20 (e – h)**. The easy release of membranes in PSµM was reported to be strongly influenced by the direction of the inherent shrinkage during the solidification [147], and complication in patterns or casting process [158]. Additionally, it was found that the detachment problems could also be caused by the hydrophobic recovery of treated PDMS [272, 273]. Subsequently, the stability of the hydrophilization process was investigated by measuring the static water contact angle for the plasma- and SDS-treated PDMS molds for different time intervals and after multiple use. It was manifested that the impact of plasma treatment at 0.75 mbar for 45 min could be retained for 24 h on storing in Milli-Q water (cf. **Figure 4.21**), whereas SDS treatment failed to last more than one casting time; consequently, it needs to be carried out each time before the casting process.

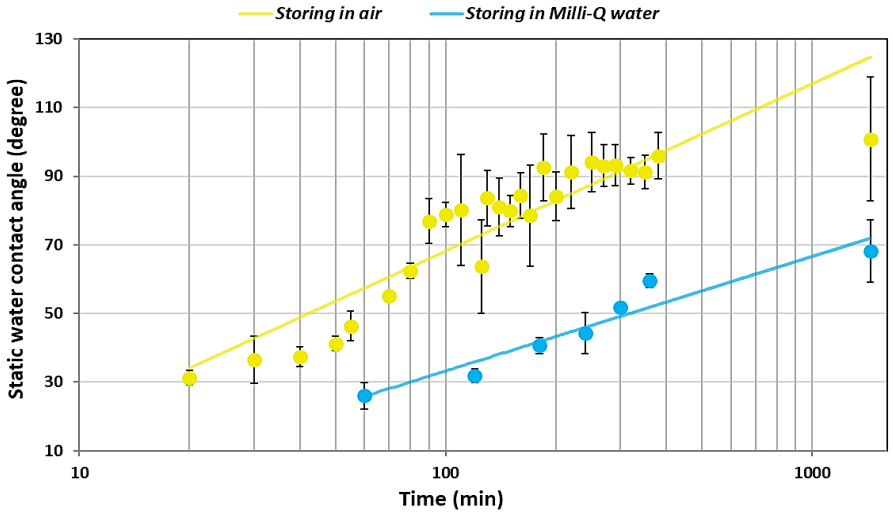

Figure 4.21: Change in surface hydrophilicity for plasma-treated PDMS molds during storing in Milli-Q water versus storing in air for 24 h at ambient temperature

In parallel, the optimum exposure time to attain isotropic well-replicated patterned membranes was emphasized to be different than that for the flat membranes. It is influenced by the composition of polymer casting solution, as well as the range and the aspect ratio of the pattern to be replicated. Different exposure times to humid air were employed, then the quality of the replication process by the membranes was assessed using an optical microscope. It was observed that 20 and 30 minutes were the best-suited exposure times to yield defect-free patterned membranes using plasma- and SDS-treated PDMS molds, respectively.

The pore size distribution is also considered as a key criterion to define the optimum exposure time. The results of gas flow/pore dewetting permporometry are presented in **Figure 4.22**. It was revealed that 30 min is the optimum exposure time to achieve well-replicated micro-patterned PES membranes (PES_PSµM) with homogenous pore size distribution of average mean flow pore diameter of 130 nm.

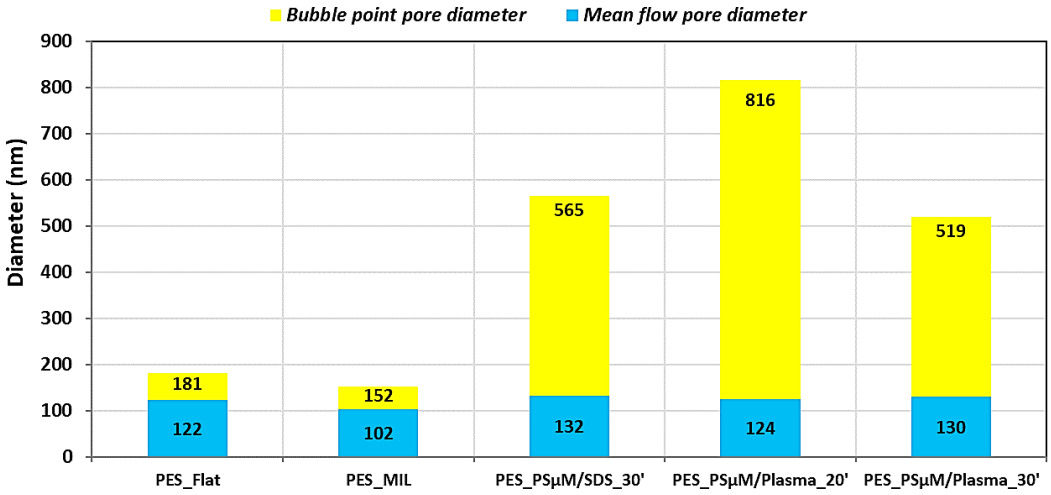

Figure 4.22: Pore characteristics from gas flow/pore dewetting permporometry for flat and micro-patterned PES base membranes

4.2.2 Micro-imprinting of flat PES supports using filtration cell

MIL and NIL have been utilized for microfabrication of many polymers and porous PES membranes (cf. **section 2.4.1.1**). Mostly sophisticated and expensive equipment is used for MIL and NIL. Nevertheless, in the current work, the utilization of a stainless-steel filtration cell, normally used for NF experiments, was investigated, for the first time, as a feasible and low-cost high-throughput custom approach for MIL of flat membranes using PDMS mold. The custom MIL set up has already been presented in **Figure 3.5**.

Apart from the mold related obstacles, three parameters were emphasized to influence the MIL process; i.e. temperature, pressure and imprinting time (cf. **2.4.1.3**). A series of different working temperatures (60 - 130 °C; i.e. below T_g of PES) and operating pressure values (6 – 11.5 bar) for various time intervals (15 – 60 min) were examined. The quality of the replication process by the membranes was investigated using the optical microscope. Examples for the optical microscope images for some membranes during the adaptation experiments of MIL conditions are shown in **Figure 4.23**.

For the reason that PES flat membranes were previously characterized to exhibit sponge-like porous structure and high permeability, major attention was paid to the changes in the barrier

pore structure due to MIL process as an indication for the alterations in the membrane's intrinsic properties. Accordingly, the best-suited working conditions were defined to be the lowest temperature and pressure values, besides the shortest time interval that can produce micro-patterned membranes exhibiting well-replicated surface features without significant compaction of the membrane pore structure.

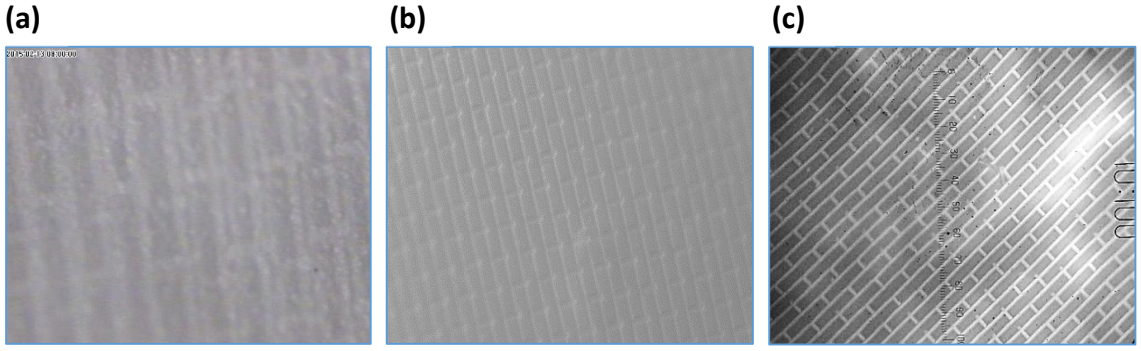

Figure 4.23: Optical microscope images at different magnifications for micro-patterned PES membranes using MIL: (a) MIL at 8 bar and 40 °C for 30 min, (b) MIL at 8 bar and 80 °C for 30 min, and (c) MIL at 10 bar and 110 °C for 35 min

Well replicated and isotropic patterned PES membranes were prepared using MIL (PES_MIL) at 10 bar, 110 °C for 35 min (cf. **Figure 4.23 (c)**). It was revealed that these experimental conditions limited the compression effects associated with the imprinting mechanism. The bubble point and the average mean flow pore diameters decreased from 181 and 122 nm in the case of the flat membrane to 152 and 102 nm for PES_MIL membrane, respectively (cf. **Figure 4.22**).

4.2.3 The fidelity of replication by PSμM versus MIL

To understand the micro-patterning mechanism for both PSμM and MIL techniques, as well as their influence on the membrane surface features, comprehensive SEM and AFM analyses were performed. The SEM micrographs for PES_PSμM and PES_MIL membranes at different magnifications and orientations are displayed in **Figure 4.24** and **Figure 4.25**, respectively. Additionally, AFM 3D images are shown in **Figure 4.26**.

The regular micro-topography of the surfaces for both membranes and the isotropic porous structure over the entire cross section were confirmed by SEM micrographs. The replicated microstructures on the membranes' surfaces are the "negative" replica of PDMS mold. For PES_PSμM membranes, the patterned lines are well-defined with clear edges and the whole pattern seems to be symmetric without any explicit deformations. For PES_MIL membranes, although the imprinted lines are wider and closer to each other, the whole pattern also appears homogenous and extended over the entire membrane surface. This implies the efficiency of the

micro-imprinting method employing NF filtration cell and elastic PDMS mold. Moreover, this obvious distinction between both membranes' surface topographies was supported by estimating the dimension terms; "line width" (L), "distance between two adjacent lines" (d) and "depth" (D) using SEM and AFM. These dimension terms are illustrated in **Figure 4.27** and the values are presented in **Table 4.6**.

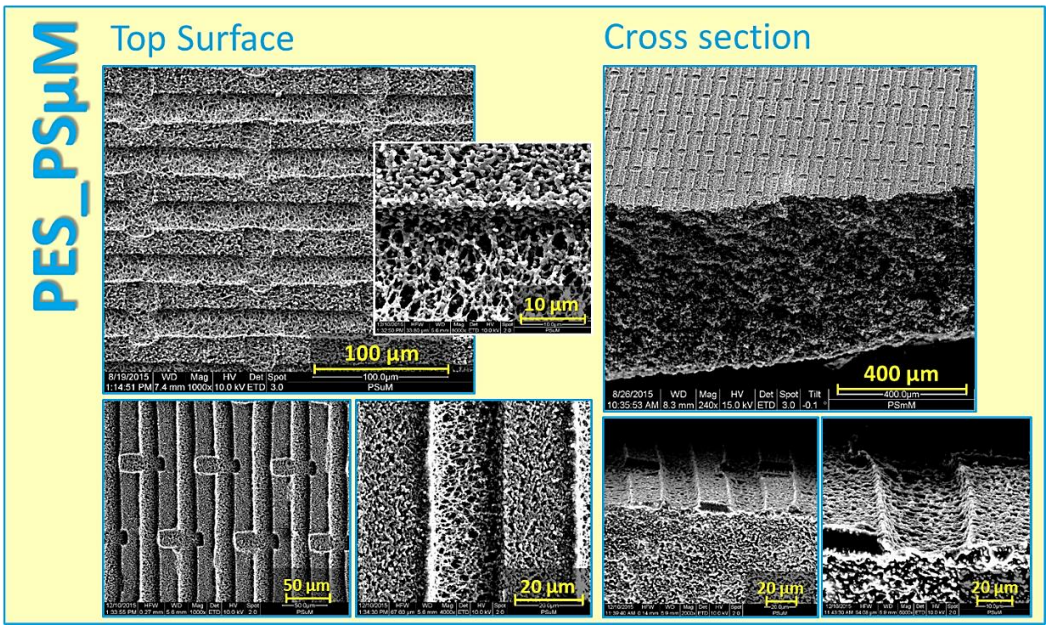

Figure 4.24: SEM micrographs for PES_PSµM membranes, showing top surface and cross section morphologies at different magnifications

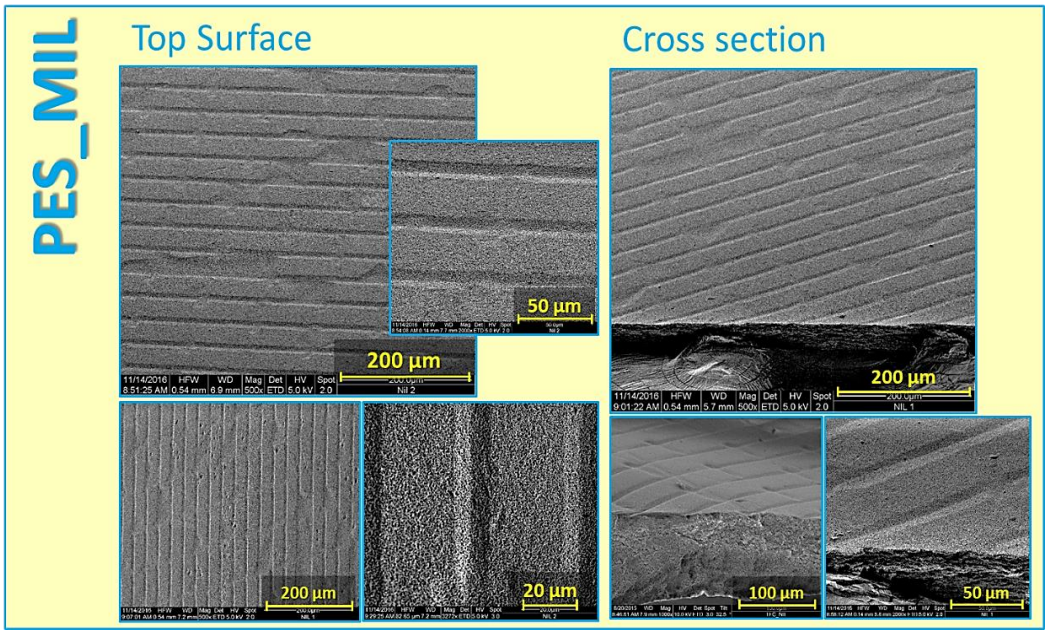

Figure 4.25: SEM micrographs for PES_MIL membranes, showing top surface and cross section morphologies at different magnifications

Table 4.6: Dimensions of surface microstructures for PDMS mold "M" and micro-patterned PES supports "m" estimated using SEM and AFM analyses

	Data collected from SEM				Data collected from AFM					
Sample	**Line width [µm]**		**Distance between two adjacent lines [µm]**		**Line width [µm]**		**Distance between two adjacent lines [µm]**		**Depth [µm]**	
PDMS mold	-- [a]		--		L_M	7.3 [b] 12.0 [c] 18.0 [d]	d_M	33.8	D_M	10.0
PES_PSµM	L_{m1}	19.6	d_{m1}	22.7	L_{m1}	26.1	d_{m1}	22.0	D_{m1}	5.3
PES_MIL	L_{m2}	37.0	d_{m2}	11.2	L_{m2}	35.8	d_{m2}	14.7	D_{m2}	2.0

a) No SEM was recorded for PDMS mold; b) Measured at depth of zero µm; c) Measured at depth of ~5 µm; d) Measured at depth of 10 µm.

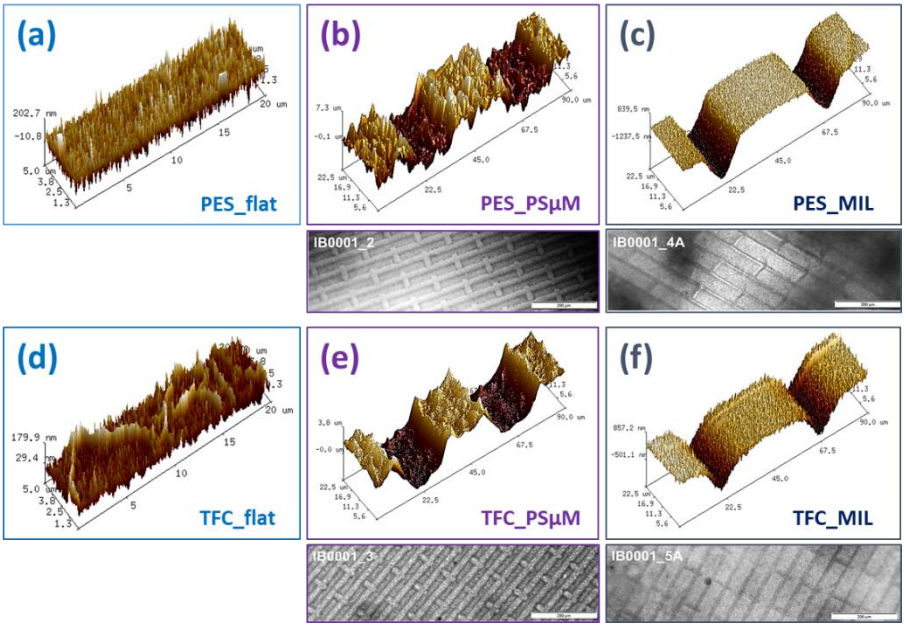

Figure 4.26: AFM 3D images for flat and micro-patterned PES supports and PA TFC membranes

The typical geometrical data for PDMS mold were deduced from AFM images to be line width, L_M, of 18 µm, depth, D_M, of 10 µm, and distance between two adjacent lines, d_M, of 34 µm. Regarding the micro-patterned PES supports, a congruence was observed between the topographical data derived from SEM and AFM which in turn accounts for the different micro-patterning mechanism in each patterning technique. For instance, the estimated line width, L_{m1}, for PES_PSµM membrane was about 23 µm, the mean value of SEM and AFM results, which is close to the estimated distance between two adjacent lines, d_{m1}, 22.4 µm. This confirms the symmetric surface micro-patterns obtained using PSµM. On the other hand, the dimensional

surface analysis in the case of PES_MIL membrane assures the asymmetric imprinted surface micro-patterns, in which the estimated L_{m2} was in the range of 36 µm while d_{m2} was in the range of 13 µm. As a result, PES_MIL is implied to be more analogous to be a negative replica of the mold rather than PES_ PSµM. The depth, D, was also estimated from AFM analysis to be in the range of D_{m1} = 5.3 µm and D_{m2} = 2 µm for PES_PSµM and PES_MIL, respectively.

According to these findings, a simplified scheme describing the micro-patterning mechanism for PSµM and MIL techniques, and interpreting the differences in surface topography between PES_PSµM and PES_MIL was suggested and introduced in **Figure 4.27**.

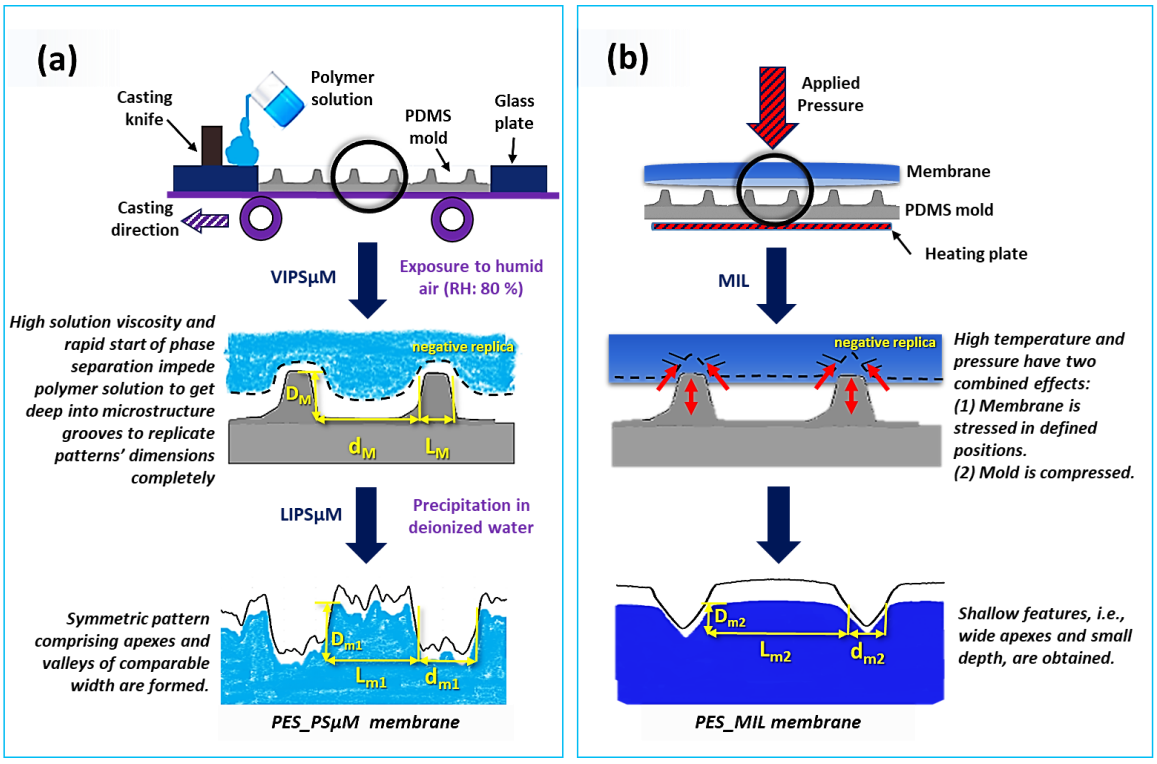

Figure 4.27: Scheme illustrating the difference in surface micro-patterning mechanisms between PSµM (a) and MIL (b) techniques

In PSµM, the viscous polymer solution is cast on the pretreated patterned PDMS mold; thereafter, the polymer film is exposed to humid air (RH: 80 %) for a particular time, VIPSµM. Hence, the phase separation process starts instantaneously over the whole microstructure as a consequence of incorporating hygroscopic non-solvent additive, i.e., TEG, in the casting solution. It is worth to mention that the incorporation of high TEG content (43.5 wt.%), along with slightly high polymer content, was found to yield extremely viscous and humid-sensitive casting solutions. The complex viscosity was applicable to be measured only at very low relative humidity (RH: 16 %); 23.5 Pa s at shear rate of 25 s^{-1}. Consequently, the high viscosity of the casting solution and the rapid start of the phase separation process were implied to

impede the polymer solution to get deep into the microstructure grooves to replicate the patterns' dimensions completely; it penetrates to about the half depth of the grooves. This interpretation was also reinforced by an estimated representation of a cross sectional profile of PES_PSμM membrane (see **Figure 4.28 (a)**), derived from AFM analysis. Furthermore, the volume reduction and the inherent shrinkage mechanisms during the polymer film precipitation upon immersion in the coagulation bath, NIPSμM, are also imagined to explain the resultant symmetric surface micro-patterns.

Conversely, in case of MIL, the flat PES membrane and the elastic PDMS mold are compressed together at high pressure and elevated temperature. Accordingly, the flat membrane undergoes an irreversible deformation in a parallel orientation to the mold features leading to an imprinting of the micro-patterns to the membrane surface. At the same time, PDMS mold itself undergoes an elastic deformation at the applied pressure and temperature (PDMS prepared from the same commercial precursors at same conditions had been found to have a compressive modulus of ~ 150 MPa at room temperature [274]). This could account for the observed shortening in the imprinted features' dimensions. Additionally, the depth of the patterned lines was found to be dependent on the experimental conditions. A representation of a cross sectional profile of PES_MIL supports is presented in **Figure 4.28 (b)**. These suggested combined effects are postulated to result in the obtained surface topography.

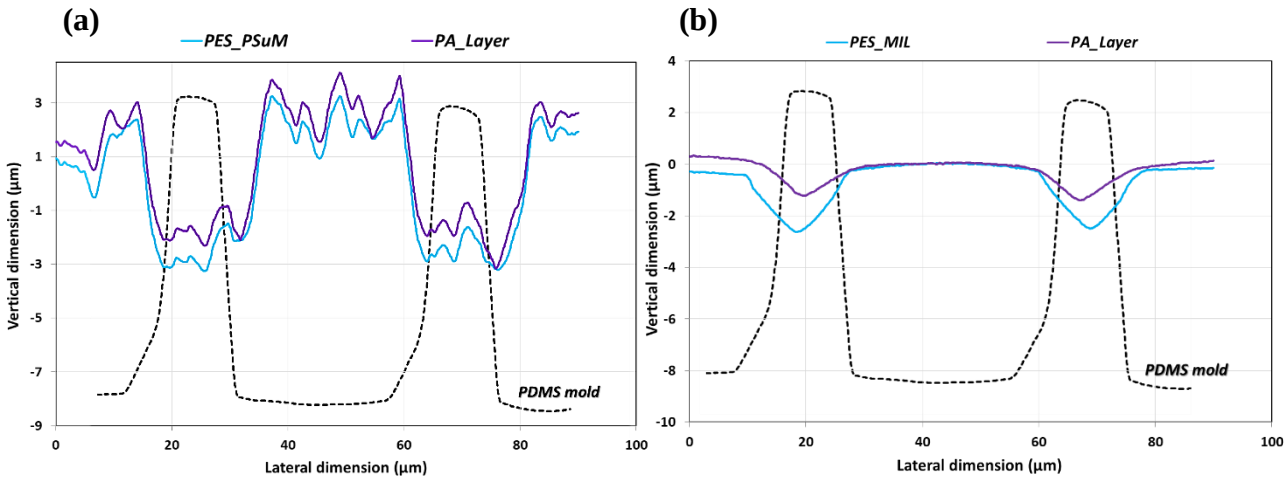

Figure 4.28: Cross sectional profiles derived from AFM analysis (cf. Figure 4.26) for the micro-patterned membranes prepared using PSμM (a) and MIL (b), before and after IP reaction, in comparison with data for the PDMS mold

4.2.4 Adaptation of PA synthesis atop micro-patterned PES supports toward high performance micro-patterned PA TFC membranes

It was a challenge to employ the developed micro-patterned PES membranes as supports for PA TFC membranes exhibiting high selectivity toward monovalent salt solutions. As discussed in **section 2.4.3**, some trials have already been reported in the literature using the common IP procedure introduced by Ghosh et al. [31]; however, none of them could achieve NaCl rejection more than 90 %. This was attributed to the intrinsic characteristics of the formed PA layer, e.g., film thickness, crosslinking density and defects. Here, this "typical method" was again investigated to prepare dense PA films on PES_PSµM and PES_MIL supports. The separation performance was evaluated employing dead-end filtration cell, using 2,000 ppm NaCl as a feed solution at operation pressure of 15 bar and under vigorous stirring, 700 rpm. The salt rejection and solution permeability results are presented in **Figure 4.29**.

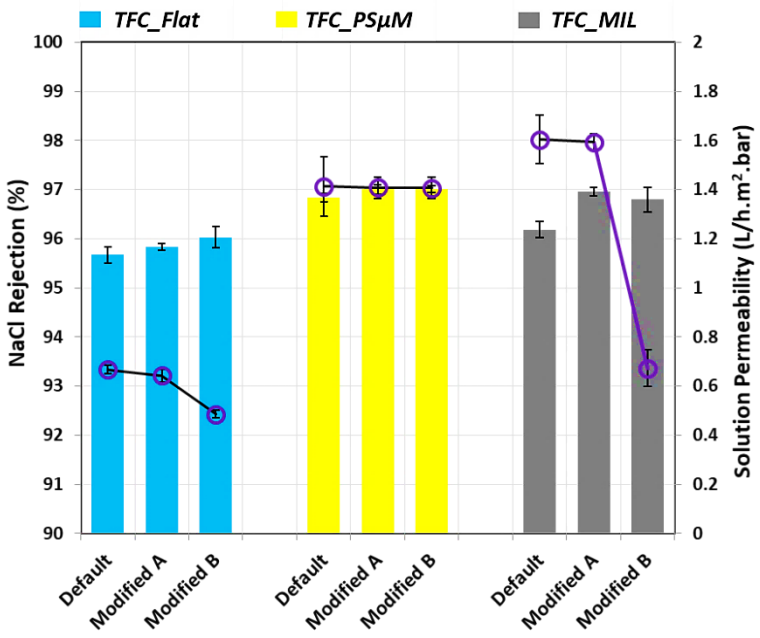

Figure 4.29: Separation performance during the adaptation of PA synthesis atop micro-patterned PES supports, measured using dead-end NaCl filtration experiments

A clear enhancement was observed in the permeability of the novel patterned TFC membranes without sacrificing the membrane selectivity. It increased from 0.7 L/h.m^2.bar in the case of TFC_Flat membrane to about 1.4 and 1.6 L/h.m^2.bar for TFC_PSµM and TFC_NIL membranes, respectively. Nevertheless, this "typical method" showed a bad reproducibility and poor control over the layer thickness required for high performance PA TFC membranes. These two problems were clearly noticed; in particular, for TFC_PSµM membranes, which might be due to the relatively wide pore size distribution of PES_PSµM support (cf. **section**

4.2.1, **Figure 4.22**), as well as its high surface area exposed to IP reaction in comparison with PES_MIL and PES_Flat.

Subsequently, two modified IP methods, (A) and (B), were proposed to eliminate these obstacles (cf. **section 3.4.4**). The modified IP procedures were based on the facts that the rate of IP reaction is diffusion controlled and increases with the reaction time as ~ $t^{0.5}$ [275], and that high initial amine monomer concentration always produces thin dense PA films with low porosity [48]. Modified method (A) was assumed to promote the imbibition of MPD through the support's patterned surface, while method (B) involved two consecutive IP steps, which should result in perfect coverage of the surface microstructures with a defect-free and dense PA layer.

As shown in **Figure 4.29**, method (A) was found to improve the salt rejection of TFC_MIL and reduce the fluctuation in permeability values. Moreover, the yield of micro-patterned TFC samples exhibiting high selectivity accompanied by high solution permeability was increased to be 60 % and 80 % for TFC_PSµM and TFC_MIL membranes, respectively. Conversely, method (B) also showed acceptable potential for the preparation of TFC_PSµM; despite of its inability to obtain high permeable TFC_MIL membranes. This might be explained by the extended patterned surface of PES_PSµM supports that needs more than one IP step to be totally covered with a dense PA layer. Consequently, method (A) was preferentially chosen as the best-suited procedure to prepare dense, selective and high permeable PA films atop the micro-patterned PES supports. Modified method (A) was accordingly employed to prepare all the micro-patterned and flat TFC PA membrane samples for all the subsequent characterization and performance tests.

The surface textural characteristics of the micro-patterned PA TFC membranes were extensively characterized using SEM and AFM to get more insights and relevant interpretations for the observed enhancement in the solution permeability without a detrimental influence on the membrane selectivity. SEM micrographs for surface micro-patterned TFC membranes at different magnifications are presented in **Figure 4.30**, AFM 3D images are shown in **Figure 4.26**.

It is explicit from SEM micrographs that the novel PA TFC membranes retained the surface microstructures after IP reaction, and, at higher magnifications, the PA nanostructure changes from simple "ridge and valley" morphology in TFC_Flat membrane to denser and more crumpled morphology that is full of protrusions in case of TFC_PSµM and TFC_MIL

membranes. Additionally, the thickness of PA layer was also estimated using SEM to be in the range of 120 and 100 nm for TFC_PSµM and TFC_MIL, respectively. Moreover, the estimated cross sectional profiles derived from AFM analysis are plotted in **Figure 4.28**.

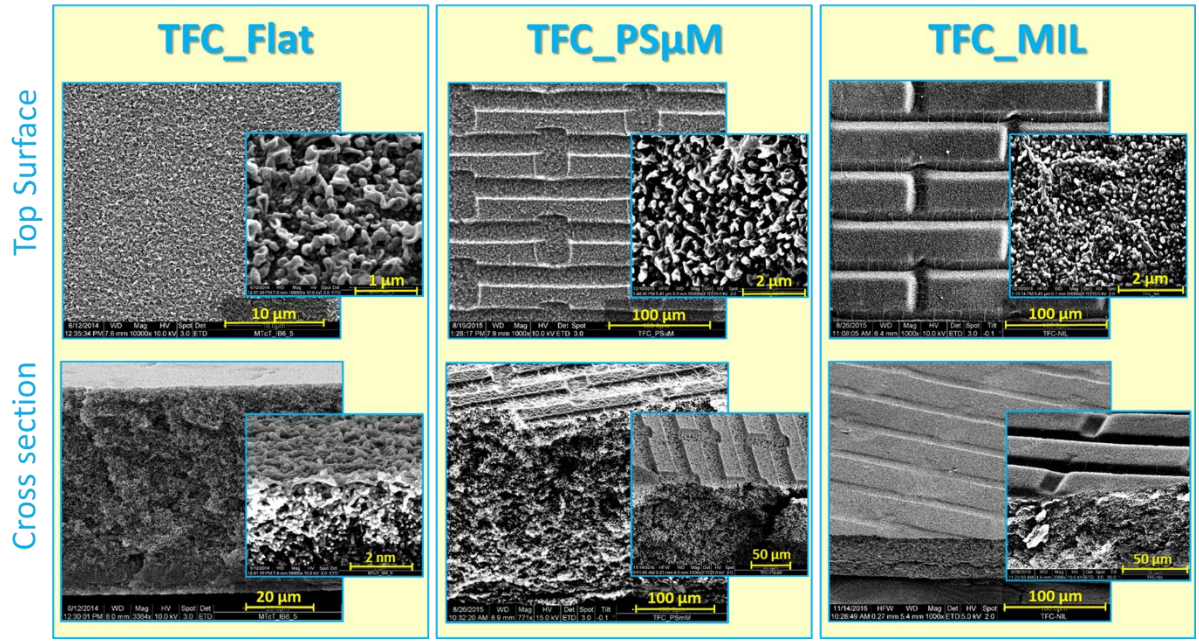

Figure 4.30: SEM micrographs for flat and micro-patterned PA TFC membranes, showing top surface and cross section morphologies at different magnifications

Table 4.7:Results of AFM surface analysis for PES supports and PA TFC membranes

	Typical 2D and 3D Roughness Parameters					
Membrane	**S_a a) [nm]**	**S_q b) [nm]**	**S_P c) [nm]**	**S_V d) [nm]**	**S_Z e) [nm]**	**$S_{kewness}$ f) [nm]**
PES_Flat	31.6	40.1	93.8	-256	350	--
TFC_Flat	16.3	20.0	58.5	-82.0	141	--
PES_PSµM	930	1166	2934	-3567	6501	-0.57
TFC_PSµM	492	598	1730	-1120	2850	0.70
PES_MIL	408	483	1254	-978	2232	0.29
TFC_MIL	276	319	788	-782	1569	0.22

a) Average roughness; b) Root mean square roughness; c) Maximum peak height; d) Maximum valley depth; e) Maximum height of the surface; f) Symmetry of surface data (cf. **section 3.6.4.2**)

Furthermore, a quantitative surface roughness analysis was numerically carried out by aid of AFM images and the roughness data are displayed in **Table 4.7**. The membrane active surface area was emphasized to be increased by a virtue of surface micro-patterning by ~ 70 % and ~ 40 % in the case of TFC_PSμM and TFC_MIL membranes, respectively. This significant development in the membrane surface area accessible for RO filtration process was implied to account for the high measured permeability of the micro-patterned TFC membranes [190, 276]. Additionally, the observed increase in the density of the surface crumpled protuberances as a result of preparation of PA on micro-patterned supports could also explain the increase of solution permeability of micro-patterned PA TFC membranes that was further reinforced by pure water permeability measurement using dead-end filtration cell, cf. **Figure 4.31**. Various theories interpreting the high permeability due to the unique PA morphology have already been discussed in **section 2.3.3.3**. In parallel, the membrane surface roughness, expressed by root mean square roughness, S_q, showed a substantial development in the microscale surface roughness upon the micro-patterning, which, in couple with the nanoscale roughness, led to an enhancement in the total membrane surface roughness values as seen in **Table 4.7**. It is worth mentioning that the upgrading in the membrane surface roughness could essentially promote the permeability of the micro-patterned PA TFC membranes [276, 277].

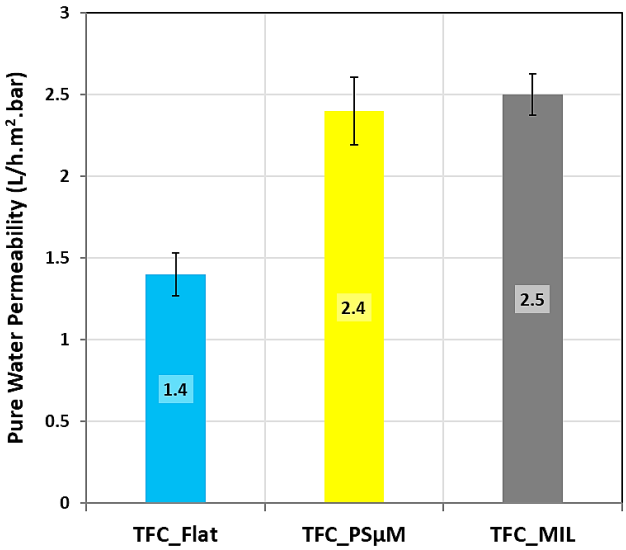

Figure 4.31: Pure water permeability values measured using dead-end configuration for micro-patterned PA TFC membranes versus flat membranes, all prepared using modified method (A)

In addition, the change in solution permeability for the micro-patterned PA TFC membranes was measured for almost 6 h of filtration of 2,000 ppm NaCl solution using dead-end filtration cell at operating pressure of 15 bar and under vigorous stirring. The graphs are presented in

Figure 4.32. TFC_MIL and TFC_PSµM membranes exhibited decline in solution permeability of ~ 10.5 % and ~ 21 %, respectively, in comparison with a permeability decline of ~ 28 % in case of TFC_Flat membranes. TFC_MIL was expected to show such stable behavior because it was already used in its compacted form, considering the compression action occurred during the MIL process. Nevertheless, surface microstructures seemed to offer relatively better stability against compression and enhanced workability for the new micro-patterned TFC membranes under the experiment conditions.

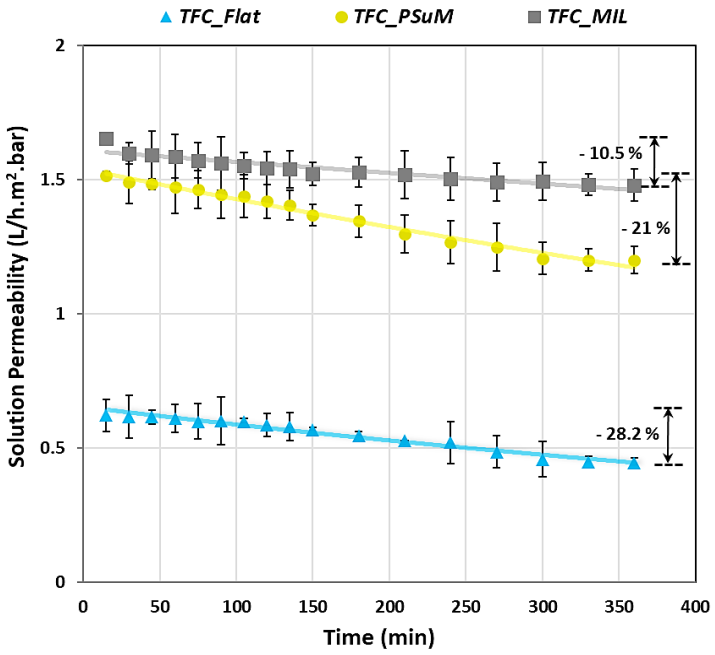

Figure 4.32: The change in solution permeability for micro-patterned PA TFC membranes versus flat membrane during 6 hours of dead-end filtration of 2,000 ppm NaCl solution at operating pressure of 15 bar under vigorous stirring

Furthermore, the micro-patterned PA TFC membranes were chemically characterized using ATR-FTIR spectroscopy and zeta potential analysis; the graphs are shown in **Figure 4.33** and **Figure 4.34**, respectively. The formation of PA layer was confirmed by the two characteristic peaks at ~1730 and ~1623 cm^{-1}, assigned to C=O stretching in pendent carboxylic acid groups and amide (II) groups, respectively. A peak attributed to S=O stretching in a sulfonic acid group was also detected at ~1040 cm^{-1}, essentially because of the incorporation of CSA as an additive during IP reaction. In addition, from the zeta potential results, the apparent zeta potential was observed to be influenced by the membrane surface topography such that ζ-potential decreased in the following order: TFC_Flat > TFC_MIL > TFC_PSµM. One possible explanation is that, in spite of the same surface chemistry, the increasing in membrane surface roughness as a consequence of the surface micro-patterning was reported to create geometry-induced changes

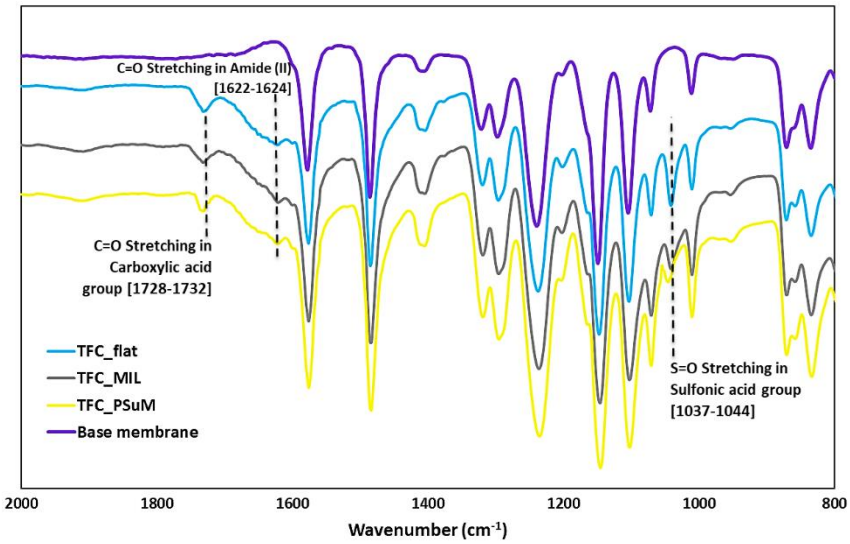

Figure 4.33: ATR-FTIR spectra for micro-patterned and flat PA TFC membranes

that influence the electro-osmotic flow and enhance the surface conductivity caused by the surface negatively groups ($-SO^{3-}$, $-COO^{-}$) [278], which increases the conduction current opposed to the streaming current, hence it decreases the magnitude of the streaming potential [279]. Another possible interpretation is the positioning of the shear plane atop the apex regions of the membrane surface patterns; consequently, the surface charge at the valley/lower regions of the surface patterns were not considered/accessible during zeta-potential measurement, leading to a lower streaming potential in comparison with TFC_Flat membranes.

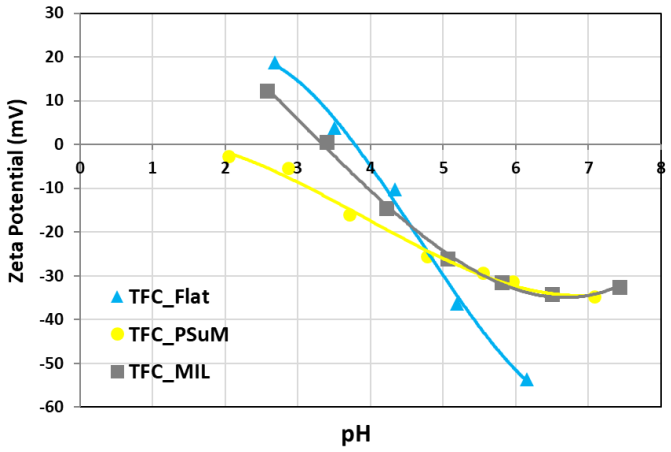

Figure 4.34: Zeta potential as function of pH value for micro-patterned and flat PA TFC membranes

Moreover, the improvement in the membrane hydrophilicity upon the surface micro-patterning was affirmed, as well. The static water contact angles measured by captive bubble method were 30 ± 6.5° and 31 ± 3.4° for TFC_PSµM and TFC_MIL membranes, respectively, versus 43 ± 5.3° in the case of TFC_Flat membrane. This improvement in the membrane

surface wettability is mainly interpreted by the development in the membrane surface roughness as a result of micro-patterning, which fits well with Wenzel model (cf. **section 2.6.1.2**).

4.2.5 Assessment of separation performance using cross-flow configuration at different feed concentrations and estimation of concentration polarization parameters

The separation performance of micro-patterned PA TFC membranes was additionally investigated via so-called "directional" cross-flow filtration experiments using different feed concentrations. "Directional" experiments refer to the direction of the replicated surface microstructures with regard to the direction of feed flow onto the membrane surface. The micro-patterned PA TFC membranes were installed in the cross-flow cell at two different orientations, i.e. with long micro-channels "parallel" and "perpendicular" to the direction of feed flow (**Figure 4.35 (b)**).

First, the pure water permeability of the micro-patterned and flat PA TFC membranes was measured at different applied pressure values and the results are plotted (**Figure 4.35 (a)**). The micro-patterned membranes exhibited superior water permeability compared to the flat membranes as a result of the development of specific surface characteristics upon the surface micro-patterning (cf. **section 4.2.3**). Nevertheless, no significant variation was noticed in the pure water permeability values upon changing the membrane orientation.

Afterward, the directional NaCl filtration experiments were conducted using two different NaCl feed concentrations; 2,000 and 10,000 ppm (**Figure 4.35 (c – f)**). The results were analyzed using the boundary layer film model (cf. **section 2.3.3.4**; **Equation 6**), and the main concentration polarization parameters were estimated (cf. **Table 4.8**, **Figure 4.36**, **Figure 4.37**). It should be noted that using the film model was only an attempt to provide a more quantitative analysis of the observed phenomena; the validity of this model is clearly limited since all experiments were performed under conditions of turbulent flow in the channel above the membrane surface (Re = 7300; cf. **section 3.7.2.2**).

In general, the micro-patterned membranes exhibited an explicit improvement in the solution permeability accompanied by a high salt rejection (> 96 % at 2,000 ppm feed), in comparison with TFC_Flat membranes. Nevertheless, the impact of variation of NaCl feed concentration is the key to understanding the behavior of the tested membranes.

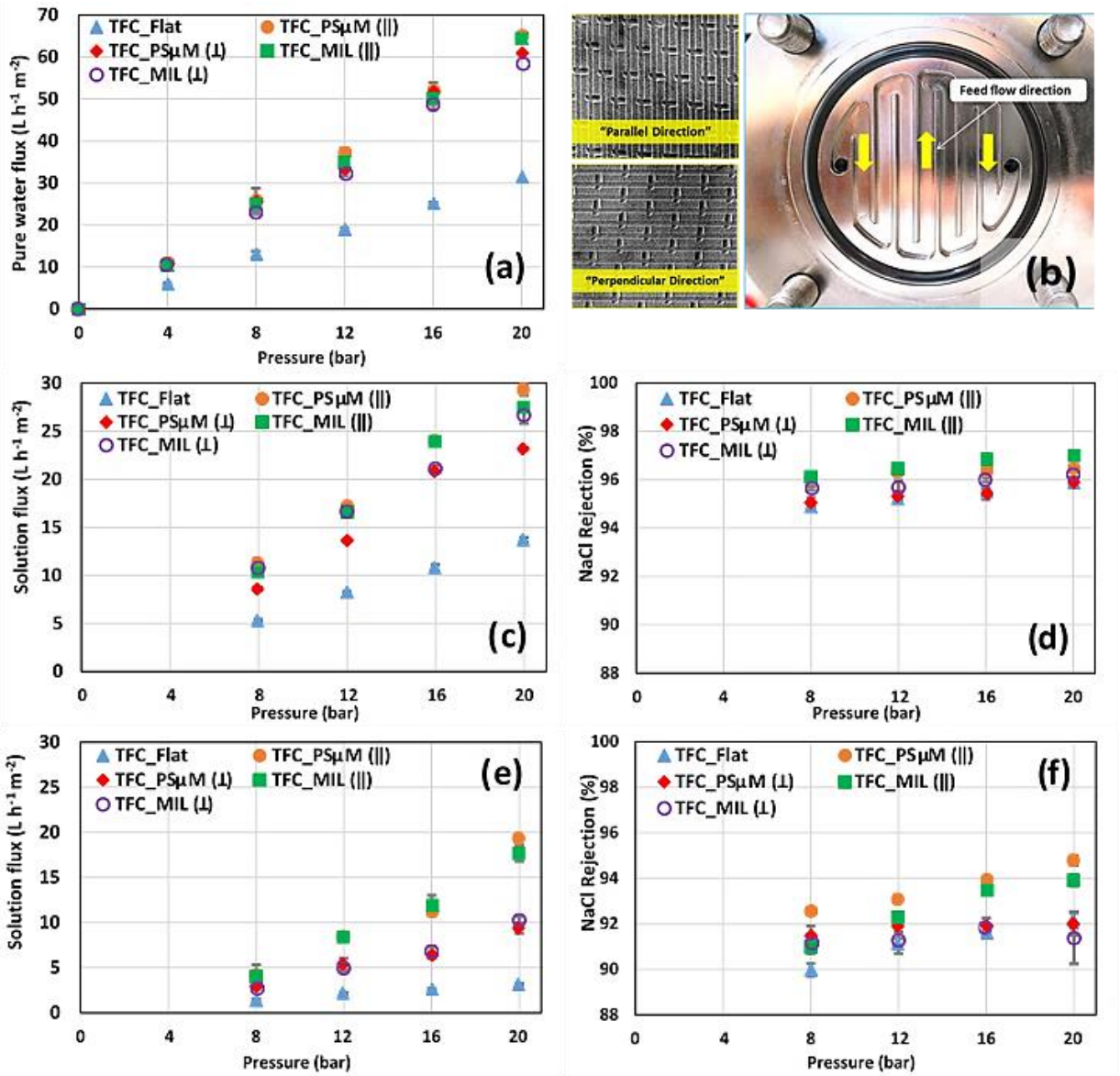

Figure 4.35: Results for pure water permeability measurements (a), and separation performance for TFC_PSμM and TFC_MIL versus TFC_Flat using 2,000 ppm (c, d) and 10,000 ppm (e, f) NaCl feeds at different membrane orientations as seen in (b), "parallel (||)" and "perpendicular (⊥)" to direction of feed flow, using cross-flow filtration configuration

At low NaCl feed concentration, a small distinction in the separation performance was observed between TFC_MIL and TFC_PSμM membranes. The higher rejection of TFC_MIL membranes indicates the tighter PA films that were formed as a result of its shallow surface features (cf. **Figure 4.30**). Moreover, the membrane orientation was emphasized to influence the separation performance to some extent; the one in a parallel orientation to the feed cross-flow was always better than that in a perpendicular orientation. The micro-patterns in a parallel orientation are implied to stabilize the liquid streamlines, equilibrate the shear stress and promote feed circulation over the entire membrane surface area [27, 191]. Conversely, the

micro-patterns in a perpendicular orientation are proposed to work as hold-backs that disturb the feed streaming over the membrane surface, and create regions of different shear stresses (cf. **section 2.4.2.3**). A vortex has been reported to be formed in the valley/lower regions (pattern's grooves) where the shear stress is found to be low, depending on the linear cross-flow velocity [27]. This could result in a partial accumulation of the solute species within the surface grooves causing a reduction in both the solution permeability and the salt rejection.

Table 4.8: Values for boundary layer thickness and measured salt rejection for cross-flow filtration experiments using 2,000 and 10,000 ppm NaCl feed solutions

	Measurement at 2,000 ppm NaCl		Measurement at 10,000 ppm NaCl	
Membrane	**$R_{measured}$ a) [%]**	**δ b) [µm]**	**$R_{measured}$ [%]**	**δ [µm]**
TFC_Flat	95.5 ± 0.08	39	91.6 ± 0.08	353
TFC_PSµM (∥)	96.4 ± 0.18	22	94.0 ± 0.07	50
TFC_PSµM (⊥)	95.4 ± 0.25	38	92.0 ± 0.02	197
TFC_MIL (∥)	96.8 ± 0.23	25	93.5 ± 0.18	74
TFC_MIL (⊥)	96.2 ± 0.09	30	91.9 ± 0.42	104

a) Measured salt rejection at operating pressure of 16 bar; b) Boundary layer thickness estimated by plotting the linear form of the film model (cf. **Equation 29**).

The outputs of the concentration polarization studies supported these hypotheses. The boundary layer thickness, δ, values for micro-patterned PA TFC membranes at the parallel orientation were always lower than those in the case of a perpendicular orientation (cf. **Table 4.8**). Nevertheless, the values for the concentration polarization modulus, *C.P.M.*, for all the tested membranes at both orientations using 2,000 ppm NaCl feed were lower than 1.14, which indicates the limited influence of the concentration polarization phenomena at low feed concentration (cf. **Figure 4.36**) [12]. Another interesting observation was that the values of δ and *C.P.M* at parallel orientation were always lower in case of TFC_PSµM than TFC_MIL, which affirms clearly the positive impact of more pronounced surface micro-patterns on the membrane performance. The latter observation was highlighted upon using of a higher NaCl feed concentration, 10,000 ppm. TFC_PSµM was found to exhibit relatively higher solution permeability and salt rejection than TFC_MIL; however, in general, both membranes showed much better performance than TFC_Flat. This implies that the influence of surface micro-patterning approach on modifying the extrinsic properties of PA layer is the predominant phenomenon rather than the discrepancies in the intrinsic properties of the barrier layer itself.

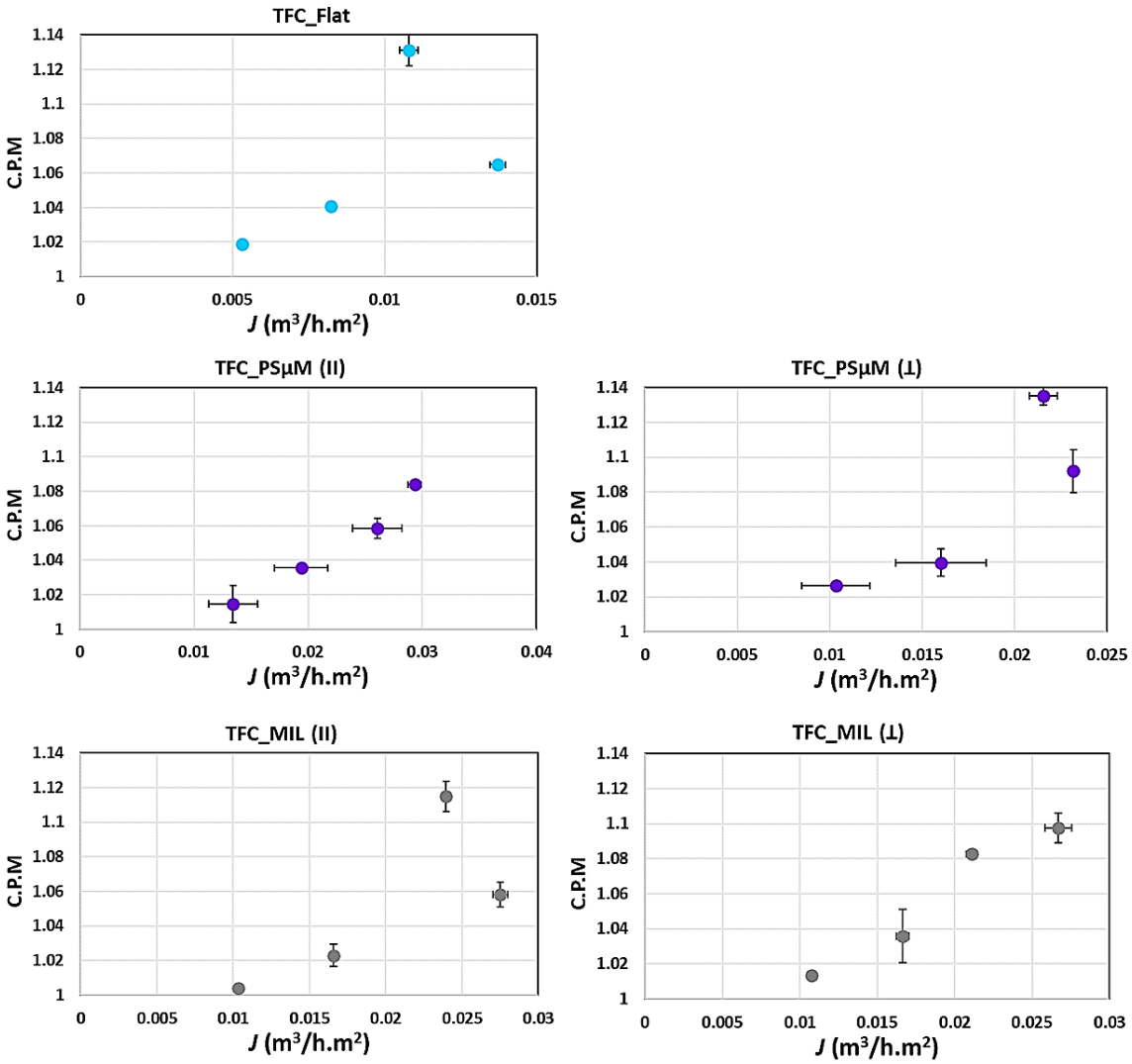

Figure 4.36: Concentration polarization modulus as a function of solution flux for cross-flow filtration experiments using 2,000 ppm NaCl feed solution

Furthermore, the consequences of the membrane orientation on the separation performance were more illustrated at high NaCl feed concentration; such that lower permeability and salt rejection were observed for the micro-patterned membranes that were employed in a perpendicular orientation. This is in congruence with the higher δ values that were estimated for TFC_MIL and TFC_PSµM, ~100 and ~200 µm, respectively in a perpendicular orientation, which are still much lower than δ in case of TFC_Flat membranes. Additionally, all the membranes exhibited higher *C.P.M* than those in case of lower feed concentration (cf. **Figure 4.37**); however, the results showed consistent trend with respect to the increasing in solution flux than in case of 2,000 ppm NaCl feed. In parallel, the concentration polarization curves for 10,000 ppm are displayed in **Figure 4.38**. The concentration polarization results at different operating pressure values showed a very good fitting (high R^2 values) for the micro-patterned membranes in both orientations while the correlation was relatively poor for the flat

membranes. This might be also related to the fact that all the concentration polarization experiments were carried out at turbulent flow conditions in a macroscopic channel above the membrane. Those conditions aren't in line with the assumptions of the boundary layer (film) model.

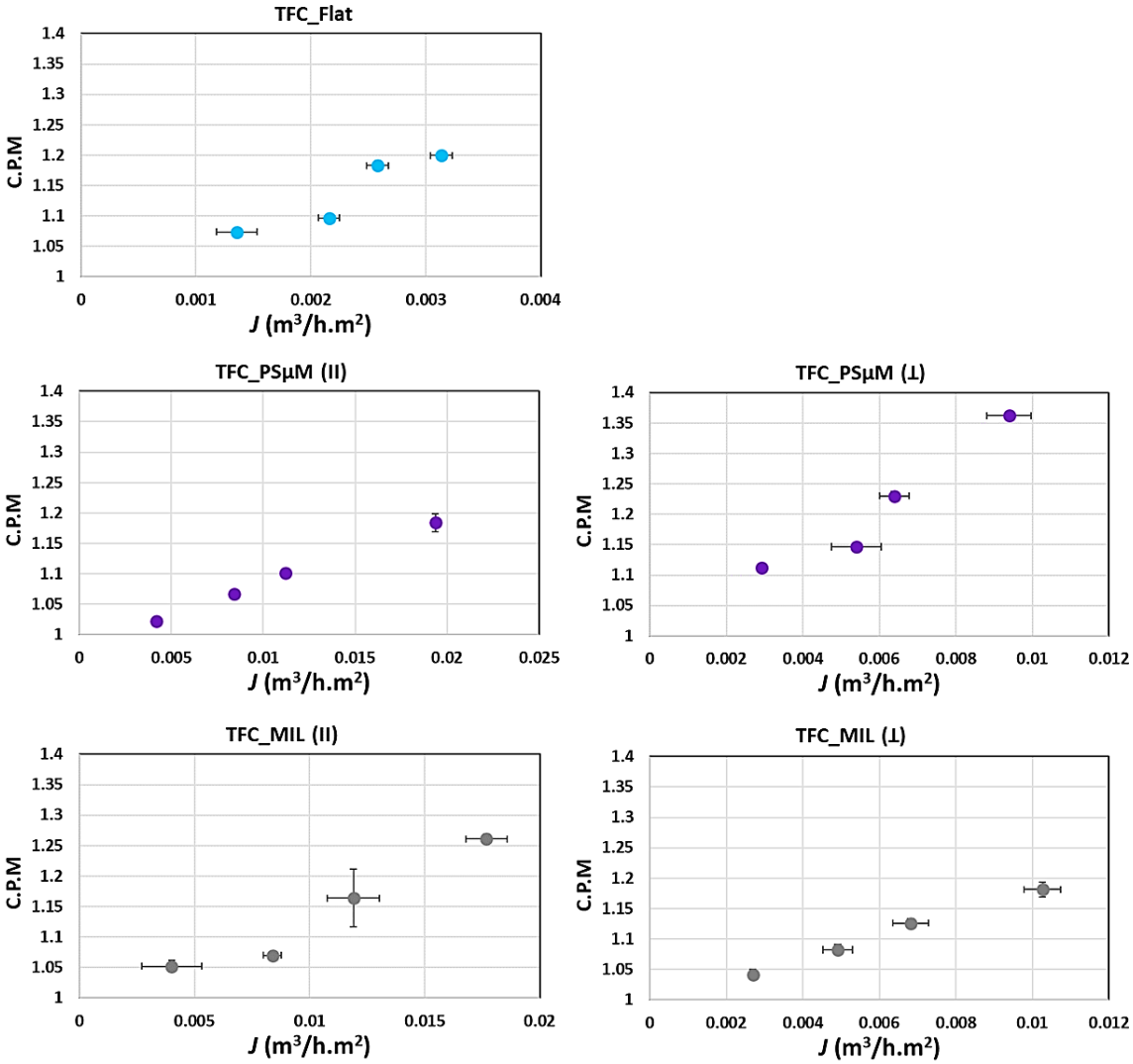

Figure 4.37: Concentration polarization modulus as a function of solution flux for cross-flow filtration experiments using 10,000 ppm NaCl feed solution

According to these findings, the newly developed surface micro-patterned PA TFC membranes are emphasized to be promising candidates toward efficient water desalination membranes with a superior separation performance. In conclusion, the development of novel surface micro-patterned PA TFC membranes has been comprehensively presented in **sections 4.1** and **4.2**, in terms of refinement of preparation procedures, evaluation of separation performance, and investigation of the influence on main the concentration polarization parameters. Later, in the forthcoming sections, surface modification trials toward the

development of PA TFC membranes with "super-switching" wettability surfaces will be introduced. Afterward, preliminary investigation of the impact of such smart surfaces on the particle fouling propensity of micro-patterned PA TFC membranes will be demonstrated.

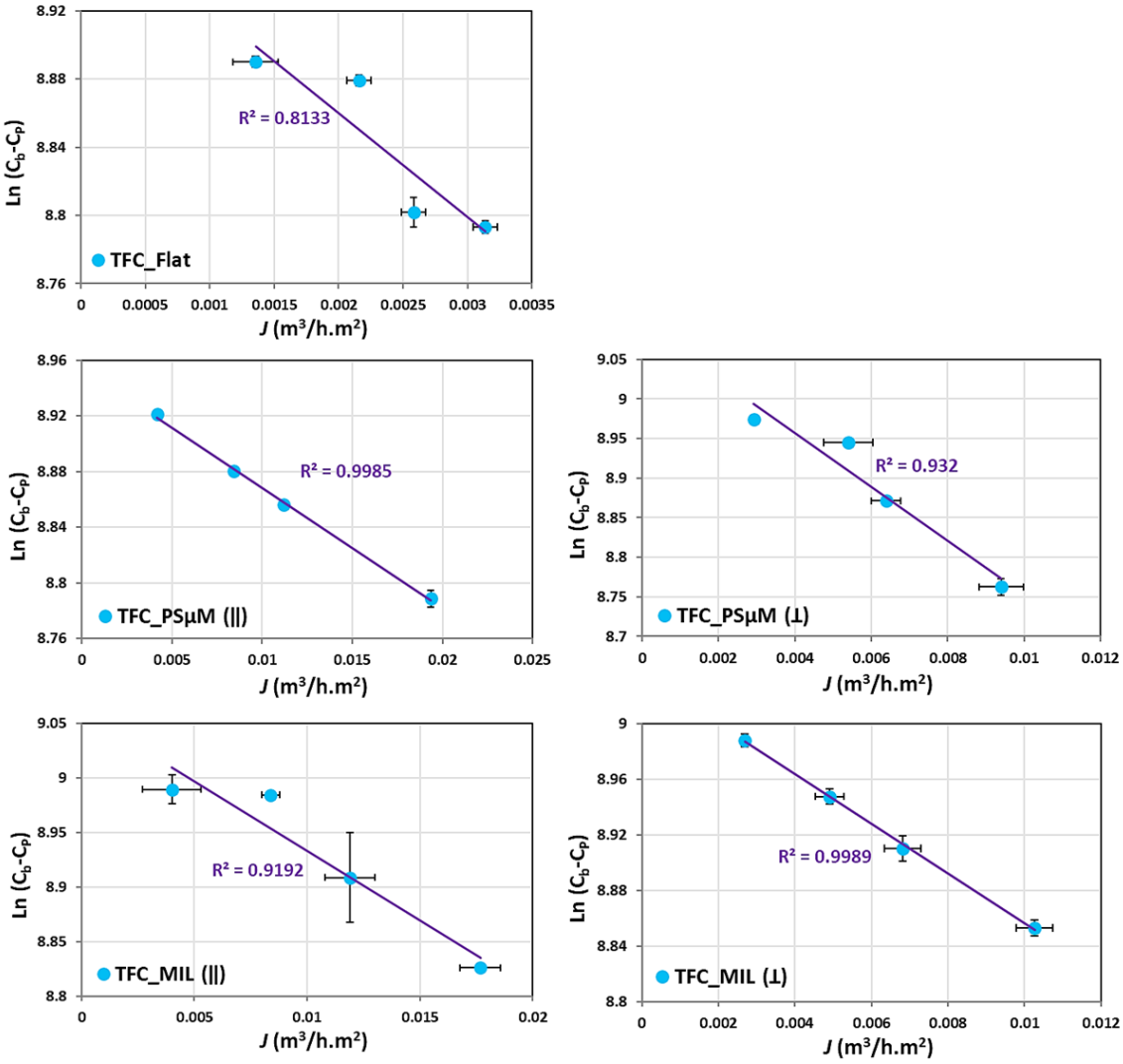

Figure 4.38: Concentration polarization curves for cross-flow filtration experiments using 10,000 ppm NaCl feed solution

4.3 Surface modification of micro-patterned PA TFC membranes toward membranes of super-switching wettability

The exploitation of super-switching wettability approach in developing novel water desalination membranes exhibiting smart surface characteristics is considered as a new interesting trend. To the best of our knowledge, the development of PA TFC membranes that are able to switch reversibly between strong hydrophilicity and strong hydrophobicity is introduced here for the first time. Nevertheless, the concept of how to obtain such smart surfaces has already been presented, and some experimental trials have been reported using silicon-based materials (cf. **section 2.6.3**).

In principle, the super-switching properties can be specifically adapted to water desalination membranes via consolidating two different phenomena; "surface micro-patterning" and "double stimuli-responsivity". Subsequently, an additional thin layer of P(NIPAAm-co-AAc) was suggested to be synthesized atop the developed surface micro-patterned PA TFC membranes. However, this additional layer and the employed synthesis procedures shouldn't have a detrimental impact on either the permeability or the membrane selectivity, which are the major functions of PA TFC membranes.

4.3.1 Qualitative determination of dominant membrane surface charge and the design of the surface modification experiments

Prior to design the surface modification experiments, a complete imaging for the surface chemistry of PA TFC membranes was required. In addition to the aforementioned characterizations of flat and micro-patterned PA TFC membranes (cf. **section 4.2.4**), an additional analysis for the dominant surface charge was performed by measuring the membrane selectivity toward different salt solutions, NaCl, Na_2SO_4 and $CaCl_2$, 2,000 ppm each, and using dead-end filtration cell. The separation performance results are displayed in **Figure 4.39**. Both the micro-patterned and the flat PA TFC membranes showed the same trend regarding the rejection of the different salts; such that the rejection followed the order: Na_2SO_4 > NaCl > $CaCl_2$. Consequently, the membranes were concluded to exhibit dominant surface negative charges that could preferentially permeate Ca^{2+} rather than Na^+ ions, and conversely, show a higher tendency to reject SO_4^{2-} ions. These surface negative charges can essentially be attributed to the surface sulfonic and carboxylic groups that had been affirmed using ATR-FTIR spectra (cf. **Figure 4.33**) and supported by ζ-potential results (**Figure 4.34**). This is also

in congruence with considerable reported work which revealed that most of PA TFC membranes exhibit negative surface charge at normal environmental pH ranges.

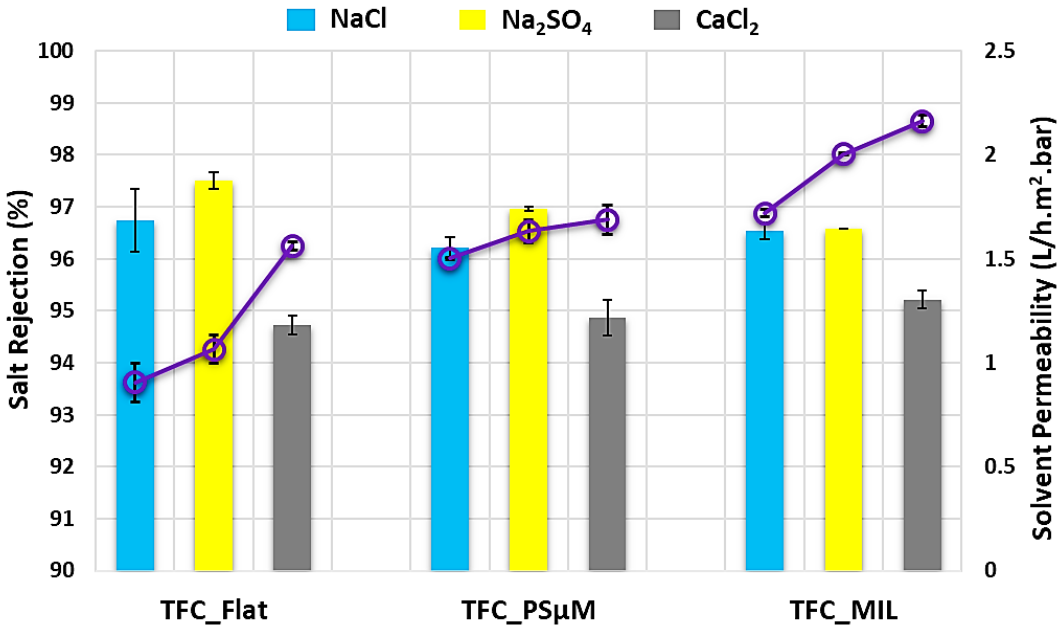

Figure 4.39: Separation performance for flat and micro-patterned PA TFC membranes measured by dead-end filtration of different salts

Subsequently, numerous experiments were designed to investigate the best-suited surface modification procedure for the developed micro-patterned PA TFC membranes. PA TFC membranes were modified using SI-ATRP, and in-situ surface coating via carbodiimide coupling chemistry, as examples for "*grafting from*" and "*grafting to*" methods, respectively. The unreacted amine groups were implied as possible reactive sites for both methods.

In the following subsections, experimental trials have been briefly reported to find out the most proper conditions for modifying micro-patterned PA TFC membranes via SI-ATRP without sacrificing the stability of PA selective layer. Afterward, more comprehensive adaptation, characterization and evaluation experiments were performed for modifying micro-patterned PA TFC membranes using in-situ surface coating method, which showed more potential toward high through-put and chemical-friendly surface modification procedure as well as its ability for scaling up.

4.3.2 Surface modification of micro-patterned PA TFC membranes using SI-ATRP

Many working groups have reported on the surface modification of commercial PA TFC NF and RO membranes using ATRP method; however, to the best of our knowledge, no previous trials have been reported on employing of ATRP method to modify synthetic, i.e., lab-made, PA TFC membranes. The big challenge of this approach is how to control the progression of

ATRP reaction and the polymer layer thickness without a detrimental influence on the membrane selectivity. Such crucial problem wasn't previously recognized because of the well-optimized manufacturing process and some protective coatings that were known to be used for some commercial membranes. Even though better controlled growth of the polymer layer was reported to be possible by using solvent mixtures including dimethyl formamide, toluene … etc.; such solvent mixtures were revealed to be less tolerant to PA barrier layer and membrane support (cf. **section 2.5.2.1.1**). Subsequently, only water-based solvent mixtures are relevant to be utilized. On the other hand, a rapid increase in the polymer layer thickness was reported in case of water-based ATRP reaction. Therefore, a refinement for the conditions of the initiator immobilization step and SI-ATRP reaction is highly required to find out the best-suited procedures.

4.3.2.1 Adaptation of the initiator immobilization step

Many preliminary experiments were carried out and it was found that the major damage of the PA TFC membranes is often occurred during the initiator immobilization step. Accordingly, more attention was devoted to the initiator immobilization step in order to attain well immobilization degree with the lowest possible impact on the membrane selectivity. Four different procedures were investigated for the initiator immobilization step (cf. **section 3.5.2.1**). Flat PA TFC membranes were exploited during the adaptation experiments, thereafter the best-suited conditions were applied to the micro-patterned counterparts. Because the well immobilization degree is strongly dependent on the reactivity of PA layer toward 2-bromoisobutyryl bromide (BMPB), the surface chemistry of PA TFC membranes were intensively studied. Earlier studies were reported to follow specific pretreatment methods to hydrophilize the surface of PA TFC membranes and create reactive primary amine groups to be furtherly reacted with BMPB via partial dissolution mechanism using an aqueous mixture comprising alcohols and protic acids [223, 237]. This method was found to be effective for hydrophilization of commercial PA TFC membranes; however, it was emphasized to be aggressive toward flat PA TFC membranes developed in this study. This could be due to the instability of PA layer, instability of PES support, dissolution of PVP incorporated in supports' matrix, or absence of any protecting layer as in case of commercial membranes.

As a result, in this work, the flat PA TFC membranes were directly reacted with BMPB as in adaptation experiments I.I.1, I.I.2 and I.I.3 (cf. **Figure 4.40**). In these experiments, high portions of BMPB were used. The unreacted amine groups along the PA chain were expected as potential reactive sites. Additionally, TEA was also used in different ratios, in comparison with BMPB, to neutralize the liberated acid during the initiator immobilization reaction. Alternatively, experiment I.I.4 was based on pre-immobilization of reactive amine groups via a stable amide bond with the pendent surface carboxylic groups existing on PA TFC membrane surface using carbodiimide crosslinking, then BMPB was immobilized in a later step. The separation performance was then evaluated for BMPB-immobilized PA TFC membranes using dead-end filtration experiments of different feed solutions, NaCl, Na_2SO_4 and $CaCl_2$, 2,000 ppm each, to investigate the stability of PA layer after the immobilization reaction.

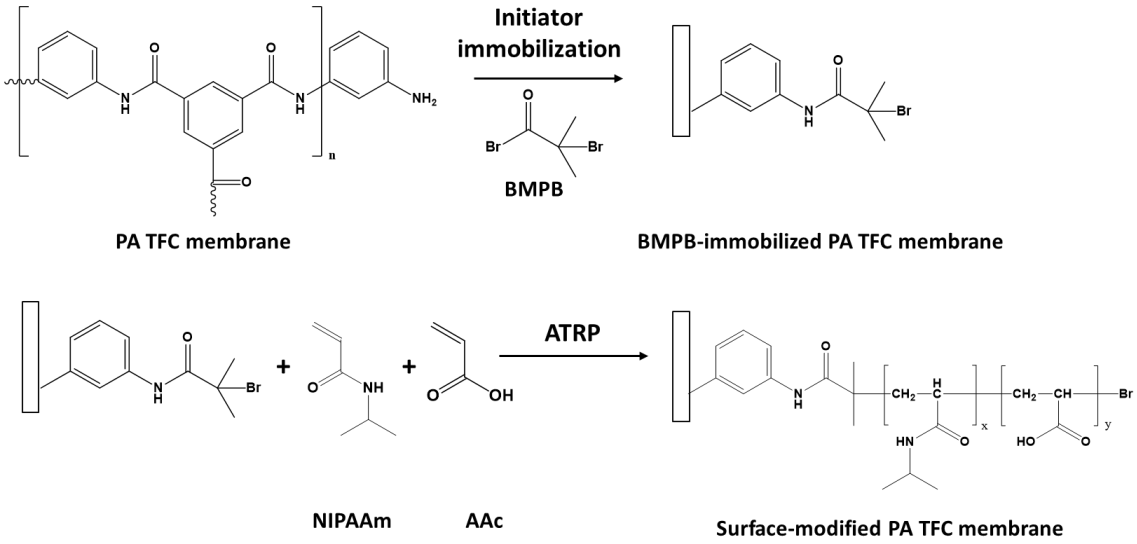

Figure 4.40: Mechanistic steps for surface modification of PA TFC membranes using SI-ATRP

Generally, PA TFC membranes, i.e., PA + PES supports, showed quite different stability towards the adaptation experiments. BMPB-immobilized PA TFC membranes prepared by experiments I.I.1 and I.I.4 were apparently stable to be further used, whereas the membranes modified by experiments I.I.2 and I.I.3 were observed to suffer from explicit damage as illustrated in **Figure 4.41**. One possible explanation could be the lower amounts of TEA used in these two experiments, i.e., I.I.2 and I.I.3, which is implied to be insufficient to neutralize all the liberated acid that was assumed to be responsible for this acute damage. Consequently, experiments I.I.2 and I.I.3 were excluded from further investigations. It is worth to note that these later two initiator immobilization procedures are usually used for modification of different commercial PA TFC membranes [122, 223], which reinforces strongly the claim

regarding how challenging to exploit the reported conditions for the tailor-made PA TFC membranes.

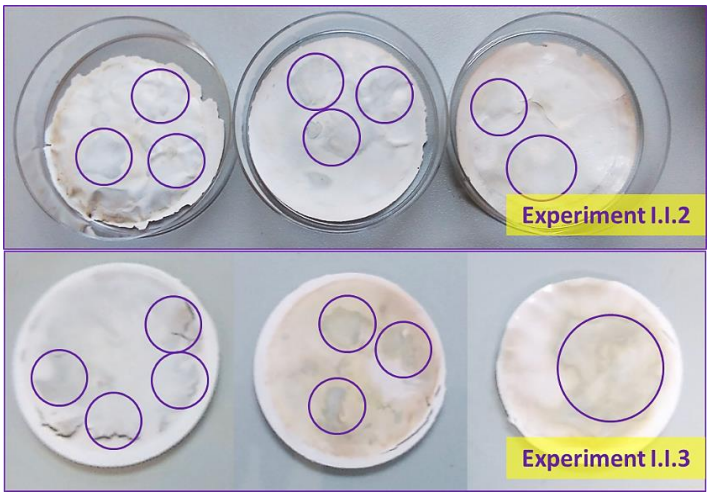

Figure 4.41: Illustration for the observed distortion upon modifying PA TFC membranes by experiment I.I.2 and I.I.3

In addition, the static water contact angle was measured for BMPB-immobilized PA TFC membranes using sessile drop method. An increase in the water contact was observed as an indication for the successful immobilization of BMPB atop flat PA TFC membranes; such that the contact angle increased from ~ 43 ± 5° in case of pristine flat PA TFC membrane to ~ 63.6 ± 5° and ~ 60 ± 4° in case of modified flat membranes using experiments I.I.1 and I.I.4, respectively.

Moreover, the separation performance for BMPB-immobilized PA TFC membranes modified by experiments I.I.1 and I.I.4 was investigated and presented in **Figure 4.42**. The modified membranes using experiment I.I.1 were observed to keep the membrane selectivity. They exhibited the best rejection behavior, 97 % for NaCl and 96.8 % for Na_2SO_4. In parallel, an improvement of the solution permeability was also noticed for the modified membranes by experiment I.I.1. This might be interpreted by a possible partial dissolution of the dense PA layer either by the reactants or the cleaning procedure afterward; interestingly, this wasn't found to impair the membrane selectivity. Similar observation was reported for commercial PA TFC membranes using specific hydrophilizing agents, as discussed before [237]. In parallel, the modification experiment I.I.4 also showed a promising potential as an alternative method to be furtherly investigated and optimized in future work. Nevertheless, the modification experiments I.I.1 was preferentially chosen as the best-suited procedure for the initiator immobilization step.

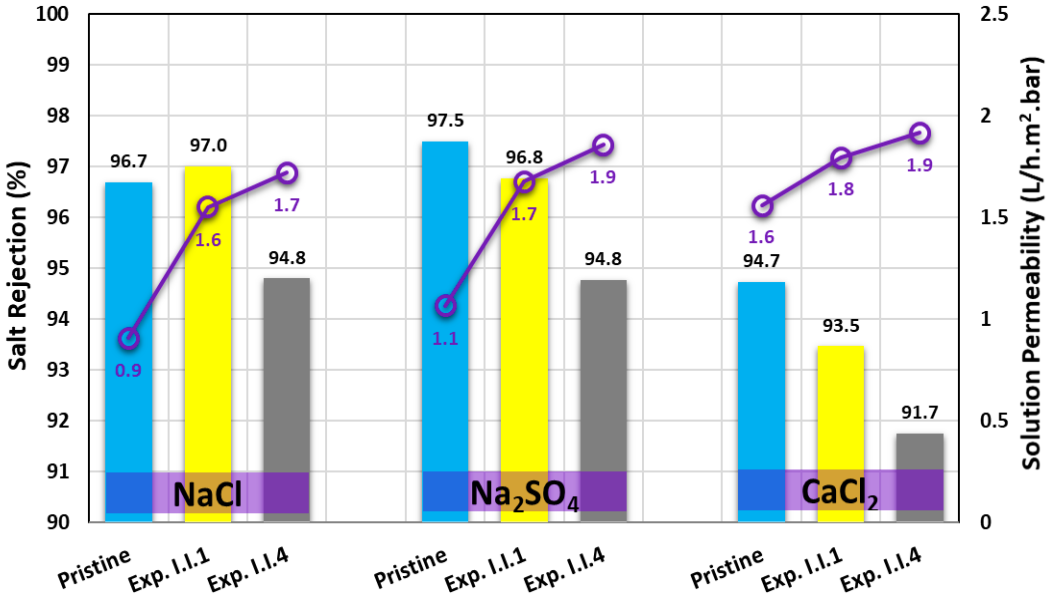

Figure 4.42: Separation performance for BMPB-immobilized PA TFC membranes using experiments I.I.1 and I.I.4 measured by dead-end filtration of different salts

4.3.2.2 Grafting of P(NIPAAm-co-AAc) from micro-patterned PA TFC membranes using SI-ATRP

Here, the preliminary results for the surface modification of micro-patterned PA TFC membranes using SI-ATRP are briefly introduced. BMPB was firstly immobilized onto the surface of TFC_Flat, TFC_PSμM and TFC_MIL membranes using modification experiment I.I.1. Thereafter, P(NIPAAm-co-AAc) copolymer comprising 3 mol.% AAc was grafted from BMPB-immobilized flat and micro-patterned PA TFC membranes by means of SI-ATRP method using specific reaction conditions adapted from [29]. Afterward, the resultant membranes were selectively characterized in regard with grafting degree, membrane morphology and separation performance.

In comparison with surface-modified flat PA TFC membranes, the surface modified micro-patterned PA TFC membranes exhibited a pretty high degree of grafting. In addition, the washing procedures had to be extended to wash out all the visible non-adherent copolymer films. After 1 h of washing followed by drying overnight under vacuum, the grafting degree was measured for surface modified TFC_PSμM and TFC_MIL membranes to be ~14 ± 1.5 and ~ 4.3 ± 0.8 mg/cm^2, respectively, while grafting degree was about 0.2 mg/cm^2 in case of surface modified TFC_flat. This very high grafting degree estimated for surface modified micro-patterned membranes was additionally supported by SEM analysis (cf. **Figure 4.43**).

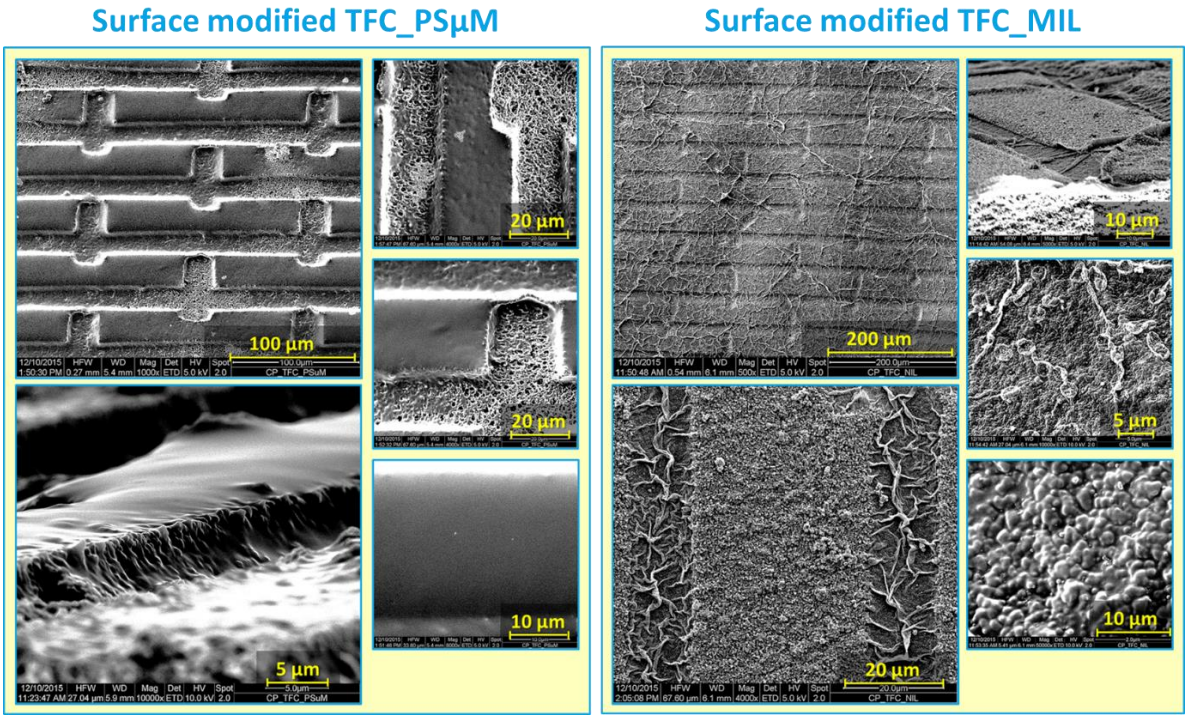

Figure 4.43: SEM micrographs for top surface morphology of surface-modified micro-patterned PA TFC membranes at different magnifications

SEM micrographs for the top surface morphology revealed the grafting of P(NIPAAm-co-3.5mol%AAc) from initiator-modified micro-patterned membranes with a quite high yield. Furthermore, the grafting density was emphasized to be heterogonous; the whole apex regions, including the previously observed crumpled PA morphology, were fully covered with the copolymer, whereas the valleys, i.e., pattern grooves, were not completely coated with the copolymer. Generally, uncontrolled polymer growth and rapid increase in polymer layer thickness were reported as common characteristics for water-based ATRP synthesis of acrylamide polymer coatings [223, 280, 281]. However, the uneven grafting of the copolymer from the surface of initiator-immobilized micro-patterned membranes has raised a controversy regarding the feasibility of the current procedure to be employed for surface modification of micro-patterned membranes. The range of the surface patterns and the aspect ratio, besides the homogeneity/efficiency of the initiator immobilization are proposed to be the key solutions to treat the aforementioned obstacles.

The separation performance for the surface modified micro-patterned PA TFC membranes was also investigated by dead-end filtration experiments of 2,000 ppm NaCl solution and the results are presented in **Figure 4.44**. In general, a loss in the membrane selectivity was observed after the surface modification using SI-ATRP in comparison with the pristine membrane. This could also be attributed to utilizing of less tolerate solvents, especially for cleaning, besides

any aggressive byproducts, e.g., hydrogen halides. Nevertheless, the solution permeability was found to decrease than BMPB-immobilized membranes that is basically explained by the increase in the hydraulic resistance because of the high grafting degree. Moreover, the solution permeability for surface modified membranes was also revealed to be higher than pristine membranes which is not compatible with the measured high grafting degree. This observation reflects the detrimental influence of the employed procedures on the density and the stability of PA layer.

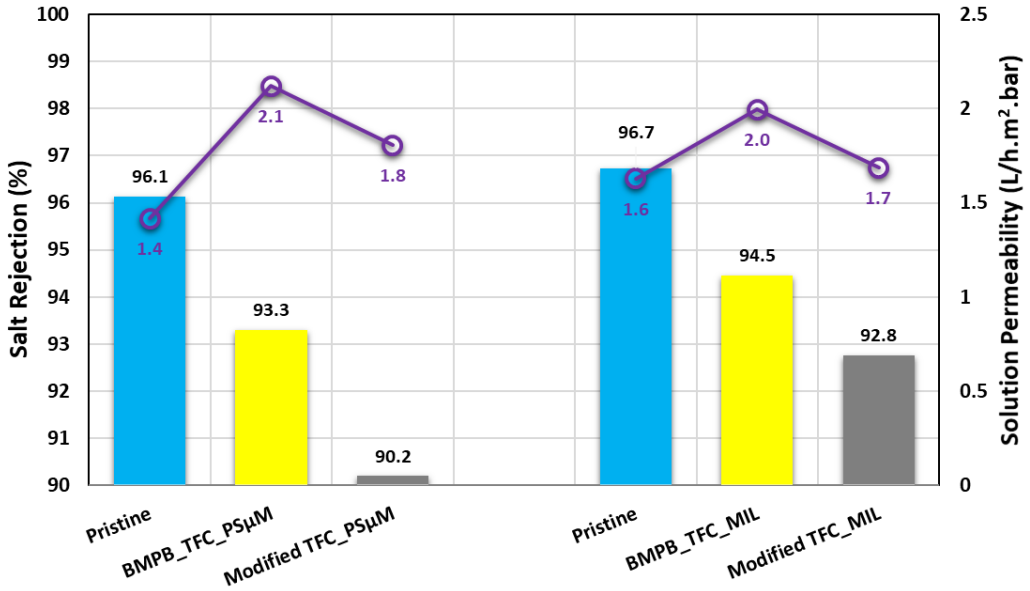

Figure 4.44: Separation performance for surface modified micro-patterned PA TFC membranes in comparison with the pristine membranes, measured by dead-end filtration of 2,000 ppm NaCl solution

In conclusion, a number of experiments were carried out to investigate the feasibility of surface modification of micro-patterned PA TFC membranes using SI-ATRP. Many obstacles were found. Some of them were properly manipulated and surface modified micro-patterned PA TFC membranes were produced. In addition to the observed reduction in the separation performance, controlling of the copolymer growth and layer thickness, as well as optimization of grafting density over the entire surface microstructures are still considered as serious challenges toward refinement of efficient surface modification procedure using SI-ATRP method.

4.3.3 Surface modification of micro-patterned PA TFC membranes with functional copolymers via in situ surface coating using carbodiimide coupling

Surface coating method, as a straightforward and high throughput approach, has also been investigated to modify the surface wettability of micro-patterned PA TFC membranes toward water desalination membranes exhibiting switching between very hydrophilicity to very hydrophobicity. In details, three acrylamide-based polymer coatings were suggested. P(NIPAAm) homo-polymer, thermo-stimuli responsive material, and two P(NIPAAm-co-AAc) random copolymers, double-stimuli responsive materials, with two different mol.% AAc, P(NIPAAm-co-3.5mol.%AAc) and P(NIPAAm-co-**7**mol.%AAc). The three polymer materials were firstly prepared employing free radical polymerization, then they were characterized to estimate the actual mol.% of AAc group incorporated in the copolymer chains. Afterward, the grafting of the prepared polymer coatings to PA TFC membranes using surface coating method was refined. The surface modified micro-patterned PA TFC membranes were comprehensively characterized; in particular, the membrane surface wettability was examined by measuring the static water contact angles at different temperature and pH values to evaluate the surface switching ability. In addition, the influence of surface modification on the membrane separation performance was assessed by a series of salt rejection experiments, including NaCl rejection at environmental pH ~ 6.8, citrate-phosphate buffer rejection at pH 3, and phosphate buffer rejection at pH 7. Thereafter, the promising surface modified micro-patterned membranes were exploited for preliminary colloidal silica fouling experiments in **section 4.4**.

4.3.3.1 Characterization of acrylamide polymer coating materials

Three acrylamide polymer materials were proposed as aforementioned. They were prepared using free radical polymerization method (cf. **sections 3.5.3.1** and **3.5.3.2**), and the chemical composition was then fully characterized. The chemical composition was characterized using ATR-FTIR spectroscopy and the graphs were plotted in **Figure 4.45**. The chemical structure of P(NIPAAm) homo-polymer was affirmed by characteristic IR peaks at ~ 1630 and 1525 cm^{-1} that are assigned to combination of C-N stretching and N-H deformation in amide (II) groups, and 1455 cm^{-1} that is attributed to C-H deformation in alkanes ($-CH_3$) [265]. P(NIPAAm-co-AAc) copolymers exhibited the same IR peaks equivalent to acrylamide segments, as well as two additional IR bands at 1723 and 1225 cm^{-1} that are assigned to C=O stretching and O-H deformation in carboxylic acid groups, respectively, as a result of incorporating AAc groups.

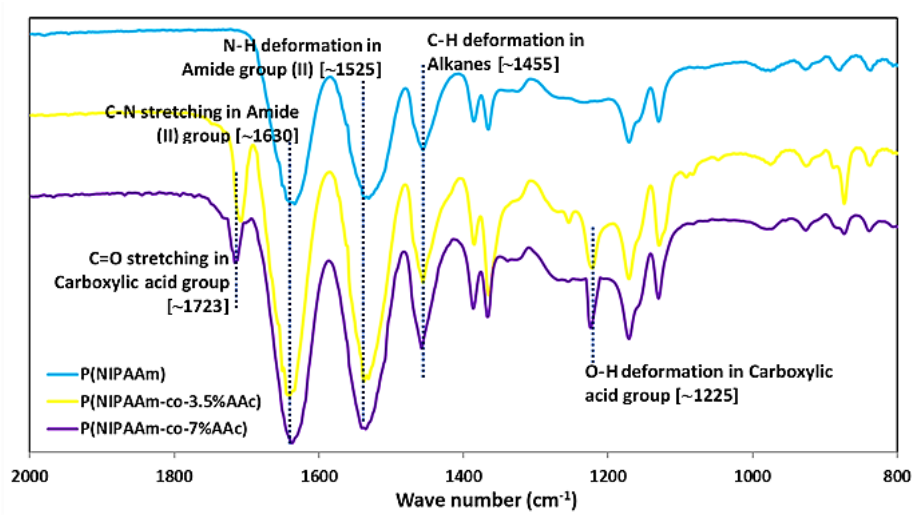

Figure 4.45: ATR-FTIR spectroscopy for the prepared acrylamide-based polymer coatings

The actual mol.% of AAc groups incorporated in the prepared copolymers were estimated using ^{1}H-NMR spectroscopy and back titration method, as well. The estimated values are listed in **Table 4.9**. The actual mol.% of AAc was observed to be 2.1 ± 0.2 and 3.4 ± 0.6 mol.% in case of P(NIPAAm-co-3.5mol.%AAc) and P(NIPAAm-co-7mol.%AAc), respectively. However, the mol.% AAc estimated using back titration method was much lower, 1.6 ± 0.3 and 2.1 ± 0.5 mol.% in case of P(NIPAAm-co-3.5mol.%AAc) and P(NIPAAm-co-7mol.%AAc), which might be explained by incapability of the titrant, NaOH, to equilibrate all the carboxylic groups; especially those which were inaccessible or shielded inside the copolymer network.

Table 4.9: Results of GPC analysis as well as quantitative determination of mol.% of AAc for the prepared acrylamide-based polymer materials

Polymer	GPC analysis		Measured AAc mol.%	
	Universal Calibration		NMR	Titration
	$\overline{M_n}$ (kDa)	PDI		
P(NIPAAm)	172.5	3.26	-	-
P(NIPAAm-co-3.5%AAc)	119.7	2.49	2.1 ± 0.2	1.6 ± 0.3
P(NIPAAm-co-7%AAc)	85.8	2.52	3.4 ± 0.6	2.1 ± 0.5

In parallel, the number average molecular weight, $\overline{M_n}$, and the polydispersity index, PDI, were measured using gel-permeation chromatography, GPC, employing universal calibration

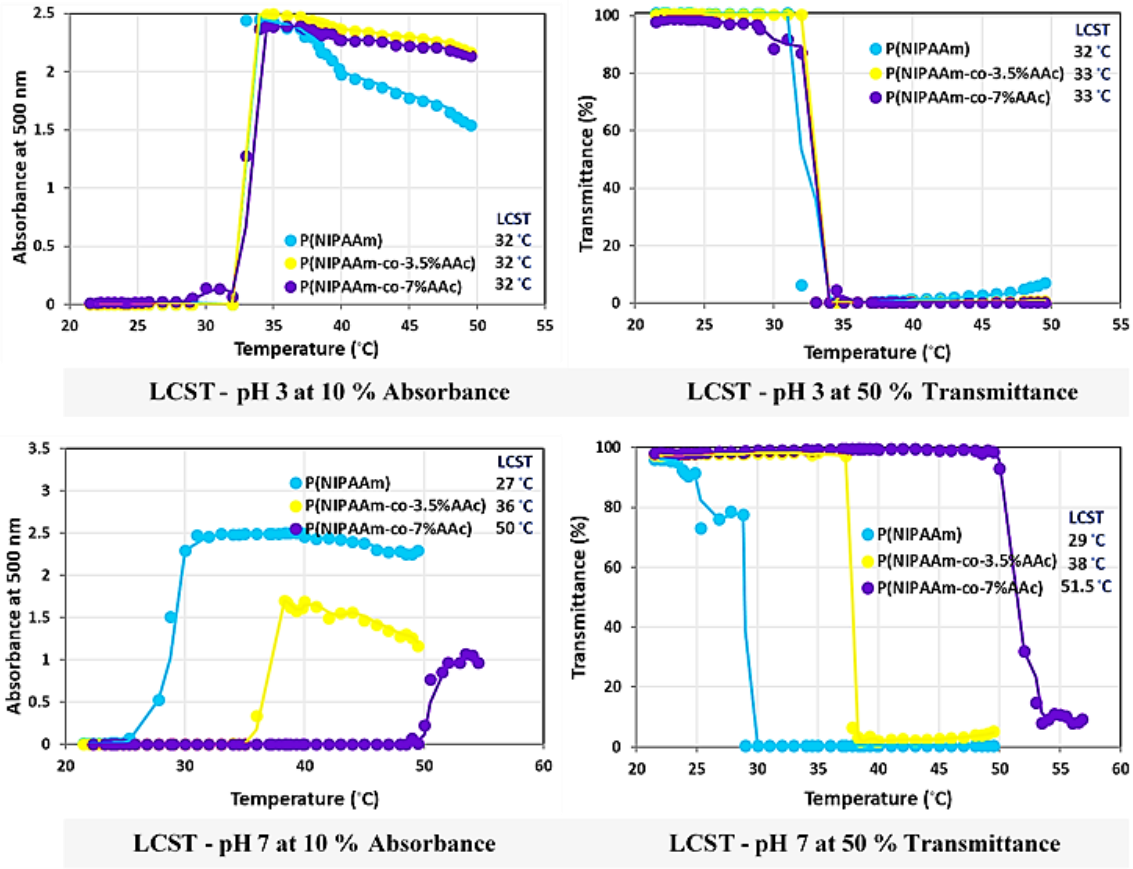

Figure 4.46: Measurement of cloud point, LCST, at different pH values for the prepared acrylamide-based polymer coating materials

method, and the results are presented in **Table 4.9**. Generally, the synthesis producers seemed to be successful and high molecular weight polymer coating were obtained. Additionally, one may observe that $\overline{M_n}$ decreases upon incorporating of AAc groups. This might be explained by partial replacement of NIPAAm segments (-CONHCH(CH_3)$_2$) by AAc segments (-COOH).

Moreover, the cloud point, or LCST, was also estimated for the prepared homo-polymer and random copolymers by measuring the change in absorbance and transmittance of an aqueous solution of the polymer by varying the environmental temperature at two pH values, i.e., below and above pK_a of AAc, (cf. **section 3.5.3.3.3**). The data were then plotted as in **Figure 4.46,** and LCST values were comparatively determined using two approaches, i.e., temperature at 10 % absorbance or temperature at 50 % transmittance. Comparable LCST values were observed for both homo-polymer and random copolymers at pH = 3 (< pK_a of AAc). This could be because most of carboxylic acid groups are protonated at pH < pK_a of AAc; accordingly, LCST of both homo-polymer and random copolymers is mainly determined by NIPAAm segments. On the other hand, the influence of increasing mol.% of AAc was more explicit at pH = 7 (> pK_a of AAc), such that the LCST values were emphasized to be shifted to higher values upon

increasing mol.% of AAc. At pH > pK_a of AAc, most of carboxylic acid groups are deprotonated, i.e., exist as $–COO^-$, which increases the hydrophilicity of the copolymer; consequently, the copolymer chains are more swollen and hydrated than homo-polymer. Subsequently, more energy is needed to breakdown such hydrophilic/hydrophobic balance and promote hydrophobic collapsed state. Therefore, LCST increases in the sequence of: LCST of P(NIPAAm-co-7mol.%AAc) > LCST of P(NIPAAm-co-3.5mol.%AAc) > LCST of P(NIPAAm).

4.3.3.2 Adaptation of surface modification of PA TFC membranes using surface coating method

The surface modification of PA TFC membranes using acrylamide-based homo- and copolymers that were prepared and fully characterized (cf. **section 4.3.3.1**) was investigated using various "grafting to" approaches. Seven surface coating procedures were suggested, considering the membranes' surface chemistry and the nature of polymer to be grafted (cf. **section 3.5.3.4.2**). Experiments C.1., C.2. and C.3. were based on physical adsorption mechanism without prior alteration of membrane surface chemistry; these experiments were investigated for membrane modification using both P(NIPAAm) homo-polymer and P(NIPAAm-co-AAc) copolymers. Experiments C.4., C.5., C.6. and C.7. were designed employing carbodiimide coupling chemistry to obtain stable coating via formation of amide bonds, ranging from one-step reaction, i.e., C.4. and C.6., to two-steps reaction, C.5. and C.7. Concerning the membrane surface chemistry, experiments C.4., C.5. and C.6. exploit unreacted amine groups as potential reaction sites along PA chains, whereas experiment C.7. was designed to pre-immobilize reactive amine groups onto the abundant carboxylic groups atop PA membrane surface using EDC/NHS coupling. Thereafter, NHS-activated copolymer was grafted to amine-modified PA TFC membrane in a separate step.

The adaptation experiments were carried out using flat PA TFC membranes, and the best-suited procedures were then applied to micro-patterned membranes. During the adaptation experiments, the modified membranes' surface chemistry was analyzed using ATR-FTIR spectroscopy (see **Figure 4.47**), and the membrane selectivity were evaluated by dead-end filtration of 2,000 ppm salt solutions, NaCl, Na_2SO_4, and $CaCl_2$ at pH 6.8 (see **Figure 4.48**).

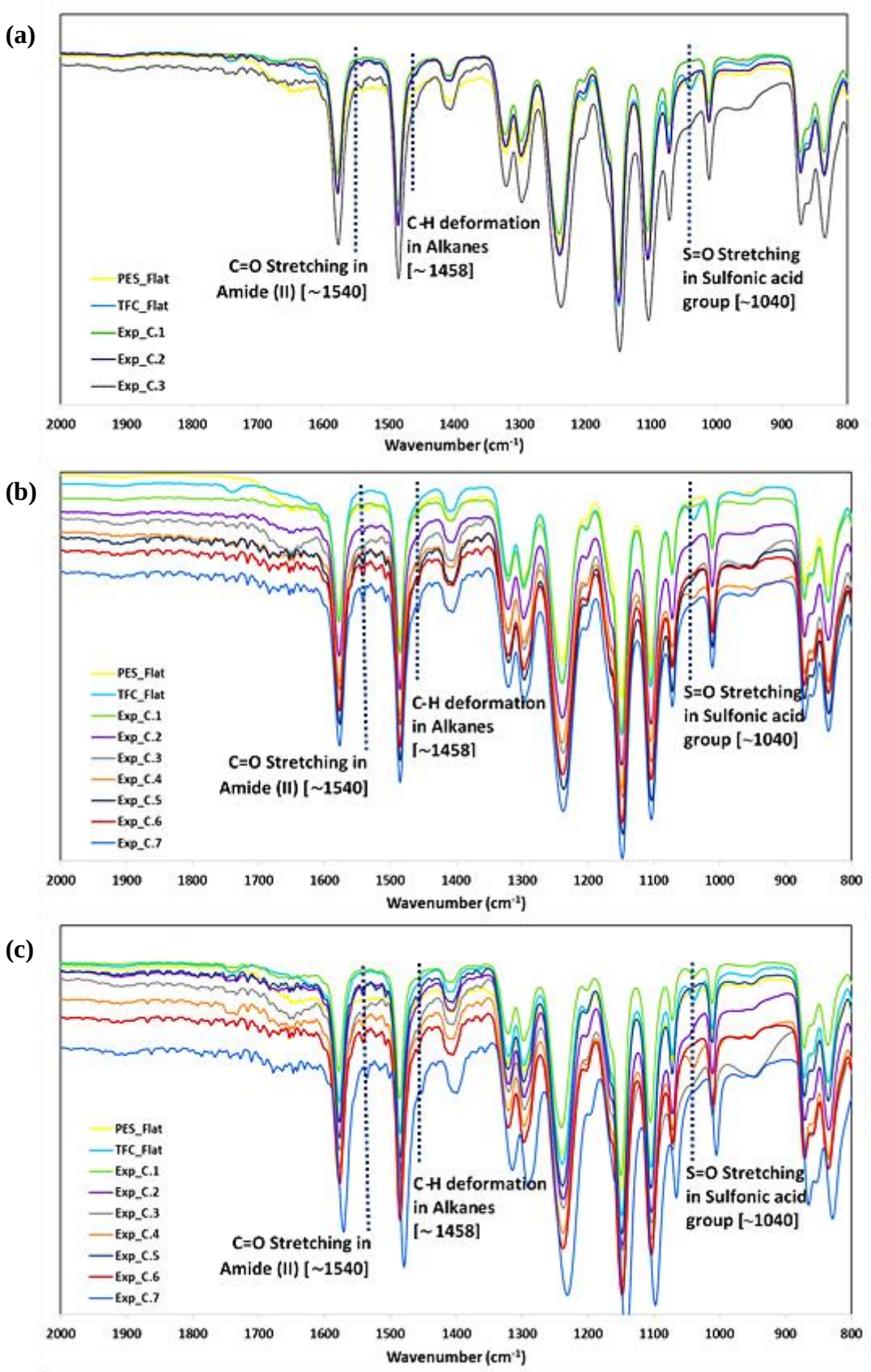

Figure 4.47: ATR-FTIR spectroscopy for the flat surface-modified PA TFC membranes during adaptation experiments using acrylamide-based polymer coatings, (a) P(NIPAAm), (b) P(NIPAAm-co-3.5%AAc), (c) P(NIPAAm-co-7%AAc)

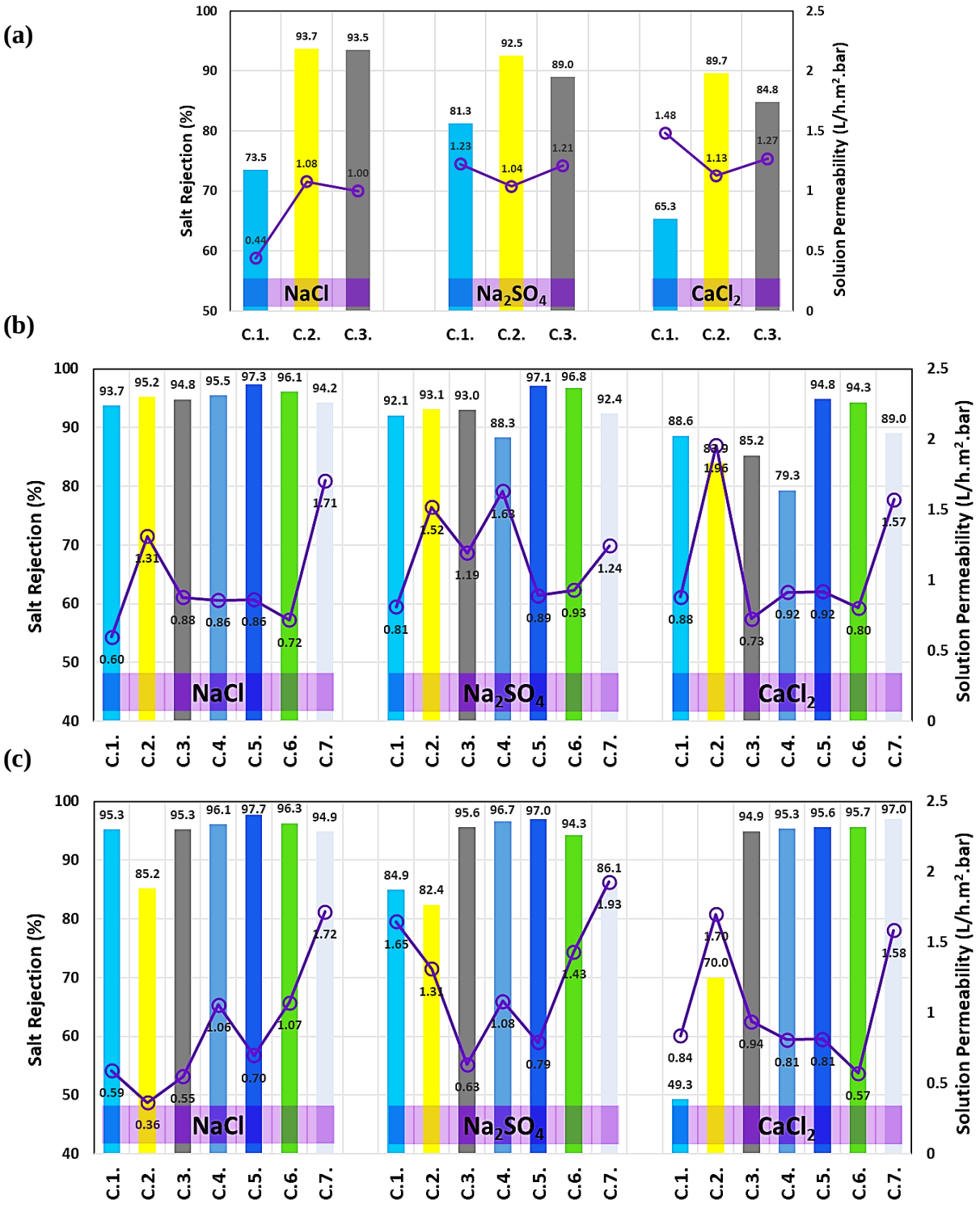

Figure 4.48: Separation performance for the flat surface-modified PA TFC membranes during adaptation experiments using acrylamide-based polymer coatings, (a) P(NIPAAm), (b) P(NIPAAm-co-3.5%AAc), (c) P(NIPAAm-co-7%AAc)

The surface modification of flat PA TFC membranes by grafting of P(NIPAAm) homo-polymers was firstly adapted. The ATR-FTIR spectroscopy for the modified flat membranes showed that the modified membranes by experiments C.2. and C.3. exhibited two small IR

bands at ~ 1540 and ~ 1458 cm^{-1} that are assigned to amide (II) and alkanes (-CH_3) groups, respectively, accompanied by disappearing of sulfonic group peak at ~ 1040 cm^{-1} because of surface coating. In addition, the separation performance experiments revealed that modified membranes by C.2. showed the highest salt rejection ability (> 94 % in case of NaCl feed solution) along with good solution permeability; consequently, C.2. was concluded to be the most-suited surface modification procedure.

In parallel, the surface modification of flat PA TFC membranes by grafting of P(NIPAAm-co-3.5mol.%AAc) and P(NIPAAm-co-7mol.%AAc) copolymers was refined. The ATR-FTIR spectroscopy for the surface-modified flat membranes showed a comparable membrane surface chemistry such that most of the membranes modified by both copolymers exhibited the characteristic IR peaks for NIPAAm segments, i.e., amide (II) and (-CH_3) groups, while the characteristic IR bands for AAc segments weren't clear because of possible interference as a result of multi-layered membrane structure. Nevertheless, the sulfonic group peak manifested different peak intensity depending on the employed procedure. Similarly, the separation performance experiments showed comparable salt rejection behavior for the surface-modified membranes along with different permeabilities. Surface-modified membranes by experiment C.5. exhibited the highest NaCl rejection, ~ 98 and 97.5 % in case of grafting of P(NIPAAm-co-7mol.%AAc) and P(NIPAAm-co-3.5mol.%AAc), respectively. They also showed a high potential to reject Na_2SO_4 salt (> 97 %) and $CaCl_2$ salt (> 94 %) accompanied by good permeability. In parallel, it is worth to note that surface-modified membranes by experiment C.7. showed a promising membrane performance, i.e., very good NaCl rejection (> 94 %) and superior solution permeability ~ 1.7 $L/h.m^2$.bar, which is expected to yield membranes of enhanced performance upon optimization of other related parameters.

Moreover, the static water contact angle values for the flat surface-modified membranes during adaptation experiments were measured using sessile drop method and the results were presented in **Figure 4.49**. The surface modified-membranes by P(NIPAAm) homo-polymers showed higher water contact angles than the pristine PA TFC membranes that could possibly be due to an increase in the amount of hydrophobic isopropyl groups. However, a decrease in the water contact angles, i.e., enhancement in surface water wettability, was observed for surface-modified membranes by P(NIPAAm-co-AAc) copolymers as a result of incorporating hydrophilic AAc groups, which was found to be additionally improved upon increasing of mol.% of AAc. The flat surface-modified membranes using experiment C.5. displayed the

highest surface wettability for modification using both copolymers; which indicates the successful modification using this procedure.

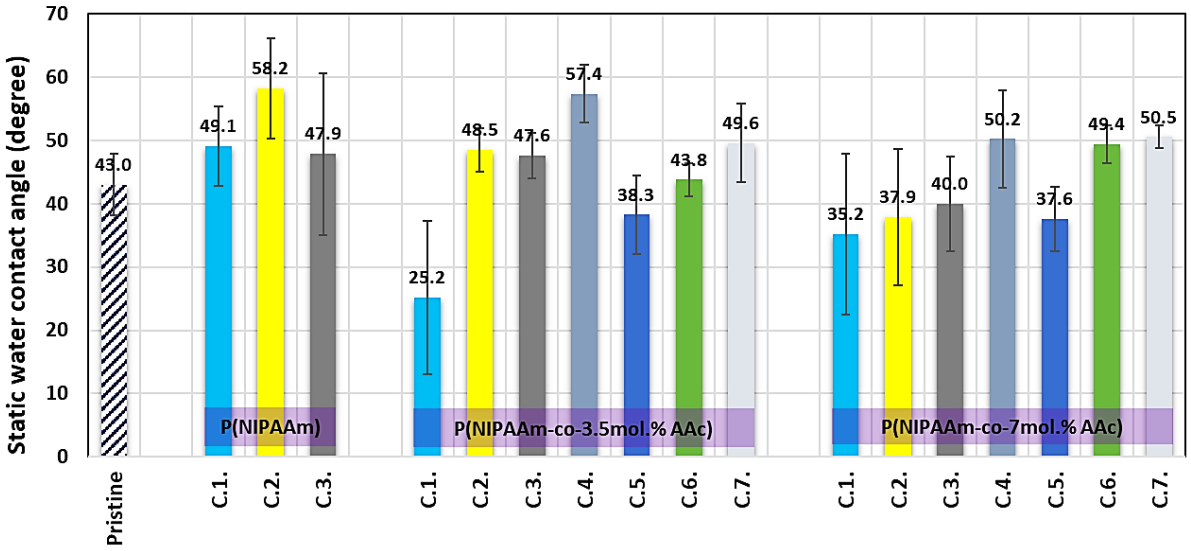

Figure 4.49: Static water contact angle values for the surface-modified flat PA TFC membranes during adaptation experiments using acrylamide-based polymer coatings

According to the findings of ATR-FTIR analysis, separation performance and contact angle measurements, surface modification employing experiment C.5. was preferentially selected as the most-suited procedure for grafting of P(NIPAAm-co-AAc) copolymers to PA TFC membranes. In parallel, surface modification by experiment C.2. was also chosen as the most-suited procedure for modifying membranes using P(NIPAAm) homo-polymer. Subsequently, these procedures were exploited to treat the micro-patterned PA TFC membranes.

4.3.3.3 Surface modification of micro-patterned PA TFC membranes

The micro-patterned PA TFC membranes were modified via grafting of P(NIPAAm) homo-polymer and P(NIPAAm-co-AAc) copolymers in order to achieve novel smart PA TFC membranes possessing the ability to switch between very hydrophilicity to very hydrophobicity at different environmental pH and temperature values. The surface modification of micro-patterned PA TFC membranes were performed using pre-adapted surface modification procedures, C.2. and C.5, respectively. The surface chemical characteristics, surface wettability and switching, surface topography, as well as the separation performance were investigated in detail for the produced surface-modified micro-patterned membranes and compared with the flat counterparts. The abbreviations used to describe the membrane samples are listed in **Table 4.10**.

Table 4.10: Abbreviations referring to the surface-modified flat and micro-patterned PA TFC membranes

	TFC_Flat	TFC_MIL	TFC_PSµM
P(NIPAAm)	CP_TFC_Flat_0%	CP_TFC_MIL_0%	CP_TFC_PSµM_0%
P(NIPAAm-co-3.5%AAc)	CP_TFC_Flat_3.5%	CP_TFC_MIL_3.5%	CP_TFC_PSµM_3.5%
P(NIPAAm-co-7%AAc)	CP_TFC_Flat_7%	CP_TFC_MIL_7%	CP_TFC_PSµM_7%

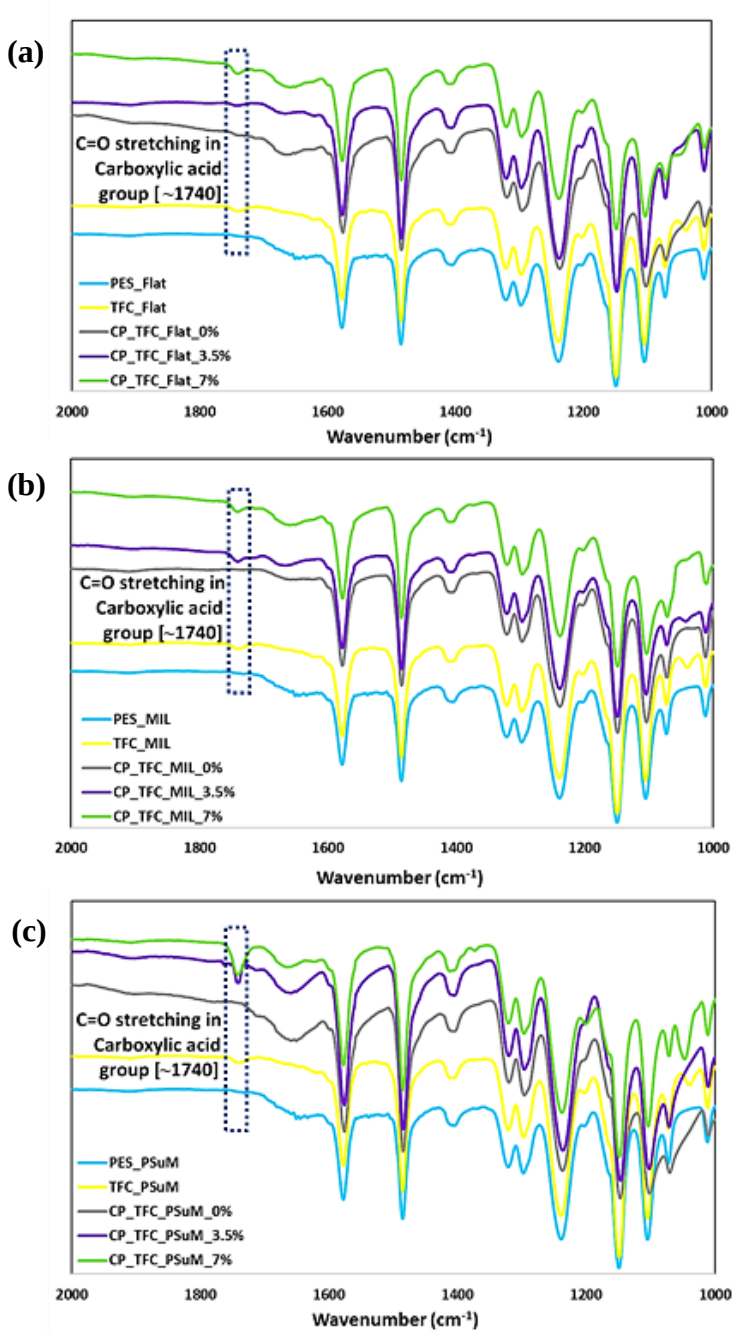

Figure 4.50: ATR-FTIR spectroscopy for surface-modified flat and micro-patterned PA TFC membranes, (a) CP_TFC_Flat, (b) CP_TFC_MIL, (c) CP_TFC_PSµM

4.3.3.3.1 Investigation of grafting degree, membrane surface chemistry and membrane surface charge

The surface-modified micro-patterned PA TFC membranes showed various grafting degrees between 0.2 – 0.5 mg/cm^2 in comparison with 0.1 – 0.16 mg/cm^2 in case of flat surface-modified membranes. In addition, the surface chemistry of the surface-modified membranes was analyzed using ATR-FTIR spectroscopy and the graphs are presented in **Figure 4.50**. Numerous IR bands were observed for different chemical function groups belonging to multiple membrane layers. ATR-FTIR spectroscopy is well-known of its low selectivity regarding the analysis of the membrane surface chemistry because the typical penetration depth of the IR beam is found to be 1 – 3 µm, at an incidence angle of 45°, depending on the wavelength [282]. Nevertheless, a small IR peak was noticed for surface-modified membranes by copolymers at wavenumber of 1740 cm^{-1}, which is assigned to C=O stretching in AAc units. The intensity of this peak was interestingly observed to increase upon increasing of mol.% of AAc and range of surface micro-patterning, i.e., CP_TFC_PSµM > CP_TFC_MIL > CP_TFC_Flat.

More precise analysis of membrane surface chemistry before and after surface modification was performed using X-ray photoelectron spectroscopy, XPS, which is a sensitive analysis tool that is able to quantify the relative fractions of different elements existing at the top 1 – 10 nm from the membrane surface [122]. Consequently, XPS analysis was performed for the flat surface-modified membranes only to avoid the possible distraction by the surface micro-structures in case of micro-patterned membranes. High resolution XPS spectra of N_{1s} and O_{1s} for flat surface-modified membranes in comparison with the pristine PA TFC membrane are displayed in **Figure 4.51**. The overlapping of similar chemistries within the membrane layers, i.e., amide and carboxylic groups, along with the absence of a precise technique to measure the actual thickness of the coating layer, as well as the possible contamination of the membranes by coupling agents and buffer solution were emphasized to prohibit the quantitative determination of actual fraction of each function group. Nevertheless, XPS can be used as an additional verification tool to confirm the grafting process. The N_{1s} spectra showed one protruding peak of different intensities for amide group (N*-C=O) of the aromatic PA layer at ~ 400 eV [283]. The amide peak intensity was observed to increase in case of CP_TFC_Flat_7% and CP_TFC_Flat_3.5% membranes, whereas CP_TFC_Flat_0% exhibited an amide peak intensity that is equal to that of the pristine membranes. This might be explained by the discrepancy in the "grafting to" mechanism as will be discussed later (cf. **section**

4.3.3.3.4). Moreover, O_{1s} spectra revealed a main peak of diverse intensities for carboxylic containing groups, at ~ 531 eV, that are characteristic for aromatic PA layer [122]. The surface-modified membranes manifested lower peak intensity than the pristine membranes, which implies the successful coverage of PA TFC membranes with a very thin layer (< 10 nm) of different polymer coatings using the adapted surface modification procedures.

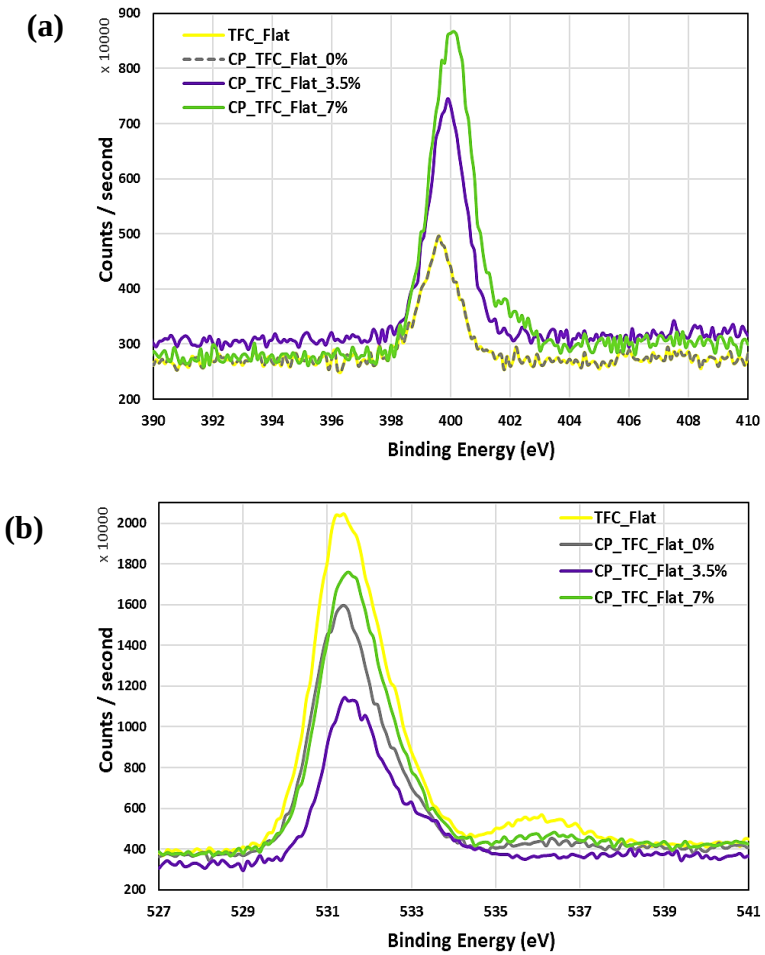

Figure 4.51: XPS spectra for the flat surface-modified PA TFC membranes: (a) N_{1s}, (b) O_{1s}

Furthermore, the surface charge of the surface-modified micro-patterned membrane was investigated by measuring zeta potential values as a function of pH (cf. **Figure 4.52**). Generally, all the surface-modified flat and micro-patterned membranes exhibited IEP in pH range 3 – 4 such that IEP was found to decrease with increasing in mol.% of AAc. In addition, the measured zeta potential values for CP_TFC_MIL membranes were observed to be lower than those in case of CP_TFC_Flat membranes, i.e., streaming potential decreases upon micro-patterning (cf. **section 4.2.4**, **Figure 4.34**). On the other hand, the measured zeta potential values for CP_TFC_PSμM membranes were unexpectedly found to be higher than those of the

flat membranes, which might be linked to higher charge density, or thicker coating layers at the valley regions that could increase the streaming potential values.

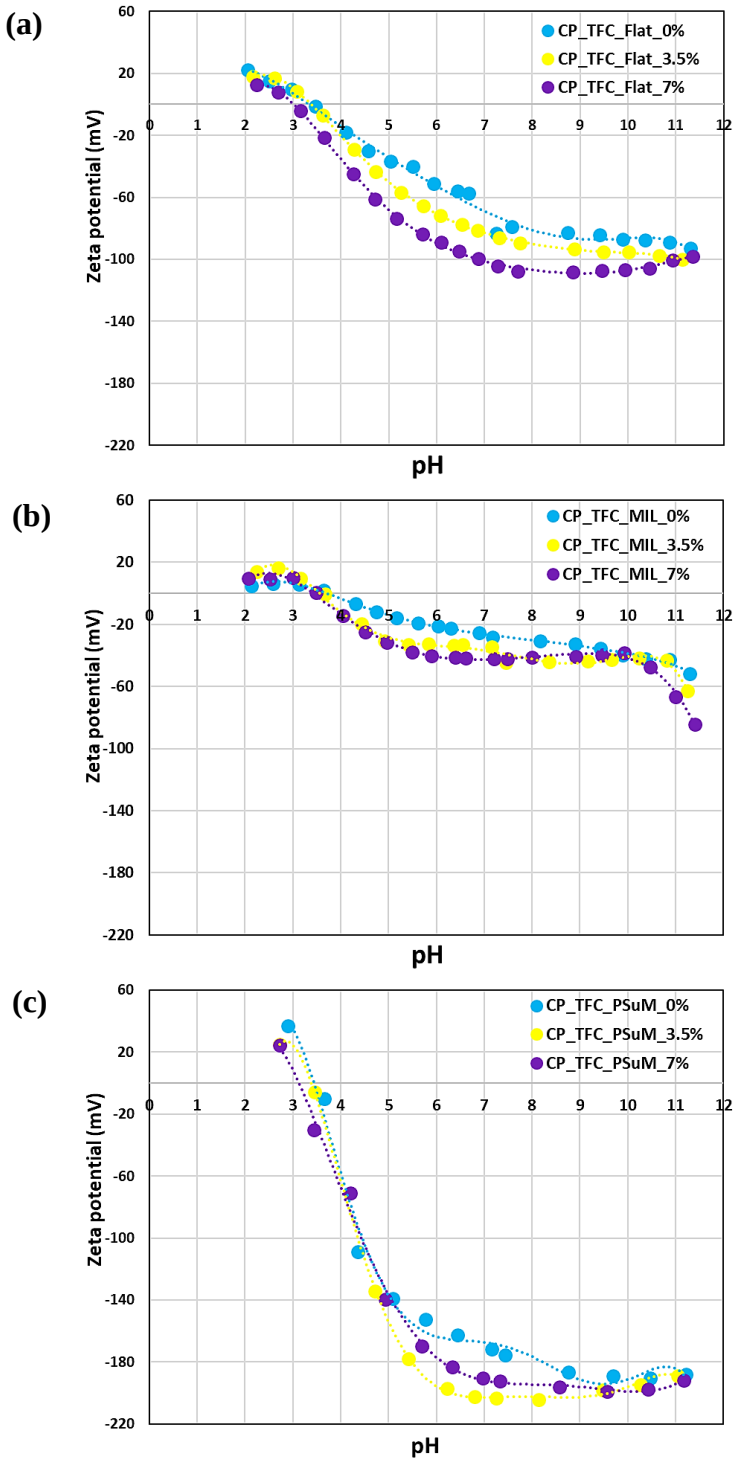

Figure 4.52: Zeta potential as function of pH value for surface-modified flat and micro-patterned PA TFC membranes, (a) CP_TFC_Flat, (b) CP_TFC_MIL, (c) CP_TFC_PSµM

4.3.3.3.2 Scanning of membrane morphology and quantitative surface roughness analysis

The membrane morphology of the surface-modified flat and micro-patterned PA TFC membranes was scanned using SEM and the micro-graphs for the top surface and cross section morphologies at different magnifications for CP_TFC_Flat, CP_TFC_MIL and CP_TFC_PSµM membranes are presented in **Figure 4.53**, **Figure 4.54**, **Figure 4.55**, respectively.

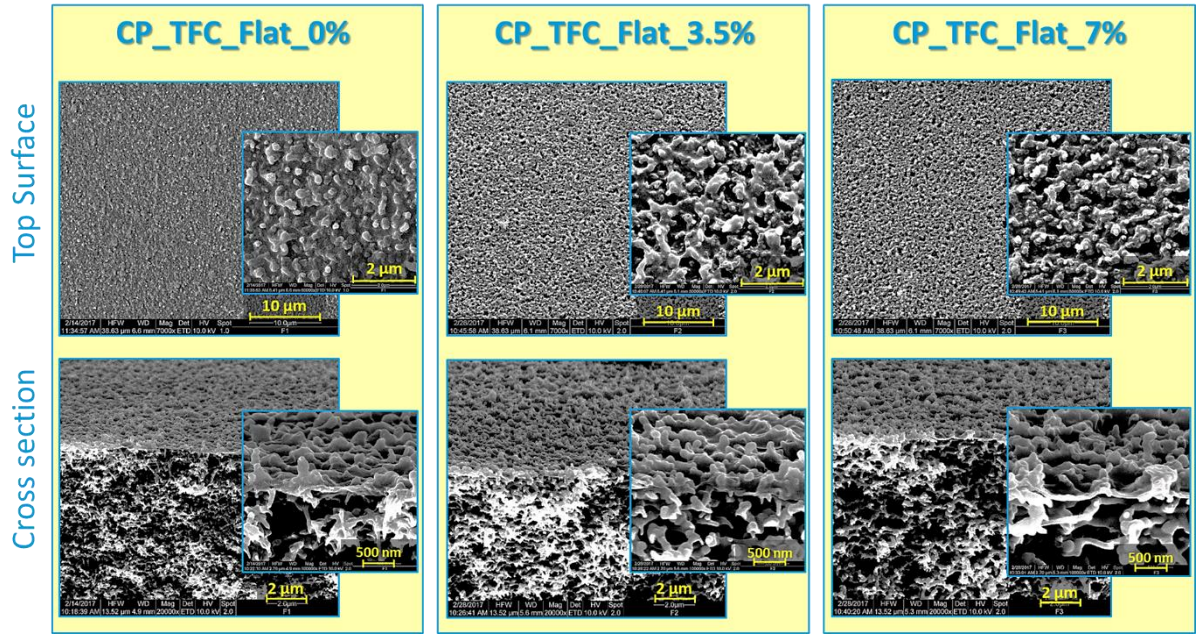

Figure 4.53: SEM micrographs of top surface and cross section morphologies at different magnifications for the flat surface-modified PA TFC membranes

The micro-patterned membranes were affirmed to hold the regular surface micro-structures over the entire membranes' surfaces. In contrast to surface-modified membranes using SI-ATRP (cf. **Figure 4.43**), the surface coating method was emphasized to produce a homogenous surface coverage atop the flat and micro-patterned membranes, i.e., all the apex and valley regions were covered with acrylamide polymer coatings. At high magnification, the dense crumpled ridge-and-valley PA morphology was observed to be totally covered by the hydrogel coating, with higher grafting degrees at the valley regions. On the other hand, the thickness of the acrylamide surface coatings was hard to be measured using SEM because of the entanglement of both hydrogel and PA layers, which implies that the thickness of the hydrogel layer is essentially much thinner than PA layer, i.e., << 50 nm.

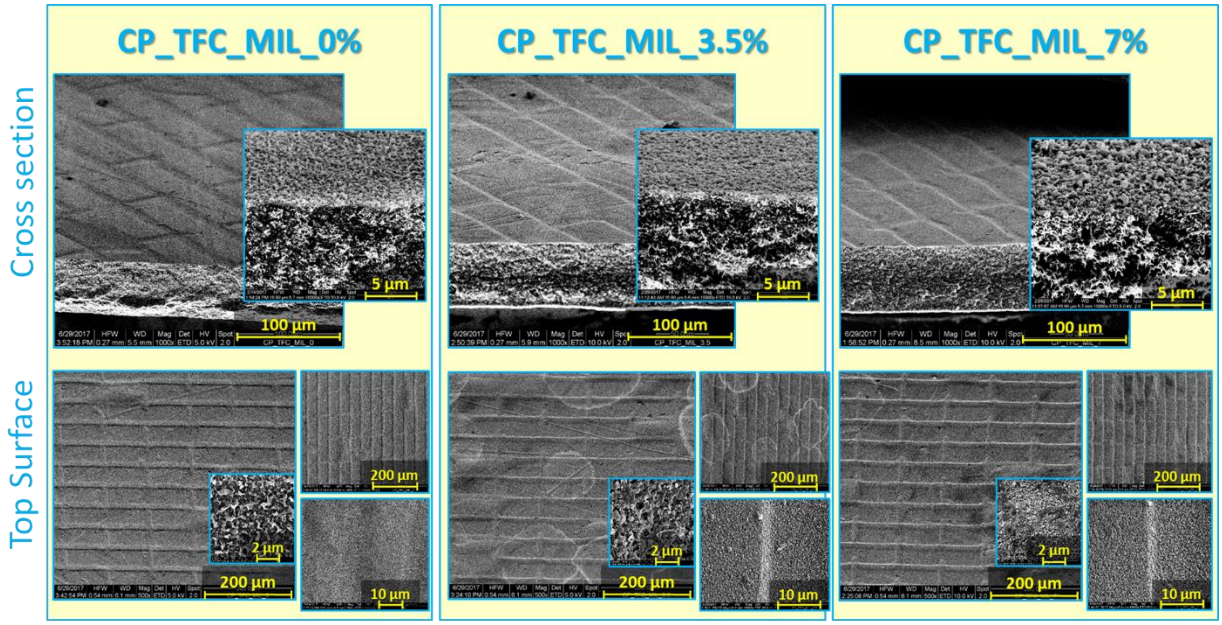

Figure 4.54: SEM micrographs of top surface and cross section morphologies at different magnifications for the surface-modified TFC_MIL membranes

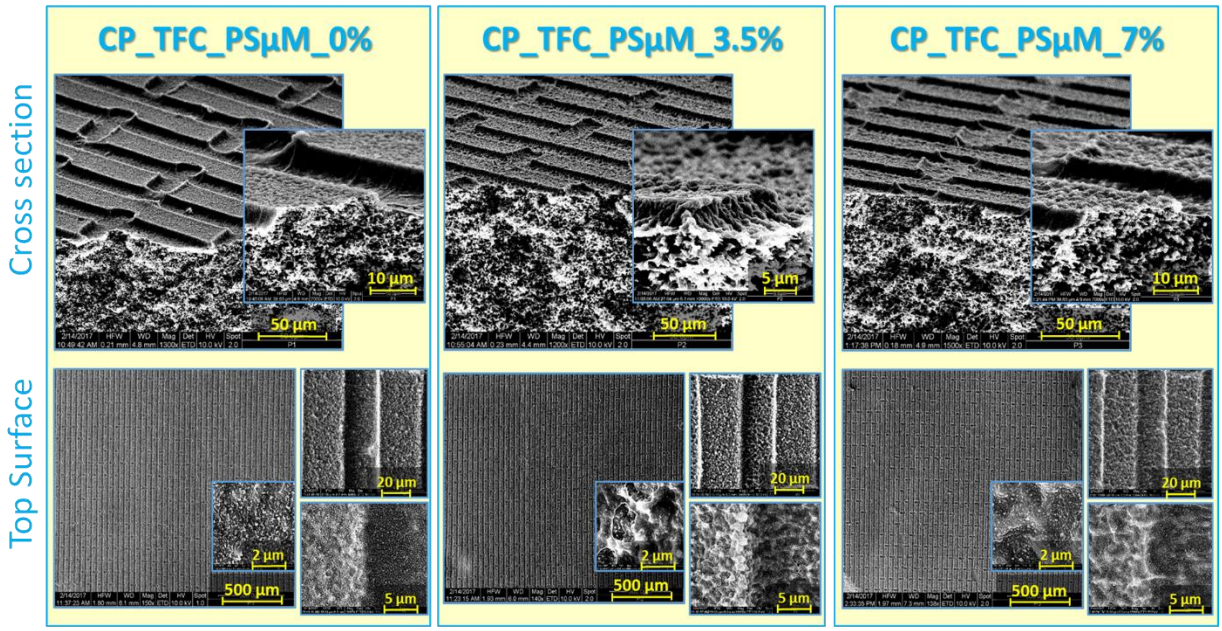

Figure 4.55: SEM micrographs of top surface and cross section morphologies at different magnifications for the surface-modified TFC_PSµM membranes

Moreover, the alteration in the membranes' surface roughness after the surface modification step was investigated using AFM and the two main roughness parameters, average roughness, S_a, and root mean square roughness, S_q, were estimated. The results of the surface roughness analysis for the surface-modified flat and micro-patterned membranes are presented in **Figure 4.56**.

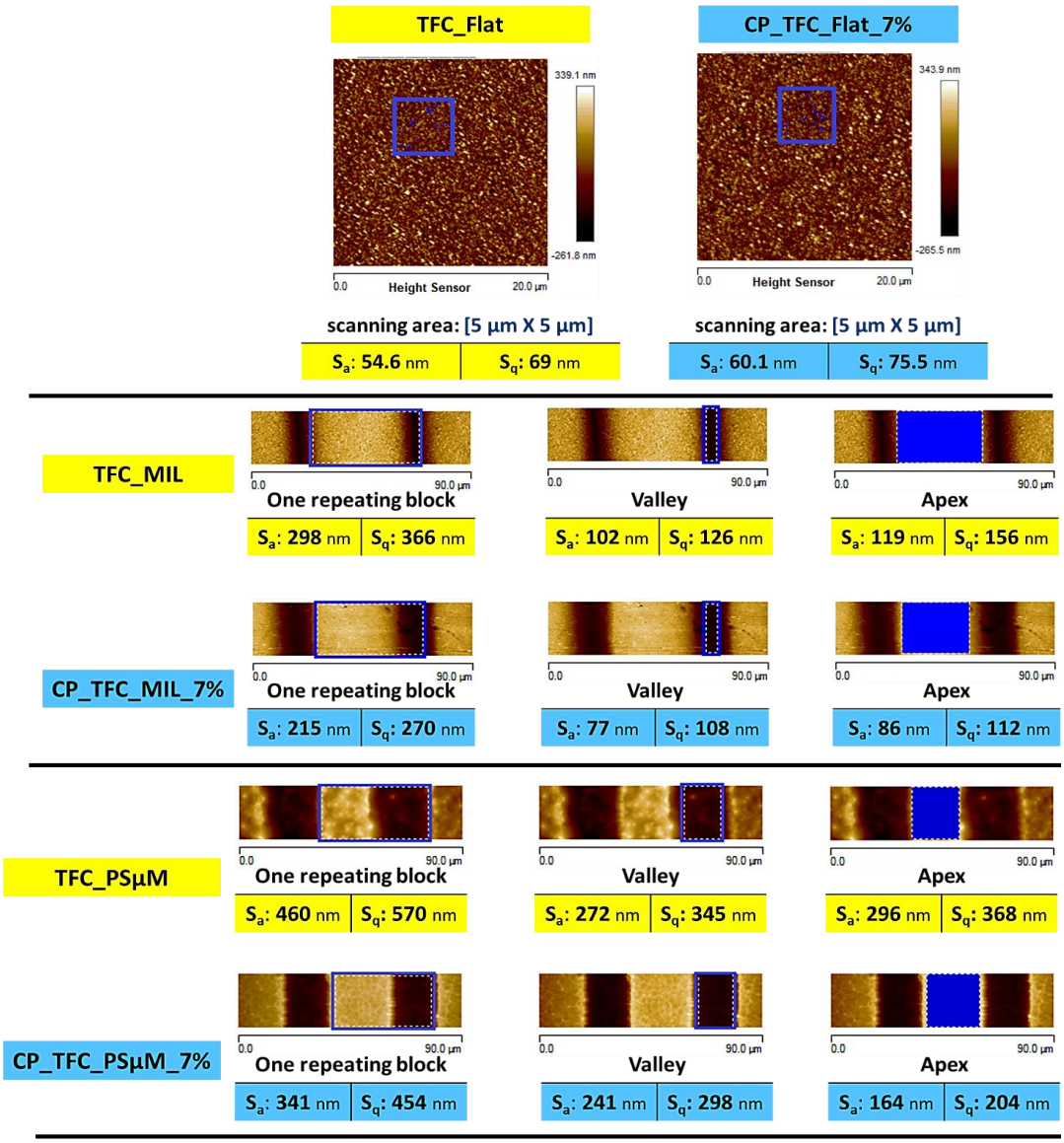

Figure 4.56: Quantitative surface roughness analysis using AFM for the surface -modified flat and micro-patterned PA TFC membranes

Two contradictory observations were found. The surface roughness of the flat membranes was shown to be slightly increased as a result of the surface modification. The same observations were reported for surface-modified commercial PA TFC membranes by different acrylamide-based polymer coatings [208, 211]. On the contrary, the surface roughness of the micro-patterned membranes was emphasized to be always decreased upon surface coating by acrylamide-based polymers. The latter observation could be interpreted by a possible smoothening action accompanied the surface coating procedure, which may decrease either the micro- or nano-scale roughness of the dense crumpled ridge-and valley PA morphology existing atop the micro-patterned PA TFC membranes (cf. **section 4.2.4**). This interpretation is supported by top surface SEM images at high magnification, and the cross sectional profiles

for the surface-modified micro-patterned membranes estimated using AFM analysis (see **Figure 4.57**).

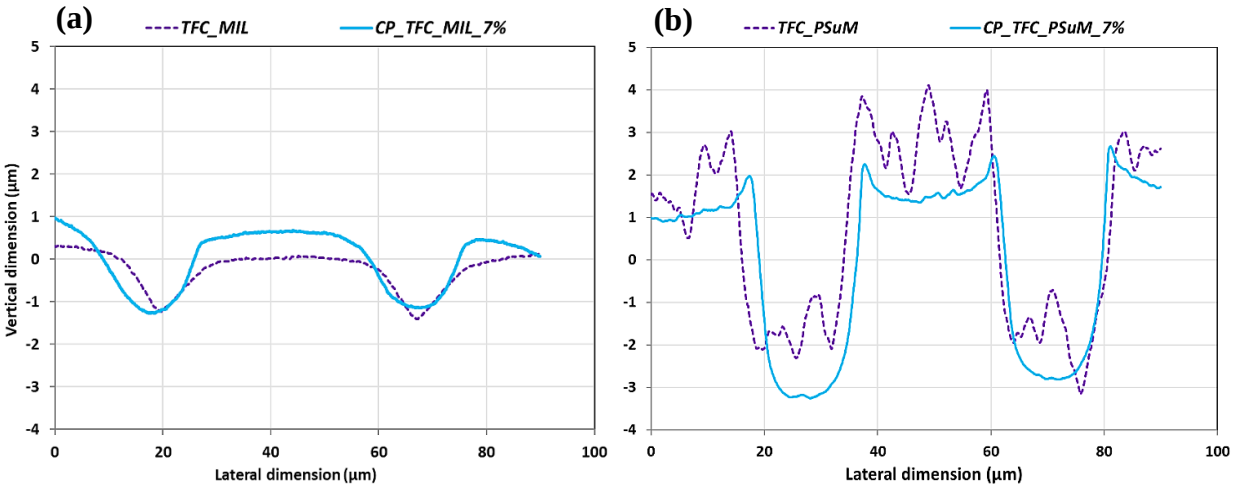

Figure 4.57: Cross sectional profiles derived from AFM analysis for the surface-modified micro-patterned PA TFC membranes, (a) MIL-based membranes, (b) PSµM-based membranes

4.3.3.3.3 Evaluation of the capability of switching between surface hydrophilicity and surface hydrophobicity

The ability of the surface-modified micro-patterned PA TFC membranes to switch between super-hydrophilicity and super-hydrophobicity was assessed via the measurement of static water contact angles at two environmental pH values, pH = 3 (< pK_a of AAc) and pH = 7 (> pK_a of AAc), and within a temperature range (25 – 55 °C), i.e., the range of cloud points of the copolymers; cf. **Figure 4.46**, using captive bubble method (cf. **section 3.6.7.2**). The results were plotted in **Figure 4.58**.

In general, a significant improvement in the switching range was observed upon the increase of membrane surface roughness via surface micro-patterning such that the switching extent improves in the following sequence: CP_TFC_PSµM > CP_TFC_MIL > CP_TFC_Flat. A substantial change in the static water contact angle from 88° (at 55 °C and pH = 3) to 28° at (at 25 °C and pH = 7) was achieved by CP_TFC_PSµM_7%. In parallel, CP_TFC_MIL_7% could also obtain a remarkable change in the static water contact angle, from 78° (at 55 °C and pH = 3) to 36° (at 25 °C and pH = 7). On the other hand, CP_TFC_Flat_7% showed a much smaller change in the water contact angle, from 66° (at 55 °C and pH = 3) to 42° at (at 25°C and pH = 7). Additionally, the experiments also showed that higher static water contact angles can be

attained by increasing the pH toward super-hydrophobicity, whereas lower water contact angles can be realized by decreasing the pH toward super-hydrophilicity.

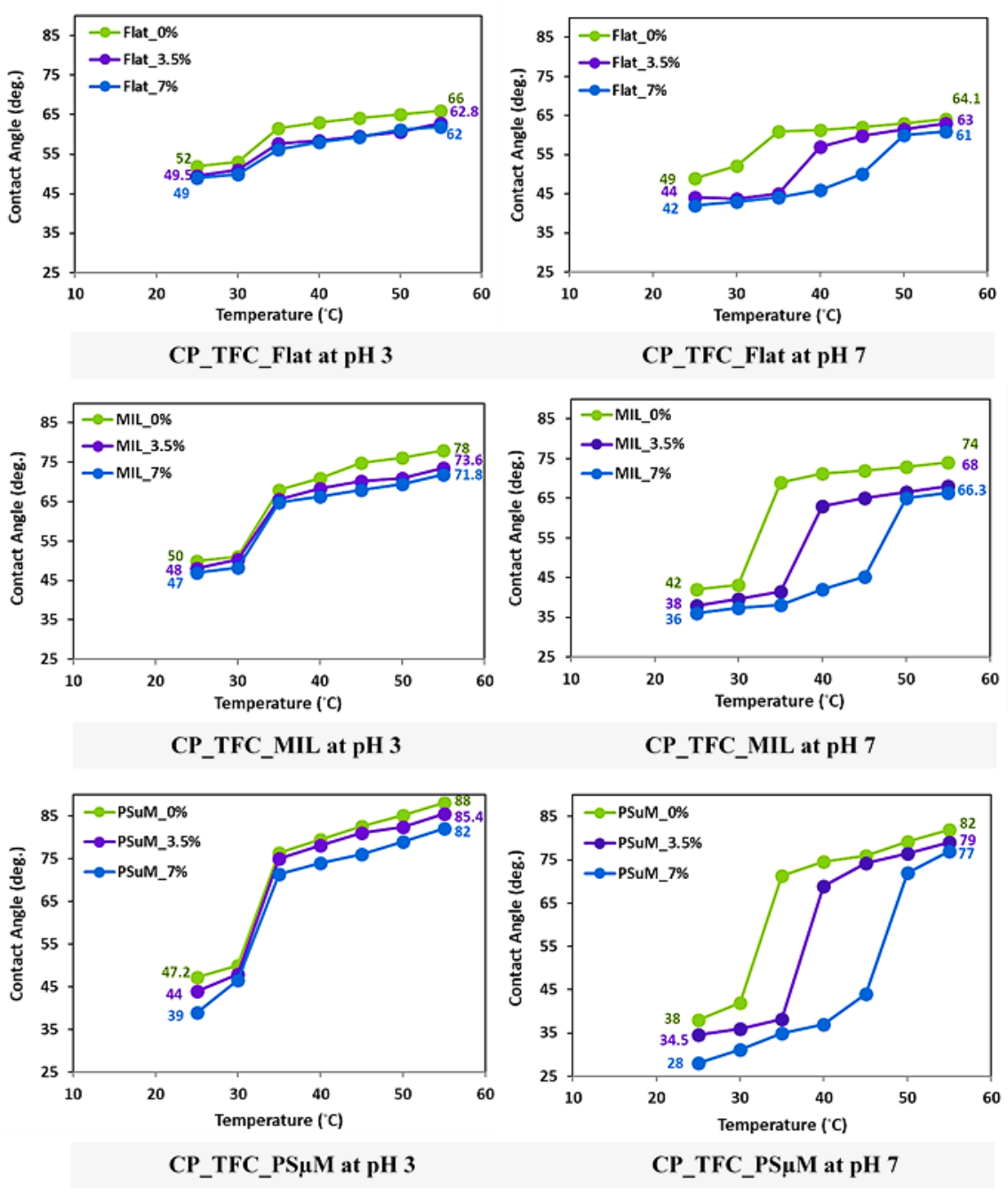

Figure 4.58: Static water contact angles for the surface-modified flat and micro-patterned PA TFC membranes measured at different temperature and pH values using captive bubble method

The switching ability was driven by the grafted acrylamide-based polymer coatings atop the flat and micro-patterned PA TFC membranes. In addition, the influences of changing the mol.% of AAc and pH values on the switching domain were highlighted. The increase in mol.% AAc was found to shift the switching domain to higher temperature values as a result of

increasing LCST (cf. **section 4.3.3.1**). In parallel, the switching action became more obvious upon increasing of environmental pH values. The consolidating of both thermo- and pH-stimuli responsivities was emphasized to broaden the switching domain and offer the capability to switch between diverse surface wettability states using the same functionalized surface (cf. **section 2.5.1.3**).

In conclusion, the joint impact of surface micro-patterning and double-stimuli responsivity on promoting the switching between strong hydrophilicity and strong hydrophobicity was confirmed. To the best of our knowledge, it is the first time ever to obtain these unique smart surface properties on the surface of polymeric membranes, in particular PA TFC membranes, which may lead to further innovative applications and more sustainable membrane processes in the near future.

4.3.3.3.4 Pure water permeability and evaluation of membranes' selectivity using different solutes at different pH values

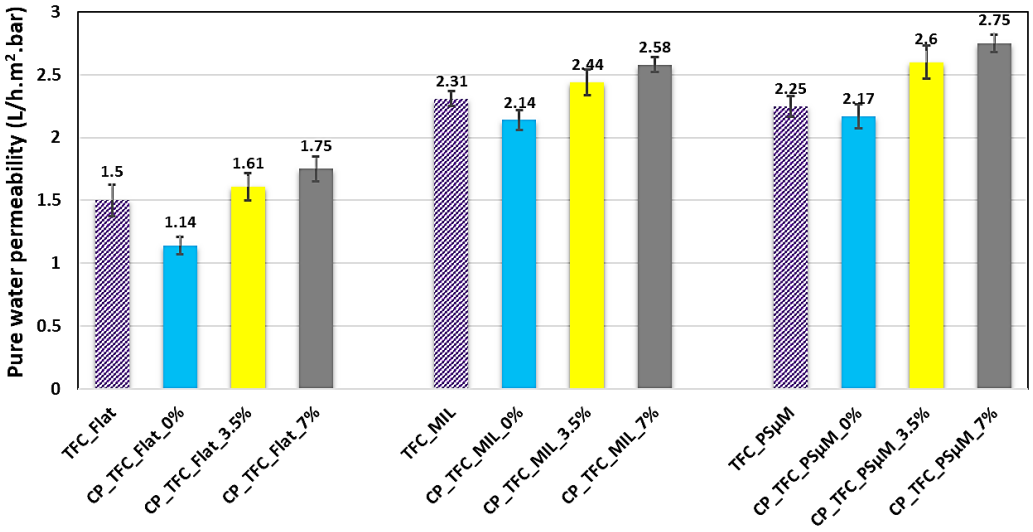

Figure 4.59: Pure water permeability for the surface-modified flat and micro-patterned PA TFC membranes measured using dead-end configuration

The pure water permeability was firstly measured for the surface-modified flat and micro-patterned membranes using dead-end filtration system at ambient temperature and the results were displayed in **Figure 4.59**. All the surface-modified membranes by P(NIPAAm) homo-polymers showed a decrease in the measured pure water permeability that could be attributed to the increase in the hydraulic resistance resulting from the grafting of an additional layer. Such decrease in pure water permeability was interestingly found to be diminished by surface micro-patterning such that CP_TFC_Flat_0% exhibited a decrease by 24 % while CP_TFC_MIL_0% and CP_TFC_PSμM_0% showed much smaller reduction, 7 and 3.5 %,

respectively. This could be explained by the higher membrane surface area available for filtration, as well as the possible irregular coating thickness along the membrane surface micro-structures.

On the other hand, all the surface-modified membranes using P(NIPAAm-co-AAc) copolymers exhibited an increase in the measured pure water permeability, which was observed to be promoted by increasing mol.% of AAc; an improvement in pure water permeability by 17, 10.5 and 18 % was found for surface-modified flat, MIL-based, PSµM-based membranes, respectively. This increase in pure water permeability despite of grafting of an additional layer could apparently be attributed to the incorporation of hydrophilic fractions, i.e., AAc groups, in the top surface layer that might facilitate the water transport through the barrier layer. Similar observation was reported by Yu et al. [208]. More interpretations regarding the surface modification mechanism and its influence on the membranes' transport characteristics will be introduced later (see below).

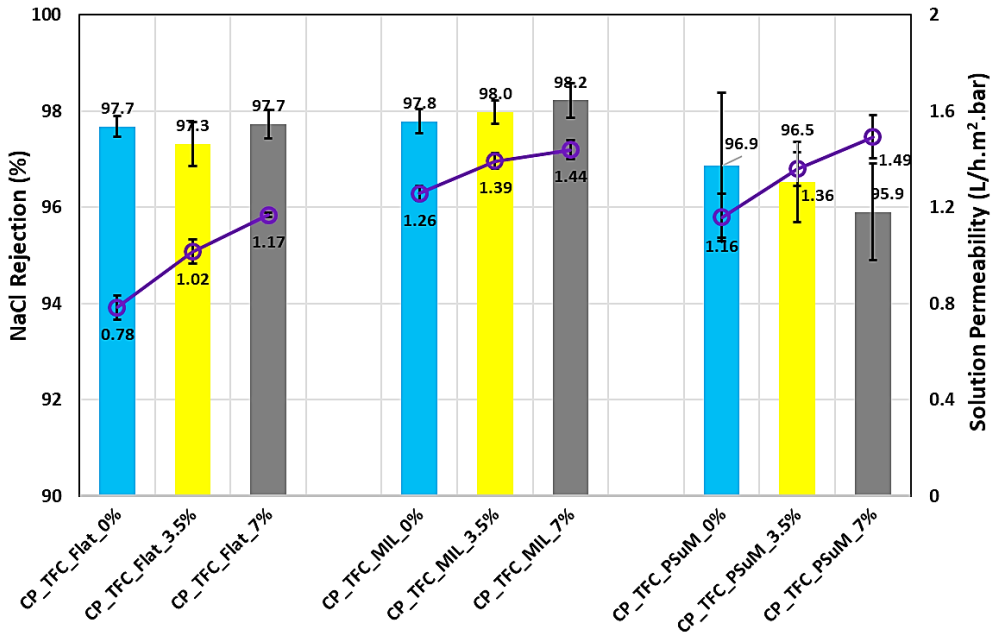

Figure 4.60: Separation performance for surface-modified flat and micro-patterned PA TFC membranes, measured by dead-end filtration of 2,000 ppm NaCl feed solution at pH 6.8

In parallel, the separation performance was evaluated via NaCl dead-end filtration experiments at feed concentration of 2,000 ppm, pH 6.8, ambient temperature and stirring of 700 rpm, then the results were plotted in **Figure 4.60**. In general, the solution permeability was found to have the same trend as the pure water permeability. For flat- and MIL-based surface-modified membranes, an improvement of the permeability was observed along with

comparable membrane selectivity. CP_TFC_MIL_7% exhibited the best membrane performance, permeability of 1.44 L/h.m^2.bar and salt rejection > 98 %. Nevertheless, PSµM-based surface modified membranes were found to have modest separation performance that might be linked to the imperfections inside PA barrier layer that were highlighted before (cf. **section 4.2.4**), besides possible PA dissolution during the surface modification process.

In order to understand the mechanism of the surface modification process and its influence on the membrane performance, two control experiments were performed using flat PA TFC membranes; one was based on treating the membranes with P(NIPAAm) homo-polymer and EDC/NHS mixtures, whereas the second was based on treating the membranes with EDC/NHS mixture only. The separation performance of the produced membranes was assessed using NaCl dead-end filtration experiments and the results were compared with pristine and surface-modified flat membranes (see **Table 4.11**).

Table 4.11: Results for control surface modification experiments using flat PA TFC membranes

Membrane sample	NaCl Rejection (%)	Solution Permeability (L/h.m^2.bar)
TFC_Flat	97	0.91
CP_TFC_Flat_0%	97.7	0.78
CP_TFC_Flat_3.5%	97.3	1.02
CP_TFC_Flat_7%	97.7	1.17
Control (I): P(NIPAAm) + EDC/NHS*	92.2	1.09
Control (II): TFC + EDC/NHS**	85	1.53

*: Homopolymer was mixed with EDC/NHS at pH 4.4 for 1 hour then pH was raised to 7 during coating on membranes

**: EDC/NHS was added directly to TFC membranes at pH 7.

It was found that the permeability enhancement during the surface modification process is mainly related to the treatment using EDC/NHS coupling agents. The grafting process of acrylamide-based polymer materials to the surface of PA TFC membranes is emphasized to include two steps, (i) activation, (ii) grafting / immobilization (cf. **section 2.5.2.2.1**). During the activation step, a partial dissolution of unbounded and not fully cross-linked PA from the membrane surface is occurred upon the reaction with EDC/NHS coupling agents (control I). Thereafter, the acrylamide-based polymer coating is anchored to the activated surface.

Consequently, the surface modification process via "*grafting to*" mechanism is believed to keep (and improve in some cases) the membrane selectivity because of the so-called "repairing action", which is suggested to fix the defects and imperfections inside PA barrier layer [284]. Also, it enhances the water permeability as a result of the introduction of nano-water channels, by incorporation of AAc groups. This proposed mechanism was found to fit very well to the observed behavior of flat- and MIL-based surface-modified membranes, while the results of PSμM-based membranes were shown to be inconsistent with this mechanism due to their susceptibility to the surface modification process.

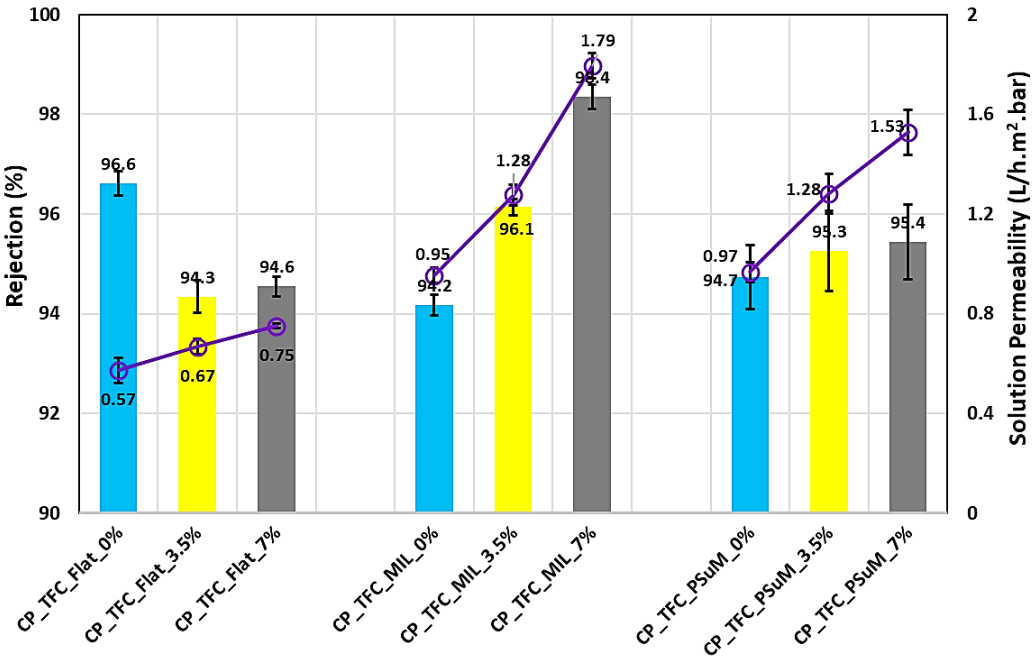

Figure 4.61: Separation performance for surface-modified flat and micro-patterned PA TFC membranes, measured by dead-end filtration of 0.1 M citrate-phosphate buffer solution as a feed at pH 3

Furthermore, the influence of the membrane surface charge at different pH values on the separation performance of surface-modified flat and micro-patterned PA TFC membranes was investigated using dead-end filtration experiments of 0.1 M citrate-phosphate buffer solution at pH 3 (cf. **Figure 4.61**), as well as 0.1 M phosphate buffer solution at pH 7 (cf. **Figure 4.62**). The experiments were carried out at ambient temperature and stirring rate of 700 rpm. The salt rejection was calculated by means of the change in solution conductivity. The feed conductivity was measured to be 2.9 and 18.6 mS/cm in case of 0.1 M citrate-phosphate buffer (~ 10550 ppm) and 0.1 M phosphate buffer (~ 13340 ppm), respectively.

Generally, MIL-based surface-modified membranes were observed to exhibit the best separation performance at both pH values, whereas PSµM-based membranes suffered from modest separation performance. In parallel, the membrane selectivity was observed to be related to the phosphate fraction, or concentration, inside the feed solution such that high phosphate feed concentration was found to result in a superior separation performance; CP_TFC_MIL_7% exhibited phosphate buffer rejection of ~ 99 % and solution permeability of 1.56 L/h.m^2.bar at pH 7. The high retention of phosphate species at elevated concentrations is attributed to the strong electrostatic repulsion between the phosphate negative groups and the "deprotonated" membrane surface negative groups at pH 7, i.e., carboxylic groups (cf. **section 4.3.3.3.1**). This could also account for the lower rejection of citrate-phosphate buffer at pH 3; however, CP_TFC_MIL_7% could also achieve salt rejection of 98.3 % that reflects its defect free and tight barrier layer structure. Additionally, the validity of the suggested repairing mechanism was supported. The solution permeability was found to be enhanced upon surface modification with P(NIPAAm-co-AAc) copolymers rather than P(NIPAAm) homo-polymer.

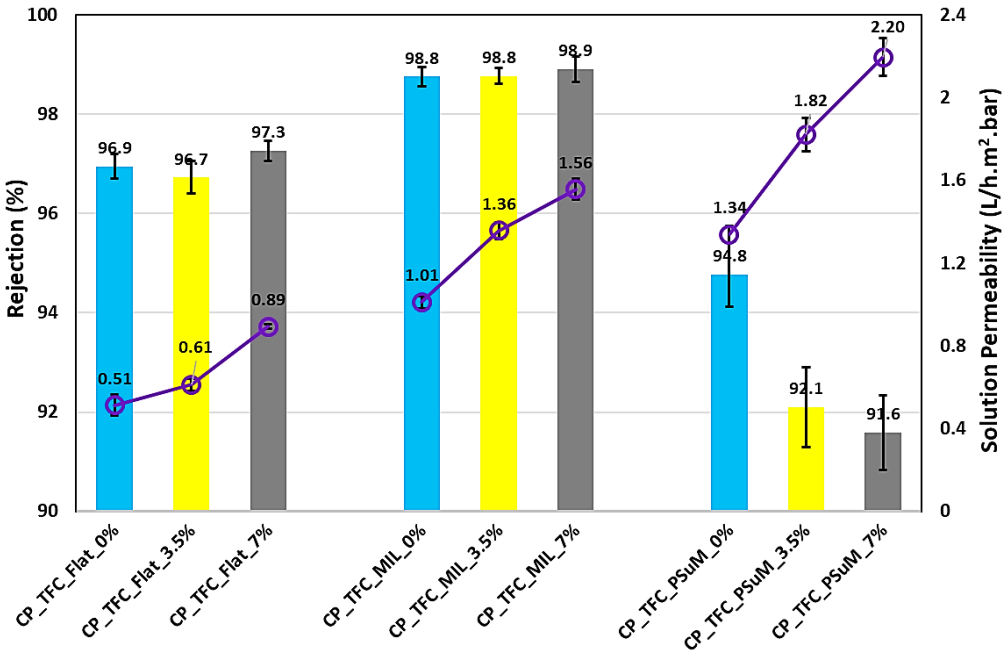

Figure 4.62: Separation performance for surface-modified flat and micro-patterned PA TFC membranes, measured by dead-end filtration of 0.1 M phosphate buffer solution as a feed at pH 7

4.4 Evaluation of antifouling propensity using colloidal silica fouling experiments

Several preliminary experiments were carried out to investigate the antifouling propensity of the novel surface-modified micro-patterned PA TFC membranes at diverse conditions, and to evaluate whether the developed smart surface properties would influence the silica particle deposition. In this section, trials to study the colloidal silica fouling of the pristine and surface-modified micro-patterned PA TFC membranes using dead-end configuration are introduced. Different experimental conditions, including foulant's particle size, temperature, and stirring, were varied to investigate the impact of each individual parameter, as well as combinations of them were applied as well. Moreover, the silica cake layer formed at different colloidal fouling experiments was analyzed using SEM at different measurement modes, i.e., wet and dry cake layer. Furthermore, a mechanism for the spatially selective deposition of silica particles on micro-patterned PA TFC membranes is introduced for the first time.

4.4.1 Selection of membrane samples and characterization of foulants' particles

MIL-based pristine and surface-modified micro-patterned PA TFC membranes were preferentially selected for colloidal silica fouling because of their competitive separation performance and stability, in addition to their high reproducibility and availability to scaling up. Prior to fouling experiments, the flat- and MIL-based membranes were compacted by filtrating 1 liter of Milli-Q water per each membrane sample (11.34 cm^2) using cross-flow filtration system at operating pressure of 20 bar and ambient temperature (cf. **section 3.8**).

Table 4.12: Basic characteristics* of the silica dispersions used as a feed during the colloidal silica fouling experiments

		Silica nanoparticles LUDOX® 50 (50 wt.%)	**Silica micro-particles** (5 wt.%)
Concentration (mg/L) in Milli-Q water		**200**	**200**
pH		**7.4**	**6.7**
DLS	**d_n (nm)**	**45**	**530**
	PDI	**0.11**	**0.17**
Zeta potential (mV)		**- 49.2**	**- 50**

*: The measurements were performed using zeta sizer (PSS NICOMP 380 ZLS).

Two types of silica particles were employed as model foulants, LUDOX® (50 nm) and silica micro-particles (500 nm). An aqueous dispersion of 200 ppm was prepared from each type to be used as a feed solution (cf. **section 3.8**). The feed solutions of both silica types were characterized, and the main solution characteristics are listed in **Table 4.12**. The fouling experiments were performed using dead-end stainless steel nano-filtration cell equipped with a temperature sensor and a digital balance (cf. **section 3.8.2**, **Figure 3.6**).

4.4.2 Colloidal fouling of flat and micro-patterned membranes by silica nanoparticles (50 nm) at no stirring condition

The colloidal fouling of pristine and surface-modified micro-patterned PA TFC membranes by silica nanoparticles, 50 nm, was investigated by filtrating a fixed feed volume, i.e., 98 – 96 ml from total volume ~ 100 ml, through the membrane sample at operating pressure of 16.5 – 17 bar and ambient temperature without stirring, then they were compared with the flat counterparts. The permeate volume and the time were collected till the end of the experiment. Subsequently, the solvent flux decline was plotted vs. permeate volume and the curves are presented in **Figure 4.63**.

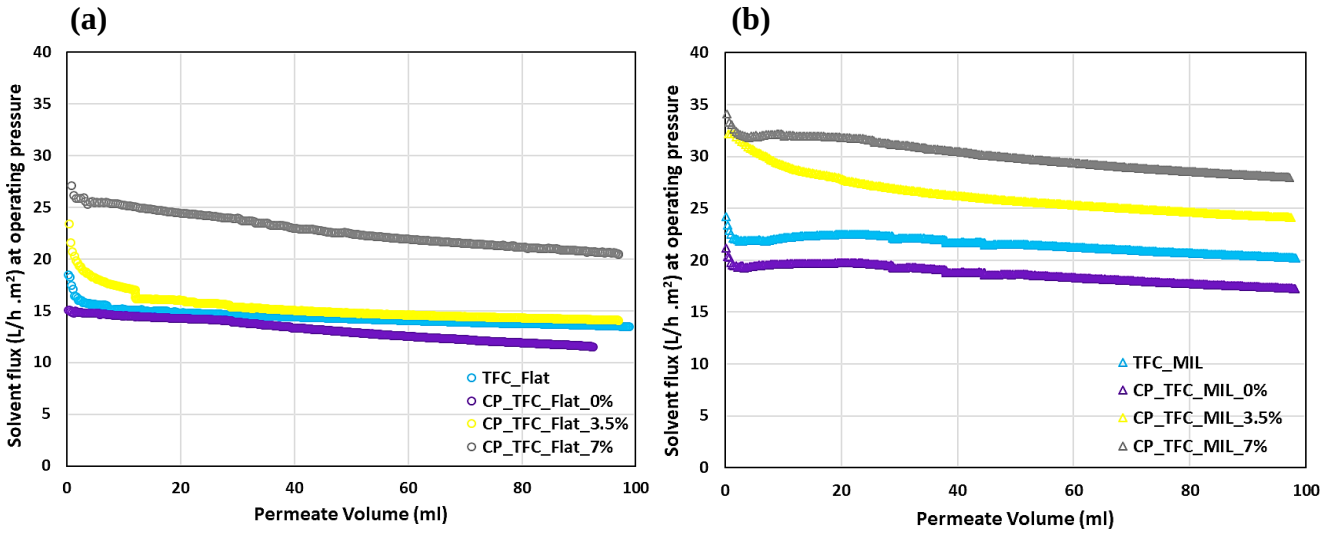

Figure 4.63: Solvent flux decline vs. permeate volume relations for the pristine and surface-modified flat (a) and micro-patterned (b) membranes during colloidal fouling experiments using silica nanoparticles (50 nm) at no stirring condition

The rate of colloidal fouling of a permeable membrane in a laminar or stagnant flow was emphasized to be controlled by an interplay between double layer repulsion and the opposing convective flow toward the membrane surface, called “permeation drag” [88, 115]. In general, the micro-patterned membranes were observed to start the fouling experiments at higher fluxes; consequently, the rate of colloidal fouling will be dominated by the surface micro-structures

and the intrinsic properties of the membrane [73]. The flat membranes showed a typical flux decline alike commercial brackish water membranes [89]. In order to highlight the difference in colloidal fouling behaviors between the flat and micro-patterned membranes, the relative flux decline was plotted vs. permeate volume and the graphs are displayed in **Figure 4.64**.

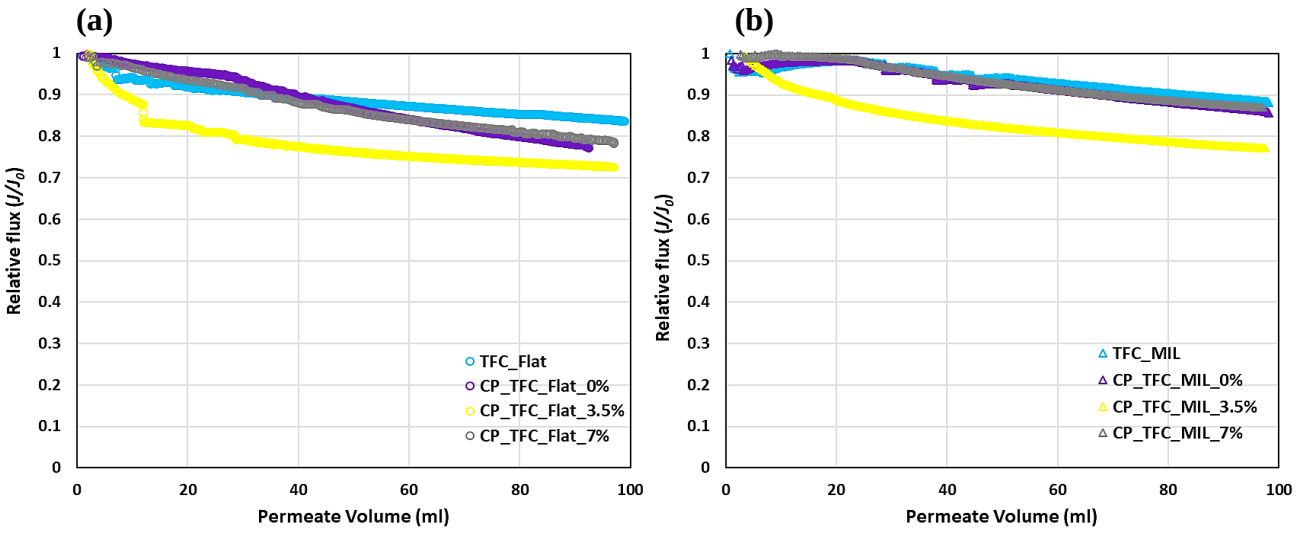

Figure 4.64: Relative flux vs. permeate volume relations for the pristine and surface-modified flat (a) and micro-patterned (b) membranes during colloidal fouling experiments using silica nanoparticles (50 nm) at no stirring condition

Notwithstanding the higher initial fluxes, a substantial delay in the onset of fouling was observed for most of the micro-patterned membranes in comparison with the flat counterparts, which could be attributed to the extended membrane surface area as a result of surface micro-patterning along with possible transverse hydrodynamic effects. In addition, the extent of colloidal fouling, deduced from the ultimate relative flux decline at the end of the experiment, was also found to be lower in case of micro-patterned membrane than for the flat membranes.

The influence of surface modification on the extent of colloidal fouling of the flat membranes can be concluded from **Figure 4.64 (a)**. The extent of colloidal silica fouling was shown to be higher in case of surface-modified membranes than the pristine membrane. This could be attributed to the enhancement in the water flux upon the surface modification (cf. **section 4.3.3.3.2**). Nevertheless, expect CP_TFC_MIL_3.5%, the influence of surface modification on the colloidal fouling of micro-patterned membranes by silica nanoparticles was insignificant.

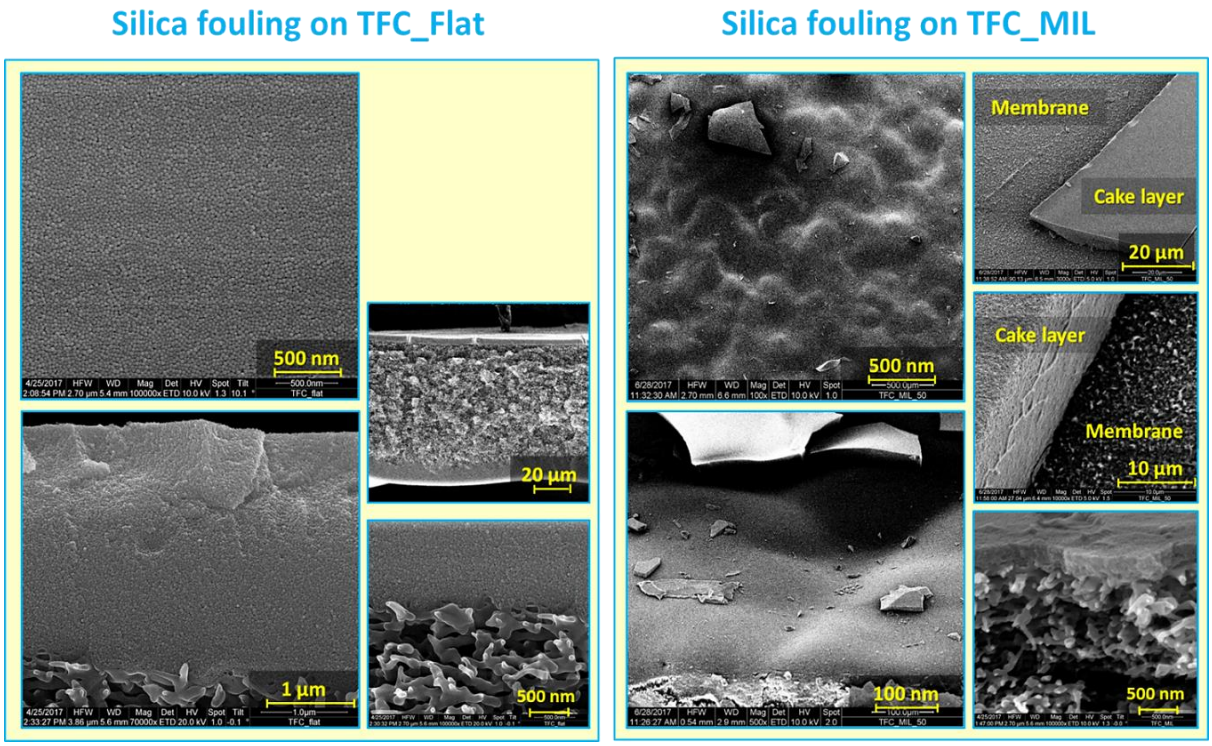

Figure 4.65: SEM micro-graphs for colloidal silica fouling of the pristine flat and micro-patterned PA TFC membranes using silica nanoparticles (50 nm) at no stirring condition

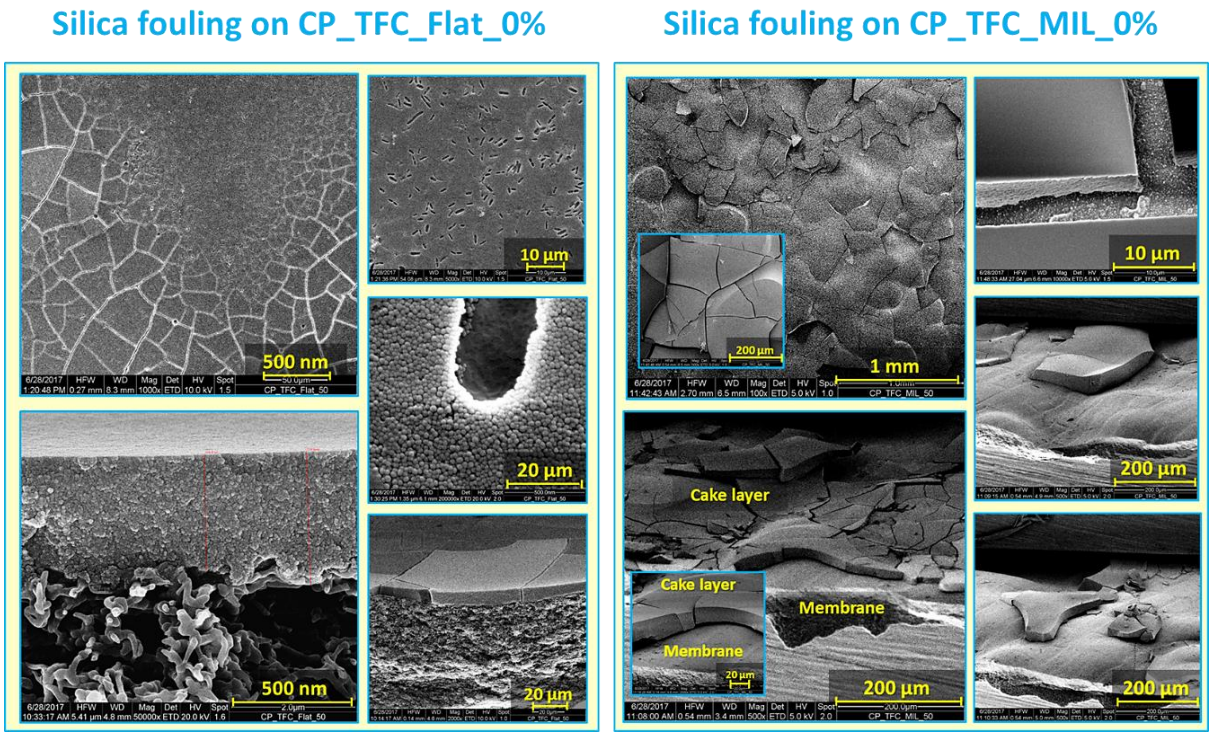

Figure 4.66: SEM micro-graphs for colloidal silica fouling of CP_TFC_Flat_0% and CP_TFC_MIL_0% membranes using silica nanoparticles (50 nm) at no stirring condition

Furthermore, selected pristine and modified membranes were analyzed by means of SEM after the colloidal silica fouling experiments. The SEM micrographs at different magnifications for fouled TFC_Flat and TFC_MIL membranes are shown in **Figure 4.65**, and SEM images for fouled CP_TFC_Flat_0% and CP_TFC_MIL_0% membranes are presented in **Figure 4.66**. SEM analysis for dry fouled MIL-based membranes revealed a non-homogenous deposition of the silica nanoparticles on the micro-patterned membrane surfaces that was believed to result in the visible cracks over the entire deposited silica layer due to the unequal stress, which is also supported by the reduced relative flux decline. It is worth to mention that these cracks in the silica cake layer were also observed during SEM analysis of the wet fouled membranes. This indicates that the stress in the silica cake layer, which resulted in enhanced antifouling behavior, is mainly due to a possible alteration in the silica deposition behavior rather than influences of the experimental procedures for membrane characterization. On the contrary, TFC_Flat exhibited a crack-free thick silica cake layer that was found to reach 3 µm thickness, while CP_TFC_Flat_0% was unexpectedly observed to have less thick silica cake layer, ~ 2 µm in spite of its higher relative flux decline than TFC_Flat membrane.

4.4.3 Influence of external stimulus on colloidal fouling by silica nanoparticles

Moreover, the influence of external stimulus on the colloidal fouling of three representative flat and micro-patterned membranes by silica nano-particles was explored. TFC_Flat was chosen as blank sample, i.e., un-modified and un-micro-patterned, while CP_TFC_Flat_0% and CP_TFC_MIL_0% were selected as representative membranes to study the joint influence of surface modification only, and the influence of surface modification consolidated with surface micro-patterning, respectively. Three stimuli were employed, temperature only, mixing only, as well as both of them simultaneously. The thermal stimulus involved gentle heating up to 40 °C. The mixing stimulus involved stirring at 700 rpm. The point, at which the external stimulus was switched on, was defined according to the fitting range of colloidal fouling systems to the cake filtration model.

4.4.3.1 Applicability of cake filtration model

The applicability of cake filtration model to the data of colloidal fouling of flat and micro-patterned membranes by silica nanoparticles was examined by plotting the reverse cumulative flux vs. permeate volume, which should yield a linear relationship if the silica fouling is governed by cake filtration mechanism [89]. The curves are displayed in **Figure 4.67**. The colloidal fouling of all flat and micro-patterned membranes was found to yield linear

relationships, therefore the dominant mechanism for all colloidal fouling systems is the cake filtration mechanism.

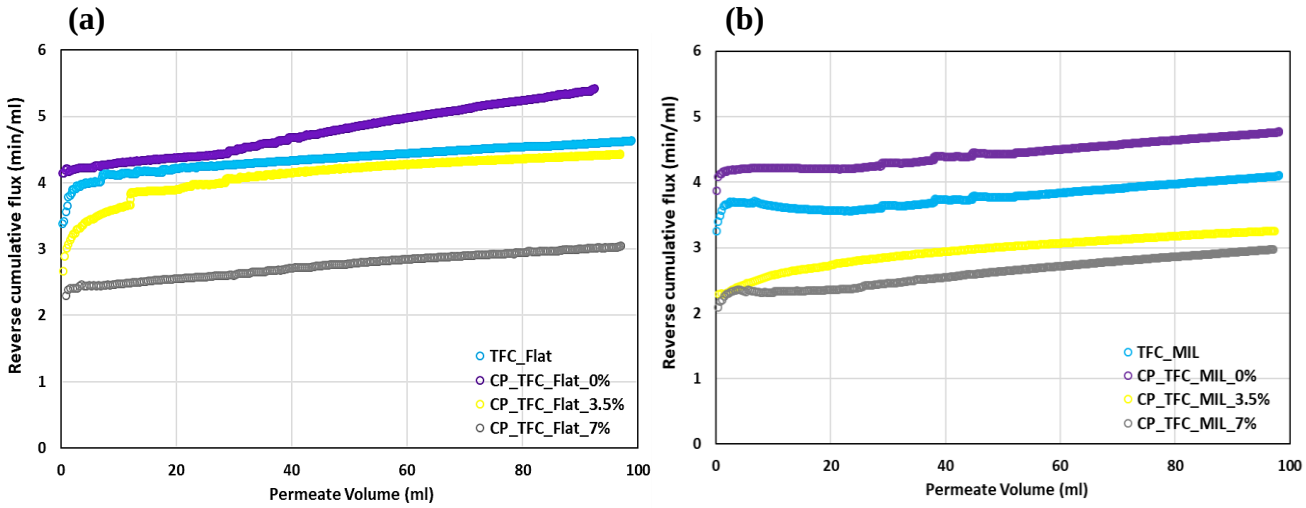

Figure 4.67: Reverse cumulative flux vs. permeate volume relations for the pristine and surface-modified flat (a) and micro-patterned (b) membranes during colloidal fouling experiments using silica nanoparticles (50 nm) at no stirring condition

The fitting range of the colloidal fouling systems to the cake filtration mechanism was investigated by re-plotting the fouling results using the cake filtration equation (cf. **Table 2.1**). The graphs are presented in **Figure 4.68**. Most of the colloidal fouling systems were affirmed to exhibit a perfect fitting to the cake filtration mechanism (> 0.95) at permeate volume starting from 15 ml. This implies that also for TFC membranes of this study blocking of defects in the active layer does play a role. However, the period/relative volume is lower than the deviation observed and explained by Wang and Tarabara [89] (cf. section **2.3.4.2**). This indicates the efficiency of the exploited preparation and surface modification procedures. Subsequently, the

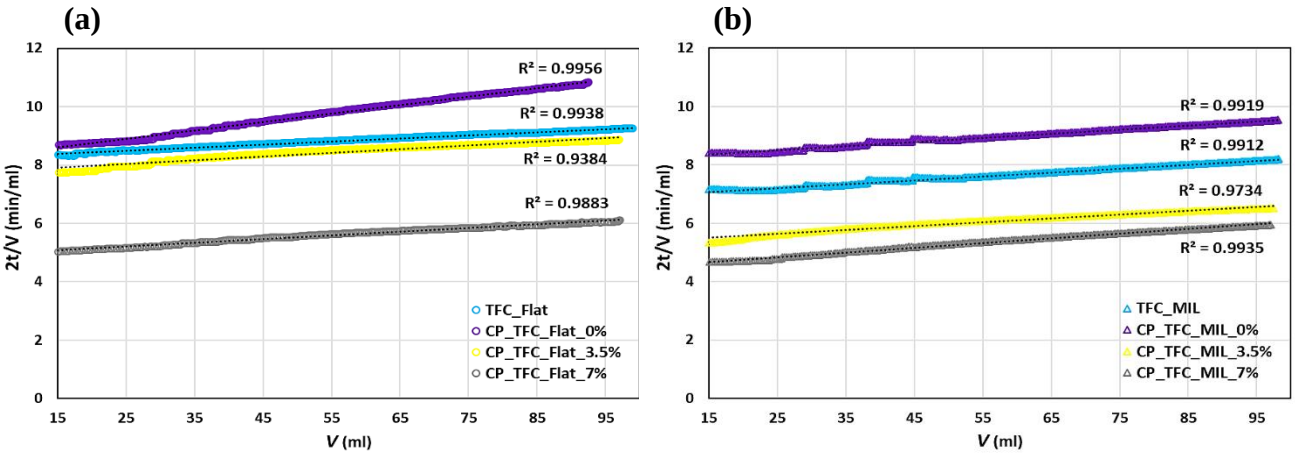

Figure 4.68: Fitting range of colloidal silica fouling of the pristine and surface-modified flat (a) and micro-patterned (b) membranes to cake filtration mechanism during colloidal fouling experiments using silica nanoparticles (50 nm) at no stirring condition

external stimulus was switched on when 40 ml of the silica feed solution was filtrated through the membranes.

4.4.3.2 Influence of external stimulus on deposition behavior of silica nanoparticles

Prior to the colloidal fouling experiments at different stimuli, control experiments were carried out to investigate the change in pure water flux for the three representative membranes upon increasing of the system temperature to 40 °C (cf. **section 3.8.2**). The curves are introduced in **Figure 4.69**. The pure water flux for all membrane samples was found to increase upon increasing of the system temperature. The water transport through PA TFC membranes is well-known to be diffusion controlled (cf. **section 2.3.3.1**); consequently, increasing the system temperature would increase the diffusion rate. Thereafter, the pure water flux was observed to decrease when the system is cooled down again to room temperature.

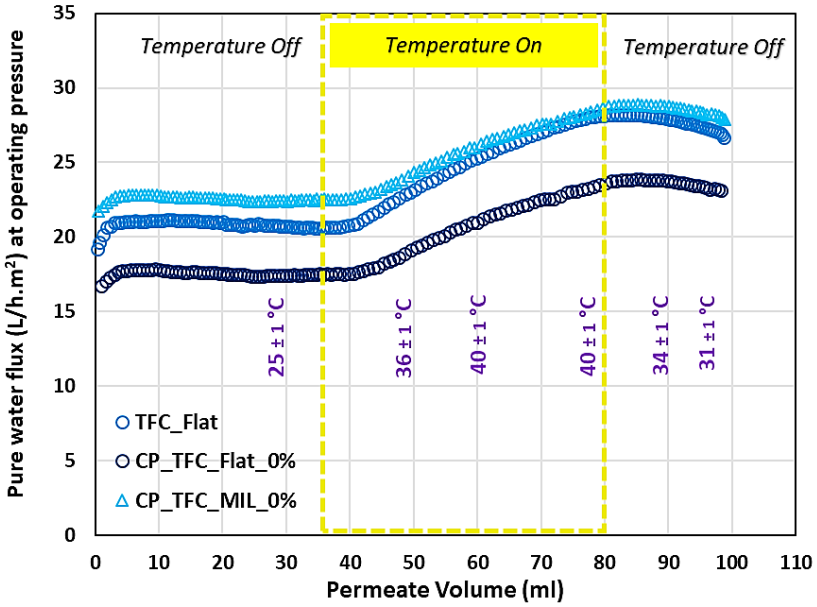

Figure 4.69: Measurement of pure water permeability using dead-end configuration at different system temperatures for selected pristine and surface-modified PA TFC membranes

Afterward, the influence of external stimuli on the colloidal silica fouling of three representative membranes was investigated and the relative flux graphs are presented in **Figure 4.70**. Generally, the relative fluxes for all membranes were shown to increase upon applying the thermal stimulus, which is essentially attributed to the increase of the diffusion coefficients, as affirmed via earlier control experiments. Nevertheless, the influence of stirring on the relative flux decline was interestingly found to differ for each membrane sample. In case of TFC_Flat, the reduction in the relative flux, due to colloidal silica fouling, was observed to stop (at ~ 0.83) as soon as the stirring was switched on. While, in case of CP_TFC_Flat_0%

and CP_TFC_MIL_0% the relative flux was found to increase as soon as the stirring was switched on. However, it is worth to notice that the relative flux was completely recovered in case of CP_TFC_MIL_0%, whereas it was partially restored (~ 0.95) in case of CP_TFC_Flat_0%. This could be explained by a possible reduction in the fouling layer

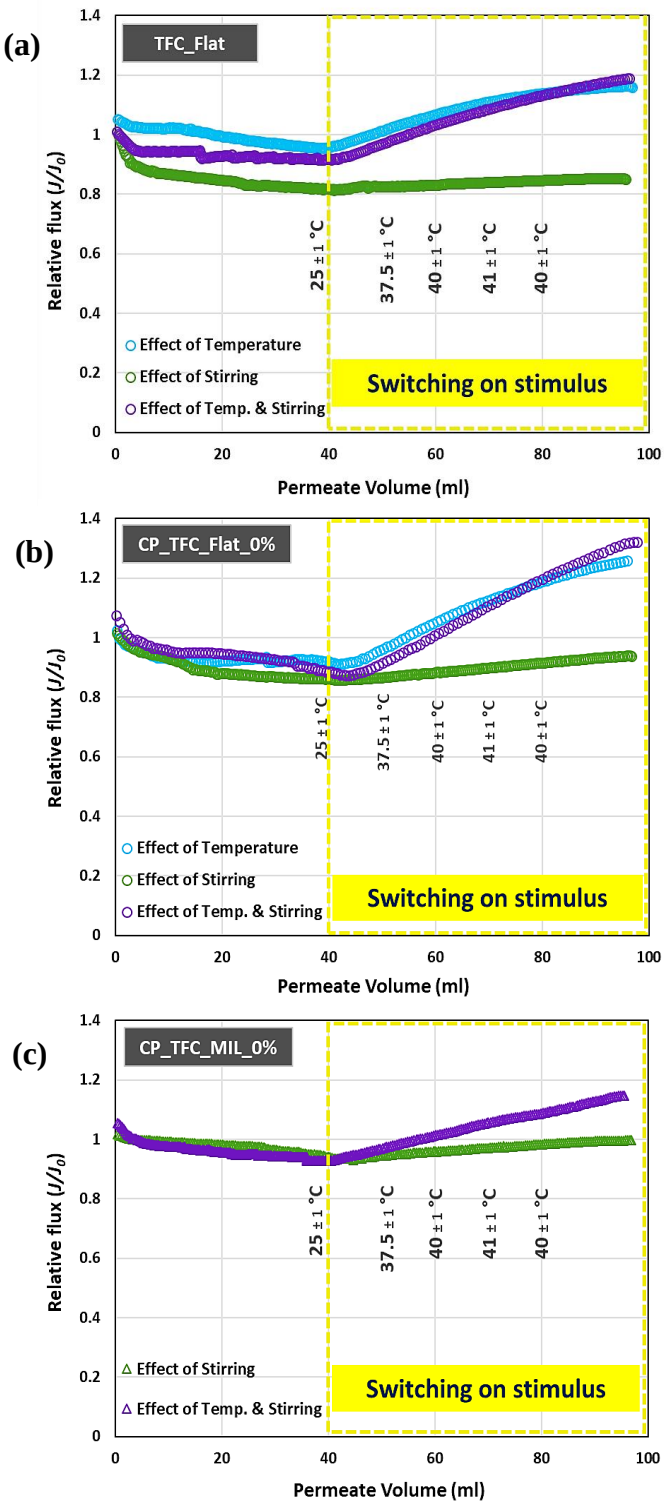

Figure 4.70: Influence of external stimulus on colloidal silica fouling of selected membranes, TFC_Flat (a), CP_TFC_Flat_0% (b), and CP_TFC_MIL_0% (c), using silica nano-particles (50 nm)

resistance on the micro-patterned and surface-modified membrane surfaces upon changing the hydrodynamics near the membrane surface, i.e., applying stirring stimulus. Nevertheless, the implementation of a combined thermal and stirring stimuli was revealed to have no substantial influence on the colloidal silica fouling.

In conclusion, the stirring may have high potential to remove particles from the micro-patterned membrane surfaces compared to the flat ones. Surface modification was revealed to have a secondary impact on the colloidal silica fouling; surface-modified membranes showed lower fouling propensity than unmodified membranes. The colloidal fouling of micro-patterned membranes by bigger silica particles was also investigated for further understanding of the impact of surface micro-structures on the particle deposition behavior.

4.4.4 Colloidal fouling of flat and micro-patterned membranes by silica micro-particles (500 nm) at no stirring condition

The colloidal silica fouling of selected micro-patterned membranes by silica micro-particles, 500 nm, was studied at no stirring conditions. Four membrane samples were chosen for these experiments. The fouling propensity of TFC_MIL and CP_TFC_MIL_0% membranes were compared with that of TFC_Flat and CP_TFC_Flat_0% membranes. The same experimental procedures were followed and the solvent flux decline was measured till 96 – 98 % of the silica feed dispersion was filtered through the membrane. The solvent flux decline was then plotted vs. permeate volume, and the curves are shown in **Figure 4.71**. The micro-patterned membranes were observed to start at higher fluxes than the flat membranes. In addition, the surface-modified flat and micro-patterned membranes by P(NIPAAm) homo-polymer exhibited lower solvent fluxes and relatively higher fouling propensity.

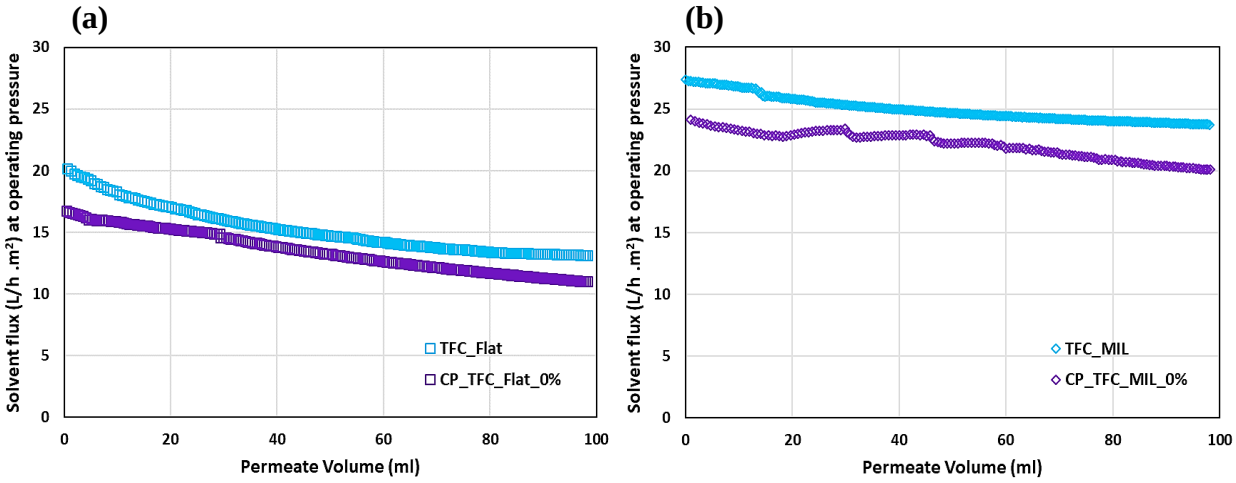

Figure 4.71: Solvent flux decline vs. permeate volume relations for the pristine and surface-modified flat (a) and micro-patterned (b) membranes during colloidal fouling experiments using silica micro-particles (500 nm) at no stirring condition

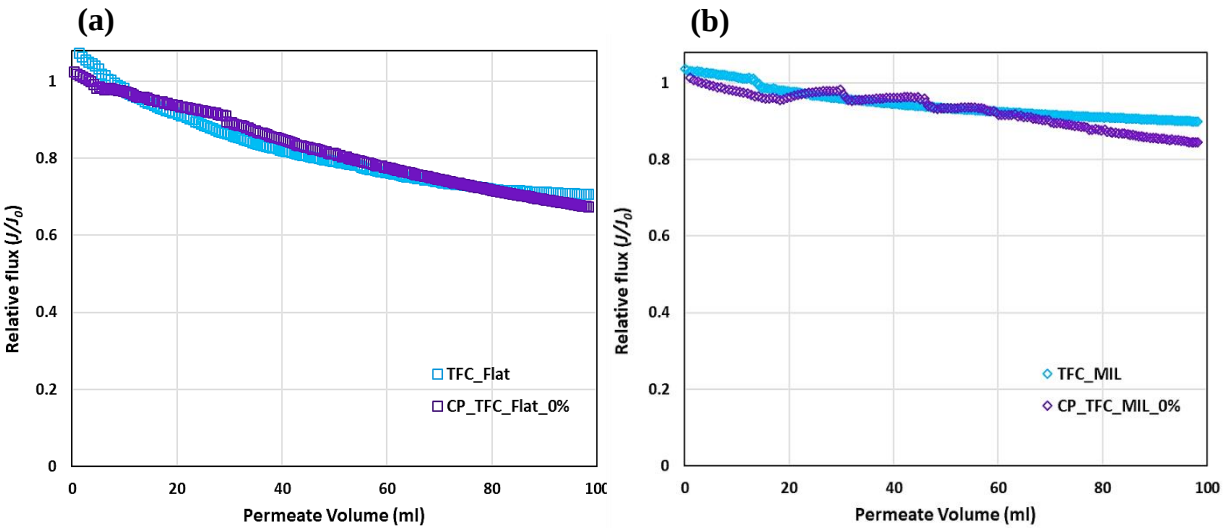

Figure 4.72: Relative flux vs. permeate volume relations for the pristine and surface-modified flat (a) and micro-patterned (b) membranes during colloidal fouling experiments using silica micro-particles (500 nm) at no stirring condition

The relative flux decline was then plotted vs. permeate volume for clearer understanding of the colloidal fouling behavior in both cases, i.e., flat and micro-patterned membranes (cf. **Figure 4.72**). A substantial improvement in the fouling resistance was emphasized for pristine micro-patterned PA TFC membrane in comparison with the flat counterpart such that ~ 50 % enhancement in the relative flux was found. However, less improvement was observed in case of CP_TFC_MIL_0%, which supports the claim concerning the secondary influence of the surface modification on the colloidal silica fouling (cf. **section 4.4.3**).

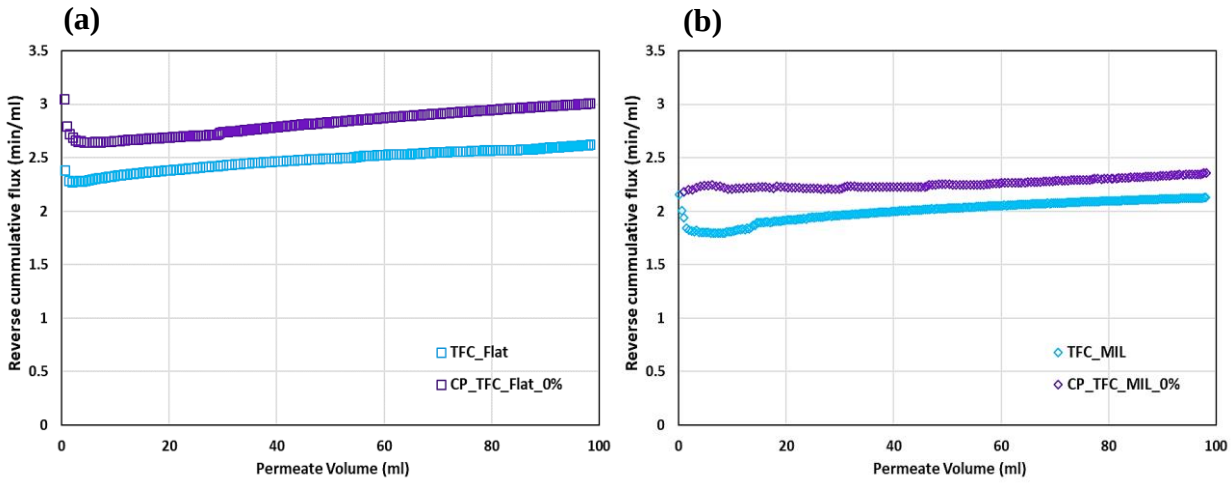

Figure 4.73: Reverse cumulative flux vs. permeate volume relations for the pristine and surface-modified flat (a) and micro-patterned (b) membranes during colloidal fouling experiments using silica micro-particles (500 nm) at no stirring condition

Moreover, the mechanism of colloidal fouling of flat and micro-patterned membranes by silica micro-particles was investigated by plotting the reverse cumulative flux vs. permeate

volume as presented in **Figure 4.73**. Linear relationships were found for relative permeate volume > 15 %; consequently, the cake filtration mechanism was affirmed to be the dominant fouling mechanism by silica micro-particles.

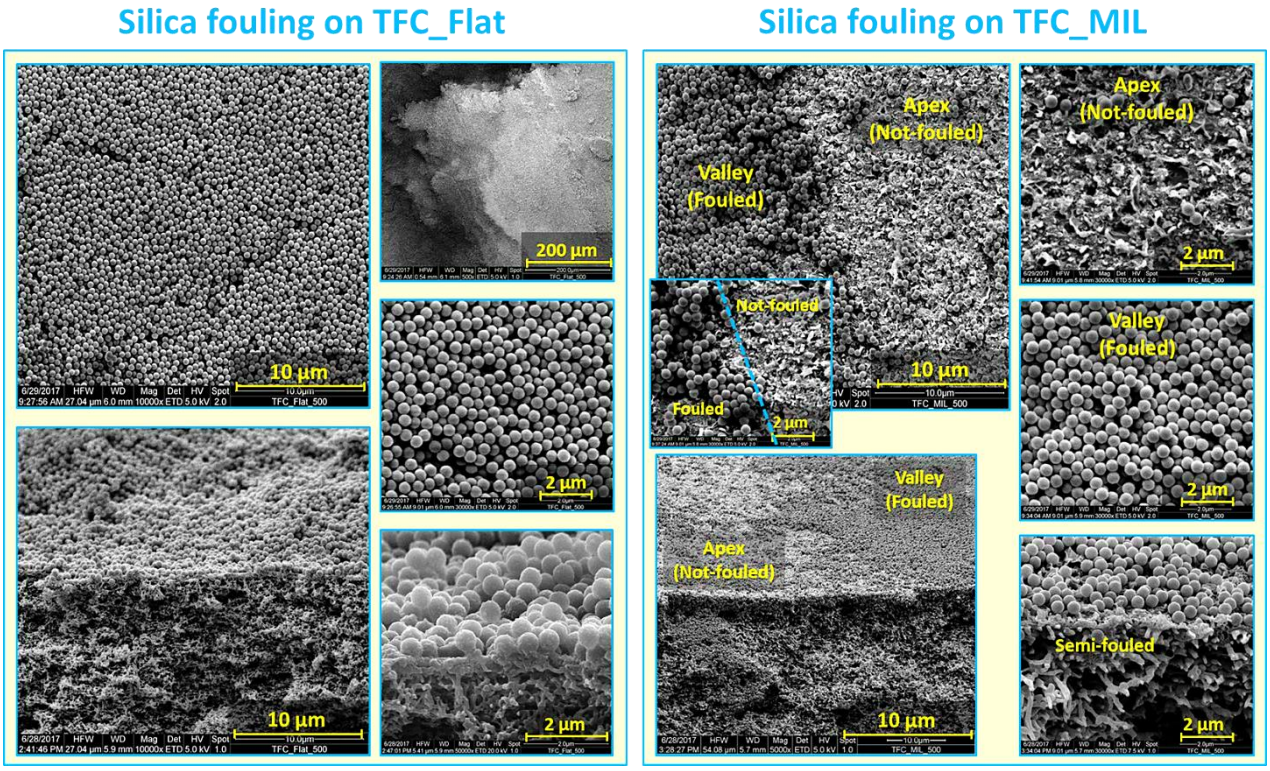

Figure 4.74: SEM micro-graphs for colloidal silica fouling of the pristine flat and micro-patterned PA TFC membranes using silica micro-particles (500 nm) at no stirring condition

Attempts were made to interpret the enhancement in the antifouling propensity of the micro-patterned PA TFC membranes. The dry fouled flat and micro-patterned PA TFC membranes were analyzed using SEM (see **Figure 4.74**). Thick and dense silica cake layer was observed in case of TFC_Flat membrane, whereas essential different silica cake layer characteristics were interestingly found in case of TFC_MIL membranes. The preponderance of the silica micro-particles was revealed to deposit / accumulate in the valley regions of the surface micro-patterns rather the apex regions, where the silica particles were found to be randomly distributed within PA characteristic ridge-and valley morphology. Furthermore, extended parts of the apex regions were shown to be uncovered by the silica micro-particles, i.e., not fouled during the experiment time. Surely, this unique phenomenon could account for the significant improvement in the fouling resistance of the micro-patterned membranes; however, more experiments are still required to investigate all the relevant circumstances resulting in this outstanding antifouling propensity.

In conclusion, the current work is supporting the earlier findings claiming that the membrane surface roughness is the most influential parameter controlling the colloidal fouling propensity of PA TFC membranes [73, 115, 119]. Additionally, surface modification could be beneficial to suppress initial stage of fouling and/or promote the release of the fouling layer under stirring or cross-flow condition (cf. **section 4.4.3.2**).

4.4.4.1 Suggested mechanism for the deposition of silica micro-particles on the micro-patterned membrane surfaces at no stirring condition

Notwithstanding the limited colloidal fouling experiments, a mechanism explaining the unique deposition behavior of silica micro-particles (500 nm) on the micro-patterned membrane surfaces at no stirring condition was suggested based on our experiments and SEM analysis, along with the reported literature on related topics. An illustration for the suggested mechanism is introduced in **Figure 4.75**.

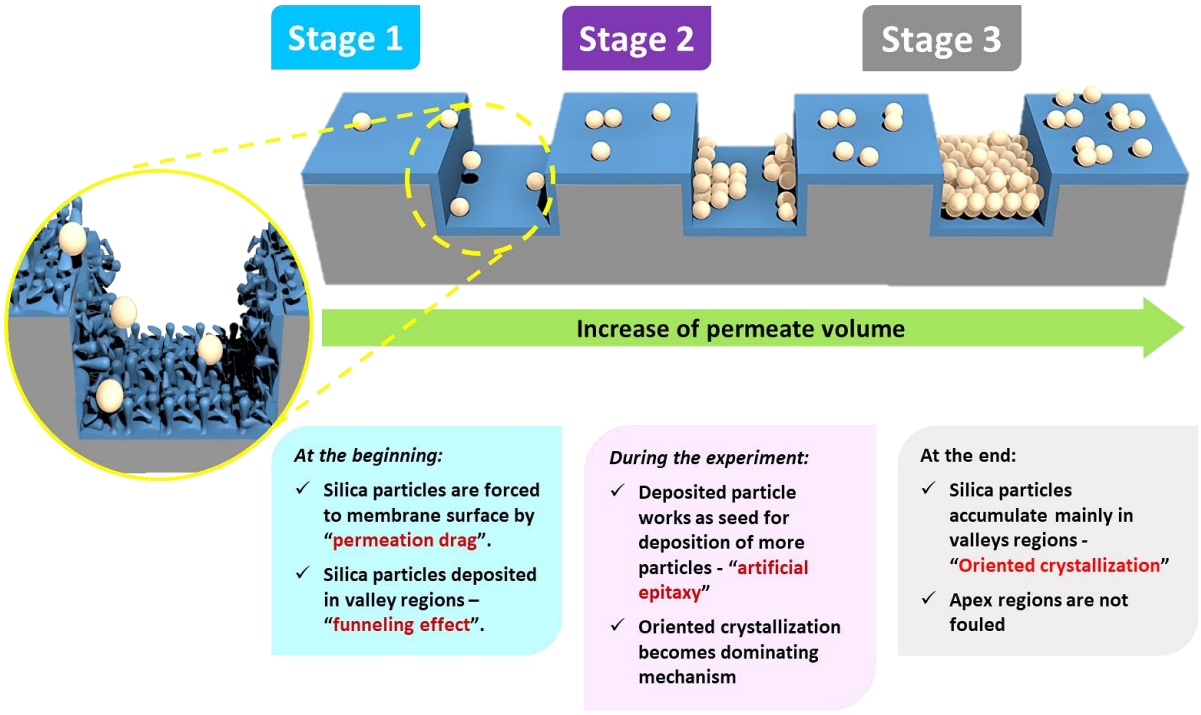

Figure 4.75: Suggested mechanism for deposition of colloidal silica micro-particles (500 nm) atop the micro-patterned PA TFC membranes at no stirring condition

The suggested mechanism of silica micro-particles on the micro-patterned membrane surfaces at no stirring condition comprises **three stages**:

Stage (i) At the beginning of the fouling experiment, the silica micro-particles were forced to the membrane surface by the so-called "permeation drag" that resulted from the high silica concentration in the bulk solution as well as the high initial flux, i.e.,

convective flow, of TFC_MIL membranes [73]. In parallel, the valley regions are imagined to act as favorable sites for the silica micro-particles, funneling effect, because of the extremely low shear stress [129]. In addition, the valley regions were simulated to exhibit low DLVO potential energy, i.e., low energy pockets, [119, 183].

Stage (ii) Deposited silica micro-particles are postulated to work as seeds for deposition of more silica micro-particles in a phenomenon known as "artificial epitaxy". This condition was previously introduced by Givargizov as one possible mechanism, namely "orientation by topographic relief", of four mechanisms interpreting the artificial epitaxy phenomenon [285, 286]. This oriented crystallization is proposed to be a dominating process during this stage.

Stage (iii) At the end of the colloidal fouling experiment, most of the silica micro-particles accumulated in the valley regions of the surface micro-pattern, while the apex regions were not fouled, which was believed to explain the distinguished antifouling propensity of the micro-patterned PA TFC membranes.

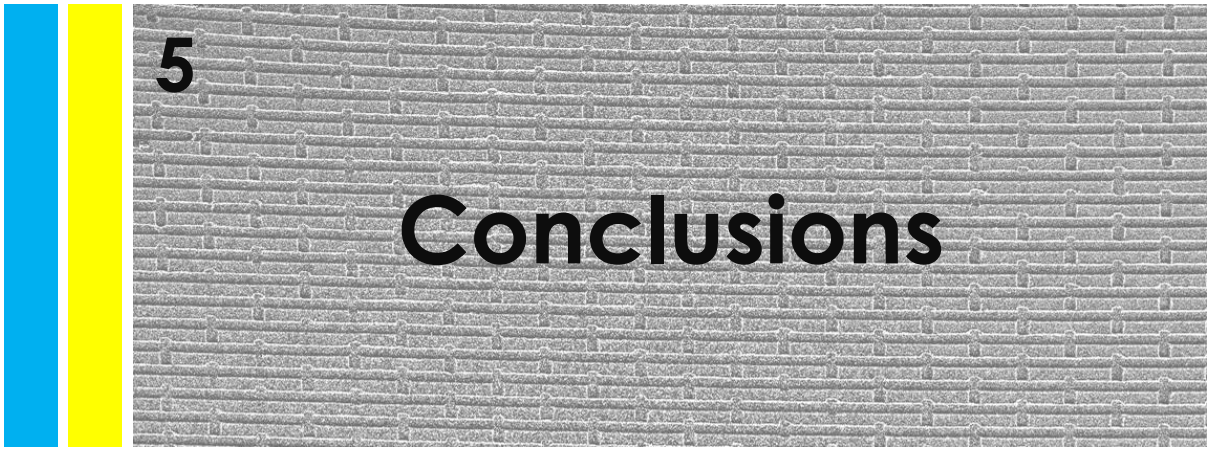

5 Conclusions

The development of micro-patterned PA TFC membranes exhibiting superior separation performance and improved antifouling propensity was introduced. To the best of our knowledge, the current work is the first successful attempt to synthesize micro-patterned RO PA TFC membranes employing tailor-made isotropic membrane supports and using custom-adapted fabrication procedures. Numerous findings were revealed during the work progression that are presented in the following points:

- The combination between VIPS and NIPS processes along with an optimized PVP/PES ratio and high TEG fractions (> 40 wt.%) in the casting solution were found to be an effective approach to attain hydrophilic, high water permeability and robust isotropic membrane structures of controlled average barrier pore diameter (~ 100 nm) with high reproducibility.
- Surface characteristics and separation performance of TFC membranes obtained by IP method were confirmed to be highly influenced by the supports' characteristics. The developed isotropic PES supports were emphasized to enhance the water permeability and mechanical stability of PA TFC membranes in comparison with conventional polysulfone anisotropic supports.
- Two surface micro-patterning techniques, PSµM and MIL, were alternatively used to prepare micro-patterned PES supports. In PSµM, a combined process of VIPSµM and NIPSµM was successfully established to yield micro-patterned supports of uniform pore size distribution. In parallel, a simplified and low-cost bench-scale setup, employing pressure filtration cell and PDMS mold, was also successfully developed to imprint flat PES membranes.

- Notwithstanding using the same PDMS mold, the utilized surface micro-pattering procedures were observed to result in micro-patterned supports of different surface topography and surface roughness. PSμM produced symmetrical patterns, whereas MIL yielded surface micro-structures that are much closer to the used mold.
- Afterward, tight PA films, obtained by IP, were specifically adapted atop the micro-patterned PES supports. In comparison with flat membranes, the developed micro-patterned PA TFC membranes showed a superior permeability without a detrimental impact on the membrane selectivity. The eminent enhancement in the permeability was implied to be strongly related to the enhanced membrane active surface area and the significant increase in the membrane surface roughness.
- Additionally, cross-flow directional separation performance experiments were performed at turbulent flow conditions employing different NaCl feed concentrations, and the main concentration polarization parameters were estimated. The orientation of the surface micro-channels to the direction of feed cross-flow was emphasized to influence the separation performance, especially at high feed concentrations; “parallel” orientation was found to reduce significantly the concentration polarization. This could be interpreted by the improvement of the flow circulation atop the surface micro-structures upon employing “parallel” orientation that led to efficient surface-induced mixing effects, high shear rate, and minimizing the boundary layer thickness.
- Moreover, surface micro-patterning approach was successfully consolidated with “dual stimuli-responsivity” phenomena to produce micro-patterned PA TFC membranes that can switch between strong surface hydrophilicity and surface hydrophobicity for the first time.
- The dual stimuli-responsive PA TFC membranes were fabricated via grafting of acrylamide-based polymer materials to micro-patterned PA TFC membranes by means of well-suited surface coating procedure using EDC/NHS coupling chemistry. The super-switching properties were evaluated by measuring the static water contact angles at different pH and temperature values.
- The surface-modified micro-patterned PA TFC membranes were observed to exhibit higher water permeability accompanied by improvement in membrane selectivity in comparison with the pristine membranes. The control experiments reinforced the suggested repairing mechanism of the defects in the active PA layer that occurred during

surface modification step. In parallel, the immobilized AAc groups were also proposed to serve as water nano-channels that promote the permeability without sacrificing the membrane selectivity.

- Surface-modified and pristine micro-patterned PA TFC membranes based PES_MIL were emphasized to exhibit better separation performance and improved membrane stability rather than those based on PES_PSµM. In addition, the fabrication of MIL-based membranes is more straightforward and less complicated to be scaled up in comparison with PSµM-based membranes.
- Eventually, preliminary experiments were carried out to investigate the influence of the surface micro-patterning and chemical surface modification on the colloidal fouling of PA TFC membranes using model silica nano- and micro-particles. It was revealed that the membrane surface topography and roughness are the most influential parameters controlling the colloidal fouling of TFC membranes.
- The chemical surface modification was concluded to have a secondary impact on the colloidal fouling of TFC membranes. No obvious improvement had been found during unstirred filtration of colloidal silica particles, but the hydrogel coating was revealed to promote the reduction of the fouling layer resistance after switching on stirring during continued filtration.
- Furthermore, the micro-patterned PA TFC membranes were emphasized to exhibit a significant enhancement in the antifouling propensity during unstirred particle filtration experiments. This could be attributed to a combined mechanism of permeation drag, funneling effect and oriented crystallization phenomena that were implied to result in a spatially selective deposition of the silica particles within the valley regions of the surface micro-patterns and keeping the apex regions not-fouled.

This page is intended to be empty

6 Outlook

Notwithstanding environmental concerns with the current desalination plants, seawater desalination could serve as a sustainable technological solution to global water shortages. The current work is considered as one of several attempts to further improve the RO desalination process and reduce the energy consumption. The exploitation of the "super-switching" concept to modify water desalination membranes, via consolidating "surface micro-patterning" and "double stimuli-responsivity" approaches, is a new interesting trend that can offer competent surface characteristics and lead to innovative membrane applications. Nevertheless, supplemental investigation and refinement studies are still required to achieve more efficient membrane systems. Some of the suggested development routes are briefly introduced in the following points:

- The contribution of the imprinted surface micro-structures atop PA TFC membranes in enhancing their separation performance and minimizing the concentration polarization, at specific membrane orientation to the feed cross-flow direction hasn't been completely understood. Further experiments should be performed using different feed solutions, at various flow conditions, i.e., various Reynolds numbers, at each relevant membrane orientation.
- Additionally, more insights into the alteration in the hydrodynamics near the membrane surface as a result of the imprinted surface micro-structures could be realized by means of particle imaging velocimetry (PIV) for various geometries and at different linear velocities.
- Most of the published experimental and computational work regarding the separation performance and the antifouling properties of surface-patterned membranes are found to be limited to the employed pattern's shape and/or pattern's dimension, besides the testing

conditions. Accordingly, a comprehensive study on the relevant interrelationships between the surface patterns' design and the membrane performance at different flow regimes should be done.

- Concerning the developed and well-adapted surface micro-patterning methods, additional experiments are needed to find out the feasibility of using different mold material, e.g., metals or thermoplastics, in order to overcome the practical limitation of the elastic PDMS materials in MIL process. In parallel, direct surface patterning of PA TFC membranes via thermal embossing lithography has recently been introduced as a possible high throughput alternative, despite of the concerns regarding its influence on the selectivity of the PA layer.
- Moreover, further optimization is recommended towards a well-controlled surface modification procedure, which is able to obtain a very thin, < 40 nm, dual stimuli-responsive layer exhibiting a homogeneous layer thickness atop the entire surface micro-patterns without a detrimental impact on the membrane perm-selective properties.
- More experiments are also recommended to interpret the spatially selective particle deposition behavior on the micro-patterned surfaces, and investigate the possible alteration in that disposition behavior in case of changing the particle size, pattern's design and/or dimension, and the flow regime.
- Furthermore, an investigation for the relevant fouling experiments' conditions is strongly required to study the antifouling propensity of the newly developed surface-modified micro-patterned PA TFC membranes towards different types of fouling.
- In parallel, the potential of membrane cleaning approach utilizing the super-switching wettability properties of these new membranes could also be one of the promising trends toward sustainable membrane operations and reducing the energy consumption.

Overall, the surface micro-patterning using imprinting lithographic technologies is emphasized to be a promising approach toward high throughput membrane micro-fabrication process. It has recently received a great attention by several membrane developers to investigate the feasibility of scaling up of the current experiments and building up the first roll-to-roll machine to prepare micro-patterned PA TFC membrane modules. In fact, very recently, the roll-to-roll surface patterning of PES UF membranes – which could be used as supports for PA TFC membranes – had been reported for the first time [287].

7 References

[1] WWAP, The United Nations World Water Development Report 2015: Water for a Sustainable World, in: U.N.W.W.A. Programme (Ed.), UNESCO, France, 2015.

[2] World Health Organization, Water, Sanitation and Hygiene Links to Health: Facts and Figures, 2004.

[3] WWAP, The United Nations World Water Development Report 2009: Water in a Changing World, in: U.N.W.W.A. Programme (Ed.), UNESCO, France, 2009.

[4] UNEP, Vital Water Graphics: An Overview of the State of the World's Fresh and Marine Waters, 2nd ed., UNEP, Nairobi, Kenya, 2008.

[5] M.A. Shannon, P.W. Bohn, M. Elimelech, J.G. Georgiadis, B.J. Marinas, A.M. Mayes, Science and technology for water purification in the coming decades, Nature, 452 (2008) 301-310.

[6] OECD, Environmental Outlook to 2050: The Consequences of Inaction, in: Organisation for Economic Co-operation and Development (Ed.), OECD, Paris, 2012.

[7] G.M. Geise, H.-S. Lee, D.J. Miller, B.D. Freeman, J.E. Mcgrath, D.R. Paul, Water Purification by Membranes: The Role of Polymer Science, Journal of Polymer Science: Part B: Polymer Physics, 48 (2010) 1685–1718.

[8] L.F. Greenleea, D.F. Lawlerb, B.D. Freemana, B. Marrotc, P. Moulinc, Reverse osmosis desalination: water sources, technology, and today's challenges, Water Research, 43 (2009) 2317–2348.

[9] M. Elimelech, W.A. Phillip, The Future of Seawater Desalination: Energy, Technology, and the Environment, Science, 333 (2011) 712-717.

[10] Q. Schiermeier, Water: Purification with a pinch of salt, Nature, 452 (2008) 260-261.

[11] K.P. Lee, T.C. Arnot, D. Mattia, A review of reverse osmosis membrane materials for desalination—Development to date and future potential, Journal of Membrane Science, 370 (2011) 1-22.

[12] R.W. Baker, Membrane Technology and Applications, Second ed., John Wiley & Sons, U.K., 2004.

[13] C. Fritzmann, J. Lowenberg, T. Wintgens, T. Melin, State-of-the-art of reverse osmosis desalination, Desalination, 216 (2007) 1-76.

[14] M. Busch, W.E. Mickols, Reducing energy consumption in seawater desalination, Desalination, 165 (2004) 299-312.

[15] A.M.T. Association, Membrane Desalination Power Usage Put in Perspective, American Membrane Technology Association, Florida, USA, 2016.

[16] R.E. Larson, J.E. Cadotte, R.J. Petersen, The FT-30 seawater reverse osmosis membrane-element test results, Desalination, 38 (1981) 473-483.

[17] D.R. Paul, Reformulation of the solution-diffusion theory of reverse osmosis, Journal of Membrane Science, 241 (2004) 371–386.

[18] K.S. Spiegler, Y.M. El-Sayed, The energetics of desalination processes, Desalination, 139 (2001) 109-128.

[19] R.W. Stoughton, M.H. Lietzke, Calculation of Some Thermodynamic Properties of Sea Salt Solutions at Elevated Temperatures from Data on NaCI Solutions, Journal of Chemical and Engineering data, 10 (1965) 254–260.

[20] H.B. Park, J. Kamcev, L.M. Robeson, M. Elimelech, B.D. Freeman, Maximizing the right stuff: The trade-off between membrane permeability and selectivity, Science, 356 (2017) 1137.

[21] J.K. Holt, H.G. Park, Y. Wang, M. Stadermann, A.B. Artyukhin, C.P. Grigoropoulos, A. Noy, O. Bakajin, Fast mass transport through sub-2-nanometer carbon nanotubes, Science, 312 (2006) 1034-1037.

[22] M. Majumder, N. Chopra, R. Andrews, B.J. Hinds, Nanoscale hydrodynamics: enhanced flow in carbon nanotubes, Nature, 438 (2005) 44.
[23] M. Kumar, M. Grzelakowski, J. Zilles, M. Clark, W. Meier, Highly permeable polymeric membranes based on the incorporation of the functional water channel protein Aquaporin Z, Proceedings of the National Academy of Sciences of the USA, 104 (2007) 20719–20724.
[24] G.M. Geise, H.B. Park, A.C. Sagle, B.D. Freeman, J.E. McGrath, Water permeability and water/salt selectivity tradeoff in polymers for desalination, Journal of Membrane Science, 369 (2011) 130-138.
[25] J.R. Werber, A. Deshmukh, M. Elimelech, The critical need for increased selectivity, not increased water permeability, for desalination membranes., Environmental Science and Technology letters, 3 (2016) 112-120.
[26] J. Johnson, M. Busch, Engineering Aspects of Reverse Osmosis Module Design, Desalination and Water Treatment, 15 (2010) 236-248.
[27] Y.K. Lee, Y.J. Won, J.H. Yoo, K.H. Ahn, C.H. Lee, Flow analysis and fouling on the patterned membrane surface, Journal of Membrane Science, 427 (2013) 320–325.
[28] P.Z. Culfaz, S. Buetehorn, L. Utiu, M. Kueppers, B. Bluemich, T. Melin, M. Wessling, R.G.H. Lammertink, Fouling behavior of microstructured hollow fiber membranes in dead-end filtrations: Critical flux determination and NMR imaging of particle deposition, Langmuir, 27 (2011) 1643–1652.
[29] F. Xia, L. Feng, S. Wang, T. Sun, W. Song, W. Jiang, L. Jiang, Dual-responsive surfaces that switch between superhydrophilicity and superhydrophobicity, Advanced Materials, 18 (2006) 432–436.
[30] H. Susanto, N. Stahra, M. Ulbricht, High performance polyethersulfone microfiltration membranes having high flux and stable hydrophilic property, Journal of Membrane Science, 342 (2009) 153-164.
[31] A.K. Ghosh, B.H. Jeong, X. Huang, E.M.V. Hoek, Impacts of reaction and curing conditions on polyamide composite reverse osmosis membrane properties, Journal of Membrane Science, 311 (2008) 34-45.
[32] Sandia, Desalination and Water Purification Roadmap – A Report of the Executive Committee, DWPR Program Report, U.S. Department of the Interior, Bureau of Reclamation and Sandia National Laboratories, USA, 2003.
[33] M.A. Sanz, V. Bonnelye, G. Cremer, Fujairah reverse osmosis plant: 2 years of operation., Desalination, 203 (2007) 91–99.
[34] P.H. Gleick, The World's Water 2006–2007, The Biennial Report on Freshwater Resources. , Island Press, Chicago., 2006.
[35] B. Van der Bruggen, C. Vandecasteele, Distillation vs. membrane filtration: overview of process evolutions in seawater desalination., Desalination, 143 (2002) 207–218.
[36] S. Loeb, S. Sourirajan, Sea Water Demineralization by Means of an Osmotic Membrane, in: R.F. Gould (Ed.) Saline Water Conversion-II, American Chemical Society, Washington, DC, 1963, pp. 117-132.
[37] Sorek Desalination Plant, Israel, www.water-technology.net.
[38] Ras Al Khair Desalination Plant, Saudi Arabia, www.water-technology.net.
[39] C.E. Reid, E.J. Breton, Water and ion flow across cellulosic membranes, Journal of Applied Polymer Science, 1 (1959) 133–143.
[40] R.G. Sudak, Reverse osmosis, in: M.C. Porter (Ed.) Handbook of Industrial Membrane Technology, Noyes Publication, New Jersey, 1990.
[41] H.H. Hoehn, J.W. Richter, Aromatic Polyimide, Polyester and Polyamide Separation Membranes, US Patent USRE30351 E (1980).

[42] L. Credali, P. Parrini, Properties of piperazine homopolyamide films, Polymer, 12 (1971) 717–729.
[43] P. Parrini, Polypiperazinamides: new polymers useful for membrane processes, Desalination, 48 (1983) 67–78.
[44] J.E. Cadotte, Reverse Osmosis Membrane, US Patent US4039440 A (1977).
[45] K.J. Mysels, W. Wrasidlo, Strength of interfacial polymerization films,, Langmuir, 7 (1991) 3052–3053.
[46] J.E. Cadotte, R.J. Petersen, R.E. Larson, E.E. Erickson, A new thin-film composite seawater reverse osmosis membrane, Desalination, 32 (1980) 25-31.
[47] J. Glater, M.R. Zachariah, S.B. McCray, J.W.McCutchan, Reverse osmosis membrane sensitivity to ozone and halogen disinfectants, Desalination, 48 (1983) 1-16.
[48] R. Oizerovich-Honig, V. Raim, S. Srebnik, Simulation of thin film membranes formed by interfacial polymerization, Langmuir, 26 (2010) 299–306.
[49] V. Polasek, S. Talo, T. Sharif, Conversion from hollow fiber to spiral technology in large seawater RO systems – process design and economics, Desalination, 156 (2003) 239–247.
[50] A.F. Ismail, M. Padaki, N. Hilal, T. Matsuura, W.J. Lau, Thin film composite membrane — recent development and future potential, Desalination, 356 (2015) 140-148.
[51] M.J.T. Raaijmakers, N.E. Benes, Current trends in interfacial polymerization chemistry, Progress in Polymer Science, 63 (2016) 86–142.
[52] M. Hu, B. Mi, Enabling graphene oxide nanosheets as water separation membranes, Environmental Science and Technology, 47 (2013) 3715–3723.
[53] E.P. Chan, W.D. Mulhearn, Y. Huang, J. Lee, D. Lee, C.M. Stafford, Tailoring the permselectivity of water desalination membranes via nanoparticle assembly, Langmuir, 30 (2014) 611-616.
[54] E.L. Wittbecker, P.W. Morgan, Interfacial polycondensation. I, Journal of Polymer Science, 40 (1959) 289–297.
[55] Y. Song, J.-B. Fan, S. Wang, Recent progress in interfacial polymerization, Materials Chemistry Frontiers, 1 (2017) 1028-1040
[56] P.W. Morgan, S.L. Kwolek, Interfacial polycondensation. II. Fundamentals of polymer formation at liquid interfaces, Journal of Polymer Science, 40 (1959) 299–327.
[57] S.A. Sundet, Morphology of the rejecting surface of aromatic polyamide membranes for desalination, Journal of Membrane Science, 76 (1993) 175-183.
[58] J. Muscatello, E.A. Müller, A.A. Mostofi, A.P. Sutton, Multiscale molecular simulations of the formation and structure of polyamide membranes created by interfacial polymerization, Journal of Membrane Science, 5271 (2017) 180–190.
[59] G.-Y. Chai, W.B. Krantz, Formation and characterization of polyamide membranes via interfacial polymerization, Journal of Membrane Science, 93 (1994) 175–192.
[60] Y. Li, M.M. Kłosowski, C.M. McGilvery, A.E. Porter, A.G. Livingston, J.T. Cabral, Probing flow activity in polyamide layer of reverse osmosis membrane with nanoparticle tracers, Journal of Membrane Science, 534 (2017) 9–17.
[61] G.-R. Xu, J.-M. Xu, H.-J. Feng, H.-L. Zhao, S.-B. Wu, Tailoring structures and performance of polyamide thin film composite (PA-TFC) desalination membranes via sublayers adjustment-a review, Desalination, 417 (2017) 19–35.
[62] W.J. Lau, A.F. Ismail, N. Misdan, M.A. Kassim, A recent progress in thin film composite membrane: A review, Desalination, 287 (2012) 190–199.
[63] J. Xu, H. Yan, Y. Zhang, G. Pan, Y. Liu, The morphology of fully-aromatic polyamide separation layer and its relationship with separation performance of TFC membranes, Journal of Membrane Science, 541 (2017) 174–188.

[64] A. Soroush, J. Barzin, M. Barikani, M. Fathizadeh, Interfacially polymerized polyamide thin film composite membranes: Preparation, characterization and performance evaluation, Desalination, 287 (2012) 310–316.
[65] J.E. Tomaschke, Interfacially synthesized reverse osmosis membrane containing an amine salt and processes for preparing the same, US Patent US4948507 A (1989).
[66] B. Khorshidia, B. Soltannia, T. Thundat, M. Sadrzadeh, Synthesis of thin film composite polyamide membranes: Effect of monohydric and polyhydric alcohol additives in aqueous solution, Journal of Membrane Science, 523 (2017) 336–345.
[67] W.E. Mickols, Method of Treating Polyamide Membranes to Increase Flux, US Patent US5755964 A (1998).
[68] A.K. Ghosh, E.M.V. Hoek, Impacts of support membrane structure and chemistry on polyamide–polysulfone interfacial composite membranes, Journal of Membrane Science, 336 (2009) 140 -148.
[69] Q. Zhang, Z. Zhang, L. Dai, H. Wang, S. Li, S. Zhang, Novel insights into the interplay between support and active layer in the thin film composite polyamide membranes, Journal of Membrane Science, 537 (2017) 372–383.
[70] S.H. Maruf, D. Ahn, J. Pellegrino, J. Killgore, A.R. Greenberg, Y. Ding, Correlation between barrier layer Tg and a thin-film composite polyamide membrane's performance, Journal of Membrane Science, 405-406 (2012) 167-175.
[71] R.B. Bird, W.E. Stewart, E.N. Lightfoot, Transport Phenomena, Second ed., John Wiley, New York, 2002.
[72] A.W. Mohammad, Y.H. Teow, W.L. Ang, Y.T. Chung, D.L. Oatley-Radcliffe, N. Hilal, Nanofiltration membranes review: Recent advances and future prospects, Desalination, 356 (2015) 226–254.
[73] E.M. Vrijenhoek, S. Hong, M. Elimelech, Influence of membrane surface properties on initial rate of colloidal fouling of reverse osmosis and nanofiltration membranes, Journal of Membrane Science, 188 (2001) 115–128.
[74] G.Z. Ramon, E.M.V. Hoek, Transport through composite membranes, part 2: Impacts of roughness on permeability and fouling, Journal of Membrane Science, 425–426 (2013) 141–148.
[75] H. Yan, X. Miao, J. Xu, G. Pan, Y. Zhang, Y. Shi, M. Guo, Y. Liu, The porous structure of the fully-aromatic polyamide film in reverse osmosis membranes, Journal of Membrane Science, 475 (2015) 504-510.
[76] L. Lin, R. Lopez, G.Z. Ramon, O. Coronell, Investigating the void structure of the polyamide active layers of thin-film composite membranes, Journal of Membrane Science, 497 (2016) 365–376.
[77] M.C.Y. Wong, L. Lin, O. Coronell, E.M.V. Hoek, G.Z. Ramon, Impact of liquid-filled voids within the active layer on transport through thin-film composite membranes, Journal of Membrane Science, 500 (2016) 124–135.
[78] P.L.T. Brian, Mass transport in reverse osmosis, in: U. Merten (Ed.) Desalination by Reverse Osmosis, MIT Press, Cambridge, MA, 1966, pp. 161–292.
[79] D. Rana, T. Matsuura, Surface Modifications for Antifouling Membranes, Chemical Reviews, 110 (2010) 2448–2471.
[80] J. Landaburu-Aguirre, R. García-Pacheco, S. Molina, L. Rodríguez-Sáez, J. Rabadán, E. García-Calvo, Fouling prevention, preparing for re-use and membrane recycling. Towards circular economy in RO desalination, Desalination, 393 (2016) 16-30.
[81] E.M.V. Hoek, J. Allred, T. Knoell, B.-H. Jeong, Modeling the effects of fouling on fullscale reverse osmosis processes, Journal of Membrane Science, 314 (2008) 33–49.
[82] M. Khayet, Fouling and Scaling in Desalination, Desalination, 393 (2016) 1.

[83] A.W. Mohammad, Y.H. Teow, W.L. Ang, Y.T. Chung, D.L. Oatley-Radcliffe, N. Hilal, Nanofiltration membranes review: Recent advances and future prospects, Desalination, 356 (2015) 226-254.
[84] K. Boussu, A. Belpaire, A. Volodin, C.V. Haesendonck, P.V.d. Meeren, C. Vandecasteele, B.V.d. Bruggen, Influence of membrane and colloid characteristics on fouling of nanofiltration membranes, Journal of Membrane Science, 289 (2007) 220-230.
[85] T. Tran, B. Bolto, S. Gray, M. Hoang, E. Ostarcevic, An autopsy study of a fouled reverse osmosis membrane element used in a brackish water treatment plant., Water Research, 41 (2007) 3915–3923.
[86] Y. Magara, M. Kawasaki, M. Sekino, H. Yamamura, Development of reverse osmosis seawater desalination in Japan. , Water Science and Technology, 41 (2000) 1-8.
[87] J.A. Reverter, S. Talo, J. Alday, Las Palmas III – the success story of brine staging, Desalination, 138 (2001) 207-217.
[88] X. Zhu, M. Elimelech, Colloidal Fouling of Reverse Osmosis Membranes: Measurements and Fouling Mechanisms, Environmental Science and Technology, 31 (1997) 3654-3662.
[89] F. Wang, V.V. Tarabara, Pore blocking mechanisms during early stages of membrane fouling by colloids, Journal of Colloid and Interface Science, 328 (2008) 464–469.
[90] A. Grenier, M. Meireles, P. Aimar, P. Carvin, Analysing flux decline in dead-end filtration, Chemical Engineering Research and Design, 86 (2008) 1281–1293.
[91] P.H. Hermans, H.L. Bredée, Principles of the mathematical treatment of constant pressure filtration, Journal of the Society of Chemical Industry, 55 (1936) 1-4.
[92] J. Hermia, Constant pressure blocking filtration laws. Application to power-law non-Newtonian fluids, Transactions of the Institution of Chemical Engineers, 60 (1982) 183-187.
[93] B. Tansel, N. Dizge, I.N. Tansel, Analysis of high resolution flux data to characterize fouling profiles of membranes with different MWCO under different filtration modes, Separation and Purification Technology, 173 (2017) 200-208.
[94] P. Aimar, Recent progress in understanding particle fouling of filtration membranes, The Fifth International Membrane Science & Technology ConferenceSydney, Australia, 2003.
[95] B. Mi, C.L. Eaton, J.H. Kim, C.K. Colvin, J.C. Lozier, B.J. Mariñas, Removal of biological and non-biological viral surrogates by spiral-wound reverse osmosis membrane elements with intact and compromised integrity., Water Research, 38 (2004) 3821-3832.
[96] E.M.V. Hoek, M. Elimelech, Cake-Enhanced Concentration Polarization: A New Fouling Mechanism for Salt-Rejecting Membranes, Environmental Science and Technology, 37 (2003) 5581–5588.
[97] E.M.V. Hoek, A.S. Kim, M. Elimelech, Influence of Crossflow Membrane Filter Geometry and Shear Rate on Colloidal Fouling in Reverse Osmosis and, Environmental Engineering Science, 19 (2002) 357-372.
[98] C.Y. Tang, T.H. Chong, A.G. Fane, Colloidal interactions and fouling of NF and RO membranes: A review, Advances in Colloid and Interface Science, 164 (2011) 126–143.
[99] S. Lee, J. Cho, M. Elimelech, Influence of colloidal fouling and feed water recovery on salt rejection of RO and NF membranes, Desalination, 160 (2004) 1-12.
[100] R.S. Faibish, M. Elimelech, Y. Cohen, Effect of Interparticle Electrostatic Double Layer Interactions on Permeate Flux Decline in Crossflow Membrane Filtration of Colloidal Suspensions: An Experimental Investigation, Journal of Colloid and Interface Science, 204 (1998) 77-86.
[101] S. Kim, S. Lee, E. Lee, S. Sarper, C.-H. Kim, J. Cho, Enhanced or reduced concentration polarization by membrane fouling in seawater reverse osmosis (SWRO) processes, Desalination, 247 (2009) 162–168.

[102] A. Braghetta, F.A. DiGiano, W.P. Ball, NOM accumulation at NF membrane surface: impact of chemistry and shear, Journal of Environmental Engineering, 124 (1998) 1087-1098.
[103] S. Hong, M. Elimelech, Chemical and physical aspects of natural organic matter (NOM) fouling of nanofiltration membranes Journal of Membrane Science, 132 (1997) 159-181
[104] R.D. Cohen, R.F. Probstein, Colloidal Fouling of Reverse Osmosis Membranes, Journal of Colloid and Interface Science, 114 (1986) 194-207.
[105] M.T. Brunelle, Colloidal Fouling of Reverse Osmosis Membranes, Desalination, 32 (1980) 127-135.
[106] R. Sheikholeslami, S. Zhou, Performance of RO membranes in silica bearing waters, Desalination, 132 (2000) 337-344.
[107] T. Koo, Y.J. Lee, R. Sheikholeslami, Silica fouling and cleaning of reverse osmosis membranes, Desalination, 139 (2001) 43-56.
[108] K.B. Krauskopf, Dissolution and precipitation of silica at low temperaturesOriginal Research Article, Geochimica et Cosmochimica Acta, 10 (1956) 1-26.
[109] G.B. Alexander, W.M. Heston, R.K. Iler, The Solubility of Amorphous Silica in Water, Journal of Physical Chemistry, 58 (1954) 453-455.
[110] R.K. Iler, The Chemistry of Silica: Solubility, Polymerization, Colloid and Surface Properties, and Biochemistry, John Wiley & Sons, New York, 1979, pp. 78-83.
[111] R. Sheikholeslami, S. Tan, Effects of water quality on silica fouling of desalination plants, Desalination, 126 (1999) 267-280.
[112] R.Y. Ning, Discussion of silica speciation, fouling, control and maximum reduction, Desalination, 151 (2002) 67-73.
[113] W. Stumm, Chemistry of the Solid-Water Interface, Wiley Interscience: New York, 1992.
[114] P.F. Weng, Silica scale inhibition and colloidal silica dispersion for reverse osmosis systems, Desalination, 103 (1995) 59-67.
[115] M. Elimelech, X. Zhu, A.E. Childress, S. Hong, Role of membrane surface morphology in colloidal fouling of cellulose acetate and composite aromatic polyamide reverse osmosis membranes, Journal of Membrane Science, 127 (1997) 101-109.
[116] G.M. Litton, T.M. Olson, Colloid deposition kinetics with surface-active agents: Evidence for discrete surface charge effects, Journal of Colloid and Interface Science, 165 (1994) 522-525.
[117] Q. Li, J. Song, H. Yu, Z. Li, X. Pan, B. Yang, Investigating the microstructures and surface features of seawater RO membranes and the dependencies of fouling resistance performances, Desalination, 352 (2014) 109-117.
[118] W.R. Bowen, T.A. Doneva, Atomic Force Microscopy Studies of Membranes: Effect of Surface Roughness on Double-Layer Interactions and Particle Adhesion, Journal of Colloid and Interface Science, 229 (2000) 544–549.
[119] E.M.V. Hoek, S. Bhattacharjee, M. Elimelech, Effect of Membrane Surface Roughness on Colloid-Membrane DLVO Interactions, Langmuir, 19 (2003) 4836-4847.
[120] E.M.V. Hoek, G.K. Agarwal, Extended DLVO interactions between spherical particles and rough surfaces, Journal of Colloid and Interface Science, 298 (2006) 50–58.
[121] A. Al-Amoudi, R.W. Lovitt, Fouling strategies and the cleaning system of NF membranes and factors affecting cleaning efficiency, Journal of Membrane Science, 303 (2007) 4-28.
[122] Q. Yang, H.H. Himstedt, M. Ulbricht, X. Qian, S.R. Wickramasinghe, Designing magnetic field responsive nanofiltration membranes, Journal of Membrane Science, 430 (2013) 70-78.

[123] Y. Maeda, Recent progress in RO elements for high purity water production, Ultrapure Water, 18 (2001) 20-28.
[124] A. Wies, M.R. Bird, M. Nystrom, The chemical cleaning of polymeric UF membranes fouled with spent sulphite liquor over multiple operational cycles, Journal of Membrane Science, 216 (2003) 67-79.
[125] K. Kosutic, B. Kunst, RO and NF membrane fouling and cleaning and pore size distribution variations, Desalination, 150 (2002) 113-120.
[126] M. Nystrom, H. Zhu, Characterization of cleaning results using combined flux and streaming potential methods, Journal of Membrane Science, 131 (1997) 195-205.
[127] S. Ebrahim, Cleaning and regeneration of membranes in desalination and waste water applications, Desalination, 96 (1994) 225-238.
[128] G. Kang, M. Liu, B. Lin, Y. Cao, Q. Yuan, A novel method of surface modification on thin-film composite reverse osmosis membrane by grafting poly(ethylene glycol), Polymer, 48 (2007) 1165-1170.
[129] S.Y. Jung, Young-JuneWon, J.H. Jang, J.H. Yoo, K.H. Ahn, C.-H. Lee, Particle deposition on the patterned membrane surface: Simulation and experiments, Desalination, 370 (2015) 17-24.
[130] W. Ehrfeld, R. Einhaus, D. Münchmeyer, H. Strathmann, Microfabrication of membranes with extreme porosity and uniform pore size, Journal of Membrane Science, 36 (1988) 67–77.
[131] T. Okada, T. Matsuura, Pattern Formation on the Surface of Cellulose Membranes Prepared by Phase Inversion Technique Industrial & Engineering Chemistry Research, 27 (1988) 1335-1338.
[132] L. Vogelaar, J.N. Barsema, C.J.M. van Rijn, W. Nijdam, M. Wessling, Phase separation micro-molding, Advanced Materials, 15 (2003) 1385–1389.
[133] S.H. Maruf, L. Wang, A.R. Greenberg, J. Pellegrino, Y. Ding, Use of nanoimprinted surface patterns to mitigate colloidal deposition on ultrafiltration membranes, Journal of Membrane Science, 428 (2013) 598–607.
[134] S.Y. Chou, P.R. Krauss, P.J. Renstrom, Imprint of sub25 nm vias and trenches in polymers, Applied Physics Letters, 67 (1995) 3114-3116.
[135] S.Y. Chou, P.R. Krauss, P.J. Renstrom, Imprint Lithography with 25-Nanometer Resolution, Science, 272 (1996) 85-87
[136] R.J. Gohari, W.J. Lau, T. Matsuura, A.F. Ismail, Effect of surface pattern formation on membrane fouling and its control in phase inversion process, Journal of Membrane Science, 446 (2013) 326–331.
[137] H. Susanto, M. Ulbricht, Polymeric membranes for molecular separations, in: E. Drioli, L. Giorno (Eds.) Membrane Operations: Innovative separations and Transformations, Wiley-VCH, Weinheim, Germany, 2009, pp. 19-43.
[138] R. Zsigmondy, W. Bachmann, Filter and method of producing same, US Patent US1421341 A (1922).
[139] A. Goetz, Method of making microporous filter film, US Patent US2926104 A (1960).
[140] M. Mulder, Basic Principles of Membrane Technology, Kluwer Academic Publishers, Dordrecht, 1996.
[141] S.-G. Li, T. Van den Boomgaard, C.A. Smolders, H. Strathmann, Physical Gelation of Amorphous Polymers in a Mixture of Solvent and Nonsolvent, Macromolecules, 29 (1996) 2053–2059.
[142] C. Stropnik, V. Musil, M. Brumen, Polymeric membrane formation by wet-phase separation; turbidity and shrinkage phenomena as evidence for the elementary processes, Polymer, 41 (2000) 9227–9237.

[143] J. Reuvers, J.W.A. Van den Berg, C.A. Smolders, Formation of membranes by means of immersion precipitation, Part I: A model to describe mass transfer during immersion precipitation, Journal of Membrane Science, 34 (1987) 45-65.
[144] H. Strathmann, K. Kock, The formation mechanism of phase separation membranes, Desalination, 21 (1977) 241-255.
[145] P. Van der Witte, P.J. Dijkstra, J.W.A. Van den Berg, B.J. Feijen, Phase separation processes in polymer solutions in relation to membrane formation, Journal of Membrane Science, 117 (1996) 1-31.
[146] H. Strathmann, K. Kock, P. Amar, R.W. Baker, The formation mechanism of asymmetric membranes, Desalination, 16 (1975) 179-203.
[147] L. Vogelaar, R.G.H. Lammertink, J.N. Barsema, W. Nijdam, L.A.M. Bolhuis-Versteeg, C.J.M. van Rijn, M. Wessling, Phase separation micro-molding: a new generic approach for microstructuring various materials, Small, 1 (2005) 645–655.
[148] J.M. Greenwood, J.S. Johnson, M.J. Witham, Preparation of polyethersulfone membranes, US Patent US6056903 A (2000).
[149] A.L. Ahmad, A.A. Abdulkarim, B.S. Ooi, S. Ismail, Recent development in additives modifications of polyethersulfone membrane for flux enhancement, Chemical Engineering Journal, 223 (2013) 246–267.
[150] M.A. Frommer, R. Matz, U. Rosenthal, Mechanism of Formation of Reverse Osmosis Membranes. Precipitation of Cellulose Acetate Membranes in Aqueous Solutions, Industrial & Engineering Chemistry Product Research and Development, 10 (1971) 193–196.
[151] H. Susanto, M. Ulbricht, Characteristics, performance and stability of polyethersulfone ultrafiltration membranes prepared by phase separation method using different macromolecular additives, Journal of Membrane Science, 327 (2009) 125-135.
[152] L.Y. Lafreniere, F.D.F. Talbot, T. Matsuura, S. Sourirajan, Effect of polyvinylpyrrolidone additive on the performance of polyethersulfone ultrafiltration membranes, Industrial & Engineering Chemistry Research, 26 (1987) 2385-2389.
[153] T. Miyano, T. Matsuura, S. Sourirajan, Effect of polyvinylpyrrolidone additive on the pore size and the pore size distribution of polyethersulfone (victrex) membranes, Chemical Engineering Communications, 119 (1993) 23-29.
[154] N.A. Ochoa, P. Pradanos, L. Palacio, C. Pagliero, J. Marchese, A. Hernandez, Pore size distributions based on AFM imaging and retention of multidisperse polymer solutes — characterisation of polyethersulfone UF membranes with dopes containing different PVP, Journal of Membrane Science, 187 (2001) 227-237.
[155] A.F. Ismail, A.R. Hassan, Effect of additive contents on the performances and structural properties of asymmetric polyethersulfone (PES) nanofiltration membranes, Separation and Purification Technology, 55 (2007) 98–109.
[156] H.T. Wang, T. Yu, C.Y. Zhao, Q.Y. Du, Improvement of hydrophilicity and blood compatibility on polyethersulfone membrane by adding polyvinylpyrrolidone, Fibers and Polymers, 10 (2009) 1-5.
[157] M. Amirilargani, E. Saljoughi, T. Mohammadi, M.R. Moghbeli, Effects of coagulation bath temperature and polyvinylpyrrolidone content on flat sheet asymmetric polyethersulfone membranes, Polymer Engineering and Science, 50 (2010) 885-893.
[158] M. Bikel, I.G.M. Punt, R.G.H. Lammertink, M. Wessling, Micropatterned polymer films by vapor-induced phase separation using permeable molds, ACS Applied Materials and Interfaces, 1 (2009) 2856–2861.
[159] Y. Zhang, M. Ishida, Y. Kazoe, Y. Sato, N. Miki, Water-Vapor Permeability Control of PDMS by the Dispersion of Collagen Powder, Transactions on Electrical and Electronic Engineering, 4 (2009) 442–449.

[160] P.Z. Çulfaz, E. Rolevink, C. van Rijn, R.G.H. Lammertink, M. Wessling, Microstructured hollow fibers for ultrafiltration, Journal of Membrane Science, 347 (2010) 32–41.
[161] Y.-J. Won, J. Lee, D.-C. Choi, H.R. Chae, I. Kim, C.-H. Lee, I.-C. Kim, Preparation and Application of Patterned Membranes for Wastewater Treatment, Environmental Science and Technology, 46 (2012) 11021−11027.
[162] Y.J. Won, J. Lee, D.C. Choi, J.H. Jang, J.W. Lee, H.R. Chae, I. Kim, K.H. Ahn, C.H. Lee, I.C. Kim, Factors affecting pattern fidelity and performance of a patterned membrane, Journal of Membrane Science, 462 (2014) 1-8.
[163] Y. Gençal, E.N. Durmaz, P.Z. Çulfaz-Emecen, Preparation of patterned microfiltration membranes and their performance in crossflow yeast filtration, Journal of Membrane Science, 476 (2015) 224–233.
[164] L.J. Guo, Nanoimprint lithography: methods and material requirements, Advanced Materials, 19 (2007) 495-513.
[165] Y. Ding, S. Maruf, M. Aghajani, A.R. Greenberg, Surface patterning of polymeric membranes and its effect on antifouling characteristics, Separation Science and Technology, 52 (2017) 240-257.
[166] Z. Wang, Y. Ding, Probing polymer deformation profiles at varying depths in nanoimprint lithography, Nanotechnology, 21 (2010) 105301-105305.
[167] Y. Ding, H.W. Ro, J.F. Douglas, R.L. Jones, D.R. Hine, A. Karim, C.L. Soles, Polymer Viscoelasticity and Residual Stress Effects on Nanoimprint Lithography, Advanced Materials, 19 (2007) 1377–1382.
[168] Y. Ding, H.W. Ro, K.J. Alvine, B.C. Okerberg, J. Zhou, J.F. Douglas, A. Karim, C.L. Soles, Nanoimprint Lithography and the Role of Viscoelasticity in the Generation of Residual Stress in Model Polystyrene Patterns, Advanced Functional Materials, 18 (2008) 1854–1862.
[169] Y. Ding, H.J. Qi, K.J. Alvine, H.W. Ro, D.U. Ahn, S. Lin-Gibson, J.F. Douglas, C.L. Soles, Stability and Surface Topography Evolution in Nanoimprinted Polymer Patterns under a Thermal Gradient, Macromolecules, 43 (2010) 8191–8201.
[170] S.H. Maruf, Z. Li, J.A. Yoshimura, J. Xiao, A.R. Greenberg, Y. Ding, Influence of nanoimprint lithography on membrane structure and performance, Polymer, 69 (2015) 129-137.
[171] Y. Ding, H.W. Ro, T.A. Germer, J.F. Douglas, B.C. Okerberg, A. Karim, C.L. Soles, Relaxation Behavior of Polymer Structures Fabricated by Nanoimprint Lithography, ACS Nano, 1 (2007) 84-92.
[172] M. Aghajani, S.H. Maruf, M. Wang, J. Yoshimura, G. Pichorim, A. Greenberg, Y. Ding, Relationship between permeation and deformation for porous membranes, Journal of Membrane Science, 526 (2017) 293–300.
[173] A.D. Stroock, S.K.W. Dertinger, A. Ajdari, I. Mezic, H.A. Stone, G.M. Whitesides, Chaotic Mixer for Microchannels, Science, 295 (2002) 647-651.
[174] A.D. Stroock, G.M. Whitesides, Controlling Flows in Microchannels with Patterned Surface Charge and Topography, Accounts of Chemical Research, 36 (2003) 597-604.
[175] G.A. Fimbres-Weihs, D.E. Wiley, D.F. Fletcher, Unsteady flows with mass transfer in narrow zigzag spacer-filled channels: a numerical study, Industrial and Engineering Chemistry Research, 45 (2006) 6594-6603.
[176] C. Picioreanu, J.S. Vrouwenvelder, M.C.M. van Loosdrecht, Three-dimensional modeling of biofouling and fluid dynamics in feed spacer channels of membrane devices, Journal of Membrane Science, 345 (2009) 340-354.

[177] A.I. Radu, M.S.H. van Steen, J.S. Vrouwenvelder, M.C.M. van Loosdrecht, C. Picioreanu, Spacer geometry and particle deposition in spiral wound membrane feed channels, Water Research, 64 (2014) 160-176.
[178] S.S. Bucs, R.V. Linares, J.O. Marston, A.I. Radu, J.S. Vrouwenvelder, C. Picioreanu, Experimental and numerical characterization of the water flow in spacer-filled channels of spiral-wound membranes, Water Research, 87 (2015) 299-310.
[179] W.A. Ducker, T.J. Senden, R.M. Pashley, Direct measurement of colloidal forces using an atomic force microscope, Nature, 353 (1991) 239–241.
[180] A. Drechsler, N. Petong, J. Zhang, D.Y. Kwok, K. Grundke, Force measurements between Teflon AF and colloidal silica particles in electrolyte, Colloids and Surfaces A: Physicochemical and Engineering Aspects, 250 (2004) 357–366.
[181] E.J.W. Verwey, J.T.G. Overbeek, Theory of the Stability of Lyophobic Colloids, Dover Publications, New York, 1948.
[182] E. Martines, L. Csaderova, H. Morgan, A.S.G. Curtis, M.O. Riehle, DLVO interaction energy between a sphere and a nano-patterned plate, Colloids and Surfaces A: Physicochemical and Engineering Aspects, 318 (2008) 45–52.
[183] M. Bendersky, J.M. Davis, DLVO interaction of colloidal particles with topographically and chemically heterogeneous surfaces, Journal of Colloid and Interface Science, 353 (2011) 87–97.
[184] I.S. Ngene, R.G.H. Lammertink, M. Wessling, W.G.J. Van den Meer, Particle deposition and biofilm formation on microstructured membranes, Journal of Membrane Science, 364 (2010) 43–51.
[185] Y.-J. Won, S.-Y. Jung, J.-H. Jang, J.-W. Lee, H.-R. Chae, D.-C. Choi, K.H. Ahn, C.-H. Lee, P.-K. Park, Correlation of membrane fouling with topography of patterned membranes for water treatment, Journal of Membrane Science, 498 (2016) 14-19.
[186] P.Z. Culfaz, M. Haddad, M. Wessling, R.G.H. Lammertink, Fouling behavior of microstructured hollow fibers in cross-flow filtrations: Critical flux determination and direct visual observation of particle deposition, Journal of Membrane Science, 372 (2011) 201-218.
[187] S.H. Maruf, A.R. Greenberg, J. Pellegrino, Y. Ding, Critical flux of surface-patterned ultrafiltration membranes during cross-flow filtration of colloidal particles, Journal of Membrane Science, 471 (2014) 65–71.
[188] K.-h. Lin, J.C. Crocker, V. Prasad, A. Schofield, D.A. Weitz, T.C. Lubensky, A.G. Yodh, Entropically Driven Colloidal Crystallization on Patterned Surfaces, Physical Review Letters, 85 (2000) 1770-1773.
[189] S.H. Maruf, A.R. Greenberg, J. Pellegrino, Y. Ding, Fabrication and characterization of a surface-patterned thin film composite membrane, Journal of Membrane Science, 452 (2014) 11-19.
[190] S.H. Maruf, A.R. Greenberg, Y. Ding, Influence of substrate processing and interfacial polymerization conditions on the surface topography and permselective properties of surface-patterned thin-film composite membranes, Journal of Membrane Science, 512 (2016) 50–60.
[191] S.T. Weinman, S.M. Husson, Influence of chemical coating combined with nanopatterning on alginate fouling during nanofiltration, Journal of Membrane Science, 513 (2016) 146–154.
[192] J.Y. Chung, J.-H. Lee, K.L. Beers, C.M. Stafford, Stiffness, strength, and ductility of nanoscale thin films and membranes: a combined wrinkling-cracking methodology, Nano Letters, 11 (2011) 3361–3365.

[193] M. Rickman, S. Maruf, E. Kujundzic, R.H. Davis, A. Greenberg, Y. Ding, J. Pellegrino, Fractionation and flux decline studies of surface-patterned nanofiltration membranes using NaCl-glycerol-BSA solutions, Journal of Membrane Science, 527 (2017) 102–110.
[194] R.J. Petersen, Composite reverse osmosis and nanofiltration membranes, Journal of Membrane Science, 83 (1993) 81-150.
[195] V. Freger, Nanoscale heterogeneity of polyamide membranes formed by interfacial polymerization, Langmuir, 19 (2003) 4791–4797.
[196] G.R. Xu, J.N. Wang, C.J. Li, Strategies for improving the performance of the polyamide thin film composite (PA-TFC) reverse osmosis (RO) membranes: surface modifications and nanoparticles incorporations, Desalination, 328 (2013) 83-100.
[197] G.D. Kang, Y.M. Cao, Development of antifouling reverse osmosis membranes for water treatment: a review, Water Research, 46 (2012) 584–600.
[198] D. Wandera, S.R. Wickramasinghe, S.M. Husson, Stimuli-responsive membranes, Journal of Membrane Science, 357 (2010) 6-35.
[199] E.M.V. Wagner, A.C. Sagle, M.M. Sharma, Y.-H. La, B.D. Freeman, Surface modification of commercial polyamide desalination membranes using poly(ethylene glycol) diglycidyl ether to enhance membrane fouling resistance, Journal of Membrane Science, 367 (2011) 273–287.
[200] B. Jeong, A. Gutowska, Lessons from nature: stimuli responsive polymers and their biomedical applications, Trends in Biotechnology, 20 (2002) 305-311.
[201] F. Liu, M.W. Urban, Recent advances and challenges in designing stimuli-responsive polymers, Progress in Polymer Science, 35 (2010) 3-23.
[202] Q. Yang, N. Adrus, F. Tomicki, M. Ulbricht, Composites of functional polymeric hydrogels and porous membranes, Journal of Materials Chemistry, 21 (2011) 2783–2811.
[203] R. Xie, Y. Li, L.-Y. Chu, Preparation of thermo-responsive gating membranes with controllable response temperature, Journal of Membrane Science, 289 (2007) 76–85.
[204] C. Zhao, S. Nie, M. Tang, S. Sun, Polymeric pH-sensitive membranes—A review, Progress in Polymer Science, 36 (2011) 1499– 1520.
[205] A.M. Mika, R.F. Childs, J.M. Dickson, B.E. McCarry, D.R. Gagnon, A new class of polyelectrolyte-filled microfiltration membranes with environmentally controlled porosity, Journal of Membrane Science, 108 (1995) 37-56.
[206] X. Lin, B.N. Quoc, M. Ulbricht, Magneto-responsive polyethersulfone-based iron oxide cum hydrogel mixed matrix composite membranes for switchable molecular sieving, ACS Applied Materials and Interfaces, 8 (2016) 29001-29014.
[207] F.-A. Plamper, A. Walther, A.-H.-E. Müller, M. Ballauff, Nanoblossoms: Light-Induced Conformational Changes of Cationic Polyelectrolyte Stars in the Presence of Multivalent Counterions, Nano Letters, 7 (2007) 167–171.
[208] S. Yu, Z. Lü, Z. Chen, X. Liu, M. Liu, C. Gao, Surface modification of thin-film composite polyamide reverse osmosis membranes by coating *N*-isopropylacrylamide-co-acrylic acid copolymers for improved membrane properties, Journal of Membrane Science, 371 (2011) 293–306.
[209] S.-K. Han, K. Na, Y.-H. Bae, Sulfonamide based pH-sensitive polymeric micelles physicochemical characteristics and pH dependent aggregation, Colloids and Surfaces A: Physicochemical and Engineering Aspects, 214 (2003) 49-59.
[210] C. Yi, Z. Deng, Z. Xu, Monodisperse thermosensitive particles prepared by emulsifier-free emulsion polymerization with microwave irradiation, Colloid and Polymer Science, 283 (2005) 1259–1266.
[211] D. Wu, X. Liu, S. Yu, M. Liu, C. Gao, Modification of aromatic polyamide thin-film composite reverse osmosis membranes by surface coating of thermo-responsive

copolymers P(NIPAM-co-Am). I: Preparation and characterization, Journal of Membrane Science, 352 (2010) 76–85.
[212] M. Shibayama, T. Tanaka, Responsive Gels: Volume Transitions in: K. Dusek (Ed.) in Advances in Polymer Science, Springer, Berlin, 1993, pp. 1-62.
[213] D.A. Musale, Method of cleaning fouled and/or scale membranes, US Patent US7674382 B2 (2010).
[214] S. Yu, X. Liu, J. Liu, D. Wu, M. Liu, C. Gao, Surface modification of thin-film composite polyamide reverse osmosis membranes with thermo-responsive polymer (TRP) for improved fouling resistance and cleaning efficiency, Separation and Purification Technology, 76 (2011) 283–291.
[215] M. Heskins, J.E. Guillet, Solution Properties of Poly(*N*-isopropylacrylamide), Journal of Macromolecular Science: Part A - Chemistry, 2 (1968) 1441-1455.
[216] V. Mittal, N.B. Matsko, A. Butte, M. Morbidelli, Synthesis of temperature responsive polymer brushes from polystyrene latex particles functionalized with ATRP initiator, European Polymer Journal, 43 (2007) 4868–4881.
[217] H.M. Zareie, E.V. Bulmus, A.P. Gunning, A.S. Hoffman, E. Piskin, V.J. Morris, Investigation of a stimuli-responsive copolymer by atomic force microscopy, Polymer, 41 (2000) 6723–6727.
[218] L.A. Connal, Q. Li, J.F. Quinn, E. Tjipto, F. Caruso, G.G. Qiao, pH-responsive poly(acrylic acid) core cross-linked star polymers: morphology transitions in solution and multilayer thin films, Macromolecules, 41 (2008) 2620-2626.
[219] D. Dupin, J. Rosselgong, S.P. Armes, A.F. Routh, Swelling kinetics for a pH-induced latex-to-microgel transition, Langmuir, 23 (2007) 4035–4041.
[220] G. Chen, A.S. Hoffman, Graft coploymers that exhibit temperature-induced phase transitions over a wide range of pH, Nature, 373 (1995) 49-52.
[221] K. Sumaru, M. Kameda, T. Kanamori, T. Shinbo, Characteristic phase transition of aqueous solution of poly(*N*-isopropylacrylamide) functionalized with spirobenzopyran, Macromolecules, 37 (2004) 4949–4955.
[222] K. Szczubialka, L. Moczek, S. Blaszkiewicz, M. Nowakowska, Photocrosslinkable smart terpolymers responding to pH, temperature, and ionic strength, Journal of Polymer Science Part A: Polymer Chemistry, 42 (2004) 3879–3886.
[223] N. Tomer, S. Mondal, D. Wandera, S.R. Wickramasinghe, S.M. Husson, Modification of nanofiltration membranes by surface-initiated atom transfer radical polymerization for produced water filtration, Separation Science and Technology, 44 (2009) 3346–3368.
[224] V. Freger, J. Gilron, S. Belfer, TFC polyamide membranes modified by grafting of hydrophilic polymers: an FT-IR/AFM/TEM study, Journal of Membrane Science, 209 (2002) 283-292.
[225] S. Mondal, S.R. Wickramasinghe, Photo-induced graft polymerization of *N*-isopropylacrylamide on thin film composite membrane: Produced water treatment and antifouling properties, Separation and Purification Technology, 90 (2012) 231–238.
[226] B. Zhao, W.J. Brittain, Polymer brushes: surface-immobilized macromolecules, Progress in Polymer Science, 25 (2000) 677–710.
[227] H.H. Himstedt, Q. Yang, L.P. Dasi, X. Qian, S.R. Wickramasinghe, M. Ulbricht, Magnetically Activated Micromixers for Separation Membranes, Langmuir, 27 (2011) 5574–5581.
[228] W.A. Braunecker, K. Matyjaszewski, Recent mechanistic developments in atom transfer radical polymerization, Journal of Molecular Catalysis A: Chemical, 254 (2006) 155-164.
[229] N. Singh, J. Wang, M. Ulbricht, S.R. Wickramasinghe, S.M. Husson, Surface-initiated atom transfer radical polymerization: A new method for preparation of polymeric membrane adsorbers, Journal of Membrane Science, 309 (2008) 64–72.

[230] A. Friebe, M. Ulbricht, Cylindrical Pores Responding to Two Different Stimuli via Surface-Initiated Atom Transfer Radical Polymerization for Synthesis of Grafted Diblock Copolymers, Macromolecules, 42 (2009) 1838-1848.
[231] K. Matyjaszewski, P.J. Miller, N. Shukla, B. Immaraporn, A. Gelman, B.B. Luokala, T.M. Siclovan, G. Kickelbick, T. Vallant, H. Hoffmann, T. Pakula, Polymers at interfaces: using atom transfer radical polymerization in the controlled growth of homopolymers and block copolymers from silicon surfaces in the absence of untethered sacrificial initiator, Macromolecules, 32 (1999) 8716–8724.
[232] G. Masci, L. Giacomelli, V. Crescenzi, Atom transfer radical polymerization of *N*-isopropylacrylamide, Macromolecules Rapid Communications, 25 (2004) 559-564.
[233] M. Teodorescu, K. Matyjaszewski, Controlled polymerization of (meth)acrylamides by atom transfer radical polymerization, Macromolecules Rapid Communications, 21 (2000) 190-194.
[234] G.D. Kang, H.J. Yu, Z.N. Liu, Y.M. Cao, Surface modification of a commercial thin film composite polyamide reverse osmosis membrane by carbodiimide-induced grafting with poly(ethylene glycol) derivatives., Desalination, 275 (2011) 252-259.
[235] J. Xu, Z. Wang, L. Yu, J. Wang, S. Wang, A novel reverse osmosis membrane with regenerable anti-biofouling and chlorine resistant properties, Journal of Membrane Science, 435 (2013) 80-91.
[236] T.F. Scientific, Carbodiimide Crosslinker Chemistry, Thermo Fisher Scientific 2017.
[237] A. Kulkarni, D. Mukherjee, W.N. Gill, Flux enhancement by hydrophilization of thin film composite reverse osmosis membranes, Journal of Membrane Science, 114 (1996) 39-50.
[238] M.A. Kuehne, R.Q. Song, N.N. Li, R.J. Petersen, Flux enhancement in TFC RO membranes, Environmental Progress, 20 (2001) 23-26.
[239] M.C. Wilbert, J. Pellegrino, A. Zydney, Bench-scale testing of surfactant-modified reverse osmosis/nanofiltration membranes, Desalination, 115 (1998) 15-32.
[240] Y. Zhou, S.C. Yu, C.J. Gao, X.S. Feng, Surface modification of thin film composite polyamide membranes by electrostatic self deposition of polycations for improved fouling resistance, Separation and Purification Technology, 66 (2009) 287-294.
[241] H. Hachisuka, K. Ikeda, Composite reverse osmosis membrane having a separation layer with polyvinyl alcohol coating and method of reverse osmosis treatment of water using the same, US Patent US6177011 B1 (2001).
[242] D. Rana, Y. Kim, T. Matsuura, H.A. Arafat, Development of antifouling thin-film-composite membranes for seawater desalination, Journal of Membrane Science, 367 (2001) 110-118.
[243] C. Wang, G.K. Such, A. Widjaya, H. Lomas, G. Stevens, F. Caruso, S.E. Kentish, Click poly(ethylene glycol) multilayers on RO membranes: fouling reduction and membrane characterization, Journal of Membrane Science, 409-410 (2012) 9-15.
[244] B.D. McCloskey, H.B. Park, H. Ju, B.W. Rowe, D.J. Miller, B.J. Chun, K. Kin, B.D. Freeman, Influence of polydopamine deposition conditions on pure water flux and foulant adhesion resistance of reverse osmosis, ultrafiltration, and microfiltration membranes, Polymer, 51 (2010) 3472-3485.
[245] S. Jiang, Z. Cao, Ultralow-fouling, functionalizable, and hydrolyzable zwitterionic materials and their derivatives for biological applications, Advanced Materials, 22 (2010) 920-932.
[246] D. Nikolaeva, C. Langner, A. Ghanem, M.A. Rehim, B. Voit, J. Meier-Haack, Hydrogel surface modification of reverse osmosis membranes, Journal of Membrane Science, 476 (2015) 264-276.

[247] X. Feng, L. Jiang, Design and Creation of Superwetting/Antiwetting Surfaces, Advanced Materials, 18 (2006) 3063–3078.
[248] W. Barthlott, C. Neinhuis, Purity of the sacred lotus, or escape from contamination in biological surfaces, Planta, 202 (1997) 1-8.
[249] L. Feng, S. Li, Y. Li, H. Li, L. Zhang, J. Zhai, Y. Song, B. Liu, L. Jiang, D. Zhu, Super-Hydrophobic Surfaces: From Natural to Artificial, Advanced Materials, 14 (2002) 1857–1860.
[250] X. Gao, L. Jiang, Water-repellent legs of water striders, Nature, 432 (2004) 36.
[251] P. Papadopoulos, X. Deng, L. Mammen, D.-M. Drotlef, G. Battagliarin, C. Li, K. Müllen, K. Landfester, A.D. Campo, H.-J. Butt, D. Vollmer, Wetting on the Microscale: Shape of a Liquid Drop on a Microstructured Surface at Different Length Scales, Langmuir, 28 (2012) 8392−8398.
[252] T. Young, An Essay on the Cohesion of Fluids, Philosophical Transaction Royal Society London, 95 (1805) 65-87.
[253] R.N. Wenzel, Resistance of solid surfaces to wetting by water, Industrial & Engineering Chemistry, 28 (1936) 988–994.
[254] A.B.D. Cassie, S. Baxter, Wettability of porous surfaces, Transactions of the Faraday Society, 40 (1944) 546-551.
[255] J. Bico, C. Tordeux, D. Quéré, Rough wetting, Europhysics Letters, 55 (2001) 214-220.
[256] T.L. Sun, L. Feng, X.F. Gao, L. Jiang, Bioinspired surfaces with special wettability, Accounts of Chemical Research, 38 (2005) 644-652.
[257] S. Shibuichi, T. Yamamoto, T. Onda, K. Tsujii, Super Water- and Oil-Repellent Surfaces Resulting from Fractal Structure, Journal of Colloid and Interface Science, 208 (1998) 287-294.
[258] M.-R. Hobabi, D. Hassanzadeh, S. Azarmi, A.A. Entezami, Effect of synthesis method and buffer composition on the LCST of a smart copolymerof *N*-isopropylacrylamide and acrylic acid, Polymers for Advanced Technologies, 18 (2007) 986–992.
[259] Bruker, User manual for Nanoscope Analysis 1.5, 2013, pp. 293-336.
[260] A.P. GmbH, SurPASS Operating Procedures, Anton Paar GmbH, Graz, Austria, 2012.
[261] V. Vitagliano, P.A. Lyons, Diffusion coefficients for aqueous solutions of sodium chloride and barium chloride, Journal of American Chemical Society, 78 (1956) 1549–1552.
[262] E. Saljoughi, M. Amirilargani, T. Mohammadi, Effect of poly(vinyl pyrrolidone) concentration and coagulation bath temperature on the morphology, permeability, and thermal stability of asymmetric cellulose acetate membranes, Journal of Applied Polymer Science, 111 (2009) 2537–2544.
[263] R.M. Boom, I.M. Wienk, T. Van den Boomgaard, C.A. Smolders, Microstructures in phase inversion membranes, 2.The role of a polymeric additive, Journal of Membrane Science, 73 (1992) 277-292.
[264] H. Strathmann, P. Scheible, R.W. Baker, A Rationale for the preparation of Loeb–Sourirajan-type cellulose acetate membranes, Journal of Applied Polymer Science, 15 (1971) 811-828.
[265] B.D. Mistry, Infrared Spectroscopy, A Handbook of Spectroscopic Data: Chemistry, Oxford Book Company, Jaipur, India, 2009, pp. 26-63.
[266] J.F. Li, Z.L. Xu, H. Yang, C.P. Feng, J.H. Shi, Hydrophilic microporous PES membranes prepared by PES/PEG/DMAc casting solutions, Journal of Applied Polymer Science, 107 (2008) 4100-4108.
[267] H. Susanto, S. Franzka, M. Ulbricht, Dextran fouling of polyethersulfone ultrafiltration membranes— causes, extent and consequences, Journal of Membrane Science, 296 (2007) 147-155.

[268] J. Ji, J.M. Dickson, R.F. Childs, B.E. McCarry, Mathematical model for the formation of thin-film composite membranes by interfacial polymerization: porous and dense films, Macromolecules, 33 (2000) 624–633.
[269] J. Gilron, S. Belfer, P. Vaisanen, M. Nystrom, Effects of surface modification on antifouling and performance properties of reverse osmosis membranes, Desalination, 140 (2001) 167-179.
[270] P.S. Singh, S.V. Joshi, J.J. Trivedi, C.V. Devmurari, A. PrakashRao, P.K. Ghosh, Probing the structural variations of thin film composite RO membranes obtained by coating polyamide over polysulfone membranes of different pore dimensions, Journal of Membrane Science, 278 (2006) 19-25.
[271] M. Fathizadeh, A. Aroujalian, A. Raisi, Effect of lag time in interfacial polymerization on polyamide composite membrane with different hydrophilic sub layers, Desalination, 284 (2012) 32-41.
[272] J.L. Fritz, M.J. Owen, Hydrophobic recovery of plasma-treated polydimethylsiloxane, Journal of Adhesion, 54 (1995) 33-45.
[273] H. Makamba, J.H. Kim, K. Lim, N. Park, J.H. Hahn, Surface modification of poly(dimethylsiloxane) microchannels, Electrophoresis, 24 (2003) 3607–3619.
[274] I.D. Johnston, D.K. McCluskey, C.K.L. Tan, M.C. Tracey, Mechanical characterization of bulk Sylgard 184 for microfluidics and microengineering, Journal of Micromechanics and Microengineering, 24 (2014) 035017.
[275] V. Freger, Kinetics of film formation by interfacial polycondensation, Langmuir, 21 (2005) 1884–1894.
[276] S.Y. Kwak, S.G. Jung, S.H. Kim, Structure-motion-performance relationship of flux-enhanced reverse osmosis (RO) membranes composed of aromatic polyamide thin films, Environmental Science and Technology, 35 (2001) 4334–4340.
[277] M. Hirose, H. Ito, Y. Kamiyama, Effect of skin layer surface structures on the flux behaviour of RO membranes, Journal of Membrane Science, 121 (1996) 209–215.
[278] Z. Kolská, Z. Makajová, K. Kolářová, N.K. Slepičková, S. Trostová, A. Řezníčková, J. Siegel, V. Švorčík, Electrokinetic potential and other surface properties of polymer foils and their modifications, in: F. Yılmaz (Ed.) Polymer Science 1, InTech, Croatia, 2013, pp. 203–228.
[279] S. Li, P. Leroy, F. Heberling, N. Devau, D. Jougnot, C. Chiaberge, Influence of surface conductivity on the apparent zeta potential of calcite, Journal of Colloid and Interface Science, 468 (2016) 262–275.
[280] D. Gopireddy, S.M. Husson, Room Temperature Growth of Surface-Confined Poly(acrylamide) from Self-Assembled Monolayers Using Atom Transfer Radical Polymerization, Macromolecules, 35 (2002) 4218–4221.
[281] D. Xiao, M.J. Wirth, Kinetics of Surface-Initiated Atom Transfer Radical Polymerization of Acrylamide on Silica, Macromolecules, 35 (2002) 2919–2925.
[282] PerkinElmer Life and Analytical Sciences, FT-IR Spectroscopy, Attenuated Total Reflectance (ATR), USA, 2005.
[283] J.S. Stevens, S.J. Byard, C.C. Seaton, G. Sadiq, R.J. Davey, S.L.M. Schroeder, Proton transfer and hydrogen bonding in the organic solid state: a combined XRD/XPS/ssNMR study of 17 organic acid–base complexes, Physical Chemistry Chemical Physics, 16 (2014) 1150-1160.
[284] S. Shultz, M. Bass, R. Semiat, V. Freger, Modification of polyamide membranes by hydrophobic molecular plugs for improved boron rejection, Journal of Membrane Science, 546 (2018) 165–172.
[285] E.I. Givargizov, Graphoepitaxy as an approach to oriented crystallization on amorphous substrates, Journal of Crystal Growth, 310 (2008) 1686–1690.

[286] E.I. Givargizov, Mechanisms of oriented crystallization in artificial epitaxy (graphoepitaxy), Thin Solid Films, 189 (1990) 389-396.
[287] J. Hutfles, W. Chapman, J. Pellegrino, Roll-to-roll nanoimprint lithography of ultrafiltration membrane, Journal of Applied Polymer Science, 135 (2017) 45993.

Appendix A

List of Abbreviations

(Ordered alphabetically)

^{1}H-NMR	Proton nuclear magnetic resonance spectroscopy
AAc	Acrylic acid
AFM	Atomic force microscopy
AIBN	*N,N'*-Azobisisobutyronitrile
ATR-FTIR	Attenuated total reflection Fourier transform infrared spectroscopy
ATRP	Atom transfer radical polymerization
BMPB	2-bromoisobutyryl bromide
C.P.M	Concentration polarization modulus
CECP	Cake-enhanced concentration polarization
CEOP	Cake-enhanced osmotic pressure drop
CP	Cloud point
CPES	Commercial polyethersulfone
CSA	D(+)-10-Camphorsulfonic acid
DLVO	Derjaguin–Landau–Verwey–Overbeek interaction energy
EDC	1-ethyl-3-(3-dimethylaminopropyl) carbodiimide
FRP	Free radical polymerization
GPC	Gel permeation chromatography
IEP	Isoelectric point
IP	Interfacial polymerization

LCST	lower critical solution temperature
LIPS	Non-solvent liquid-induced phase separation
LIPSμM	Liquid-induced phase separation micro-molding
MED	Multiple-effect distillation
MF	Microfiltration
MIL	Micro-imprinting lithography
MPD	1,3-Benzenediamine (*m*-Phenylenediamine)
MSF	Multi-stage flash distillation
NF	Nanofiltration
NHS	*N*-Hydroxysuccinimide
NIL	Nanoimprinting Lithography
NIPAAm	*N*-Isopropylacrylamide
NMP	*N*-Methyl-2-pyrrolidone
P(NIPAAm-co-AAc)	Poly(*N*-isopropylacrylamide-co-acrylic acid) random copolymers
PA	Polyamide
PAAc	poly(acrylic acid)
PB	Phosphate buffer
PDMS	Polydimethylsiloxane
PES	Polyethersulfone
PMMA	Poly(methyl methacrylate)
PNIPAAm	Poly(*N*-isopropylacrylamide)

PSμM	Phase Separation Micro-Molding
PSF	Polysulfone
PVDF	Polyvinylidene fluoride
PVP	Polyvinylpyrrolidone
RO	Reverse Osmosis
SDS	Sodium dodecyl sulfate
SEM	Scanning electron microscope
SI-ATRP	Surface-initiated atom transfer radical polymerization
TDS	Total dissolved solids
TEA	Triethylamine
TEG	Triethylene glycol
TFC	Thin-film composite
TMC	1,3,5-Benzenetricarboxylic acid chloride (Trimesoyl chloride)
UF	Ultrafiltration
VIPS	Non-solvent vapor-induced phase separation
VIPSμM	Vapor-induced phase separation micro-molding
XPS	X-ray photoelectron spectroscopy

List of Symbols and Letters

(in order of appearance)

pH	Numeric scale describes acidity or basicity of an aqueous solution	--
J_i	Flux of component *i*	L/h.m^2
D_i	Diffusion coefficient	m^2/h
J_v	Water flux	L/h.m^2
A'	Water permeability	L/h.m^2.bar
ΔP	Transmembrane pressure	bar
$\Delta\pi$	Osmotic pressure difference across the membrane	bar
M	Salt molar concentration in feed solution	mol./L
R	Universal gas constant	J/mol.K
T	Absolute temperature	°K
π	Osmotic pressure	bar
J_{salt}	Salt flux	mol./h.m^2
B	Salt permeability	m/h
C_{feed}	Solute concentration in feed solution	mol./L or ppm
$C_{permeate}$, C_p	Solute concentration in permeate solution	mol./L or ppm
C_b	Solute concentration at the bulk	mol./L or ppm
C_m	Solute concentration near the membrane surface	mol./L or ppm
δ	Boundary layer thickness	nm
V	Total permeate volume	L
T	Filtration time	min
Q_0	Initial flow rate	L/h
K_c	Constant for cake filtration mechanism	--
R_e	Reynold number	--

R_m	Membrane resistance	m^{-1}
R_c	Cake layer hydraulic resistance	m^{-1}
$\Delta\pi_m^*$	Cake-enhanced osmotic pressure drop	bar
M_d	Mass of deposited cake layer per unite membrane surface area	g/m^2
ϵ	Cake layer porosity	%
d_p	Particle size	nm
ρ_p	Particle density	g/cm^3
δ_c	Colloid cake layer thickness	nm
pK_a	Acid dissociation constant at logarithmic scale	--
T_g	Glass-transition temperature	°C
T_m	Melting temperature	°C
ε^*	Onset of cracking	%
θ_Y	Young's contact angle	degree (°)
γ_{SV}	Interfacial tension at solid/vapor	mN/m
γ_{SL}	Interfacial tension at solid/liquid	mN/m
γ_{LV}	Interfacial tension at liquid/vapor	mN/m
r	Roughness factor	--
θ_W	Wenzel apparent contact angle	degree (°)
θ_C	Cassie apparent contact angle	degree (°)
f_{SL}	Area fraction of the solid/liquid interface	--
f_{LV}	Area fraction of the liquid/vapor interface	--
RH	Relative humidity	%
p	Differential gas pressure required to displace liquid from sample's pores	bar
γ	Surface tension of wetting liquid	mN/m
D	Pore diameter	nm

ρ_{bulk}	Bulk density	g/cm^3
$\rho_{particle}$	Particle density (density of pure material)	g/cm^3
S_q	Root mean square roughness	nm
S_a	Average roughness	nm
S_V	Maximum valley depth	nm
S_P	Maximum peak height	nm
S_Z	Maximum height of the surface	nm
$S_{kewness}$	Symmetry of surface roughness data	--
ζ	Zeta potential	mV
η	Electrolyte viscosity	N.s/m^2
ε_0	Vacuum permittivity	F/m
ε	Dielectric constant (relative permittivity)	--
L	Length of the streaming channel	m
A	Cross section of the streaming channel	m^2
m	Mass of a permeate	g
$L_{M,m}$	Line width (in a surface pattern)	µm
$d_{M,m}$	Distance between two adjacent lines (in a surface pattern)	µm
$D_{M,m}$	Depth (in a surface pattern)	µm

List of Tables

List of Figures

List of Equations

Appendix B

Curriculum vitae

“The biography is not included in the online version for reasons of data protection"

“The biography is not included in the online version for reasons of data protection"

“The biography is not included in the online version for reasons of data protection"